Integral Probabilistic Reliability Assessment for Flood Defences

The Impact of Correlations

P.E. Kindermann

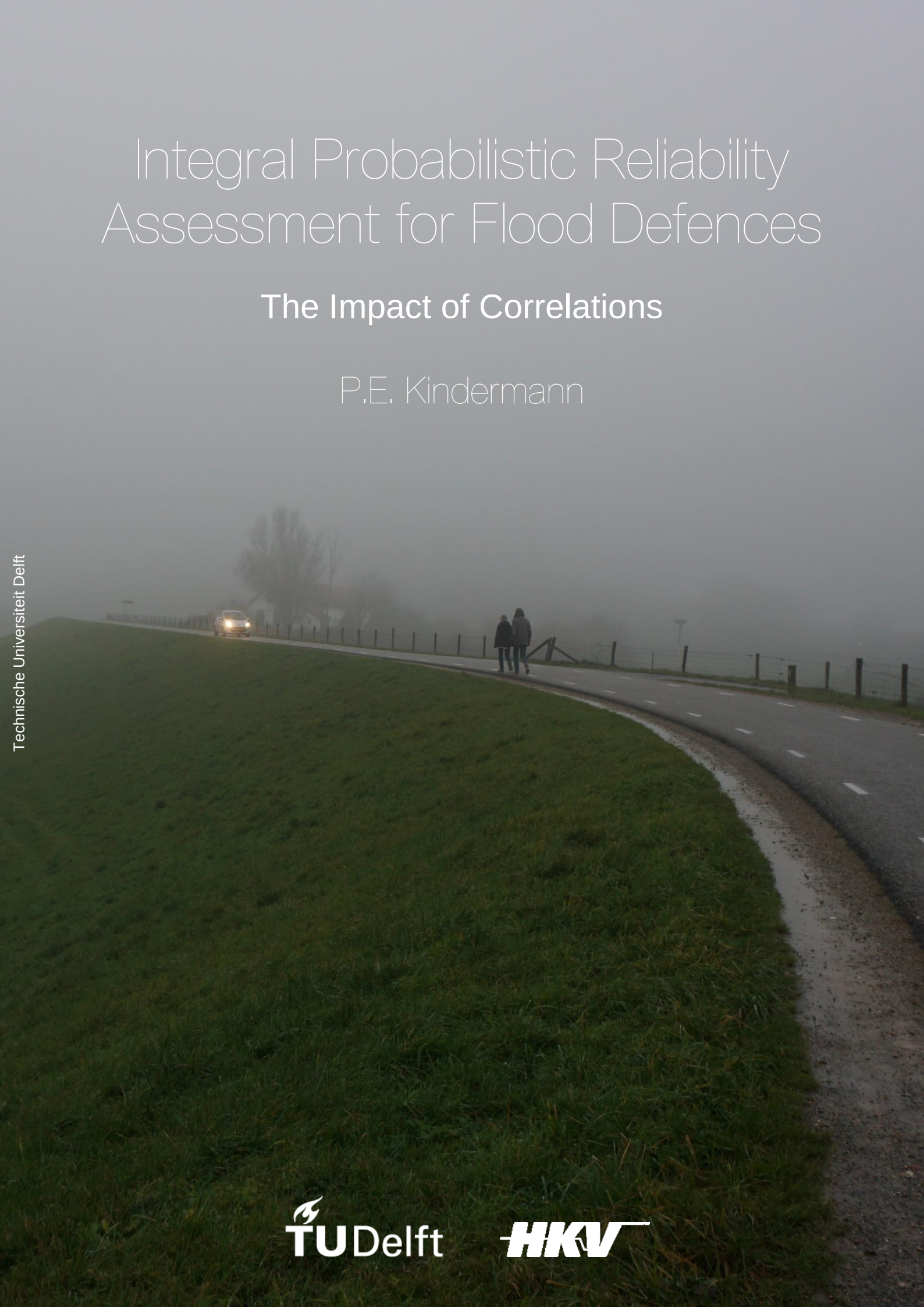

Technische Universiteit Delft

Integral Probabilistic Reliability Assessment for Flood Defences

The Impact of Correlations

by

P.E. Kindermann

to obtain the degree of Master of Science
at the Delft University of Technology,
to be defended publicly on Wednesday April 14, 2021 at 15:00.

Student number:	4366999	
Project duration:	July 16, 2020 – April 14, 2021	
Thesis committee:	Prof. dr. ir. M. Kok,	TU Delft, chair
	Ir. G. Pleijter,	HKV, daily supervisor
	Dr. ir. A.P. van den Eijnden,	TU Delft
	Ir. J.C. Pol,	TU Delft & HKV

An electronic version of this thesis is available at `http://repository.tudelft.nl/`.

TU Delft

HKV LIJN IN WATER

Preface

Flood safety is and will always be a challenging issue in the Netherlands and many other places around the world. Therefore, it is important that we keep on exploring the causes, consequences and solutions of flooding. Probabilistic tools enable us to approach flood safety from a risk perspective. They help us to provide an answer to questions like: 'What are the chances that a certain town gets flooded?' Thanks to centuries of experience and the efforts of many, these chances are very small in the Netherlands. Yet, new challenges such as climate change ensure that flood safety is an ever-present point of attention for humanity.

With this study into an integral probabilistic assessment of the failure probability of a Dutch flood defence, I finalise my Master of Science in Hydraulic Engineering at the faculty of Civil Engineering and Geosciences of Delft University of Technology. The research was conducted in collaboration with HKV Lijn in water.

First of all, I would like to thank my graduation committee for their support and expertise within this study. Gerbert, for his positivity and open-mindedness that motivated me a lot and helped me to keep seeing the relevance and applicability of my research. Joost and Bram, for their scientific perspective and their ability to constantly challenge me with difficult questions and remarks. Matthijs, for his guidance and enthusiasm. And of course his willingness to offer me a thesis topic at HKV in the first place, which can be seen as my entrance ticket to a career in flood safety, that I am really looking forward to getting started on.

Furthermore, I would like to express my gratitude to my colleagues at HKV for always being helpful and for making me feel like I am part of a team, even in times of working from home. Special thanks to David and Guus for answering so many questions for me. Besides, I thank the water board Rivierenland for providing the required data to base my study on. Also thanks to Juan Aguilar Lopez for providing answers, but especially more questions and challenges.

Last but not least, I would like to thank my friends and family for their support and love. Special thanks to my housemates, or collegues in 'home office' Lisa, Simone and Lieke. To Bart, for joining me on a long and rainy walk along 'my' dike. To Gijs, Mick and Bart for their reading and feedback.

Writing a thesis is in itself quite individual work, let alone during nine months of lockdown. Still, all these people made it possible to fully enjoy this period.

Enjoy reading!

Paulina Kindermann
Delft, April 2021

Abstract

Since 2017, Dutch flood defences are assessed according to new safety standards. These standards are based on flooding probabilities and rely on several assumptions and approximations. There are concerns that the combination of these assumptions leads to conservative results. Recently computed probabilities of failure are often much higher than expected by dike managers and the outcomes of former assessment methods. This conservative bias results in a large and expensive reinforcement task in the coming years which can be reduced by improving the current assessment procedure.

One of the reasons for the current conservatism is the assumption of mutual independence of dike sections and failure mechanisms. Currently, the different elements are assessed independently, while failure mechanisms and failure at different dike sections are likely to occur during the same extreme load event. Furthermore, correlations in space and between different parameters are present within the subsoil characteristics. Neglecting these correlations results in rather high estimations of the failure probabilities.

The aim of this thesis is to investigate how correlations affect the reliability assessment of a dike trajectory. To achieve this, an integral, full probabilistic model is developed that enables simultaneous assessment of dike sections and failure mechanisms while accounting for uncertainties and (spatial) correlations within the model input. The model is based on Monte Carlo simulation. The failure probability of a dike trajectory is computed by counting failure if one or more limit state function $Z_{j,k}$ for failure mechanism j of dike section k returns a negative realisation. Correlations between the model input parameters are provided by means of a Gaussian copula. A particular aspect of the model is the implementation of metamodeling for the assessment of macrostability. This failure mechanism cannot be described by an analytical limit state function that is easily implemented in the Monte Carlo framework. Therefore, metamodels are created by means of Gaussian process regression. This method makes it possible to assess macrostability within an integral, full-probabilistic framework that is able to include interdependencies between e.g. macrostability and piping, within acceptable computation costs. The model is applied to a case study of dike trajectory 43-4, which is located along the Waal between Sprok and Sterreschans, in the east of the Netherlands.

The effects of different plausible correlations have been studied. This research shows that including certain correlations can significantly reduce the assessed failure probabilities, by a factor ten or more in some situations. However, the impact of correlation strongly depends on the situation. The most significant reduction can be achieved for cases in which (1) parameters that play a dominant role in failure of the corresponding mechanism are correlated; (2) the failure probabilities of the different elements are similar, i.e. for a flood defence where failure is not dominated by one dike section or one failure mechanism; and (3) the failure probabilities of the corresponding elements are smaller than approximately 10^{-3}.

The model forms a solid, flexible basis that can easily be adapted or extended to improve the understanding about interactions between failure mechanisms, even though some aspects are simplified or neglected. All in all, the conservatism in current safety assessments can be partly solved by considering the interdependencies between mechanisms and dike sections and by approaching a dike trajectory as an integral system.

Contents

1

Introduction

1.1. Background

In the Netherlands, the majority of the inhabitants lives in flood-prone areas, located along rivers, in the delta and in the coastal area. If flooding would occur, 60% of the country would be inundated with water depths of more than five metres as a result (de Bruijn and van der Doef, 2011), as presented in Figure 1.1a. The flood defence systems along the rivers, coasts and lakes are thus of critical importance for the safety and liveability of the country. The flood protection is therefore legally laid down in the Water Act ('Waterwet'). Since 2017, new Dutch safety standards are applied that are based on the concept of flooding probabilities. By examining the flooding probability, both the loads and the strength are considered, while the old standards only considered the loads. The new standards are the result of a risk-based approach. This means that both the probability and the consequences of flooding play a role.

A primary flood defence, or dike ring, is divided in trajectories that are characterised by an equal threat and, in the event of a breach, by more or less equal consequences (Kok et al., 2017). Each dike trajectory has its own standard in terms of a required failure probability, that is based on (1) an allowable individual risk; and (2) on considerations for the societal and economic risks. The resulting norms are shown in Figure 1.1b.

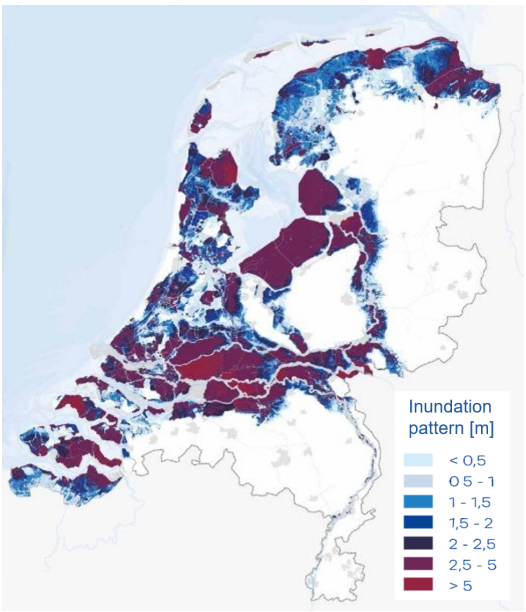

(a) Inundation pattern (Kok et al., 2017).

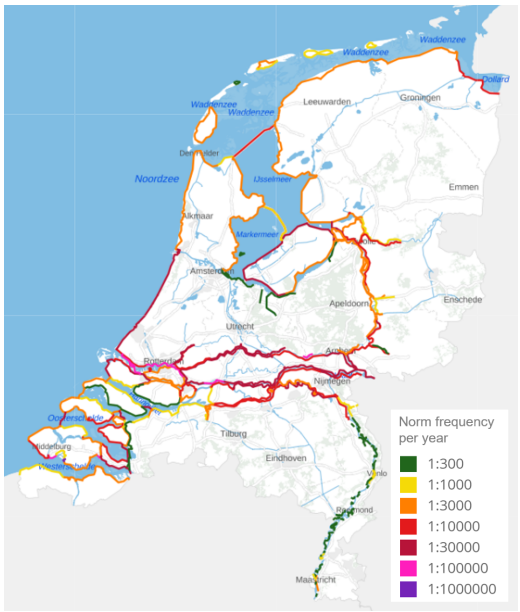

(b) Dike trajectories and their norms (HWBP, 2021).

Figure 1.1: The Netherlands: flooding consequences and protection norms.

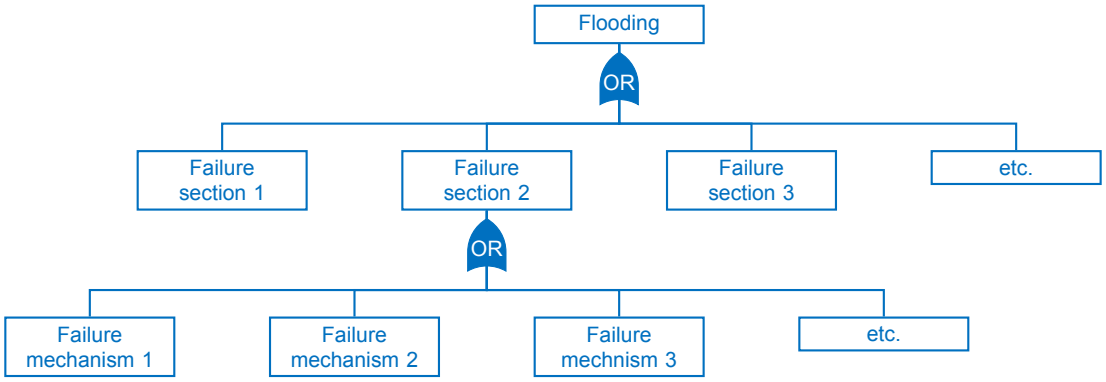

Figure 1.2: Fault tree of a dike trajectory.

1.1.1. Current assessment method

The new procedures for the safety assessment of the primary flood defences are described in the Legal Assessment Instrument ('Wettelijk Beoordelingsinstrumentarium'), from now on called the WBI. In this section, the WBI assessment procedure will be briefly described. For a theoretical background and more details, it is referred to Chapter 2 and Appendix B.6.

The safety standards are defined such that the overall risk becomes acceptable. Three different perspectives of risk have been applied in the standards: individual risk, societal risk and economic risk. The most stringent of the three perspectives determined the safety standard of a certain region. Risk is defined as probability of failure multiplied by the consequences due to failure. For each dike trajectory, the possible consequences of flooding have been analysed in terms of number of fatalities and economic damage. Based on a certain acceptable risk, the required annual failure probability, called the norm or target reliability, has been determined per dike trajectory.

A dike trajectory is characterised as a series system, in terms of dike sections and failure mechanisms, as illustrated in Figure 1.2. It means that only one dike section has to fail for one failure mechanism to induce system failure, i.e. breaching of the flood defence. This characterisation plays a major role in how the different elements are included in the assessment method. The required failure probability of a trajectory is divided over the different failure mechanisms ('faalkansbegroting') and subsequently divided over the corresponding sections by accounting for the so-called length-effect. This leads to a failure probability norm per section per mechanism (Rijkswaterstaat, 2017). The definitions of the different spatial scales are visualised in Figure 1.3. A dike section is defined such that its characteristics can be seen as constant over the section. Dike sections have a length varying from about a 100 metre to several kilometres, depending on the homogeneity of the dike stretch. Additional to the dike elements there may be dune stretches and structural elements within a flood defence system (Vrouwenvelder, 2006).

The assessment of a flood defence comes down to the comparison of the actual failure probability to the norm. This comparison is performed for the total dike trajectory, but also per section per mechanism. A normative cross-section is chosen for computing the actual failure probability of the corresponding dike section. The assessment is subdivided into assessment tracks ('toetssporen'). An assessment track is the way in which a certain failure mechanism is assessed. These assessments differ significantly from each other, depending on the available calculation methods. The tracks make use of deterministic, semi-probabilistic or probabilistic computation methods. In a probabilistic analysis, the uncertainty of parameters is taken into account. Any possible combination of strength and resistance values is assessed, in order to determine a failure probability. Most of the tracks, however, consist of deterministic or semi-probabilistic calculations, since a probabilistic method is not yet available. In semi-probabilistic methods, the parameters are included as design values, meaning that their uncertainty is not explicitly accounted for. The result is therefore not a failure probability, but an assessment category. To be more specific, the result is often a factor of safety (semi-probabilistic case) or a statement *satisfies* versus *does not satisfy* (deterministic case), that are translated into a deviation from the norm (Diermanse et al., 2016).

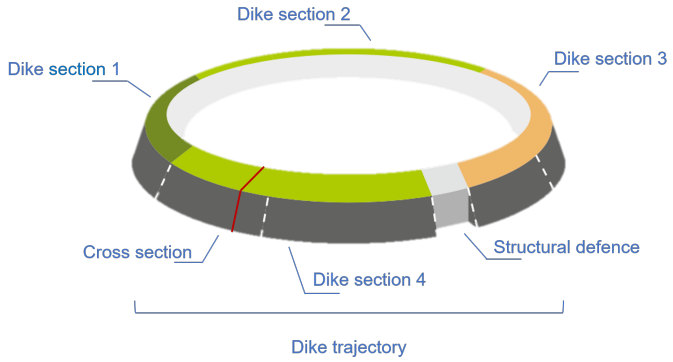

Figure 1.3: Definitions of the different spatial scales (Kok et al., 2017).

Subsequently, the assessment results per mechanism per dike section are translated into a total failure probability of the dike trajectory. The procedures of upscaling failure probabilities from sections to trajectories and combining the failure mechanisms is called *assemblage*. If an assessment track resulted in a failure probability, sections are combined to trajectories under the assumption of either mutual (full) dependence or mutual independence. This provides a relatively simple, but reasonable approximation for the combined failure probability of the trajectory. Mutual dependence is mainly a result of the fact that extreme loads for these sections occur during the same events and is a good approximation for failure mechanisms like overtopping. For geotechnical assessment tracks, however, the assumption of mutual independence between sections is considered more appropriate. Despite the differences in the degree of mutual dependence between sections, a generic approach is applied, that should be followed for each assessment track. It is summarised in the following steps (Diermanse et al., 2016):

1. Estimate the failure probability of the dike trajectory, assuming mutual independence of the sections (upper bound);
2. Estimate the failure probability of the dike trajectory, based on the largest failure probability of the sections (i.e. mutual dependence) and the estimated length-effect (lower bound);
3. Choose the minimum of the two estimated failure probabilities. By taking the minimum, a large overestimation of the trajectory failure probability is avoided.

Thereafter, these trajectory failure probabilities per failure mechanism are combined to the total failure probability of a dike trajectory. For this, the mechanisms are combined under the assumption of mutual independence.

For assessment tracks that lead to an assessment category instead of a probability, sections and failure mechanisms are combined to trajectories by the principal of the weakest section or mechanism is normative (de Waal, 2016). So, the most unsafe section or mechanism determines the assessment result for the trajectory. The last step is the comparison to the trajectory norm, to conclude whether the safety requirement is fulfilled or not.

1.2. Problem Definition

These assessment methods are quite new and still in development. The procedure, as explained in Section 1.1, is based on several assumptions and approximations of reality. The combination of these assumptions leads to the fact that the current approach is conservative and contributes to the high failure probabilities that have been the result of recent assessments. The lately computed (or by factors of safety implied) probabilities of failure are often much higher than expected by experience and by the outcomes by former assessment methods (ENW, 2020). A conservative bias does not pose a problem for trajectories that, despite the conservatism, fulfill the norm. But for trajectories with relatively high failure probabilities, this is different. A less conservative assessment might lead to a smaller number of required dike reinforcements, or to smaller dimensions of such reinforcements. More realistic and

credible estimates of the failure probabilities are needed. Possibilities for improvement of the current assessment method mainly lie in the following aspects:

1. Not every track is currently assessed in the same way, in terms of load definition, accuracy of the results and interpretation of the norms. Several failure mechanisms cannot be assessed by a probabilistic computation yet. It is therefore not possible to compute a failure probability for all failure mechanisms. Moreover, it means that the uncertainty of the strength and resistance parameters is not explicitly included for all mechanisms.
2. In semi-probabilistic computations, design (peak) values are considered, implying that, in case of failure mechanisms with more than one relevant load parameter, these peaks occur at the same time, which is not realistic and leads to conservative conclusions (Rongen et al., 2019).
3. The mutual correlation between sections and failure mechanisms is not considered explicitly, leading to less accurate results. The current assumption of mutual independence is a conservative assumption. In reality, the different failure mechanisms are likely to occur at the same time during an extreme load event. Neglecting this fact, means that the same failure event is wrongly included multiple times when the failure probability of a trajectory is computed. This leads to unnecessary conservative results, especially in the case of large failure probabilities. Also the omission of correlations in space and between parameters can result in too high estimates of the failure probabilities.
4. Within the assessment tracks, failure is often defined as occurrence of the mechanism under consideration, instead of as inundation of the hinterland, implying that residual strength is not considered. Also, the variation of the loads in time during a flood event is not included. Both assumptions lead to conservative results.

For a more accurate assessment of the actual failure probabilities, these aspects should be included.

1.3. Research Objective

This thesis will focus on an improvement for the items 1 and 3 of the enumeration in the previous section, with the main focus on item 3: correlations. Particularly, the aim is to incorporate both the uncertainties and correlations in order to investigate the effect of these adaptations on the failure probability of a flood defence, in an integral manner. The objective of this research can be summarised by the following research question:

What is the effect of assessing the failure probability of a dike trajectory in one integral full-probabilistic framework that includes correlations?

This question is answered by elaborating on a method for integral and full-probabilistic assessment of the total failure probability of an earthen dike. The failure probabilities per dike section per failure mechanism will be computed within one integral probabilistic framework, by means of a Monte Carlo simulation. The method takes into account the uncertainty of the input variables, by considering the marginal distribution of each variable per dike section. Furthermore, the correlations between the variables can be included by means of a multivariate distribution function using copulas. Random, correlated samples of the variables will be drawn from the copula. For every realisation, the limit state functions Z of each failure mechanism and each dike section are evaluated. If at least one evaluation results in $Z < 0$, failure is counted. These steps will be repeated for N iterations. It results in the sectional failure probabilities per mechanism and in the total failure probability of the trajectory.

The method is applied to a case study: the dike trajectory 43-4 from Sprok to Sterreschans in the east of the Netherlands, as illustrated in Figure 1.4. For this trajectory the input parameters are known and sectional failure probabilities have been assessed according to the WBI procedure.

This probabilistic model, from now on often called ‘the model’, will be used to investigate the impact of different correlations. The impact is expressed in an increase or decrease of the corresponding failure probabilities and in a resulting correlation between the Z-realisations of the corresponding elements. In addition, the total failure probabilities that result from the model will be compared to failure probabilities according to the WBI assemblage procedure.

The described approach is intended to come to an answer to the main research question. The following sub questions can be formulated, that form the basis of the methodology:

1. **Which limit state functions are available in the literature that can be applied in a probabilistic framework for the different failure mechanisms?**
   This question will be answered by means of a literature study. It results in an overview of the current assessment methods of the WBI and other possible approaches to define the different failure mechanisms. The aim is to decide how the different failure mechanisms will be described through limit state functions that are suitable for the probabilistic model of this study.
2. **What is the impact of incorporating the different correlations on the failure probabilities and what correlations have the strongest impact?**
   A sensitivity analysis is performed to assess the effects of including the different correlations on the failure probabilities. The main interest lies in finding the correlations with the highest impact.
3. **What are resulting dependencies between different failure mechanisms and sections?**
   Correlations in the input variables may lead to dependencies in failure of different mechanisms or neighbouring dike sections. Scatter plots of the resulting limit state evaluations will be created to investigate this.
4. **How do the total failure probabilities that result from the integral probabilistic assessment compare to those based on the WBI assembly procedure?**
   The total failure probabilities are determined by counting failure if at least one negative limit state evaluation occurs within an iteration of the Monte Carlo simulation. The resulting failure probabilities will be compared to those estimated according to the WBI assemblage procedure. Situations with and without correlations will be compared.

1.4. Scope

This research will be based on the assessment of the case study. Therefore, only failure mechanisms that are relevant for the dike trajectory under consideration will be implemented in the model. However, the aim of the research is not to exactly reproduce the failure probabilities that result from the assessment of the case study by the water authority. The aim is to determine the impact of correlations and of the integral approach in a qualitative way, i.e. in comparison to a reference situation. Some aspects, especially in the determination of the hydraulic loads, will be simplified or neglected, due to time constraints. Therefore, the resulting failure probabilities of this study should not be used to assess the actual safety of the flood defence. Also other aspects, like residual strength or time dependence are not taken into account within this thesis.

Figure 1.4: Case study: Dike trajectory 43-4 between Sprok and Sterreschans.

I

Literature

2

Reliability Theory

In this chapter, an introduction to the theory behind different techniques and concepts, that are relevant for the model, will be presented. About several topics, more information can be found in Appendix A. The discussed theory is the basis for certain model decisions, that will be elaborated in Section 2.6.

2.1. Failure Probability

Simply said, the safety of a system can be assessed by verifying whether the resistance R is larger than the load S, such that no failure occurs. This is usually described by a limit state function Z:

$$Z = R - S \tag{2.1}$$

So, failure occurs if $Z < 0$, or $R < S$. Both the resistance and the load are generally not constant, but stochastic and can be described by probability density functions. The stochastic nature of the variables originates from several factors, as will be briefly explained in Section 2.2.

Therefore, failure should be assessed by means of the *probability* of failure. Obviously, the probability of failure equals the probability that the limit state function is smaller than 0: $P_f = P(Z < 0)$. If the probability density functions of R and S are known, the failure probability $P(F_i)$ or $P_{f,i}$ of element i is defined as:

$$P_{f,i} = P(S_i > R_i) \tag{2.2}$$

If R and S are independent, the joint probability density function $f_{RS}(r,s)$ follows by multiplication of their marginal distributions. Now, the probability of failure of the system is equal to the volume of the joint probability density function in the unsafe region, as can be seen in Figure 2.1. Mathematically, this can be expressed by:

$$P_f = \int\int_{Z<0} f_R(r) f_S(s)\, \mathrm{d}r\, \mathrm{d}s \tag{2.3}$$

The failure probability of a flood defence is defined as 'the probability of losing the water retaining capacity of a dike trajectory, as a consequence of which the area protected by the dike trajectory may overflow such that fatalities or substantial economic damage occur' (KPR, 2019). In that case, the failure probability is the result of a series system where each basic element, i.e. the failure mechanism j for section k can be described by a complex limit state function $Z_{j,k}$. For these complex systems, R and S depend on a number of quantities. In other words, they are functions of variables X that can be both stochastic or deterministic: $R = R(X_1, X_2, \ldots, X_m)$ and $S = S(X_{m+1}, X_{m+2}, \ldots, X_n)$. Every stochastic parameter X can be described by a certain distribution function with a mean and standard deviation. The distribution functions of R and S therefore depend on the distribution functions of these variables:

$$P_f = \int\int\int_{Z<0} \ldots \int f_R(x_1, x_2, \ldots, x_m) \cdot f_S(x_{m+1}, x_{m+2}, \ldots, x_n)\, \mathrm{d}x_1\, \mathrm{d}x_2 \ldots \mathrm{d}x_n \tag{2.4}$$

where f_R is the m-dimensional probability density function (PDF) of the m resistance variables and f_S is the $(n-m)$-dimensional probability density function of the $n-m$ load variables.

Finding a solution for Equation 2.4 is difficult for two reasons: (1) the Z-function is too complex and (2) the variables X can have mutual dependencies and different marginal distributions, as will be explained in Section 2.4. These issues can be solved by approximating the failure probability using probabilistic computation techniques (Section 2.3) and by the definition of a multivariate joint distribution function using copulas (Section 2.5).

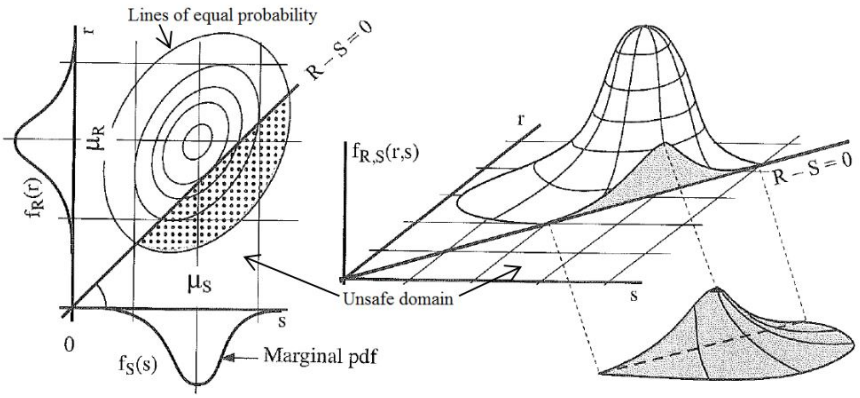

Figure 2.1: Probability of failure (Jonkman et al., 2017).

2.2. Uncertainties

There are different types of uncertainties that contribute to the total uncertainty of safety assessments of flood defences. Uncertainties mainly arise from the natural variability of parameters, sometimes called aleatory/inherent uncertainties or randomness. On the one hand, this involves uncertainty in time, for example the maximum yearly river discharge. Even with more measurements, this uncertainty can hardly be reduced. This variability is handled by capturing e.g. the river discharge in a probability distribution. On the other hand, there is variability in space, which is mainly an issue for geometric parameters and soil properties. For example, the crest height of a dike or the permeability of the soil is not the same everywhere. Soil properties show a large fluctuation in the depth direction and a smaller fluctuation in the length direction, as illustrated in Figure 2.2. The spatial variability is partly dealt with by dividing a flood defence trajectory into sections - typically 200 to 1000 m long - that can be seen as homogeneous, meaning that the statistical characteristics of the stochastic variables remain constant within that dike section (Vrouwenvelder, 2006). This does not imply that the value of a stochastic is constant: it often shows a spatial variation over the length of a section, which can be handled by assigning probability distributions to the parameters per dike section. The vertical variability is often handled by averaging over a certain soil layer (Schweckendiek et al., 2017). Another method to deal with these uncertainties is by taking into account different scenarios during the assessment/ For example, of the soil layer structure.

Another source of uncertainty is knowledge - or epistemic - uncertainty. These are uncertainties about aspects that could in principle be known, but that are not in practice. For example, the strength of a soil type is a property that we are able to measure. However, due to a limited accuracy and/or spatial resolution of the measurements, there remains uncertainty about the real value of this property. This is called statistical uncertainty. The difference, though, with natural variability is that we can reduce the uncertainty by e.g. taking more measurements. Finally, there are also uncertainties that arise when translating reality into a model, called model uncertainties.

Most stochastic variables cover a continuous range of possible values. For these variables the uncertainty is often modelled by continuous probability distributions. The most used distributions in flood safety assessments are the normal and lognormal distributions. The lognormal distribution is suitable for parameters for which a value smaller than zero is physically not possible. Variables for which the probability distribution of the extreme values is important - e.g. the water level - are often modelled by generalized extreme value (GEV) distributions.

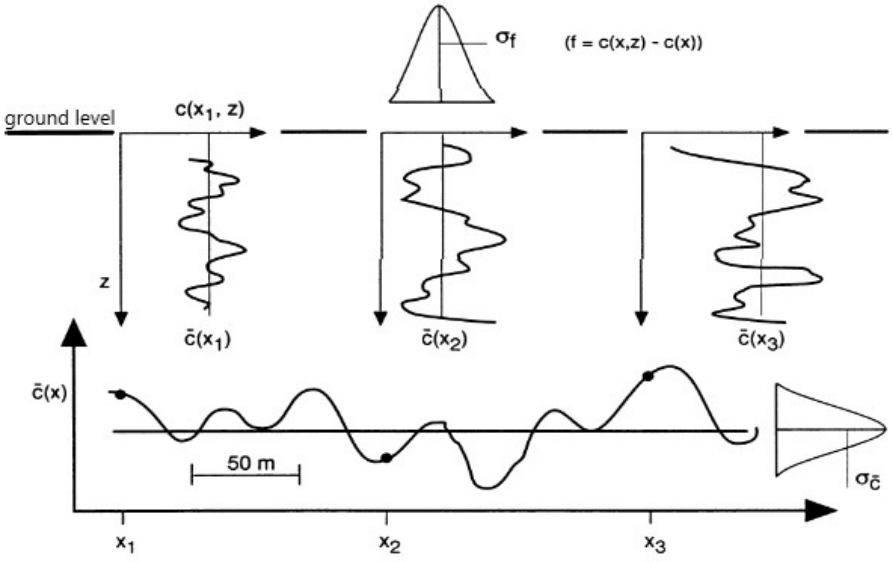

Figure 2.2: Spatial variation of a soil parameter (Vrouwenvelder, 2006).

2.3. Reliability Methods

Methods to estimate the failure probability can be divided into the following groups, that will be elaborated below:

1. Level 0 methods: deterministic calculations
2. Level I methods: semi-probabilistic design
3. Level II methods: approximation / FORM
4. Level III methods: numerical integration or Monte Carlo

2.3.1. Level 0 methods: deterministic calculations

The assessment of safety is based on one nominal value for the resistance, one for the strength and on one global (empirical) safety factor (Jonkman et al., 2017):

$$R_{nom} \leq \gamma \cdot S_{nom} \tag{2.5}$$

The uncertainty and variability of the strength and resistance is not accounted for. This approximation is only acceptable in a very limited amount of situations.

2.3.2. Level I methods: semi-probabilistic design

In fact, a semi-probabilistic assessment does rely on safety standards, limit state functions and statistical properties of the statistic variables, making it closely related to a probabilistic assessment. Yet a semi-probabilistic assessment rests on a number of simplifications and approximations, giving it the appearance of a deterministic procedure (Kanning et al., 2015). The uncertain parameters are modeled by one characteristic value for the load and resistance. For the load parameters, the characteristic value S_c corresponds to a high percentile of the distribution. For strength parameters, the characteristic value R_c corresponds to a low percentile of the distribution. Furthermore, partial factors γ_i are used, that are based on level II calculations (Jonkman et al., 2017). The combinations of characteristic values and partial factors form the design values. The design values of stochastic resistance and load variables, R_d and S_d, with a given mean value μ_i and standard deviation σ_i are equal to:

$$R_d = \mu_R + \alpha_R \cdot \beta_T \cdot \sigma_R = R_c/\gamma_R \tag{2.6}$$

$$S_d = \mu_S - \alpha_S \cdot \beta_T \cdot \sigma_S = S_c \cdot \gamma_S \tag{2.7}$$

where α_i are the FORM influence coefficients, that will be explained in the next section. β_T is the target reliability index, as explained in Appendix A.1. In the WBI 2017, the γ_S value is often set equal to 1.0 (Kanning et al., 2015).

This semi-probabilistic approach is common practice for most of the failure mechanisms in the current assessment method, as illustrated in Table B.1 on page 102.

2.3.3. Level II methods: approximation / FORM

In a level II method, the uncertain parameters are modelled by the mean values and the standard deviations, and by the correlation coefficients between the stochastic variables. Also, the stochastic variables are implicitly assumed to be normally distributed (Jonkman et al., 2017). The most common method is the First Order Reliability Method (FORM). In a FORM analysis, the limit state function is linearised in the design point, using Taylor expansion. The design point is the location along the limit state ($Z = 0$) where the probability density is maximal. In other words, the most probable failure point. In the FORM analysis, the specific location of the design point is determined by an iterative procedure. FORM is executed in the standard normal space U. In this space, the design point is easily defined, since it is the location along the limit state that is closest to the origin, since the highest probability density is at the origin for standard normally distributed variables. The distance from the origin to the design point is equal to the reliability index β, as defined in Equation A.4 of Appendix A.1 (p.94). If β is known, the probability of failure can be easily computed with this equation. The linearised and normalised limit state function resulting from a FORM analysis looks like:

$$Z_{FORM} = \beta - \sum_{i=1}^{n} \alpha_i u_i \tag{2.8}$$

The advantage of FORM is that the computational effort is reduced by linearisation of the limit state function. Another advantage is the definition of the α_i-values. These are in fact the direction cosines of the perpendicular or vector $\vec{\beta}$. They are called the sensitivity factors, because they are a measure for the relative importance of the standard deviation of a basic variable to the reliability index. The α_i-values are the components of the unit vector according to $\overrightarrow{OD} = \beta\vec{\alpha} = \vec{\beta}$. The FORM approach is visualised in Figure 2.3. Note that there will always be an error in the determination of the failure probability, as long as the real Z-function is non-linear. However, due to the linearisation in the design point, it is a good approximation for points in the vicinity of the design point, which is generally the case for failure events.

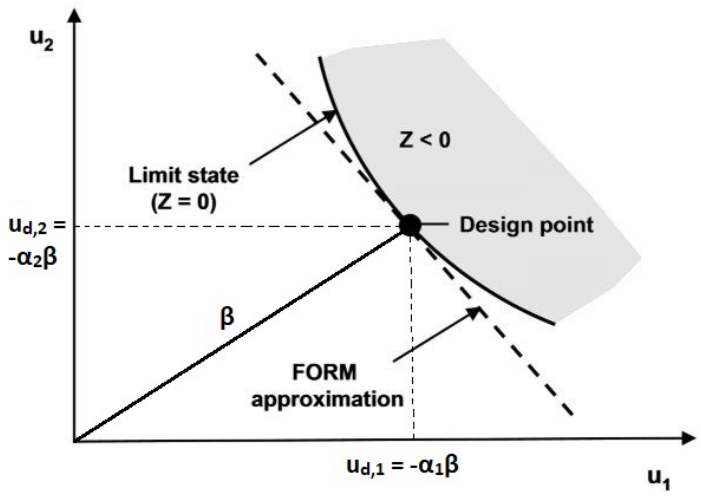

Figure 2.3: Visualization of FORM.

2.3.4. Level III methods: numerical / Monte Carlo

In level III methods, the uncertain quantities are modelled by their joint distribution functions. The probability of failure is calculated exactly, by numerical integration or Monte Carlo simulation.

Numerical integration

Numerical integration computes the failure probability by discretising the random variables $X_1 ... X_n$ that describe the resistance and strength. Each variable is discretised over a range that is relevant for failure, and subsequently each combination of discretised values of the X-variables is used to compute the limit state function. The probabilities of all the combinations that lead to $Z < 0$ are summed, resulting in an estimate of the overall probability of failure (van Balen et al., 2016). The disadvantage of numerical integration is that the number of integration steps increases exponentially with the number of stochastic variables, which makes standard numerical integration techniques computationally intensive.

Monte Carlo simulations

As previously mentioned, the calculation of P_f through numerical integration is rather difficult in the case of more than two variables. In those cases, Monte Carlo simulations (MCS) provide a suitable alternative in order to calculate P_f. The method that will be elaborated is called crude Monte Carlo. Crude Monte Carlo sampling refers to the repeated sampling of the variables from their multivariate distribution function $f_X(x)$ or, if the variables are mutually independent, sampling from the corresponding marginal distribution functions $f_{Xi}(x_1), ..., f_{X_n}(x_n))$. So, Monte Carlo allows us to model interdependency between input variables, by sampling from their joint distribution. A single sample x_i refers to a vector of length n that contains one randomly sampled value for each variable, with n the number of random variables. The samples x_i basically represent *events*, although the sampling may also involve variables that present the resistance of the flood defence, instead of only the loads. For each sample x_i, the resulting value of the limit state function $Z(x_i)$ is computed. The probability of failure is estimated as the ratio of samples for which $Z(x_i) < 0$ - denoted as N_f - to the total number of samples N:

$$P_f = \frac{N_f}{N} = \frac{\sum_{i=1}^{N} I(Z(x_i) < 0)}{N} \tag{2.9}$$

in which $I(Z(x_i) < 0) = 1$ if $Z < 0$ and 0 otherwise. Naturally, the number of required simulations N increases as P_f decreases. For the reliability assessment of flood defences, that generally have a very low failure probability, it means that the computation time of a Monte Carlo simulation can be rather long. The required number of samples, N_{min}, to provide a reliable estimate of the probability of failure can be determined based on the desired uncertainty (van Balen et al., 2016). To quantify the uncertainty on the computed failure probability, its coefficient of variation V_{P_f} can be calculated as:

$$V_{P_f} = \sqrt{\frac{1 - P_f}{N \cdot P_f}} \tag{2.10}$$

As the probability of failure of a Dutch flood defence is typically in the order of 10^{-5} and the desired coefficient of variation is for example 0.05, then, already $4 \cdot 10^7$ model evaluations N are needed. This can result in unacceptably high computation costs, depending on the complexity of the system.

To increase the efficiency of the crude Monte Carlo method, i.e. to decrease the computation costs, a so-called 'importance sampling' technique can be used. The aim of this technique is to obtain more realisations of the random sample vector x_i that are located in the unsafe domain D_f. This will decrease the number of samples and Z-function evaluations required to produce a reliable estimate of the failure probability. In order to achieve this, the density function is essentially shifted towards the failure domain, so that the likelihood of a failure sample increases. This is done by defining a sampling function $f_S(x)$, that is chosen such that its maximum is located in the domain that contributes most to P_f. Then, the following formula is used to compute the failure probability:

$$P_f = \frac{1}{N} \sum_{j=1}^{N} I[Z(x_j) < 0] \frac{f_X(x_j)}{f_S(x_j)} \tag{2.11}$$

where f_X is the real distribution and f_S is the sampling PDF. The samples x_j are distributed according to $f_S(x)$. The fraction f_X/f_S is in fact a correction term to make the estimate of P_f unbiased. The efficiency of this importance sampling technique is strongly dependent on the choice of $f_S(x)$. One can for example locate $f_S(x)$ at the design point. In that case, the number of realisations in the unsafe domain is approximately 50% (Jonkman et al., 2017).

Importance sampling can be applied very successfully in reliability problems with a not too large number of stochastic parameters. However, applications to high-dimensional reliability problems are more complex and much research is still done into its development (Liu and Elishakoff, 2020).

2.4. Dependence

Modelling dependencies is an important and widespread issue in risk analysis. It often occurs in reality that variables of the strength or resistance show some amount of mutual dependence. A is dependent on B if the occurrence of A does influence the probability of occurrence of B. Dependence is based on physical attributes of the events or variables under consideration. Calculating under the assumption of independence is generally easier, but, assuming independence when in fact the contrary is true can lead to large inaccuracies (Jonkman et al., 2017). Based on the results of the study of Aguilar López et al. (2014) - that investigated the correlation between the hydraulic conductivity k and the grain size d_{70} for piping - it could be proved that when the correlation increases, the probability density function changes as the area in the tails is more populated. This means that the frequency for values located along the PDF will change. For the case of piping, a higher correlation degree between the two studied variables will always imply a lower probability of failure of the flood defence. Aguilar López et al. (2014) also mentioned several studies that show that the influence of correlation greatly affects events of low frequency. It indicates that including correlations is of major importance for reliability assessments of flood defences that often consider (flood) events of low frequency.

The measure of mutual dependence of two stochastic variables can be expressed by the Pearson's product moment correlation-coefficient $\rho_{XY} = \rho(X,Y)$ that is defined as:

$$\rho_{XY} = \frac{\mathrm{cov}(XY)}{\sigma(X)\sigma(Y)} \tag{2.12}$$

where $\mathrm{cov}(XY)$ is the covariance (see Appendix A.2 on p.94). The correlation coefficient has the following properties:

- If X and Y are independent: $\rho_{XY} = 0$
- If X and Y are completely positive linear dependent: $\rho_{XY} = +1$ (See Figure 2.4a)
- If X and Y are completely negative linear dependent: $\rho_{XY} = -1$ (See Figure 2.4b)
- In general: $-1 \leq \rho_{XY} \leq +1$

However, Pearson's correlation only assesses linear relationships. In reality, it happens that dependence is nonlinear, for example events might have a higher degree of dependence for extreme values. An alternative is Spearman's rank correlation coefficient, $r_{X,Y} = r(X,Y)$ or ρ, which is a non-parametric measure of rank correlation. The Spearman correlation between two variables is equal to the Pearson correlation between the rank values of those two variables:

$$r(X,Y) = \rho(F_X(X), F_Y(Y)) = \frac{\mathrm{cov}(rX, rY)}{\sigma(rX)\sigma(rY)} \tag{2.13}$$

where F denotes the cumulative distribution function (CDF) of the variables X and Y respectively, which is equal to the ranks rX and rY. F can be a parametric distribution estimate - e.g. a Gaussian CDF - or based on an empirical estimate: $\hat{F}_X(x) = \#\,\mathrm{samples} \leq x/(N+1)$.

Spearman's correlation coefficient can be used to express *monotonic dependence*, which holds for both linear and nonlinear relationships. A perfect Spearman's correlation of ± 1 occurs when the observations of two variables have identical ranks (= the relative position label of an observation within the variable).

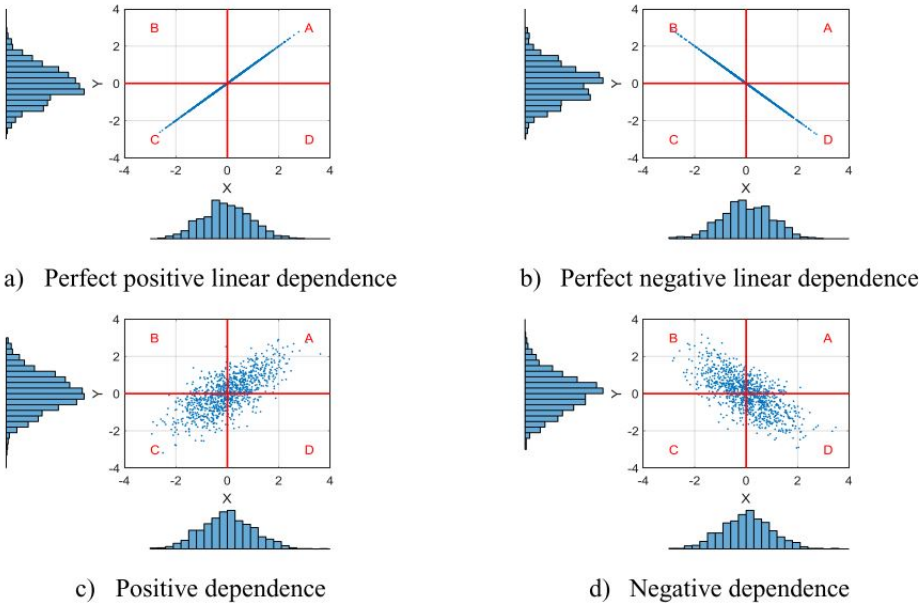

Figure 2.4: Dependence pattern examples for bivariate normal distributions (Jonkman et al., 2017).

2.4.1. Spatial correlations

Spatial correlation means that the value of X at location 1 and the value of X at location 2 are dependent, but it can also occurs between two different parameters in space (X at location 1 and Y at location 2). Spatial correlation exists for many soil properties. It arises from the fact that soil layers, that extent over a large area in space, originate from the same geological deposit. Extensive research has been done about the effect and assessment of spatial correlation of load and resistance estimation on flood defences in the Netherlands (Vrouwenvelder, 2006), (Kanning, 2012). How a variable depends on itself is called *autocorrelation*. It exists along both space and time, but for this research only correlation in space is considered. If the spatial variability of a stochastic variable is large, it means that its spatial autocorrelation is small. Similarly, a small spatial variability means that the spatial autocorrelation of the stochastic variable is large. The spatial correlation structure of each stochastic variable X_k can be described by a one-dimensional correlation function ρ_k (Vrouwenvelder, 2006):

$$\rho_k(\Delta x) = \rho_{x,k} + (1 - \rho_{x,k}) \exp\left(-\frac{\Delta x^2}{{d_{x,k}}^2}\right) \tag{2.14}$$

where:

- ρ_k = Correlation between two cross-sections within the same section ($\rho \geq 0$)
- Δx = Distance between two cross-sections / points of consideration [m]
- $\rho_{x,k}$ = Constant that represents the residual correlation of variable X_k / lower limit of ρ_k
- $d_{x,k}$ = Correlation length [m]

The correlation length $d_{x,k}$ represents how quickly the correlation of variable X_k decreases over distance in x, also called the fluctuation scale. For a large d_x, the correlation coefficient ρ_k between two cross-sections is also large and the spatial variability is thus small. If the value for the residual correlation $\rho_{x,k}$ increases, the correlation coefficient ρ_k between two cross-sections also increases. However, this effect diminishes if the two cross-sections are closer to each other. For geotechnical properties, the spatial correlation should not only be considered in the horizontal direction, but in the vertical direction y as well. However, this effect is not further elaborated within this research.

The failure probability of a section is thus length-dependent due to the spatial variability of the stochastic variables: The probability of the limit state function being less than zero increases with length and

decreases when spatial correlations are strong (Jongejan et al., 2013), which is also referred to as the length-effect, as mentioned earlier. This type of length-effect can also be represented as follows:

$$\text{length-effect-factor} = \frac{P_f(\text{dike section})}{P_f(\text{dike cross-section})} \tag{2.15}$$

The larger the correlation between two cross-sections, the larger the correlation length d_x and the smaller the length-effect factor. If there is no spatial variation (i.e. total dependence between two points), the correlation coefficient ρ_k is equal to 1, the correlation length goes to infinity and the length-effect factor is also 1. If there is extremely much spatial variability (i.e. total independence between two points), the correlation coefficient is equal to zero, as well as the correlation length. The length-effect factor would be extremely large, meaning that the failure probability of the dike section is much larger than that of one cross-section (Thonus, 2003). The selection of the spacing of dike sections highly depends on the spatial variance. Thus, it depends on the autocorrelation in space of the load and resistance variables and is associated to the length-effect. The relation between the correlation length, the residual correlation and the spatial auto-correlation ρ is illustrated in Figure 2.5.

Only for a limited number of variables, like crest height and some soil parameters (e.g. the friction angle), it is possible to base the parameters d_x and ρ_x on measured data (Vrouwenvelder, 2006). In other cases, engineering judgement needs to be used. In some cases, similarity with the above mentioned better-documented variables could be used. The correlation model of Equation 2.14 can in principle be applied for each strength variable. Load variables can generally be assumed to have correlation 1 within one dike section (van Balen et al., 2016).

This definition of spatial correlations is implemented in the spatial upscaling technique that is used to estimate the reliability of a dike section. It is, for example implemented in the Hydra-Ring software (van Balen et al., 2016). It is important to mention that the spatial correlations that result from this approach are not based on the actual structure of geological deposits. The method does not depend on local information of the spatial distribution of geological deposits, in combination with the spatial division into dike sections. The method is mainly based on theory and expert judgement and is thus hardly location-dependent. This is a disadvantage of the method.

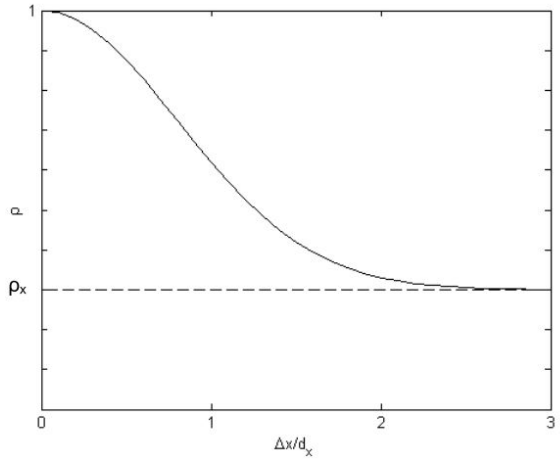

Figure 2.5: Correlation function to describe spatial variability (Diermanse et al., 2013).

2.5. Copulas

The joint distribution function of variables with mutual dependence can be described by multivariate distributions. The main limitation of this approach, however, is that the individual behaviour of the variables must be characterised by the same parametric family of univariate distributions (Genest and Favre, 2007). Furthermore, some of the standard multivariate distributions can model only limited types of dependence. These restrictions can be avoided by means of copulas. Copulas are an interesting mathematical tool to represent correlations between probability distributions. They can be used to represent complex dependencies in multivariate risk models, when more basic tools such as multivariate

Gaussian distributions are inappropriate. One commonly used application of copulas is the sampling from correlated random variables (Risk Engineering, 2017).

Copulas are in fact a bridge between marginal distributions and a joint distribution. Copula functions are a tool to separate the specification of marginal distributions and the dependence structure. Therefore, unlike most multivariate statistics, copulas allow the combination of different marginal distributions (Marsden, 2017). The copula provides the correlation structure between the variables. This method is applicable for both bivariate and higher dimension distributions. For illustration purposes, the bivariate case is considered. Sklar (1959) states that any joint cumulative distribution function $H(x, y)$ of the random vector (X, Y) of continuous variables can be expressed with a copula C:

$$H(x,y) = F_{XY}(x,y) = P(X \leq x, Y \leq y) = C(F_X(x), F_Y(y), \theta) = C(u, v; \theta), \qquad x, y \in R \tag{2.16}$$

where $F_X(x)$ and $F_Y(y)$ are the marginal distributions that can be different and are defined by some parameters of their distributions. θ is the parameter of the copula, which represents the dependence structure. The copula captures the dependency between the random variables, the marginals capture individual distributions and Sklar's theorem 'glues' them together. The shape and degree of joint tail dependence are properties of the copula and are independent of the marginal distributions. The main advantage provided by this approach is that the selection of an appropriate model for the dependence between X and Y, represented by the copula, can proceed independently from the choice of the marginal distributions. Even after transformations of X and Y, they would still be described by the *same* copula as the original X and Y. In other words, it means that the unique copula associated with a random pair (X,Y) is invariant by monotone increasing transformations of the marginals (Genest and Favre, 2007). The mathematical background of copulas is further explained in Appendix A.3.

There are several different parametric copula family types. The most common are the Gaussian, which is built as a function of the normal distribution, the Archimedean (e.g Gumbel or Clayton) which allows to generate the samples correlated in different tails of the distribution, and the Empirical ones that allow to build the correlated models as a function of empirical univariate distributions. The latter are especially useful when the underlying copula is not known in advance - but data is available - to visualise the scatter plot of the data to aid the selection of copula families. As the degree of correlation increases, the three types of copulas tend to unite. More kinds of copulas are available. The goodness-of-fit test statistics, such as the Cramér–von Mises statistic (S_n) and the Kolmogorov–Smirnov statistic (T_n), can be employed to select suitable copula functions (Genest and Favre, 2007).

2.6. Choice for the Model

Based on a literature study, as briefly summarised above, it has been decided to implement a Monte Carlo simulation as the reliability method of this model. This choice is based on a the following considerations:

- A Monte Carlo simulation is very suitable for the sampling of mutually dependent variables.
- A Monte Carlo simulation gives accurate results - as long as the number of samples is sufficient.
- It is possible to assess different Z-functions within the same realisation of variables, which is essential for the purpose of this research.
- The transparency and simplicity of the computation method make Monte Carlo very convenient to work with.
- FORM is based on the design point, which is difficult to define for this situation, as there are multiple different Z-functions that are considered within one reliability analysis. Besides, FORM is less accurate than a Monte Carlo simulation and complex dependence structures are difficult to implement.
- As the number of input variables will be large for this model, numerical integration would be very time-consuming.

Still, the large computation costs are a disadvantage of Monte Carlo. Therefore, the Z-functions should be defined as simple as possible, in order to reduce the computational effort.

Correlations and copula
In order to model the dependencies between the input variables, a copula is used. Subsequently, this copula can be used to draw random, correlated samples. The advantage of using a copula is that the input variables can have any type of marginal distribution.

The model will be used to assess the reliability of a Dutch earthen dike. Many of the input variables consist of geo(hydro)logical parameters for which not much data is available. This means that it will not be possible to reliably define the type of dependence structures based on data. Many correlations between the input variables must be based on literature and expert judgement in that case. For the spatial correlations, different subsoil schematisations will be consulted in order to estimate the degree of spatial correlations based on the actual location of geological deposits.

If there is no evidence for a particular type of correlation, as is the case for this study, the Gaussian copula is the best choice. Moreover, other copulas, like the Gumbel copula, are only available for the bivariate case. Besides, the Gaussian copula is the only one that can be defined based on a predefined correlation matrix in many Python modules. If correlations could be derived from large data sets, much more would be possible.

3

Failure Mechanisms

A dike trajectory can fail due to different failure mechanisms. The most commonly encountered failure mechanims for dikes are illustrated in Figure 3.1. The four most important failure mechanisms in a reliability analysis for dikes are (Vrouwenvelder, 2006):

- Overflow and overtopping, followed by erosion of the inner slope
- Damage of the outer slope revetment, followed by erosion of the dike body
- Piping
- Slope stability

Therefore, only these four failure mechanisms will be included in the model and described in this chapter. Additional information about these and other failure mechanisms can be found in Appendix B. The aim of this chapter is to describe the underlying processes, causes and consequences of the relevant failure mechanisms and to numerate possible approaches to model these failure mechanisms, based on the WBI procedure and other research. Finally, the best approach for the probabilistic model is chosen further elaborated.

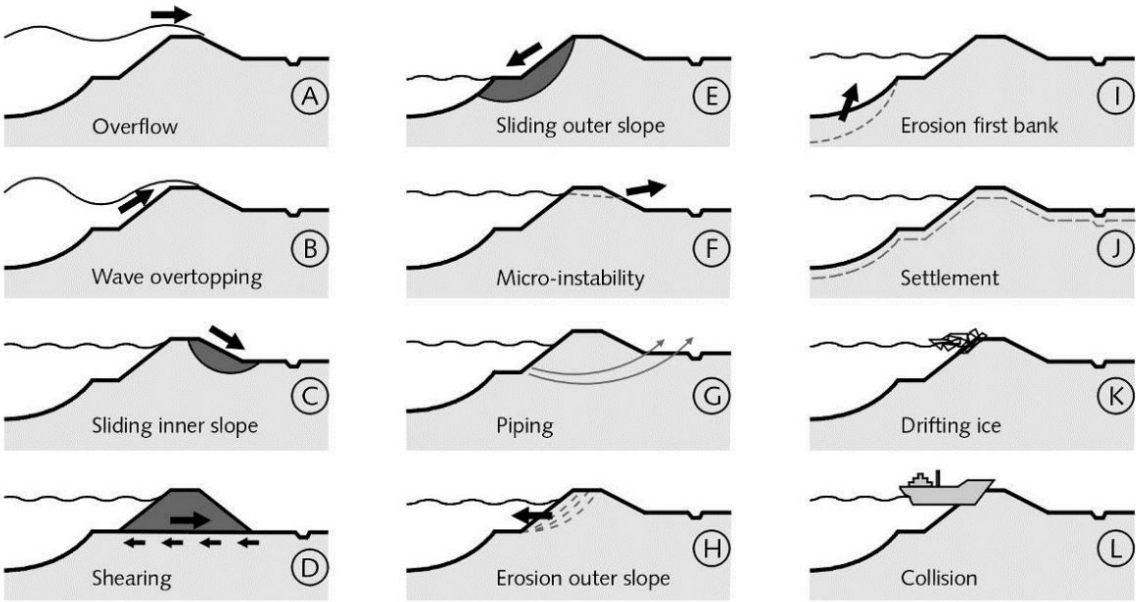

Figure 3.1: Schematic overview of the most relevant failure mechanisms of flood defences (Jonkman et al., 2018).

3.1. Overflow and Overtopping

Overtopping or overflowing water can erode the inner slope which can lead to progressive damage and eventually to dike collapse. Overflow happens when the (design) water level is higher than the crest level of the dike and the water can thus just flow over the dike. The limit state function for overflow is:

$$Z_{overflow} = h_c + \Delta h_c - h_a \tag{3.1}$$

in which h_c is the crest height in metres, Δh_c is the additional height for overflow to occur in metres and h_a represents the actual water level in metres(van Balen et al., 2016).

If the water level is below the crest height, the waves can still cause a flow of water over the top of the dike, which is called overtopping. The limit state function for overtopping is:

$$Z_{overtopping} = log(m_c \cdot q_c) - log(m_a \cdot q_a) \tag{3.2}$$

in which q_c and q_a denote the critical and actual overtopping discharge in $[m^3/s/m]$. m_c and m_a represent model factors. The model uncertainty is considered as the accuracy with which a model or method can describe a physical process or a limit state function. Therefore, the model uncertainty describes the deviation of the prediction from the measured data due to this method (Pullen et al., 2007). Since the values for the overtopping discharge are usually relatively small (i.e. $q << 1\ m^3/s/m$), the effects are modelled by means of a logarithm (van Balen et al., 2016).

Failure is defined as failure of the grass revetment at the inner slope, either due to overflow or due to overtopping. So, the failure mechanism can be described as a series system as shown in Figure 3.2.

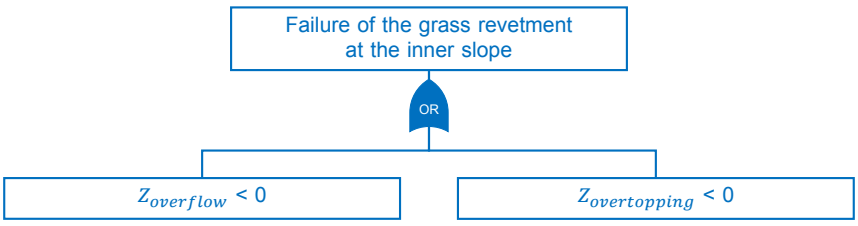

Figure 3.2: Fault tree for the failure mechanisms overflow and overtopping.

3.1.1. Critical overtopping discharge

The critical overtopping rate represents the erosion resistance of the inner slope revetment. It depends on the grass quality and on the wave height, since a fixed volume of water does more damage if it tops over in a few high waves than when it tops over in many small waves. In the literature, different values for the critical overtopping discharge can be found. For example, according to TAW (2002), the following mean discharges are normative for erosion of the inner slope:

- $0.1\ l/m/s$ for sandy soil with a grass revetment of bad quality.
- $5.0\ l/m/s$ (for $H_s = 2-3\ m$) or $10.0\ l/m/s$ (for $H_s < 2\ m$) for clay soil with a relatively good quality, closed, grass revetment.
- $10.0\ l/m/s$ for a clay cover and grass revetment according to the requirements for the outer slope or for a cover structure.

In recent years, it is also common practice to characterise the critical overtopping discharge by a log-normal distribution with an expected value and standard deviation that depend on the wave height and grass quality. This approach is for example described by van Hoven (2019) in the 'Schematiserings-handleiding grasbekleding' of the WBI 2017 and the values are shown in Table 3.1.

Table 3.1: Parameters for the critical overtopping discharge, depending on the grass quality and wave height.

Wave height class	Closed sod		Open sod	
	$\mu[m^3/s/m']$	$\sigma[m^3/s/m']$	$\mu[m^3/s/m']$	$\sigma[m^3/s/m']$
0 - 1 m	0.225	0.250	0.100	0.120
1 - 2 m	0.100	0.120	0.070	0.080
2 - 3 m	0.070	0.080	0.040	0.050

3.1.2. Actual overtopping discharge

The actual mean overtopping rate can be approximated by the formula of Van Der Meer and Bruce (2014):

$$\frac{q}{\sqrt{g \cdot H_{m0}^3}} = \frac{0.023}{\sqrt{\tan \alpha}} \cdot \gamma_b \cdot \xi_{m-1,0} \cdot \exp\left\{-\left(2.7 \cdot \frac{R_c}{\gamma_b \cdot \gamma_f \cdot \gamma_\beta \cdot \gamma_v \cdot \xi_{m-1,0} \cdot H_{m0}}\right)^{1.3}\right\} \tag{3.3}$$

where q is the wave overtopping discharge $[m^3/m/s]$, H_{m0} is the spectral significant wave height $[m]$, g is the gravitational acceleration $[m/s^2]$, α is the slope angle [°], R_c is the crest freeboard $[m]$, which is the difference between the crest level y_N and the still water level h. $\xi_{m-1,0}$ is the breaker parameter based on the spectral period $T_{m-1,0}$ $[s]$:

$$\xi_{m-1,0} = \frac{\tan \alpha}{\sqrt{(H_{m0} \cdot 2\pi)/(g \cdot T_{m-1,0}^2)}} \tag{3.4}$$

Equation 3.3 holds for the breaking-wave regime. In the non-breaking wave regime, observations have shown that the mean overtopping rate reaches a maximum given by:

$$\frac{q}{\sqrt{g \cdot H_{m0}^3}} = 0.09 \cdot \exp\left\{-\left(1.5 \cdot \frac{R_c}{H_{m0} \cdot \gamma_f \cdot \gamma_\beta}\right)^{1.3}\right\} \tag{3.5}$$

For a probabilistic analysis, the coefficients values A and B (in Equation 3.3: $A = 0.023$ and $B = 2.7$), should be included as stochastic with a defined mean and standard deviation. The values can be found in the paper by Van Der Meer and Bruce (2014). The formulas of Van Der Meer and Bruce (2014) are based on recent scientific insights, and appear to be supported very well by the theoretical work of Battjes from the 1970s. However, it is important to notice that most of the practical design guidelines for wave overtopping contain a slightly older version of the prediction formulas. It is called the TAW formula (TAW, 2002) and describes the dimensionless overtopping discharge for breaking waves ($\xi_{m-1,0} \leq 5$):

$$Q_b = \frac{0.067}{\sqrt{\tan \alpha}} \cdot \gamma_b \cdot \xi_{m-1,0} \cdot \exp\left(-f_b \frac{y_N - h}{H_{m0}} \cdot \frac{1}{\gamma_{\beta o} \cdot \gamma_f \cdot \gamma_b \xi_{m-1,0}}\right) \tag{3.6}$$

And for non-breaking waves ($\xi_{m-1,0} < 7$):

$$Q_n = 0.2 \cdot \exp\left(-f_n \frac{y_N - h}{H_{m0}} \cdot \frac{1}{\gamma_{\beta o} \cdot \gamma_f}\right) \tag{3.7}$$

where $y_N - h$ is the freeboard, f_b and f_n are model factors (usually $f_b = 4.75$ and $f_n = 2.60$). These formulas have been derived from empirical observations and do not have an explicit theoretical basis. The coefficients in the formulas have been fitted to match the observed data. The difference between the Equations 3.3 / 3.5 and 3.6 / 3.7 is almost indiscernible, especially if the freeboard is not too small (Jonkman et al., 2018).

The γ's in the formulas above are reduction factors, to include the reducing effect on the run-up and overtopping of certain aspects:

- γ_b = reduction due to a berm
- γ_f = reduction due to friction caused by roughness of the slope
- γ_β = reduction due to oblique waves
- γ_v = reduction due to a wall on top of the slope.

Extensive research has been done to quantify these reducing effects. A brief overview can for example be found in Section 5.4 of the Flood Defences Lecture Notes (Jonkman et al., 2018).

3.1.3. WBI assessment method: GEKB

In the WBI, assessment track for the failure mechanisms overflow and overtopping is called GEKB (Gras Erosie Kruin en Binnentalud). Failure is defined as the moment when approximately 20 cm of the top layer on the crest or inner slope has eroded, such that the revetment does not protect the subsoil against erosion any more. The assessment can performed by a full-probabilistic approach that compares the probability distribution of the actual overtopping discharge to the probability distribution of the critical overtopping discharge that applies for the grass quality under consideration. For this approach, the TAW formulas are applied (Equation 3.6 and 3.7).

3.1.4. Choice for the model

One of the objectives of this research is to make a comparison with a current WBI assessment, to investigate the impact of including correlations. Therefore, it is more important to stay close to the current assessment procedure than to apply the most accurate formulas. For this reason, the computation kernel that is also used in the WBI assessments - e.g. in Ringtoets and Hydra-Ring - will be called within the model. This kernel makes use of the TAW formulas. The 'overtopping' kernel, that was created as part of the WTI (Wettelijk Toets Instrumentarium) 2017 failure mechanism library, can be called by means of a `dll`-file[1]. A short overview of the most important parameters and calculation steps within the kernel is provided below. A full description of the module can be found in its Functional Design report by Kuijper et al. (2017).

The primary output of this module consists of:

- the 2% wave run-up height [m]
- the mean overtopping discharge [$m^3/m/s$]
- the value of the limit state function Z for the wave overtopping discharge.

In the model, the mean overtopping discharge will be called to evaluate the Z-function using Equation 3.2 in combination with the lognormal distribution for the critical overtopping discharge, as mentioned in Table 3.1. The module explicitly pertains to the wave overtopping discharge only, so it holds for water levels that do not exceed the crest level. If the water level exceeds the crest, a different kernel for overflow will be called, by means of another `dll`-file[2]. However, the functional design of this kernel will not be further elaborated.

The input of the overtopping module consists of:

- Load parameters: the still water level h and the wave parameters (H_{m0}, $T_{m-1,0}$ and the wave direction φ) at the toe of the dike.
- Cross-sectional data: dike segments from the toe of the dike to the outer crest level, as will be described in subsection *Dike profile schematisation*.
- Model factors, that are elaborated in the subsection *Model factors*.

No foreland is used within the overtopping module. But the kernel takes into account berms and foreshores and their effect on the wave height.

[1] `dllDikesOvertopping64.dll`
[2] `CombOverloopOverslag64.dll`

Dike profile schematisation
The dike profile has to be schematised by certain rules, the so-called 'schematiseringsregels', that are elaborated in the 'Schematiseringshandleiding Hoogte' (Rijkswaterstaat, 2019b). According to these rules, the cross-sectional data should satisfy the following requirements:

1. The outer dike profile is schematised by a series of M (at least two) (x, z)-profile points that are mutually connected by straight lines. The z-values should be given in $m+NAP$. The straight lines between the profile points are called profile sections.
2. The x-coordinates must increase and the y-coordinates must be non-decreasing. The profile points start at the outer toe and end at the outer crest.
3. Two types of profile sections are allowed: slope sections with a schematised slope between 1:8 and 1:1 or berm sections with a schematised slope between 1:00 and 1:15
4. The first and the last dike section have to be a slope section.
5. A maximum of two berms is allowed per profile. A berm can consist of multiple consecutive berm sections.
6. The lowest profile section is connected to the toe and the highest profile section to the crest. These sections are slope sections.
7. The roughness factor should be defined for every profile section $(M-1)$ in accordance with Appendix B of the 'Schematiseringshandleiding' (Rijkswaterstaat, 2019b). The roughness factors lie in between 0.5 (very rough) and 1.0 (very smooth).
8. Preferably a minimum horizontal distance of 2 metre between two profile points should be taken.
9. If the outer crest is not the highest point of the profile, extend the highest slope section to the level of the actual dike crest.
10. If a profile section is too steep to be a slope section, decrease the slope to the maximum allowable slope of 1:1, by shifting one of the two profile points of that profile section horizontally. Make sure that the slopes of the other profile sections don't change, so you have to move them as well in that case.
11. Negative slopes are not allowed.
12. The crest level is to be forced.

The dike orientation ψ is implemented through the dike normal (imaginary line normal to the dike). The direction of the dike normal is defined with respect to North in degrees [$^{\circ}N$]. If the dike normal varies over the dike section, choose the direction of the dike normal that gives the smallest angle with respect to the wave direction. After all, normal incident waves give the largest wave load. The definition of the dike orientation ψ is closely related to the definition of the wave direction φ: in case of full wave attack on the dike, it holds that: $\psi = \varphi$.

Model factors
The following model factors [-] are required as input, with proposed stochastic properties as listed in Table 3.2:

- f_b : model factor for breaking waves
- f_n : model factor for non-breaking waves
- $f_{shallow}$: model factor for shallow water waves
- m_{z2} : model factor describing the uncertainty of the wave run-up $z_{2\%}$
- m_c : model factor describing the uncertainty of q_c
- m_a : model factor describing the uncertainty of q_a

Table 3.2: Distributions for the model factors (Kuijper et al., 2017).

Parameter	Distribution	μ	σ	σ / μ	Design
m_{z2}	Normal	1.00	0.07	0.07	1.07
f_b	Normal	4.75	0.50		4.30
f_n	Normal	2.60	0.35		2.30
$f_{shallow}$	Normal	0.92	0.24		0.6778

Wave run-up
The functions that are applied in the kernel to calculate the 2% wave run-up $z_{2\%}$ are mainly based on the TAW report about wave overtopping and overflow (TAW, 2002). A brief description of the most important calculation steps is given below. For a full description of the calculations in the kernel, the reader is referred to Kuijper et al. (2017) and (TAW, 2002).

A first important parameter is the breaker parameter, as defined in Equation 3.4. It is based on the relative slope angle, which is the average slope in the zone between the still water level $SWL - 1.5 \cdot H_{m0}$ and $SWL + z_{2\%}$, disregarding berms. Next, the intersection point $\hat{B}$ for breaking and non-breaking waves is calculated, by considering the breaker parameter at the transition point. For small breaker parameters, the 2% wave run-up for breaking waves is computed as follows:

$$z_{2\%} = m_{z2} \cdot H_{m0} \cdot f_{runup1} \cdot \gamma_f \cdot \gamma_{\beta z} \cdot \gamma_b \cdot \xi_{m-1,0} \tag{3.8}$$

Otherwise, the 2% wave run-up for non-breaking waves is defined as:

$$z_{2\%} = m_{z2} \cdot \max\left(H_{m0} \cdot \gamma_f \cdot \gamma_{\beta z} \cdot \left(f_{runup2} - \frac{f_{runup3}}{\sqrt{\xi_{m-1,0}}} \right); 0 \right) \tag{3.9}$$

with $f_{runup1} = 1.65$, $f_{runup2} = 4.00$ and $f_{runup3} = 1.50$. The uncertainty in $z_{2\%}$ is accounted for by m_{z2}.

Wave overtopping
Also for the overtopping discharge, the computations are mainly based on the TAW report about wave overtopping and overflow (TAW, 2002). A brief description of the most important calculation steps is given below. For a full description of the calculations in the kernel, the reader is referred to Kuijper et al. (2017) and (TAW, 2002). As mentioned, the kernel is based on the TAW formulas (Equation 3.6 and 3.7) that compute the dimensionless overtopping discharge. The actual overtopping discharge is then:

$$q_a = \sqrt{g H_{m0}^3} \cdot \min(Q_b; Q_n) \qquad \text{for} \qquad \xi_{m-1,0} \leq 5 \tag{3.10}$$

There is also a third formula that is applicable for shallow water ($\xi_{m-1,0} > 5$). For more information, the reader is referred to Kuijper et al. (2017) or TAW (2002). In a probabilistic assessment, the uncertainty of q_a is usually accounted for by considering the model factors f_b, f_n and $f_{shallow}$ as stochastic variables and assigning a fixed value of 1.0 to m_a (Kuijper et al., 2017).

Reduction factors
The kernel computes the applicable reduction factors for the dike section under consideration, as mentioned in Section 3.1.2. The reduction factor $\gamma_{\beta z}$ for the angle of wave attack for 2% wave run-up is:

$$\gamma_{\beta z} = 1 - 0.0022 \cdot \min(\beta; 80) \tag{3.11}$$

and for overtopping:

$$\gamma_{\beta o} = 1 - 0.0033 \cdot \min(\beta; 80) \tag{3.12}$$

where β is defined as:

$$\beta = \begin{cases} |\theta - \psi| & \text{for } |\theta - \psi| \leq 180^\circ \\ 360 - |\theta - \psi| & \text{for } |\theta - \psi| > 180^\circ \end{cases} \tag{3.13}$$

It can be seen that $\beta = 0^\circ$ for perpendicular wave attack.

The reduction factor γ_f for the roughness is based on the roughness factor that is defined for each dike segment. The definition of the reduction factor for the berm is described in Section 5.2.7 of the Functional Design report of the overtopping kernel (Kuijper et al., 2017).

The product of the reduction factors should not be less than 0.4. If that is the case, the kernel adapts the factors in such a way that their product is equal to 0.4.

3.2. Macrostability

Besides overtopping, slope instability, or macrostability, is the most common failure mechanism leading to dike breaches world-wide (Jonkman et al., 2018). Slope instability refers to the instability of the inner slope, when large pieces of soil slide along a straight or curved slip plane. It is caused by a loss of equilibrium, or stability, of a soil body. The equilibrium is formed by (1) a driving moment, that is the weight of the soil body to the left of the center point of a circular slip plane (water side), by (2) a resisting moment, that is the soil mass to the right of the center point (land side), and (3) by the shear strength along the slip plane. The failure mechanism is driven by the infiltration of water into the dike body and its foundation, which leads to a rise of the phreatic line and thus an increase of the pore pressures. As a result, the soil weight increases, the effective stress and the shear resistance decrease, and consequently a loss of equilibrium can occur. For example during long-lasting floods, that can typically occur in rivers, this can happen, and lead to sliding of the inner slope. It is important to note that shallow slidings are part of the failure mechanisms for revetments or micro-instability (see Appendix B.2 on p.99).

The ratio of the moments, as described above, is used as the definition of the factor of safety FoS in reliability assessments:

$$FoS = \frac{M_R}{M_S} \tag{3.14}$$

Subsequently, the limit state function can be defined as:

$$Z_{macro} = FoS \cdot m_d - 1 \tag{3.15}$$

where m_d is the model uncertainty factor. The distribution parameters for m_d can be found in the 'Handreiking Faalkansanalyse Macrostabiliteit' by Schweckendiek et al. (2017), in Table 3.1, p.37. If the model is exact, it can be taken as a deterministic value of 1 with no standard deviation.

3.2.1. CSSM & SHANSEP

The dike's resistance against slope instability can be determined according to the CSSM (Critical State Soil Mechanics) theory. According to CSSM, the undrained shear strength of soils, s_u [kPa], is modelled as:

$$s_u = \sigma'_v S (OCR)^m \tag{3.16}$$

with

$$OCR = \frac{\sigma'_{v,y}}{\sigma'_{v,i}} = \frac{\sigma'_{v,i} + POP}{\sigma'_{v,i}} \tag{3.17}$$

where $\sigma'_{v,i}$ denotes the in-situ effective vertical stress [kPa], $\sigma'_{v,y}$ denotes the vertical yield stress [kPa], OCR represents the over-consolidation ratio [-], POP indicates the pre-overburden pressure [kPa], S denotes the undrained shear strength ratio (normally consolidated) [-] and m is the strength increase exponent [-]. S defines the ratio between the undrained shear strength and the effective vertical stress of the soil under normally consolidated conditions (i.e. the effective stress is equal to the limit stress). m determines to what extent (with respect to the limit stress) a decreasing effective stress affects the undrained shear strength. If m is close to 1, the strength hardly decreases if the effective stress decreases, as a result of higher pore pressures during a flood event for example (Schweckendiek et al., 2017).

The undrained shear strength can also be evaluated using the SHANSEP (Stress History and Normalised Soil Engineering Properties) method, that takes into account the stress history and path of the soils (Simanjuntak et al., 2019).

These models are applicable for the undrained shear strength of soils. This is the case for e.g. clay or peat layers - where the permeability is low and little or no drainage will occur during sliding. Therefore, undrained soil behaviour should be considered for these kind of soil layers.

3.2.2. Mohr-Coulomb

If the permeability of the soil is large - e.g. for sand - drainage can occur during sliding and drained soil behaviour should be considered. In that case, the shear stress can be calculated according to Mohr-Coulomb:

$$\tau = c' + \frac{\cos\psi \cdot \sin\varphi'}{1 - \sin\psi \cdot \sin\varphi'} = \sigma' \sin\varphi' \tag{3.18}$$

where φ' indicates the effective friction angle [°], which is a measure for the friction between soil particles. If the normal stress of the soil increases, the friction between soil particles increases proportionally, under drained conditions. σ' represents the vertical effective stress along the slip plane [kPa]. The cohesion c' is zero for sand in the critical state, as well as the angle of dilatancy ψ [°], that's why the formula can be simplified as shown at the right hand side.

3.2.3. Correlations

It is well known that there is a negative cross-correlation between c' and φ' of a soil type and that this cross-correlation affects reliability analyses of geotechnical structures (Wang and Akeju, 2016). Besides, there is evidence that the undrained shear strength parameters S and m are correlated (Schweckendiek et al., 2017). Moreover, it seems that the value of S increases with decreasing volumetric weight of the soil γ (Leferink, 2020), which suggests a negative correlation between S and γ of a soil type. About other a possible relations - e.g. between φ and γ - nothing specific is found in literature.

In many cases, the soil characteristics of the soil layers present in a dike cross-section originate from the same geological deposit as soil layers in a neighbouring dike cross-section. Therefore, it is likely that the soil characteristics of neighbouring dike sections are identical or strongly correlated (Schweckendiek et al., 2017) (Simanjuntak et al., 2019). In particular, it is assumed that mutual correlations between neighbouring dike sections should be assumed for the strength parameters S, m and φ, for the hydraulic conductivities k and for the volumetric weights γ.

3.2.4. Limit Equilibrium Models

There are several possible approaches to determine the moments and thus the factor of safety, as defined in Equation3.14. These approaches are called Limit Equilibrium Models (LEM). The most relevant LEM's are briefly explained below, in order of increasing complexity.

Bishop

This method checks the moment equilibrium of a circular slip plane. Also, the method ensures that the vertical equilibrium is fulfilled, i.e. that the vertical forces between the slices are in balance. Internationally, it is the most commonly applied method for slope stability (Jonkman et al., 2018).

Uplift-Van

The Uplift-Van model assumes that the slip plane consists of a horizontal part bounded by two circular parts, as shown in Figure 3.3. The safety is assessed by an equilibrium of the horizontal forces acting on the compressed area between the active and passive slip circles. If water penetrates the aquifer beneath the dike's weak (clay) layers, this can lead to an increased pore water pressure and a reduction of the effective stresses and shear resistance at the interface of these two layers. This can result in uplift, where the clay layer virtually floats on the aquifer. In this situation, the critical sliding surface typically looks like the elongated slip plane as proposed by Uplift-Van, and not circular as in the Bishop model. Moreover, the Uplift-Van model not only considers the vertical equilibrium, but the horizontal forces - that are important for base sliding - as well. The Uplift-Van method can be reduced to the Bishop model by reducing the horizontal part to zero (Kanning et al., 2015).

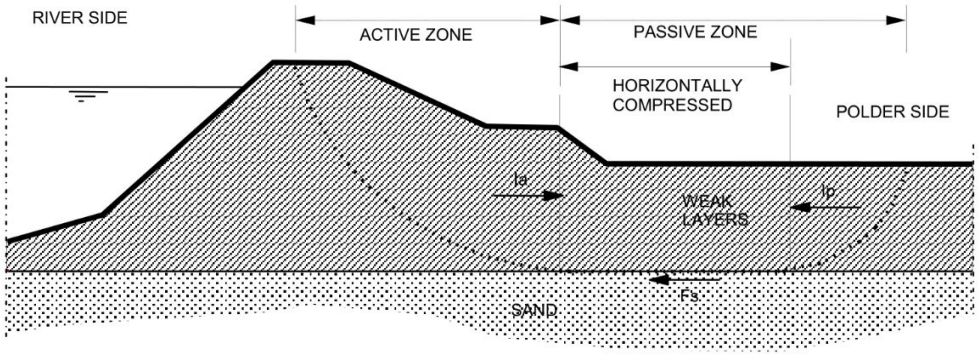

Figure 3.3: Schematic representation of the Uplft-Van model (van der Meij, 2019).

Spencer
The Spencer method can take any shape of slip plane and it can therefore be used to freely search the slip plane with the smallest resistance. This is done by considering piecewise linear elements. The Spencer model treats all three equilibria. Therefore, the method offers the greatest flexibility and applicability to all sorts of sliding surfaces. The disadvantage of the method is that it is quite new, so that there is little experience. In recent years, however, genetic algorithms have been developed to find the sliding surface with the minimum factor of safety within pre-defined bounds. This is called the Spencer - Van der Meij method.

3.2.5. Software D-Stability

The software D-Stability, developed by Deltares, can be used for the application of the above mentioned methods in order to determine the factor of safety (van der Meij, 2019). For the undrained shear strength, the SHANSEP method or a SU table - which will not be further discussed in this report - can be applied. For the SHANSEP method, the user has to define the unit weight in kN/m^3, the shear strength ratio S [-] and the strength increase exponent [-] for the soil layer under consideration. For the drained shear strength, D-Stability makes use of the Mohr-Coulomb model. The user has to define the unit weight in kN/m^3, the cohesion c, the friction angle φ and the dilatancy angle ψ in degrees for the corresponding soil layer. Inside the software, the Waternet Creator is used for the generation of the pore pressure.

All three LEM's are available in D-Stability. The software offers two possibilities for the determination of the critical slip plane. Firstly, the user can define the slip plane manually for one of the LEM's and the program will execute a single calculation of the FoS for the given plane. Secondly, the user has the option to let the search algorithm find the critical slip plane by defining the limit equilibrium method and the search boundaries between which the algorithm will search for the critical slip plane. This is called the optimisation procedure. Each optimisation procedure will generate slip planes within these limits and will search for the slip plane with the lowest factor of safety, for the given LEM. The search boundaries are defined in different ways, depending on the limit equilibrium method.

D-Stability enables different reliability methods for the calculation: deterministic, semi-probabilistic (using design values) and probabilistic (Level II). General theory about reliability methods can be found in Section 2.3. A probabilistic computation requires the material properties to be entered as stochastic, by defining the mean and standard deviation. Only a lognormal distribution can be used to define the distributions of the parameters. This is the most common type of distribution for geotechnical parameters and it prevents parameter values to become smaller than zero (van der Meij, 2019). Correlations between material properties can be assigned, however only full correlation ($\rho = 1$) or no correlation ($\rho = 0$) is possible in D-stability. Also correlations between entire materials and state points are possible.

It is important to emphasise that the probabilistic computation is in fact not fully probabilistic. A full probabilistic calculation would be too time-consuming to be combined with an optimisation method for the slip planes. Therefore, a calculation with design values is made first, to find the representative slip

plane. Then, the conditional failure probability of this slip plane is calculated by means of a FORM analysis, for a given outside water level. So, per water level - and corresponding schematisation of the pore water pressures - the relevant slip plane(s) is/are chosen and a FORM analysis (per slip plane) is performed. The limit state function, as in Equation 3.15, is evaluated to find the conditional failure probability. In order to calculate the failure probability of the cross-section, a fragility curve and the probability density function of the water levels is needed. To construct a fragility curve, one needs to repeat the process for several outside water levels. The combination of the fragility curve with the PDF of the water levels can be achieved via linear interpolation and numerical integration over all water levels. This must be done outside D-Stability, for example by means of the Probabilistic Toolkit.

The scientific background of the software is elaborated in Part III of the D-Stability User Manual by van der Meij (2019).

3.2.6. WBI assessment method: STBI

In the WBI, failure is defined as sliding of the soil at the inner slope, resulting in a lowering of the dike crest such that the defence loses its function. The assessment track is called STBI (stabiliteit binnenwaarts) and is only applicable for dikes without any structural elements (i.e. anchors) or artificially reinforced soil. Based on the hydraulic loads, a phreatic line can be schematised. Different approaches exist for the schematisation of the phreatic line, as briefly explained in the Appendix C.3.1 and the 'Schematiseringshandleiding Macrostabiliteit' by Rijkswaterstaat (2019a). In general, the inner slope stability is determined by means of the Uplift-Van method, based on Mohr-Coulomb and SHANSEP for the drained and undrained shear strength respectively. The parameters are based on local measurements, expert judgement or on effective stresses. The software D-Stability is generally used for the analysis. The calculation is based on a semi-probabilistic approach, using design values. To account for the uncertainty and variation in space of the soil properties and subsoil layer structure, several scenarios are assessed per cross-section. This approach is elaborated in Appendix B, of the 'Bijlage III Sterkte & Veiligheid' by Rijkswaterstaat (2017). The failure probability per cross-section is based on the factor of safety per scenario:

$$P_{f;i} = \Phi\left(-\frac{\left(\frac{FoS_{d;i}}{\gamma_d}\right) - 0.41}{0.15}\right) \tag{3.19}$$

where:

- $P_{f;i}$ = the failure probability for scenario i [$1/year$]
- Φ = the standard (cumulative) normal distribution [-]
- $FoS_{d;i}$ = the computed FoS for scenario i, based on the design value for the shear strength (= characteristic value divided by the material factor) [-]
- γ_d = the model factor [-]

To get to the total failure probability of the cross-section, the failure probability per scenario should be multiplied by the probability of occurrence of that scenario. This product is summed for all scenarios:

$$P_{f;cs} = \sum_{i=1}^{n} (P(S_i) \cdot P_{f;i}) \tag{3.20}$$

with $P_{f;cs}$ the failure probability per cross-section [$1/year$] and $P(S_i)$ the probability of occurrence of scenario i [$1/year$] . This failure probability is compared to the required failure probability of a cross-section - under consideration of the length-effect - to determine the assessment result for the section.

This assessment procedure is elaborated in the 'Regeling veiligheid primaire waterkeringen 2017 - Bijlage III Sterkte en veiligheid' by Rijkswaterstaat (2017) and in the 'Schematiseringshandleiding Macrostabiliteit' by Rijkswaterstaat (2019a).

3.2.7. Choice for the model

The probabilistic model of this research makes use of a Monte Carlo simulation. As explained in Section 2.3.4, Monte Carlo simulations can become an extremely time-consuming process - especially when complex systems, like the assessment of macrostability, are involved. This led the path to the use of metamodels. A metamodel, or surrogate model, predicts a model's response based on a limited set of model evaluations, called a training set (in this case slope stability calculations). Thus, predictions of the model response can be obtained without evaluating the computational model itself (Echard et al., 2011). This is very beneficial in the case of Monte Carlo simulations, where repetitive evaluation of the model would be computationally expensive. Especially in the case of complex models like D-Stability. Therefore, it has been decided to create a metamodel for the implementation of macrostability into the probabilistic model of this research.

Metamodeling

A metamodel is a function $y(x)$ that approximates an unknown function $Z(x)$ describing the response of a system. The function y is based on a set of points in the parameter space where the response is known. An interpolation method is used to approximate the system's response at points where it is unknown. This concept is very convenient when the response of the system is obtained by an expensive computational model. For multivariate systems with a non-linear model response, as is the case for slope stability calculations, different interpolation methods exist.

Two methods for metamodeling have been investigated. Firstly, the ERRAGA model by Deltares (2020), that is based on Gaussian Mixture Modelling and Kriging algorithms that incorporate machine learning and correlation patterns in the interpolation (see Appendix C.1). It turned out that this model is in fact too complex and not exactly suited for the purposes of this research's model. Therefore it has been decided to create a more simple metamodel based on Gaussian process regression (GPR). The metamodel will be trained by D-Stability slope stability calculations, with the FoS being the system's response to be approximated. Every dike section will be considered separately. In other words, separate prediction functions will be obtained for each dike section. The input variables that will be used for the training and test data depend on the geometry, and can differ per dike section. However, the water level will be included in any case for each metamodel. It has been decided to create training data sets of 1000 training data points.

Gaussian process regression

Gaussian processes (GP) are powerful generic supervised learning methods, that are designed to solve regression and probabilistic classification problems in different fields (Rasmussen and Williams, 2006). GP are Bayesian non-parametric approaches, as they find a distribution over all possible prediction functions $f(x)$ that are consistent with the observed data, instead of predefining the function $f(x)$ and its parameters beforehand. The difference between parametric and non-parametric is further explained in Appendix C.2.1.

As the name suggests, Gaussian processes assume that the probability distribution over possible functions $p(f(x_1), ..., f(x_N))$ is jointly Gaussian - or normally distributed - defined by a mean vector μ and covariance matrix Σ. The covariance matrix is given by $\sum_{ij} = k(x_i, x_j)$, where k is a positive definite covariance function, which is often called the kernel function. As with all Bayesian methods, GP begins with a prior distribution and converts this to the posterior distribution over functions, as soon as data points have been observed (Murphy, 2021). However, with an infinite amount of parameters possible, there are potentially infinitely many functions that would fit the set of training data points. Gaussian processes offer an elegant solution to this issue by putting some constraints on it. Firstly, a domain of interest is defined for every input variable x. Secondly, the mean of the target variable y should be chosen such, that it represents the most probable characterisation of the data ($y = f(x) + \in$). And thirdly, the smoothness of the function is specified by means of the covariance matrix. In this way, it is ensured that values that are close to each other in the input space will produce output values that are close together as well. This covariance matrix - along with a mean function to output the expected value of $f(x)$ - defines a Gaussian process by assigning a probability to each of the possible functions. An elaborated description of GP is given in Appendix C.2.

One main advantage of GP is that the prediction is probabilistic. Therefore, it is possible to compute empirical confidence intervals, that can be used to decide whether one should refit the prediction in

some region of interest. A disadvantage of GP, that should definitely be kept in mind for this research, is that they lose efficiency in high dimensional spaces – namely when the number of features exceeds a few dozens (Pedregosa et al., 2011). In general, it holds that the predictions are better for a smaller number of input variables.

Scikit-learn

`Scikit-learn` is an open source machine learning library that supports supervised and unsupervised learning (Pedregosa et al., 2011). Included among its library of tools is a Gaussian Process module.

For regression tasks - with the purpose of predicting a continuous response variable - a `GaussianProcessRegressor` is applied by specifying an appropriate kernel (covariance function). Fitting proceeds by maximising the log of the marginal likelihood. The `GaussianProcessRegressor` does not allow for the specification of the mean function, as it always assumes it to be zero. This highlights the diminished role of the mean function in calculating the posterior, as also mentioned in the Appendix C.2 on page 104. `Scikit-learn` offers a library of about a dozen kernels to choose from. A flexible choice to start with is the Matèrn covariance (Fonnesbeck, 2017). A GP kernel can be specified as the sum of additive components, if a combination of different kernels is desired.

Methodology

The purpose of the metamodels is to assess the factor of safety for macrostability without calling D-Stability, in order to decrease the computational costs. It has been decided to use 10 parameters as input variables for the metamodel, as listed in Table C.1. This choice is based on the consideration that on one hand the metamodel loses efficiency in high dimensional spaces (Pedregosa et al., 2011) and on the other hand that many parameters and soil layers are involved in failure due to macrostability. The metamodel is trained by 1000 D-Stability computations in which the input variables of the metamodel are slightly varying with every realisation. This assures that the metamodel is able to predict the factor of safety for different values of the input variables. The D-Stability computations for the training data are based on the Uplift-Van model. To make sure that the metamodel provides accurate predictions for the complete domain of possible variables, it will be trained by values of the input variables that are sampled from distributions with a larger standard deviation than the real distributions of the parameters. Moreover, Latin hypercube sampling (LHS) will be applied to create the training data set. Latin hypercube sampling is a method to generate random samples of parameter values that are equally distributed over the variable space. The practical implementation of the metamodeling is elaborated in Section 5.6.1.

Subsequently, the metamodels will be implemented within the Monte Carlo simulation to determine the FoS for each evaluation of the limit state function (Equation 3.15). The model factor m_d will be based on the uncertainty of the Uplift-Van model and the metamodels itself.

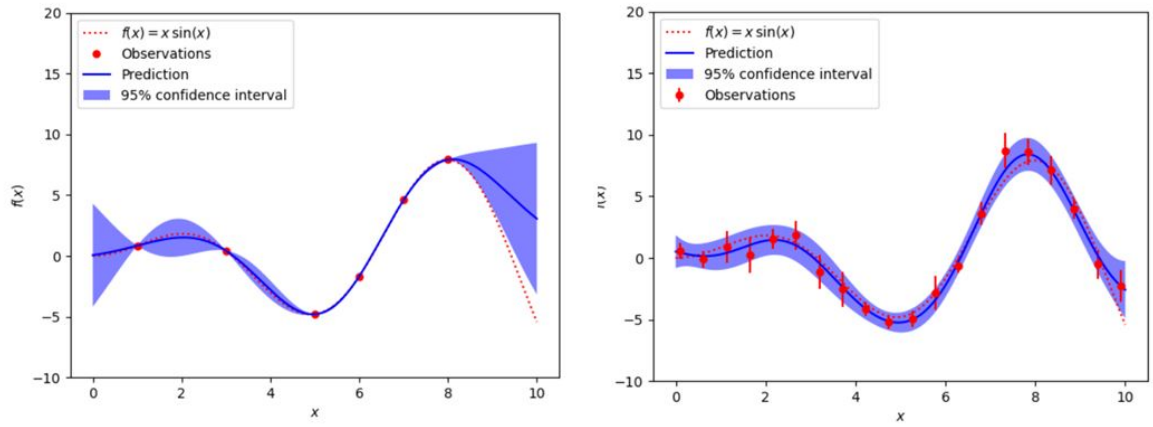

Figure 3.4: Left: Noise free case for GP regression. Right: Noisy case and more training data points (Pedregosa et al., 2011).

3.3. Piping

Backward erosion piping (or just *piping*) is the relevant type of internal erosion for dikes with low-permeability dike bodies. There are three main sub-mechanisms that play a role in the piping process: *uplift, heave* and *backward erosion / piping*. According to the current state of knowledge, uplift, heave and backward erosion evolve in the phases as illustrated in Figure 3.5. The process might stop at several points in time. The limit states and assessment models that will be elaborated below are based on this conceptual model of the piping process (Jonkman et al., 2018).

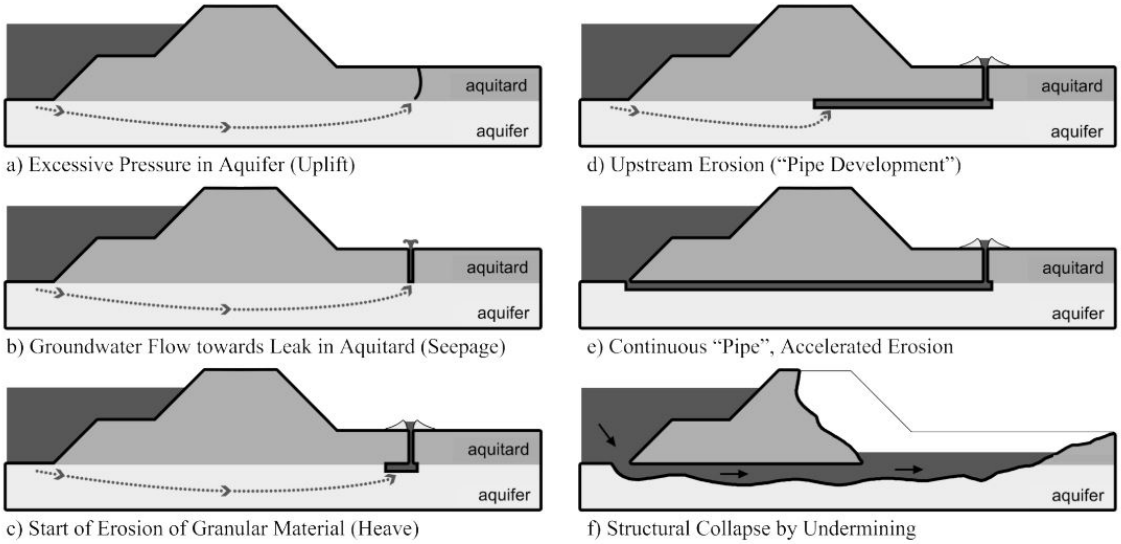

Figure 3.5: Phases of the piping process (Jonkman et al., 2018).

Definitions

The definitions of the relevant piezometric heads Φ and phreatic levels h, that are important for the evaluation of the sub-mechanisms, are presented in Figure 3.6. The situation presented in the figure, with an aquifer underlying a blanket layer / aquitard, is very common in the Netherlands.

The potential at the exit point, Φ_{exit} is defined as:

$$\Phi_{exit} = h_p + \lambda(h - h_p) \tag{3.21}$$

where h_p is the phreatic level of the hinterland (at the exit point), with respect to mean sea level [m+NAP], which is assumed to be equal to the piezometric head in the far hinterland. The damping factor λ [-] can be estimated using groundwater flow models, by data calibration or based on expert judgement. If a Dupuit flow model is used, the damping factor is approximated by Equation 3.22. The Dupuit flow model assumes predominantly horizontal flow with vertical leakage.

$$\lambda = \frac{\lambda_h}{L_f + B + \lambda_h} \exp\left((B/2 - x_{exit})/\lambda_h\right), \qquad x_{exit} > B/2 \tag{3.22}$$

where:

- L_f is the length of the (effective) foreshore [m]
- B is the width of the dike [m]
- x_{exit} is the distance of the exit point from the center of the dike footprint [m]
- λ_h is the leakage-factor for the hinterland section [m], given by $\lambda_h = \sqrt{kDd/k_h}$, with:
  - k the hydraulic conductivity of the aquifer [m/s]

– D the thickness of the aquifer [m]

– d the thickness of the hinterland aquitard at the exit point [m]

– k_h the hydraulic conductivity of the hinterland section [m/s] .

The exit-gradient i is the gradient in the aquitard at the exit point and it is defined as:

$$i = (\Phi_{exit} - h_p)/d = \lambda(h - h_p)/d \tag{3.23}$$

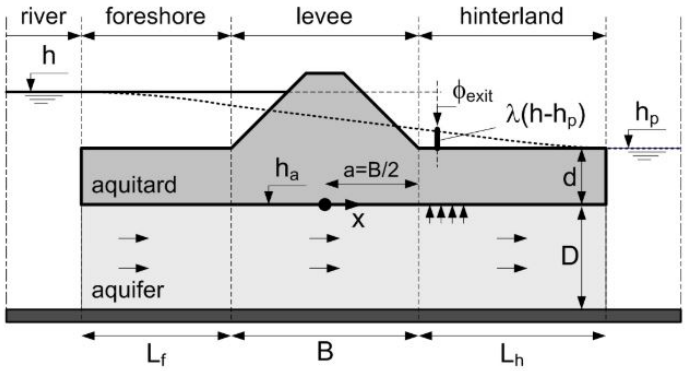

Figure 3.6: Schematic representation of the situation and the associated groundwater flow model (Jonkman et al., 2018).

Uplift

Uplift is concerned with the rupturing of the low-permeability cohesive aquitard. The uplift model that is used in safety assessments is based on a comparison of the pore pressures at the upper boundary of the aquifer with the weight of the aquitard layer (Jonkman et al., 2018). This can be translated into a limit state function as follows :

$$Z_u = g_u(x) = m_u \cdot \Delta\Phi_{c,u} - \Delta\Phi \tag{3.24}$$

where m_u is the model factor [-], addressing the uncertainty of the critical head difference. And with:

$$\Delta\Phi_{c,u} = d \cdot \frac{\gamma_{sat} - \gamma_w}{\gamma_w} \tag{3.25}$$

$$\Delta\Phi = \Phi_{exit} - h_p \tag{3.26}$$

where $\Delta\Phi_{c,u}$ denotes the critical head difference [m] , γ_{sat} the saturated volumetric weight of the aquitard [kN/m^3] and γ_w the saturated volumetric weight of water ($= 10\ kN/m^3$) . The corresponding factor of safety [-] is defined as:

$$FoS_u = \frac{\Delta\Phi_{c,u}}{\Delta\Phi} \tag{3.27}$$

Heave

Heave considers the start of erosion of aquifer material (usually sand). The exceedance of a critical heave gradient $i_{c,h}$ is considered a necessary condition. The corresponding limit state function Z_h [-] is defined as:

$$Z_h = g_h(X) = i_{c,h} - i \tag{3.28}$$

where i is the exit gradient (see Equation 3.23). The corresponding factor of safety [-] is defined as:

$$FoS_h = \frac{i_{c,h}}{i} \tag{3.29}$$

Several approaches have been proposed in literature to define the critical (exit) heave gradient $i_{c,h}$. For example, by Terzaghi (1996):

$$i_{c,h} = \frac{(1-n)(\gamma_s - \gamma_w)}{\gamma_w} \approx 1.65(1-n) \tag{3.30}$$

where n is the porosity [-] and γ_s is the volumetric weight of sand grains ($= 26.5\ kN/m^3$). . This approach results in rather high values of $i_{c,h}$. The critical heave gradient can also be assumed a-priori to be lognormal distributed with the following mean and standard deviation: $i_{c,h} = LN(0.7, 0.1)$ (Jonkman et al., 2018). This implementation is applied within the WBI.

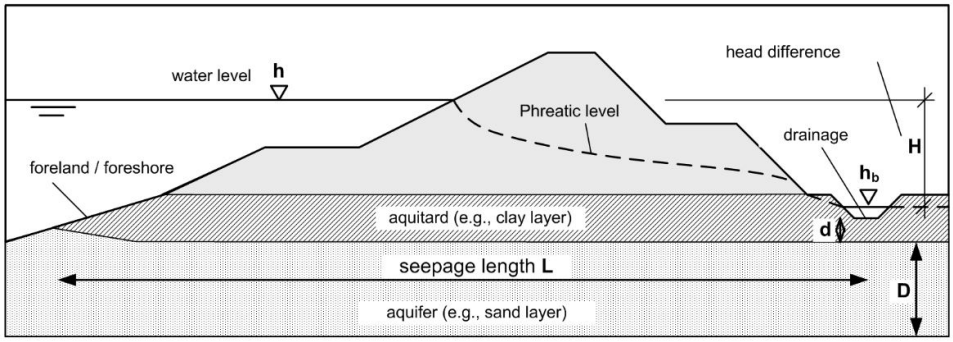

Figure 3.7: Definitions for backward erosion assessment by the revised Sellmeijer model (Jonkman et al., 2018)..

Backward erosion

Backward erosion resistance is usually expressed in terms of a critical head difference H_c [m] . Sellmeijer developed a theory on backward erosion stability based on the flow pattern generated by the head difference between the water side and the land side water level - which is the driving force of internal erosion - and the erosion resistance of the sand grains in a partially developed piping channel (Jonkman et al., 2018). The Sellmeijer model has been revised after extensive physical model tests in the Netherlands, which has led to the following limit state function:

$$Z_p = g_p(X) = m_p \cdot H_c - H = m_p \cdot H_c - (h - h_p - 0.3d) \tag{3.31}$$

where m_p is the model uncertainty factor [-] and H is the head difference [m]. The definitions of the parameters are illustrated in Figure 3.7. In the revised version, the critical head difference is given by:

$$H_c = F_1 \cdot F_2 \cdot F_3 \cdot L \tag{3.32}$$

with:

$$F_1 = \eta \left(\frac{\gamma_s}{\gamma_w} - 1 \right) \tan \theta \tag{3.33}$$

$$F_2 = \frac{d_{70m}}{\sqrt[3]{(\upsilon k L)/g}} \left(\frac{d_{70}}{d_{70m}} \right)^{0.4} \tag{3.34}$$

$$F_3 = 0.91 (D/L)^{0.28/\left((D/L)^{2.8} - 1\right) + 0.04} \tag{3.35}$$

where:

- L is the seepage length in metres
- θ is the bedding angle in degrees
- η is the drag factor coefficient [-]
- υ is the kinematic viscosity of water ($= 1.33 \cdot 10^{-6}\ m^2/s$)
- d_{70} is the 70%-fraction of the grain size distribution in metres
- d_{70m} is the reference value for d_{70} in metres

The grain size d_{70} refers to the piping-sensitive layer, which is fine sand underlying an aquitard. If the d_{70} is smaller than 63 or larger than 500 , the Sellmeijer model is not applicable (Rijkswaterstaat, 2017). The factor of safety FoS_p [-] is defined as:

$$FoS_p = \frac{H_c}{h - h_p - 0.3d} \tag{3.36}$$

Fault tree

Failure due to piping can only occur if all three sub-mechanism limit states are exceeded ($Z_i < 0$, or P_f, i). So, the sub-mechanisms form a parallel system and the total failure probability is:

$$P_{f,piping} = P_{f,u} \cap P_{f,h} \cap P_{f,p} = \{\{g_u(x) < 0\} \cap \{g_h(x) < 0\} \cap \{g_p(x) < 0\}\} \tag{3.37}$$

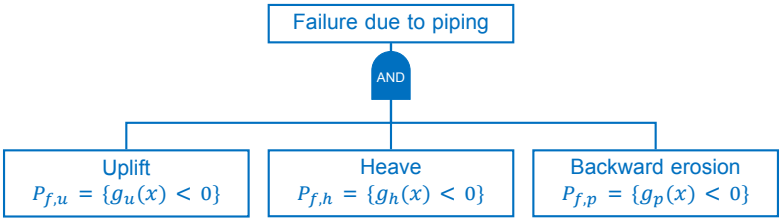

Figure 3.8: Fault tree for the failure mechanism piping.

Importance of the parameters

By means of a FORM analysis, the sensitivity factors, or α-values, can be derived. These factors quantify the importance of each stochastic parameter that is included in the piping assessment. The analysis is executed for a typical Dutch dike section, for which the parameter values where derived from Vrouwenvelder (2006) and Aguilar-López et al. (2016). The results are summarised in a qualitative way in Table 3.3. They are in line with the expectations based on the equations above. However, it is important to notice that the magnitude of the sensitivity factors highly depends on the values for the mean and standard deviation of each stochastic parameter. In other words, the results could be different for another location. The outcome is therefore mainly used to understand which parameters contribute to the load and which to the resistance, and to get a rough feeling of the importance of the different parameters.

Table 3.3: Example of the contribution of the piping parameters.

Parameter	Uplift	Heave	Backward erosion
h	-	-	load, large
d	resistance, small	resistance, small	resistance, small
h_p	resistance, large	resistance, large	resistance, small
Φ_{exit}	load, medium	load, medium	-
k_{v3}	resistance, medium	resistance, medium	-
γ_{sat}	resistance, small	-	-
D	-	-	load, small
d_{70}	-	-	resistance, medium
k	-	-	load, large
L	-	-	resistance, medium

Correlations

As defined in Equation 3.21, Φ_{exit} and h_{exit} are related to each other by the damping factor, that is expressed as in Equation 3.22. If the damping factor is not explicitly defined within an assessment, it can be derived from this equation that positive correlations should be assumed for (Φ_{exit} - h_p), (Φ_{exit} - k) and (Φ_{exit} - D_{cover}) and a negative correlation between (Φ_{exit} - k_h).

In literature, evidence could be found that the grain size d_{70} and the hydraulic conductivity k are positively correlated (Chapuis, 2012), (Aguilar López et al., 2014). In fact, for studies where in-situ measurements are scarce, the hydraulic conductivity is even commonly estimated based on the soil representative diameter and the porosity, by application of the Kozeny-Carman equation (Aguilar-López et al., 2016).

3.3.1. WBI assessment method: STPH

Within the WBI, the assessment track for piping is called STPH (stabiliteit na piping en opbarsten (heave)). Failure due to piping is defined as the exceedance of the critical piping gradient for which the progressive erosion process cannot find an equilibrium any more. The failure probability due to piping is determined by the smallest failure probability of the three sub-mechanisms, as they are assumed to form an independent parallel system. Just like for macrostability, several scenario's are assessed. The failure probabilities due to uplift, heave and backward erosion per section are approximated as follows:

$$P_{f,u} = \Phi\left(\frac{\ln\left(\frac{FoS_u}{0.48}\right) + 0.27 \cdot \beta_{norm}}{0.46}\right) \tag{3.38}$$

$$P_{f,h} = \Phi\left(\frac{\ln\left(\frac{FoS_h}{0.37}\right) + 0.3 \cdot \beta_{norm}}{0.48}\right) \tag{3.39}$$

$$P_{f,p} = \Phi\left(\frac{\ln\left(\frac{FoS_p}{1.04}\right) + 0.43 \cdot \beta_{norm}}{0.37}\right) \tag{3.40}$$

where β_{norm} is the reliability index of the dike trajectory . The total failure probability of the section for scenario i is then:

$$P_{f;i} = \min\left(P_{f,u;i}; P_{f,h;i}; P_{f,p;i}\right) \tag{3.41}$$

The total failure probability of the cross-section is then computed in the same way as for macrostability, as described by Equation 3.20. To get to the trajectory failure probability for piping, the length-effect factor N is considered.

3.3.2. Choice for the model

The limit state functions of the three sub-mechanisms, as described above, will be implemented in a full-probabilistic framework. An existing Python script by HKV will be utilised, in which the different limit state functions have been programmed. One main difference with the approach above is the implementation of the exit point potential Φ_{exit}. For the case study, the exit point potential is explicitly defined as an input variable, instead of by computation according to Equation 3.21. However, the model of this study will be built such that application of the Equations 3.21 and 3.22 is possible as well, since it can be useful for future research. The critical heave gradient $i_{c,h}$ will be implemented by the lognormal distribution, according to the WBI. The input will be defined in Chapter 5.

3.4. Erosion of the Grass Revetment at the Outer Slope

This failure mechanism concerns erosion of the grass revetment on the outer slope of a dike. The strength of the grass cover is determined by the interplay between the grass and the underlying clay layer. Together they form a layer of about 20 cm. An important part of the grass revetment are the roots. From laboratory experiments it has been found that the density of the root network of a grass revetment is even more important than the erosion resistance of the soil ('t Hart et al., 2016). A non-uniform grass layer - with variation in the shape and size of the roots - performs much better than uniform grass. The erosion resistance of the underlying clay layer depends on its plasticity and its sand content (Jonkman et al., 2018). Erosion can occur as the result of two load types: (1) wave impact and (2) wave run-up.

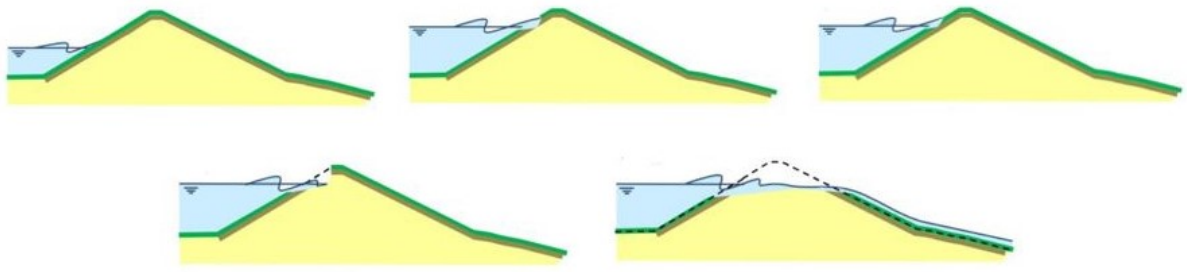

Figure 3.9: Schematisation of the failure of a sandy dike, due to erosion of the grass by wave impact ('t Hart et al., 2016).

3.4.1. Wave impact

Wave impact leads to an impulsive local increase of the water pressure on the slope. This impulse penetrates the grass revetment and causes a pressure gradient that can damage the sod and even remove parts of it: Just after the wave impact is over, the pressure in the grass revetment is still high, which can lead to an outward directed pressure gradient that can push out the grass. Both the wave height and the duration of wave impact loads are important. Repetitive wave impacts can, even for strong roots, lead to erosion. This is the first sub-mechanism of this failure mechanism. The second is the erosion resistance after development of a gap in the revetment. The revetment close to the gap will be undermined. The erosion rate of the subsoil depends on the soil type. Sand will erode much quicker than clay. Failure of the dike (i.e. flooding of the hinterland) occurs if erosion continues such that the residual dike profile is lower than the water level. This process is schematised in Figure 3.9. It is also possible that the erosion process provokes another failure mechanism. For example, due to the narrowing dike profile, it is possible that the inner slope becomes unstable as a result of an increase of the pore pressures in the dike (micro-/macro-instability).

The dike's resistance against wave impact is often assessed by comparing the load duration to the resistance time of the grass revetment. The resistance time - the measure of strength of the grass revetment - is the duration that the grass revetment can resist a certain wave height. The load duration is defined as the time that a certain point on the grass revetment is exposed to wave impact during a storm event. It is assumed that wave impact occurs in the zone between mean sea level and half a significant wave height below. However, with a varying water level h and wave height H_{m0} during a storm event, the exposure zone varies in time during an event. To deal with this variation, a storm event is treated as a series of stationary time intervals ΔT: the water level and wave height are assumed to be constant within one interval. Also, a certain amount of discrete points on the outer slope is chosen, that form a series of evaluation levels.

For each evaluation level z_j and each time interval t_i of stationary hydraulic load parameters at the toe of the dike, a so-called failure fraction can be computed (de Waal and van Hoven, 2019):

$$F_{f,top,z_j,t_i} = \frac{t_{load,z_j,t_i}}{t_{s,top,z_j,t_i}} \tag{3.42}$$

where:

- F_{f,top,z_j,t_i} = Contribution of time interval t_i to failure fraction of top layer at evaluation level z_j [-]
- t_{load,z_j,t_i} = Load duration of time interval t_i at evaluation level z_j in hours
- t_{s,top,z_j,t_i} = Strength duration of top layer in time interval t_i at evaluation level z_j in hours

This failure fraction explicitly refers to the top layer, i.e. the grass sod. The underlying clay layer will be evaluated separately, after the grass has failed. This will be explained later on.

Resistance time of the grass layer

The resistance time or strength duration of the top layer, in hours, can be computed as follows:

$$t_{s,top} = \begin{cases} t_{s,top,min} & \text{for } f_\beta \cdot H_{m0} \geq a + c \text{ or } a = 0 \\ t_{s,top,max} & \text{for } f_\beta \cdot H_{m0} \leq c \\ \min\left[\max\left\{\frac{1}{b}\ln\left(\frac{f_\beta \cdot H_{m0} - c}{a}\right); t_{s,top,\min}\right\}; t_{s,top,\max}\right] & \text{for } c \leq f_\beta \cdot H_{m0} \leq a + c \end{cases} \tag{3.43}$$

where a, b and c are constants in the relation between the significant wave height and the strength duration ($a \geq 0$ $[m]$, $b < 0$ $[1/hr]$ and $c \geq 0$ $[m]$). The parameter $t_{s,top,min}$ is primarily introduced to avoid dividing by zero in Equation 3.42. Its value should be set to much smaller than likely values for the time interval duration ΔT, for example $0.001hr$. The parameter $t_{s,top,max}$ is primarily introduced to avoid infinite values for $t_{s,top}$. Its value should be set to a recognisable dummy value, like $1000hr$ (de Waal and van Hoven, 2019).

The reduction factor f_β for the angle of wave attack [-] is introduced to obtain the 'effective wave height':

$$f_\beta = \begin{cases} \max\left\{(\cos\beta)^p ; q\right\} & \text{for } \beta \leq 90° \\ \max\left\{q \cdot \left(\frac{100-\beta}{10}\right); 0\right\} & \text{for } \beta > 90° \end{cases} \tag{3.44}$$

with $p = 0.67$ and $q = 0.35$ (de Waal and van Hoven, 2019). The angle of wave attack β, relative to perpendicular wave attack, is calculated from the direction of the waves and the orientation of the dike normal, as shown in Equation 3.13.

Load duration
If $(h - 0.5 \cdot H_{m0}) \leq z_j \leq h$, the evaluation level z_j [m+NAP] will be exposed to wave impact load of duration $t_{load} = \Delta T$. Otherwise $t_{load} = 0$.

For each evaluation level, the failure fractions are accumulated over the previous time intervals, to eventually obtain the cumulative failure fraction for the storm event:

$$F_{f,cum,top,z_j,t_i} = \sum_{1}^{t_i} F_{f,top,z_j,t_i} \tag{3.45}$$

As soon as this sum exceeds 1 after a certain time interval t_i at a certain evaluation level z_j, the critical value of the failure fraction is exceeded and the grass revetment has failed at that location during that storm. From that moment onward, the underlying clay layer starts to erode. Different approaches exist of how to deal with the erosion of the clay. It mainly depends on the material of the dike core. If the dike core consists of mainly sand or clay with a high sand fraction, the residual strength of the dike core is generally neglected. In that case, only the resistance of the underlying clay layer of the grass root zone is considered, because the roots give extra strength to the layer. However, in recent years, new insights have resulted in computational models that do take into account the residual strength of the dike core, even if it consists of sand (Rongen et al., 2019). The various approaches for these different situations will be elaborated below.

Resistance of the root zone or sub layer
In fact, each time interval t_i contributes a failure fraction F_{f,cmb,z_j,t_i} to the failure fraction of the combination of top layer and sub layer. But, this contribution depends on the phase of the failure mechanism process (de Waal and van Hoven, 2019):

$$F_{f,cmb,z_j,t_i} = \begin{cases} \frac{t_{load,z_j,t_i}}{t_{s,top,z_j,t_i} + t_{s,sub,z_j,t_i}} & \text{for } F_{f,cum,top,z_j,t_i} < 1 \\ \frac{t_{load,z_j,t_i}}{t_{s,sub,z_j,t_i}} & \text{for } F_{f,cum,top,z_j,t_i} \geq 1 \end{cases} \tag{3.46}$$

where t_{s,sub,z_j,t_i} is the strength duration of the sub layer in time interval t_i at evaluation level z_j [hr] :

$$t_{s,sub} = \begin{cases} t_{s,sub,min} & \text{for } d_c \leq 0.2 \text{ or } a = 0 \\ t_{s,sub,max} & \text{for } f_\beta \cdot H_{m0} \leq 0.5 \text{ and } d_c \geq 0.5 \\ \min\left(\frac{\min(d_c;0.5)-0.2}{c_d(\tan\alpha)^{1.5}\max\left(f_\beta \cdot H_{m0}-0.5;0.001\right)}; t_{s,sub,max}\right) & \text{otherwise} \end{cases} \tag{3.47}$$

Where d_c is the thickness of the top and underlying clay layer [m]. $t_{s,sub,max} = 1000$ and $t_{s,sub,min} = 0.001$ are the maximum and minimum value for the strength duration of the sub layer [hr], c_d is the correction factor for the sand content of the clay [-] and $\tan\alpha$ is the representative slope [-], which is generally 1/3. For the constant c_d, the following relationship can be applied:

$$c_d = 1.1 + \max\left(0; 8\left(F_{sand} - 0.7\right)\right) \tag{3.48}$$

with F_{sand} the sand fraction in the clay [-]. From these formulas, the following can be noted: A steeper slope, a larger sand content and a larger wave height result in less resistance.

Again, the failure fraction of the combination of grass and underlying clay layer is accumulated over the time intervals of the storm for each evaluation level:

$$F_{f,storm,z_j} = \sum_t F_{f,cmb,z_j,t_i} \tag{3.49}$$

The decisive failure fraction for the grass section is the maximum from the values of the different evaluation levels and is called $F_{f,storm}$.

Residual strength of a clayey dike core
Some dikes consist of a clay dike core or a clay layer underneath the root zone. To include the residual strength of the clay, the approach by Mourik (2015) can be applied. According to Mourik (2015), the erosion volume V_e $[m^3/m]$ per time interval t can be computed as follows:

$$V_e = \begin{cases} 466 \cdot c_e \cdot H_s^2 \cdot (H_s - 0.4)^2 \cdot (\tan\alpha)^2 \cdot \min\left(3.6; \frac{0.0061}{{s_{op}}^{1.5}}\right) \cdot \left(1 - e^{\frac{-0.079 \cdot t}{{H_s}^2}}\right) & \text{for } H_s > 0.4\text{m} \\ 0 & \text{for } H_s \leq 0.4\text{m} \end{cases} \tag{3.50}$$

in which c_e is the erosion coefficient for the clay $[m^3/s]$ and s_{op} is the wave steepness $H_s/\left(1.56 \cdot T_p^2\right)$, with T_p the wave spectral peak period $[s]$. A schematisation of this erosion volume is presented in Figure 3.10. It can be noted that shallow waves and a steep slope lead to more erosion. Consequently, the erosion depth can be computed with:

$$d_e = \sqrt{V_e \cdot \tan\alpha} - 0.14 \tag{3.51}$$

for $V_e \geq 0.75\ m^3/m$ and $\tan\alpha$ in the range of $1/3$ to $1/4$. The formulas can be applied for clay with a sand fraction of less than 40% (clay category 1 or 2). Based on these formulas, it is possible to define the erosion profile for every time interval and to determine whether the residual profile is still sufficient. The dimensions of a sufficient residual profile depend on the situation.

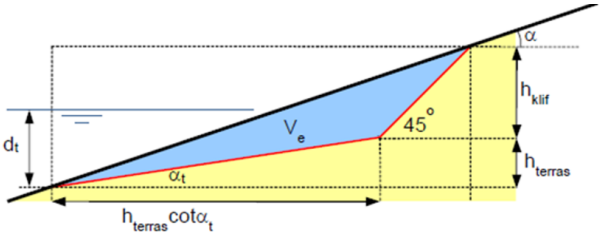

Figure 3.10: Erosion profile after wave impact (Mourik, 2015).

Residual strength of a sandy dike core
In most cases, the residual strength of a sandy layer or core is neglected, because sand erodes relatively quickly compared to clay. However, Rongen et al. (2019) adopted the following formula from Klein Breteler et al. (2012) for the erosion rate of a sand body:

$$\frac{\partial V}{\partial t} = \frac{{H_s}^2}{T_p}\left(\frac{0.15}{{s_{op}}^{1.3}} \tan(\alpha)^{0.8} \left(135 - 1500 \cdot s_{op}\right) \cdot \exp\left(-0.0091 \cdot \left(\frac{B_t}{H_s}\right)^2\right)\right) \tag{3.52}$$

in which B_t is the width of the erosion terrace, i.e. the shallow part of the erosion profile $[m]$. A wider terrace breaks the waves, resulting in less erosion.

3.4.2. Wave run-up

Erosion due to wave run-up is the result of a flow on the outer slope due to wave run-up (and run-down). The flow of running-up wave is turbulent, resulting in a rapidly varying pressure on the grass revetment underneath. Due to penetration of this pressure and the spatial variability of the pressure, the revetment is exposed to outward pressure gradients at some locations, that can rip out parts of the grass revetment. Run-up occurs in the zone above the mean water level until the maximum level that is reached by the waves running up the slope. Therefore, the analysis of run-up is restricted to:

$$z_{eval} > \max_{\text{storm event}}(h) \tag{3.53}$$

with z_{eval} the level of interest on the outer slope [m+NAP].

Erosion due to wave run-up is generally assessed by the so-called 'cumulative overload'. The load is mainly dependent on the wave front velocity. If at a certain level of interest, z_{eval}, the effective front velocity load of a single wave run-up event exceeds a critical velocity load, then the run-up event adds to the cumulative overload D_{load} at z_{eval}. The formula describing this process is (de Waal and van Hoven, 2015):

$$D_{load,z} = \sum_{i=1}^{N} \max\left(\alpha_{M,z} U_{i,z}^2 - \alpha_{S,z} U_c^2; 0\right) \tag{3.54}$$

where:

- N = Number of incident waves [-]
- $U_{i,z}$ = Front velocity along the slope of running-up wave i at level z [m/s]
- U_c = Critical front velocity along the slope [m/s]
- $D_{load,z}$ = Cumulative overload at level z [m^2/s^2]
- $\alpha_{M,z}$ = Factor for increased load at transitions and objects, $\alpha_{M,z} \geq 1$ (1.0 by default) [-]
- $\alpha_{S,z}$ = Factor for decreased strength at transitions and objects, $\alpha_{S,z} \geq 1$ (1.0 by default) [-]

The number of running-up waves is assumed to be equal to the total number of incident waves N at the dike toe during the time interval ΔT [hr]:

$$N = \frac{3600 \cdot \Delta T}{T_m \cdot \gamma_\beta} \tag{3.55}$$

in which T_m is the mean wave period in seconds: $T_m = c_{T_{m\_}T_{m-1,0}} \cdot T_{m-1,0}$ and γ_S is a reduction factor for the angle of wave attack:

$$\gamma_\beta = \min\left(1; \max\left(\frac{110 - \beta}{30}; 0\right)\right) \tag{3.56}$$

where β is the angle of wave attack, relative to the dike normal, as described by Equation 3.13.

The front velocity $U_{i,z}$ depends on the level of interest z. From experiments it is known that the wave front velocity is constant for about 75% of the distance that the wave runs up from the mean water level ('t Hart et al., 2016). Therefore, it is advised to use the maximum front velocity $U_{\max}$ between the still water level and 75% of the run up level. $U_{i,max}$ of run-up event i [m/s] is described by:

$$U_{i,\max} = c_u \sqrt{g \cdot Ru_i} \tag{3.57}$$

with constant $c_u = 1.1$ and the run-up level Ru_i defined with respect to still water level [m].

Between 75% and 100% of the run-up level of a particular wave run-up event, it is assumed that the velocity decreases linearly. Here, the front velocity $U_{i,z}$ is given by:

$$U_{i,z} = U_{\text{i,max}} \cdot \max\left(0; \min\left(1; \frac{Ru_i - z}{0.25 \cdot Ru_i}\right)\right) \tag{3.58}$$

The run-up level Ru_i can be calculated from a probability of exceedance $P(\underline{Ru} > Ru)$. The run-up height - in metres relative to the still water level - for a wave field reaching a dike is assumed to be Rayleigh distributed (disregarding any change in slope angle or roughness along the slope):

$$Ru = Ru_{2\%} \cdot \sqrt{\frac{\ln(P(\underline{Ru} > Ru))}{\ln(0.02)}} \tag{3.59}$$

The 2% run-up can be computed by the TAW formulas (TAW, 2002), as described by the Equations 3.8 and 3.9. It is assumed that the run-up height Ru follows a Rayleigh distribution, as it scales linearly with the wave height. But not every wave in the time period reaches the evaluated level. This can be solved by sampling several waves from the Rayleigh distribution, and calculating the load for each wave (de Waal and van Hoven, 2015). However, this approach can be numerically expensive. As an alternative, Rongen et al. (2019) adopted a different approach, based on Smale, 2018. In that approach, the load at a level z is evaluated on a specified range of Ru, to avoid requiring very large sample sizes to obtain enough high waves. The range is defined from the run-up height for which U_c is just exceeded (Ru_{min}) until the upper level that is defined as $3 \times Ru_{2\%}$:

$$Ru_{min} = \frac{U_c^2}{c_u^2 \cdot g} \cdot \frac{\alpha_S}{\alpha_M} \tag{3.60}$$

This range is divided into 100 steps and the load is computed for each step of Ru_i. The probability mass for each step of Ru_i is:

$$f(Ru_i) = 2 \cdot \frac{Ru_i}{{Ru_{i,rms}}^2} \cdot \exp\left(-\left(\frac{Ru_i}{Ru_{i,rms}}\right)^2\right) \cdot \text{stepsize} \tag{3.61}$$

with:

$$Ru_{i,rms} = \sqrt{\frac{-{Ru_{2\%}}^2}{\ln(0.02)}} \tag{3.62}$$

The actual velocity $U_{i,z}$ at level z for wave i is then evaluated for each step of Ru_i, using Equation 3.58. The damage is computed for every step, then multiplied by the density mass of the step and finally summed over the steps and multiplied by N:

$$D_{load,z} = N \cdot \sum \max\left(\alpha_M \cdot {U_{i,z,step}}^2 - \alpha_S \cdot {U_c}^2; 0\right) \cdot f(Ru_i) \tag{3.63}$$

The cumulative overload value is computed for a storm event by accumulating the results over the time intervals at the considered level on the outer slope. If the cumulative overload exceeds a certain critical value D_{crit}, then the grass will start to erode - i.e. show damage at that evaluation level. The failure mechanism can thus be described by the following limit state function:

$$Z_{run-up} = D_{crit} - D_{load} \tag{3.64}$$

Note that this failure mechanism description does not explicitly take residual strength of the dike core into account. However, the value of D_{crit} can be chosen such that it implies failure of the dike. In that case, a value of $7000\ m^2/s^2$ is usually applied. After erosion has occurred, failure of the dike does evolve in fact just as described for erosion of the sub layers due to wave impact. But now the starting point is somewhat higher on the slope. Anyway, not much is known about the processes leading to flooding due to erosion by wave run-up

In general, the loads due to wave impact are more critical than the loads due to wave run-up. In many cases, the wave impact zone is covered with a hard revetment and the grass revetment above is only exposed to wave run-up (’t Hart et al., 2016). In those cases, there will always be an interface between hard and grass revetment. This interface is a weak spot.

3.4.3. WBI assessment method: GEBU

In the WBI, the assessment track for erosion of the grass revetment on the outer slope is called GEBU (Gras Erosie Buitentalud). Failure is defined as the moment at which a hole is present in the grass revetment (grass + clay sub layer) due to erosion, so that the subsoil is no longer protected against erosion (Rijkswaterstaat, 2017). The residual strength of the dike core is generally not considered. The assessment is based on a semi-probabilistic approach. The resistance of the dike - the resistance time of the grass revetment for wave impact and the critical wave front velocity for wave run-up - depends on the quality of the grass, for which three categories exist: a closed, open or fragmentary sod.

For the upper reaches of the Dutch rivers, a constant water level is used, with a storm period of 12 hours. For every water level, the wave conditions corresponding to the return period of the norm failure probability of the cross-section are computed. Therefore, the water level with the highest wave height is normative.

Wave impact

In the assessment, the load duration is compared to the resistance time, including any strength of the clay layer underneath. The assessment is based on the approach by de Waal and van Hoven (2019), as described by the Equations 3.42 to 3.49. The following values are used for the parameters that determine the resistance time of the grass:

- Closed sod: $a = 1$, $b = -0.035$, $c = 0.25$
- Open sod: $a = 0.8$, $b = -0.07$, $c = 0.25$

The decisive failure fraction of Equation 3.49 is used for the definition of a factor of safety:

$$FoS = \begin{cases} FoS_{\max} & \text{for } F_{f,storm} \leq \frac{1}{FoS_{max}} \\ \frac{1}{F_{f,storm}} & \text{for else} \end{cases} \tag{3.65}$$

The parameter FoS_{max} is primarily introduced to avoid dividing by zero and can be set to 10 for example (de Waal and van Hoven, 2019). Or in terms of a limit state function:

$$Z_{impact} = 1 - F_{f,storm} \tag{3.66}$$

Wave run-up

Failure due to erosion of the grass revetment on the outer slope by wave run-up is defined as the moment when the top layer with a thickness of 0.2 m is locally ruptured and the erosion of the sub layer starts. Only erosion of the grass revetment is determined, because there is no erosion model for the underlying layers available for the run-up zone. The resistance of the clay layer is thus not taken into account. The approach by de Waal and van Hoven (2015), as explained above, is applied for one single normative (lowest) evaluation level of the grass revetment on the outer slope (Rijkswaterstaat, 2017). Usually this is at the transition between 'hard' (e.g. block, asphalt) and grass revetment. For discrete time steps, the distribution of the run-up velocities is determined and used to evaluate the limit state function, as described by Equation 3.64. For the critical wave front velocity, the following values are applied:

- Closed sod: $6.6\ m/s$
- Open sod: $4.3\ m/s$

3.4.4. Prototype time-dependent loads on revetments

In the current assessment methods, peak values for the loads are used to evaluate the resistance against erosion. In reality, these peak values are often not likely to occur at the same time and the loads vary during an extreme event. Therefore, the current assessment method is too conservative. Rongen et al. (2019) have developed a prototype for the calculation of the strength of a grass revetment on dikes under hydraulic conditions varying in time. In other words, the progressive damage during a storm is assessed by evaluating a time series of water level, wind speed and wind direction. For the assessment of the grass revetment, the approach by de Waal and van Hoven (2019) is applied, as explained by Equation 3.42 etc. However, the resistance of the grass root zone is taken out of the equation, since the model also takes the residual strength of the dike core into account, as described by Equations 3.50 - 3.52. More information about this prototype can be read in Appendix B.5.

3.4.5. Choice for the model

Python scripts of the protoype, as introduced in Section 3.4.4, are used as reference for the model. In these Python script, some of the formulas that are also applied in the WBI kernel for the assessment of GEBU are implemented. It comes down to the following approach in the model:

- For the assessment of erosion of the grass revetment due to wave impact, the approach by de Waal and van Hoven (2019) is applied (Equations 3.42, 3.49 etc.).
- For the erosion of the clayey dike core, Equation 3.50 is applied. The reason for this is that it is also applied in the WBI assessment of the specific case study that will be considered. To stay close to the assessment of the case study, the same approach will be applied.
- Wave run-up will be assessed by the approach as elaborated in Section 3.4.2 and by calling the `dllDikesOvertopping64.dll`, in which the 2% run-up is computed, conform the WBI.

However, the time-dependent load aspect of the protoype will initially not be used in the model, in order to keep it similar to the WBI assessment. But, including time-dependent loads would be a possible improvement for the model.

4

Hydraulic Loads

Beside the limit state functions for the different failure mechanisms, the hydraulic boundary conditions are required. A good representation of the hydraulic loads is essential in the assessment of flood defences. Hydraulic models are needed to derive the local water levels and wave conditions from the more general basic variables like the sea level and the river discharge.

The most important hydraulic loads are water levels, wave action, currents, groundwater flow and pore pressures. The water level in turn is dependent on several phenomena: river discharge, tide, storm surge etc. Its determination differs for river and sea water levels. The magnitude and direction, but also the duration of these loads, are very important to include in the assessments. For example, the longer the duration of extreme water levels, the higher the probability of overflow or overtopping. Furthermore, the water will penetrate into the dike's subsoil during a longer period, thus increasing the pore pressures and decreasing the soil's effective stress and therefore the dike's stability (Jonkman et al., 2018).

The difficulty of defining the loads lies in their natural variability - and thus uncertainty. The loads vary in time and in space. It is important to incorporate these uncertainties in the assessments, which makes it important to define the load parameters as stochastic (random) variables. From the corresponding probability density functions, the probabilities of occurrence of e.g. a certain water level can be derived. Examples of uncertain variables that can be described as continuous stochastic variables are the wind direction or river discharge. In the safety assessments of flood defences, the focus obviously lies on extreme load values, with a small probability of exceedance, so on the right-hand tail of the distribution. Therefore, the statistics of the extreme values are often used, that can be described by GEV distributions. Some uncertain variables are not easily described as continuous. Think of the wind direction, which is better described as discrete stochastic, implying that a finite number of realisations is defined, each with a certain probability. The sum of those is 1 (de Waal, 2016).

4.1. Current Assessment Method

Local statistics of water levels and waves are not available for each dike section or each flood defence of the Netherlands. In practice, these local statistics are derived from the source (global) variables of the local hydraulic loads and the physical relation between the source variable and the local hydraulic load. Source variables are river discharges, wind velocities and sea water levels. These are called the basic stochastic variables. These parameters are linked to a reference location, for example the river discharge at Lobith or the wind speed at Schiphol. The definition of the basic stochastic variables is focussed on extreme values. For every water system of the Netherlands, a specific combination of basic stochastic variables and their corresponding reference location has been defined. In the WBI, the definition of the physical relation between a basic stochastic variable at a reference location and the local hydraulic load at the flood defence is a process that has been pre-defined and the results are provided in databases. In these tables, local extreme values are provided for certain load events, based on combinations of the basic stochastic variables. This is done for many different locations (x,y-locations). For the assessment of a dike section, a normative location is chosen and the hydraulic loads are derived from the corresponding suitable database. Interpolation between two locations is not done. As an example, for a certain location at a flood defence along an upper river reach, it is possible to find the local water levels for certain values of the corresponding discharge and the local values of

the river bottom level and fetch length for the different wind directions. These can subsequently be used to derive the local wave climate, by means of the Bretschneider equations:

$$H_s = \frac{0.283u^2\alpha}{g}\tanh\left(\frac{0.0125}{\alpha}\left(\frac{gF}{u^2}\right)^{0.42}\right) \quad , \quad \alpha = \tanh\left(0.530\left(\frac{gd}{u^2}\right)^{0.750}\right) \tag{4.1}$$

$$T_s = \frac{2.4\pi u\beta}{g}\tanh\left(\frac{0.077}{\beta}\left(\frac{gF}{u^2}\right)^{0.25}\right) \quad , \quad \beta = \tanh\left(0.833\left(\frac{gd}{u^2}\right)^{0.375}\right) \tag{4.2}$$

where F is the (effective) fetch length $[m]$, u is the wind speed $[m/s]$ and d is the water depth $[m]$. The formulas are applicable for narrow waters without significant flow velocities, like the Dutch Rhine.

The combination of hydraulic loads that are relevant depends on the system that is considered. The different systems that are defined in the Netherlands are: tidal rivers, non-tidal rivers, lakes, estuaries and seas. Brief descriptions of the basic stochastic variables are provided below.

1. Wind
Wind is the driving force for waves and it can be a source for high water levels. Wind is a so-called fast stochastic variable, implying that its value fluctuates rapidly in time. Wind has two components: wind direction and wind speed. The wind speed is defined as a discrete stochastic variable with a finite number of realisations, mostly 16 directions, corresponding to a certain interval of directions. The wind direction is a continuous stochastic variable, whose statistics are measured at specific locations. In the current WBI approach each period of 12 hours is independent of the last or following 12 hours. However, this is not the case in actual weather conditions (Rongen et al., 2019).

2. Sea water level
The sea water level is defined as a continuous stochastic variable, expressed as a probability distribution for a certain wind direction. The probability distribution refers to a maximum water level during a tidal period. For the determination of the local sea water level, interpolation is applied (de Waal, 2016).

3. River discharges
The river discharge is a slow stochastic variable. The statistical information for the discharge consists of exceedance frequencies and extreme durations. Reference locations are used for the statistical information.

4. Lake water levels
The lake water level is the spatially averaged water level in a lake, and therefore a measure for the water volume of the lake. It is a slow stochastic variable and thus the duration plays a role as well.

5. Storm surge barrier
The status of a storm surge barrier is a fast stochastic variable. It is discrete, often with two possible realisations: *open* or *closed*. It is only necessary to include a storm surge barrier as a stochastic variable if the uncertainty of operation has to be accounted for.

The way in which the hydraulic loads and their uncertainties are incorporated in the assessments differs per assessment track. For a semi-probabilistic approach, a design value is determined for every relevant load parameter. The design value of a load parameter is the value that corresponds to a probability of exceedance that is equal to the failure probability norm of the dike trajectory under consideration. The design values are determined using extreme value statistics.

For assessment tracks that are exposed to more than one load parameter, it is more complicated to define the design values, since the combination of parameters should satisfy the probability of exceedance corresponding the norm. This problem can be avoided by a probabilistic approach, like it is done for overtopping and overflow. For the assessment tracks related to the revetment this is not yet possible in the current assessment procedure. Therefore, dike revetments are assessed based on design values of both water levels and wave conditions (wave height, wave period and wind speed). However, peak values in wave conditions and water levels do often not occur at the same time, which makes this approach quite conservative (Rongen et al., 2019). Moreover, the normative load for revetments is in

reality not only determined by the peak value of the load, but also by the duration and by the variation of in time during an event. Some pragmatic choices have been made to incorporate these aspects - by the so-called *Q-Variant* - but not in a very accurate way. An alternative for the Q-variant has recently been proposed by Rongen (2020). The implementation of time dependent loads on revetments has been investigated by means of a prototype by Rongen et al. (2019). These improvements are briefly discussed in Appendix B.5 and Section 3.4.4.

4.2. Models

Models are needed for the derivation of the statistics of the basic stochastic variables and for the translation from basic stochastics variables to other load variables (e.g. river water levels or waves). Some relevant models are shortly introduced below.

RACMO
For the wind statistics, it is possible to make use of the RACMO model. The RACMO wind data consists of 800 years of hourly values of the potential wind speed and wind direction (van Meijgaard et al., 2008). The potential wind speed is the wind speed as it is measured on an open grass field at 10 metre height. The RACMO data is generated by means of a weather model, which contains realistic patterns, such as autocorrelation of the direction and wind speed.

GRADE
The statistics of the river discharge at Lobith and Borgharen can be determined by GRADE. GRADE stands for Generator of Rainfall and Discharge Extremes. It is an instrument to derive physically-based design discharges and associated flood hydrographs for the rivers Rhine and Meuse. Stochastic simulation of the weather and hydrological / hydrodynamic modelling are the key elements of this method. The GRADE method includes a stochastic weather generator, a rainfall-runoff model and hydrological and hydrodynamic routing, for example by SOBEK (Hegnauer et al., 2014). Based on a 50,000 year long rainfall series, 50,000 years of discharges at Lobith (Rhine river) or Borgharen (Meuse river) were calculated using hydrological and hydrodynamic models, resulting in frequency discharge curves and flood hydrographs. In this set, the daily as well as the very extreme conditions are present (up to once in $\pm$50,000 years), giving a good representation of the variety of possible conditions.

Hydra-NL
Hydra-NL is a probabilistic model to compute the statistics of the hydraulic loads for the assessment of flood defences in the Netherlands. It is consistent with the WBI 2017. Hydra-NL computes water levels, wave conditions, hydraulic load levels and occurring overtopping discharges for revetments. The model can also be used for the assessment of the crest height for overtopping and overflow.

4.3. Climate Change

A flood defence is generally assessed for a certain year in the future, for example 2050 or 2100. Therefore, the hydraulic loads, that are applied in the assessment, should be adapted such that they are representative for this reference year. This is where climate change comes into play. It is likely that the discharge and wind conditions will be different in the future. However, there is a large uncertainty in the forecasts by different climate models. In 2006, the Royal Dutch Institute for Meteorology (KNMI) has created four climate scenarios, based on results of extensive climate research and different models. Climate scenarios are consistent and plausible images of the future climate. They give an impression of the changes in temperature, precipitation, wind and sea level for a climatological period of 30 years (KNMI, 2006). Every scenario is plausible and it is hard to say which one is the most likely to occur. The four scenarios are:

- G: Moderate; 1°C temperature increase in 2050, with respect to 1990. No changes in the air flow patterns in Western Europe.
- G+: Moderate+; 1°C temperature increase in 2050, with respect to 1990. Milder and wetter winters due to more western winds and hotter and dryer summers due to more eastern winds.
- W: Warm; 2°C temperature increase in 2050, with respect to 1990. No changes in the air flow patterns in Western Europe.

- W+: Warm+; 2°C temperature increase in 2050, with respect to 1990. Milder and wetter winters due to more western winds and hotter and dryer summers due to more eastern winds.

These scenarios are used in design and in exploratory studies. In flood defence practice, implementing a climate scenario generally results in higher probabilities for extreme discharges and wind speeds and a change in the distribution of the wind directions. For coastal flood defences, the sea level rise is obviously included as well.

4.4. Uncertainties

As mentioned above, there is a large uncertainty present in the determination of the hydraulic loads. Different causes of uncertainty have been discussed in Section 2.2. Two particular forms of uncertainty that are incorporated in the WBI assessments will be elaborated on below: statistical uncertainty and model uncertainty.

4.4.1. Statistical uncertainty

There are four generic models to describe statistical uncertainties: (1) the additive model, (2) the multiplicative model, (3) the additive model with truncation and (4) the multiplicative model with truncation. For the basic stochastic variable discharge, the additive uncertainty model is generally applied and for the wind speed the multiplicative model (Geerse, 2015). In the additive model, the uncertainty stochastic variable Y is added to the basic stochastic variable without uncertainty X: $V = X + Y$, where V is the basic stochastic variable with the uncertainty included. In the multiplicative model, the uncertainty stochastic variable is multiplied by the basic stochastic variable: $V = X \cdot Y$. Y is normally distributed with mean $E(Y|X = x) = 0$ for the additive model and $E = (Y|X = x) = 1$ for the multiplicative model. So, the statistics of Y depend on the realisation x of X. Now, the probabilities of exceedance of the basic stochastic variable including uncertainty (V) can be computed by numerical integration, as follows (Geerse, 2015):

For the additive model:

$$P(V > v) = \sum_{i=1}^{n} f(x_i)\Delta x \left[1 - F_{Y|X=x_i}(v - x_i)\right] \tag{4.3}$$

For the multiplicative model:

$$P(V > v) = \sum_{i=1}^{n} f(x_i)\Delta x \left[1 - F_{Y|X=x_i}(v/x_i)\right] \tag{4.4}$$

where x_i is a realisation of X. X is often provided by a table with probabilities of exceedance.

Including the uncertainty results in smaller return periods - i.e. larger probabilities of occurrence - of certain discharges or wind speeds, and thus larger failure probabilities with respect to the situation without uncertainty. By accounting for the uncertainty in the statistics of the basic stochastic variables, the effect of uncertainties is also included in semi-probabilistic assessments, without introducing an extra variable (Diermanse and Jongejan, 2016). The process described above is often called *integrating out* (in Dutch: 'uitintegreren').

4.4.2. Model uncertainty

Discharges are commonly translated to local water levels by means of models like SOBEK or WAQUA. In general, models are not able to reproduce the exact actual water level. The main source of uncertainty is the roughness and morphological changes under extreme circumstances (Chbab and Groeneweg, 2015). So, there is always an error Δh^* in the local water level, that is defined as the difference between the actual water level and the predicted water level by the model (Duits and Kuijper, 2019):

$$\Delta h^* = h_{loc,w} - h_{loc,mod} \tag{4.5}$$

However, the local water level is an uncertain parameter. This uncertainty is incorporated by assuming that the error Δh^* is normally distributed: $\Delta h^*\ N(\mu_{\Delta h^*}, \sigma_{\Delta h^*})$. In Hydra-NL this model uncertainty is

incorporated by a surcharge to the water level (additive model):

$$V_{incl} = V_{excl} + (\mu + \sigma \cdot E_N) \tag{4.6}$$

in which E_N is a stochastic variable with a prescribed distribution.

For the wave height and wave period, the model uncertainty arises from the application of the Bretschneider equations or the SWAN model, for the translation of the basic stochastic variable to the local wave conditions. These model uncertainties are incorporated by multiplying the parameters by a factor f that is normally distributed as well (multiplicative model):

$$V_{incl} = V_{excl} \cdot (1 + \mu + \sigma \cdot E_N) \tag{4.7}$$

In general, including these uncertainties leads to somewhat higher hydraulic loads (Chbab and Groeneweg, 2015). The model uncertainty parameters for the upper reaches of a Rhine branch (specifically the Waal) are listed in Table 4.1. The μ and σ values for the wave conditions are relative values. A negative value of the mean for the model uncertainties of the wave conditions implies that the applied model underestimates reality.

The way in which the hydraulic loads will be implemented in the model of this study, will be explained in the next chapter.

Table 4.1: Overview of the model uncertainty parameters .

Notation	Distribution	Expected value [m]	Standard deviation [m]
$\gamma_1 = \Delta h^*$	$N(\mu_1, \sigma_1)$	0	0.15
$\gamma_2 = f_H$	$N(\mu_2, \sigma_2)$	-0.04	0.27
$\gamma_3 = f_{T_{m-1,0}}$	$N(\mu_3, \sigma_3)$	$+0.03$	0.13
$\gamma_4 = f_{T_P}$	$N(\mu_4, \sigma_4)$	$+0.03$	0.13

II

Data

5

Model Set Up

In this chapter, relevant information regarding the case study, its safety assessment by the water authority and the resulting model input will be presented. Subsequently, the general model set up of the probabilistic assessment framework will be explained.

5.1. Trajectory Sprok-Sterreschans

The probabilistic framework will be applied to the dike trajectory Sprok-Sterreschans as a case study. This dike trajectory has been recently assessed by the water authority 'Waterschap Rivierenland' (WSRL), in collaboration with HKV. Therefore, a lot of data is available, that can be used for this study. The case study entails the primary flood defence along the North side of the Waal River, between Sprok and Sterreschans, to the east of Nijmegen. The dike trajectory has a length of about 25.8 km, between the dike posts DD133 and DD001, and is part of the dike trajectory 43-4. The water authority has performed a WBI assessment for the reference years 2025 and 2075. However, within this study, the dike trajectory will only be assessed for the year 2075.

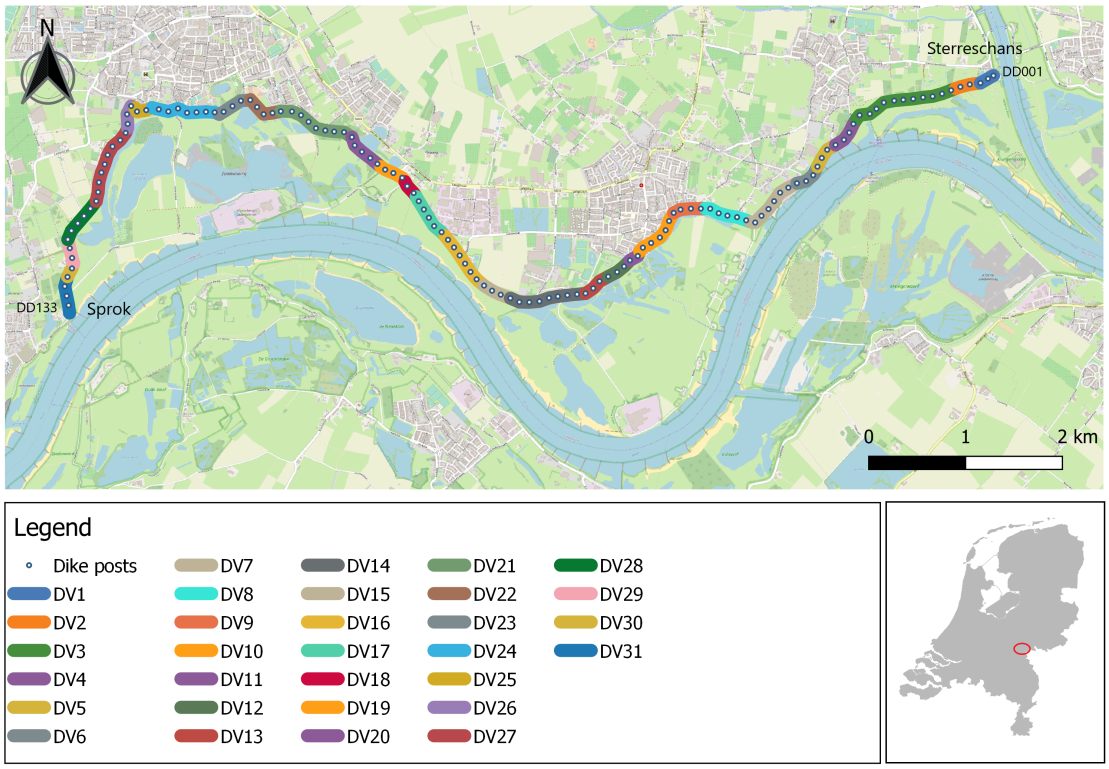

Figure 5.1: Overview and dike section division of the trajectory Sprok-Sterreschans.

The maximum allowable failure probability of the trajectory is set to 1/10,000 per year. For the distribution of the allowable failure probability over the different failure mechanisms, the default WBI values for the contributions per mechanism (ω_j), as elaborated in Appendix B.6, have been used. For the length-effect, Equation B.2 on page 103 has been applied. The used values and results for the allowable sectional failure probabilities are shown in Table 5.1.

Table 5.1: Maximum allowable failure probabilities per cross section per failure mechanism.

Failure mechanism	ω (WBI)	Length effect factor N	$P_{norm,cs}$	$\beta_{norm,cs}$
Overflow and Overtopping (GEKB)	0.24	1	$2.40 \cdot 10^{-5}$	4.07
Piping (STPH)	0.24	$78.40(a = 0.90; b = 300)$	$3.06 \cdot 10^{-7}$	4.99
Macrostability (STBI & STBU)	0.04	$18.028(a = 0.033; b = 50)$	$2.22 \cdot 10^{-7}$	5.05
Erosion outer grass revetment (GEBU)	0.05	1	$5.00 \cdot 10^{-6}$	4.42

5.1.1. Dike section division

Originally, the dike trajectory had been divided into 23 general dike sections, with additional subdivisions for piping and macrostability into 28 dike sections. For piping, for example, the division had been chosen such that the variation in cover layer thickness is minimal within a section. For the present study, however, it is important to use the same division for each failure mechanism, since each section will be assessed within one integral probabilistic computation for the different failure mechanisms simultaneously. Therefore, some of the existing dike sections have been split up in order to have the same division for every failure mechanism. The dike sections will be assessed for piping and macrostability. For overtopping, overflow and erosion of the grass revetment, assessments will be performed for the dike posts. The new section division and the dike posts are presented in Figure 5.1 and listed in Table D.1 on page 115, together with the old dike section division.

5.2. Model Input

The case study data forms the basis of the applied model input. Local data and the documentation of the water authority (Leeuwendrent and van Zwol, 2020) have been consulted to define the stochastic and deterministic input parameters of the model. An elaboration will be given below.

5.2.1. Dike geometry

The geometry of the dike has been determined by the water authority based on AHN3 data, at each dike post location. These have been defined in `.prfl`-files, that will be used for the assessments of this research. In general, inaccuracies in geometry measurements are so small that their contribution to the failure probability is negligible (Schweckendiek et al., 2017). Therefore, the dike geometry will be considered as deterministic. This concerns the crest height, outer slope geometry and dike orientation at the dike posts. Settlements of the soil are not included for the reference years 2025 and 2075, since these are negligibly small.

5.2.2. Geo(hydro)logical properties

The soil structure within the trajectory Sprok-Sterreschans is characterised by Holocene layers from the ground level at NAP + 10 m until a maximum depth of NAP + 5 m. These Holocene layers consist of both sand and clay layers. Underneath are the Pleistocene deposits. The first of these layers is a permeable sand layer (‘Kreftenheye zandlaag’), that covers the complete trajectory. The next layer is also a sand layer, the ‘Waalre pakket’. In between these two layers it is assumed that a clayey layer exists. The spatial distribution of these layers - according to GeoTOP - is illustrated in Figure 5.2, for dike section 7 to 16 as an example. For the other dike sections, the subsoil schematisations are presented in Appendix D.4 on page 120. A soil section according to REGIS is shown in Figure D.4 on page 118.

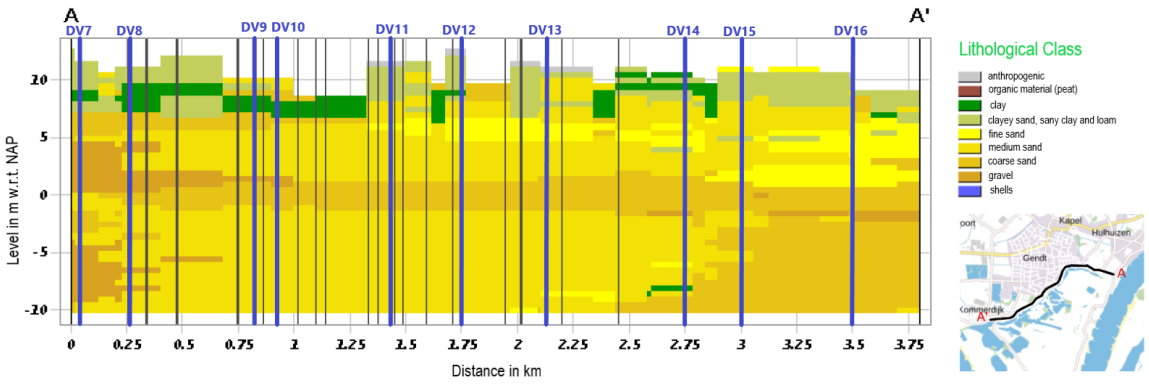

Figure 5.2: Spatial variation of the Holocene soil layers according to the GeoTOP model, from dike section 7 to 16.

Spatial distribution of geological deposits
It can be seen that most of the Holocene and Pleistocene soil layers extend over multiple dike sections along the trajectory. In Section 3.2.3 it is explained that soil characteristics are often spatially correlated within one geological deposit. In order to define the spatial correlations that should be considered within the model, it is analysed whether it can be assumed that soil layers in neighbouring dike sections indeed originate from the same geological deposit. There are different ways to analyse the spatial variability of the subsoil. For this study the following three schematisations were consulted: (1) D-stability schematisations of the normative profiles per dike section, that are based on extensive soil investigations along the trajectory; (2) the SOS (Stochastic Subsoil Schematisation), that has been created as part of the WTI and summarises the relevant variations of the sub soil in different scenarios of the soil structure, including their probabilities (Hijma and Lam, 2015); and (3) the model GeoTOP from the DINOloket. GeoTOP provides more detail about the upper (Holocene) soil layers (TNO, 2020).

For the reliability assessment of the case study, the Holocene layers and the first Pleistocene aquifer ('Kreftenheye' sand) are relevant. The D-Stability schematisations of the normative dike profiles are taken as the starting point, since they are used for the assessment by the water authority - and will be used for the metamodels, as explained later on. The other two soil models are consulted and compared for extra evidence. If the soil layers seem to originate from the same geological deposit and the cross sections are not too far from each other - i.e. the dike sections are not too large - it is assumed that the soil properties are correlated. As an example, the stretch from dike section 7 to 16 is considered. In Figure 5.2 it can be seen that there is a clay layer (dark green) that extends from about 0.7 to 2.3 km distance. It is very likely that this layer originates from the same geological deposit and that its properties are correlated over its entire extent. The same conclusion can be drawn from Figure 5.3, that is derived from the SOS in D-Soil model. In this figure, the uppermost clay layer (light green) is present in every possible scenario, showing that this layer probably extents over a large part of the stretch. Thus, it is assumed that the properties of the clay layer that is schematised in the D-stability file of dike section 7 are correlated to the properties of the clay layer in the D-stability schematisation of dike section 8.

The same kind of reasoning is applied for every dike stretch and every soil layer. If both models agree with each other *and* with the layers present in D-stability, spatial correlations will be considered within the model input, for properties of the same geological deposits. An overview of the layers that are assumed to be correlated is shown in Table D.2 on page 122. The subsoil schematisations of SOS and GeoTOP that are used for the analysis of the other trajectory stretches are shown in Appendix D.4. Not every correlated layer will also be included in the metamodel of the corresponding dike section. The ones that are included, are shown in bold.

All models and also Figure D.4 agree that the first Pleistocene sand layer spans the complete trajectory, implying that the properties of this layer are spatially correlated over all dike sections. This sand layer is seen as the aquifer that plays an important role for the mechanism piping. The relevant properties of this layer will be elaborated in the next section.

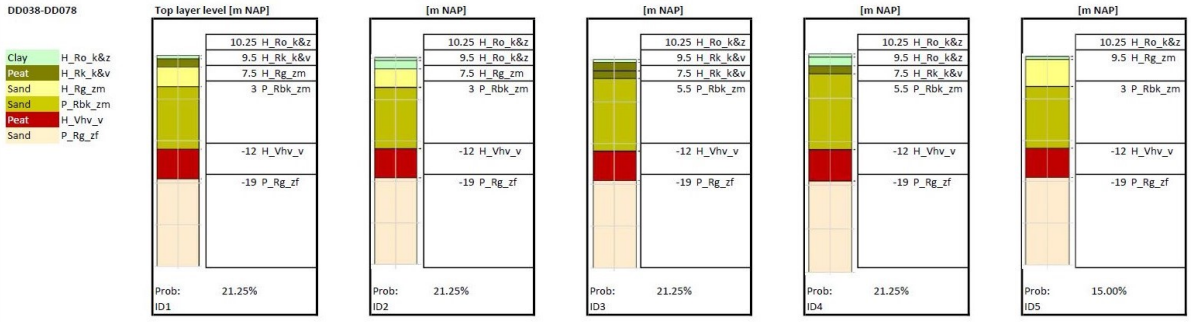

Figure 5.3: Subsoil structure scenarios according to SOS, from DD038 to DD078 (dike section 7 to 15). Abbreviations of the soil types are explained in Appendix C of the 'Schematiseringshandleiding Macrostabiliteit' by Rijkswaterstaat (2019a).

It is important to mention that this analysis is not very accurate. The two models do not agree with each other on some locations and the results are quite uncertain. Furthermore, it is not known how strong the applied spatial correlations should be, i.e. in what order of magnitude Pearson's correlation coefficient should be chosen. More soil samples should be investigated to improve the knowledge about spatial correlations. However, the aim of this research is mainly to study the impact of including correlations in the assessment of the failure probability, instead of quantifying the exact degree of correlation.

The soil properties, that play in important role for the assessment of piping and macrostability, are generally associated with high uncertainties that arise from the spatial variability of the soil characteristics and subsoil composition. In general, only point measurements are available while large uncertainties in the length-direction of the dike are present and possibly unaccounted for. Therefore, including the parameters as stochastic is a very logical and important step. The input distributions of the soil strength parameters of the different soil layers are listed in Table 5.2. They are equal to the default distributions determined by the water authority for dike trajectories along the Waal - based on soil sample collections (Waterschap Rivierenland, 2018).

Table 5.2: Distributions of the soil strength parameters for the macrostability assessment.

Soil type	Parameter	μ	σ / CV	Distribution
Dike material	γ	18.54	0.05 (CV)	normal
	φ	34.8	0.07 (CV)	lognormal
	S	0.42	0.04 (σ)	lognormal
Silty sandy clay	γ	18.73	0.05 (CV)	normal
	φ	32.5	0.07 (CV)	lognormal
	S	0.35	0.03 (σ)	lognormal
	m	0.84	0.03 (σ)	lognormal
Silty clay	γ	16.82	0.05 (CV)	normal
	φ	35.7	0.09 (CV)	lognormal
	S	0.31	0.04 (σ)	lognormal
	m	0.85	0.07 (σ)	lognormal
Humous clay	γ	15.16	0.05 (CV)	normal
	φ	34.1	0.14 (CV)	lognormal
	S	0.30	0.04 (σ)	lognormal
	m	0.71	0.05 (σ)	lognormal
Holocene / pleistocene sand	γ	20.0 / 18.0	0.05 (CV)	normal
	φ	36.7	0.05 (CV)	lognormal

Aquifer properties
The first Pleistocene layer is considered to function as the aquifer. Even though this layer extends over the entire trajectory, it can be seen in Figure D.4 that the hydraulic conductivity k and aquifer thickness D vary along the trajectory. This is also evident from MORIA data, as illustrated in Figure D.5. In general, REGIS and MORIA give results in the same order of magnitude. Only in the east of the trajectory, the thickness according to MORIA is larger than the thickness according to REGIS and field measurements. Also the conductivity is smaller in MORIA. The water authority therefore considers MORIA to be somewhat less reliable than REGIS, since it better matches their field data. Still, both can be used for the determination of the thickness and hydraulic conductivity of the aquifer for the different dike sections. The water authority decided to apply a value of $60\ m/day$ for the hydraulic conductivity of the aquifer for the piping assessment and a value of $100\ m/day$ for macrostability. For the thickness of the aquifer, the thickness of the Kreftenheye sand layer had been applied. The corresponding values along the trajectory are summarised in Table 5.3.

For the model input, it has been decided to deviate from the decision by the water authority to use different values of the hydraulic conductivity for piping and macrostability. From the Figures D.4 and D.5, it can be concluded that especially the choice of $k = 100\ m/day$ for macrostability is a rather conservative choice. Furthermore, it can be concluded that there is quite some variation in k along the trajectory. Based on these considerations, it has been decided to derive a specific mean value for the distribution of k for each dike section, based on the two figures mentioned above. A lognormal distribution and a coefficient of variation CV of 0.5 will be applied in the model input for the aquifer hydraulic conductivities of the different dike sections, which are derived from the WBI parameter list (Deltares, 2016).

For the thickness of the aquifer D the values as listed in Table 5.3 are used for the mean values of the distributions for the corresponding dike sections. A lognormal distribution is applied and $CV = 0.1$, according to the parameter list (Deltares, 2016).

Table 5.3: Choices for the aquifer thickness by the water authority.

Dike posts	Aquifer thickness
DD001 - DD036	25 m
DD036 - DD076	20 m
DD076 - DD098	25 m
DD098 - DD115	30 m
DD115 - DD133	15 m

The value for the aquifer grain size d_{70} has been based on measurements, as shown in Figure D.7. It can be seen that there is no spatial trend visible in the grain size. Based on a sensitivity analysis by the water authority, it was advised to use the local values instead of the regional values that are often applied in assessments. Therefore, the water authority applied a design value of $390\ \mu m$ for the complete trajectory. In this study, a lognormal distribution with a mean value of $425.43\ \mu m$ and a standard deviation of $196.14\ \mu m$ will be applied, based on the local measurements (Deltares, 2016).

Blanket layer (aquitard) properties
Due to the lack of multiple monitoring wells in the area, pragmatic and somewhat conservative values have been assumed by the water authority for the cover, or blanket, layer properties. Based on the soil type of the fore- and hinterland, it is not likely that the permeability of the cover layers deviates a lot along the trajectory. Values of $k_{v1} = 0.4\ m/day$ for the foreland and $k_{v3} = 0.2\ m/day$ for the hinterland had been applied, based on measurements at other locations than Sprok-Sterreschans. These values are applied for the entire trajectory, except for the part between DD070 and DD077 (sections 14 and 15), where the blanket layer is significantly thicker and $k = 0.1\ m/day$ is applied. The determination of the blanket layer thickness per dike section is mainly based on the DINO database. If there are ponds in the dike section, it is assumed that the hydraulic conductivity is $0.1\ m/day$ and the blanket layer thickness is $0.5\ m$.

For macrostability, the saturated volumetric weight of the blanket layer - γ_{sat} - is based on soil investigations, as shown in Figure D.6. Since there is a large scatter and no visible trend along the trajectory, the water authority decided to apply one value for the assessment of piping, namely $17\ kN/m^3$ for the complete trajectory.

Since there is little data available for the hydraulic conductivities of the fore- and hinterland blanket layers, the values for k_{v1} and k_{v3}, as assumed by the water authority, will be considered as the mean values of the distributions for this study. A lognormal distribution is used, with a coefficient of variation $CV = 0.5$, just like for the hydraulic conductivity of the aquifer. For the volumetric weight, the values that had been applied for macrostability by the water authority are used for both macrostability and piping in the probabilistic model. A shifted lognormal distribution (shift = 10) is applied, with $CV = 0.05$, conform the WBI parameter list. The uncertainty mainly arises from measurement uncertainty and the limited number of soil tests, i.e. statistical uncertainty (Schweckendiek et al., 2017).

For macrostability, it was too complicated to vary the blanket layer thickness within the D-Stability schematisations of the training data for the metamodels. Therefore, the blanket layer thickness is considered as a deterministic value per dike section. For the piping assessment, the thickness of the hinterland blanket layer, d, is included as stochastic variable. A lognormal distribution is applied, conform the WBI parameter list. For each dike section, a list of input parameter data is available for the possible exit points within that section. The data are based on ArcGIS computations, geohydrological measurements and analyses. A distribution has been fit on these data to derive the mean and standard deviation of the lognormal distribution that is applied as model input for the blanket layer thickness of the corresponding dike section. Since not much data is available, these fits are quite uncertain.

Phreatic lines and head lines
As explained above for the blanket layer thickness, data could be derived from ArcGIS computations for different piping exit points within each dike section. This also holds for the seepage length L, the phreatic level at the exit point h_{exit} and for the potential at the exit point Φ_{exit}. A lognormal distribution is fit on the seepage length data and a normal distribution for h_{exit} and Φ_{exit}, conform the WBI parameter list. The phreatic level of the hinterland is assumed to be equal to the ground level, since it is assumed that the polder level cannot be maintained during a flood event. It is known that much seepage occurs in the area during flood events, due to the relatively thin blanket layers. For macrostability, the implementation of the phreatic lines and head lines will be elaborated in Section 5.6.1.

Summary
A summary of the applied distributions and values for the model input is given in Table 5.4. *Nominal* implies that the value depends on the dike section. The input distributions of the piping and macrostability parameters are shown in Figure D.8 on page 119 for dike section 6, as an example.

Table 5.4: Summary of stochastic input parameters that are based on case study data.

Parameter	Distribution	μ	σ / CV
Aquifer hydraulic conductivity k	Lognormal	nominal	$CV = 0.5$
Aquifer thickness D	Lognormal	nominal	$CV = 0.1$
Grain size d_{70}	Lognormal	$4.25 \cdot 10^{-4}\ m$	$\sigma = 1.96 \cdot 10^{-4}\ m$
Blanket layer hydraulic conductivities k_{v1}, k_{v3}	Lognormal	nominal	$CV = 0.5$
Volumetric weight γ	Lognormal*	nominal	$CV = 0.05$
Blanket layer thickness d	Lognormal	nominal	nominal
Seepage length L	Lognormal	nominal	nominal
Hinterland phreatic level h_{exit}	Normal	nominal	nominal
Exit point potential Φ_{exit}	Normal	nominal	nominal

*(shift=10)

5.2.3. Hydraulic loads

The hydraulic boundary conditions that were applied by the water authority during the assessment of the trajectory Sprok-Sterreschans can be divided into two parts: the so-called HBN ('Hydraulisch belasting niveau') and the design, or norm, water level. The HBN is the minimum required crest height for a certain overtopping discharge. The design water level was used for the assessment of macrostability and piping and corresponds to the maximum allowable failure probability of the trajectory (1/10,000 per year). The following relevant assumptions and starting points have been applied by the water authority for the derivation of the hydraulic boundary conditions (Leeuwendrent and van Zwol, 2020):

- Scenario W+ has been applied to include the effects of climate change, as explained in Section 4.3
- Statistical uncertainties have been 'integrated out' according to the WBI method, as explained in Section 4.4. It means that the uncertainty is not included as a separate stochastic variable, but is incorporated in the statistics for a probabilistic model (in this case Hydra-NL)
- The discharge statistics of the Rhine at Lobith are based on GRADE, as explained in Section 4.2
- For the wind statistics, the measuring station at Deelen is used as reference location
- The discharge at Lobith is capped at $18,000\ m^3/s$
- Loads due to earthquakes, ship collision and ice are not included.

The water authority applied a so-called 'DPa database physica' for reference years 2050 and 2100[1]. As explained in Section 4.1, the DPa database is used to derive the local water levels and wave conditions at several locations along the trajectory. For the assessment of overtopping, overflow and erosion of the grass revetment, the hydraulic boundary conditions were derived from a combination of this DPa database and the WBI database. These databases have 13 overlapping locations, so-called illustration points. Subsequently, the databases were combined with the so-called HLCD for reference years 2050 and 2100, in order to link the discharges, and thus water levels, to probabilities. The HLCD (Hydraulic Loads Configuration Database) contains the relevant statistical data, including statistical uncertainties and correlations, for the load stochastic variables of all locations along Dutch flood defences. For the year 2075, the data for 2050 and 2100 have been interpolated.

Model input

The wind and discharge statistics have been derived from Hydra-NL[2] input files. For the discharge, these contain the probabilities of exceedance for certain values of the peak discharge at Lobith, with an assumed duration of the trapezium of 30 days, including statistical uncertainty, according to the WBI. The discharge statistics are created for climate scenario W+, within the GRADE project (Hegnauer et al., 2014). The reference years 2050 and 2100 are interpolated to obtain the discharge statistics for 2075. The resulting probabilities of exceedance are shown in Figure 5.4.

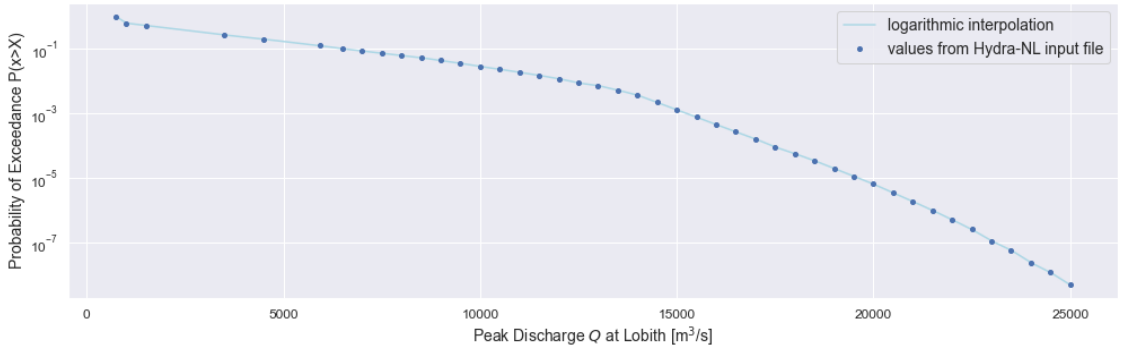

Figure 5.4: Probabilities of Exceedance for the peak river discharge at Lobith, derived from the OI2014 input file for Hydra-NL, for climate scenario W+, including statistical uncertainties and interpolated for the year 2075.

[1] `DPa_Riv_Rijn_oever_2015_ref_S10_DM1p1p12_v02`

[2] Files: `Ovkans_Lobith_piekafvoer_OI2014_W_2050_metOnzHeid` ; `Ovkans_Lobith_piekafvoer_OI2014_W_2100_metOnzHeid` ; `Ovkanswind_Deelen_2017_metOnzHeid` ; `Richtingskansen_Deelen_2017`

The assessments by the probabilistic model will be executed conditional on the river discharge, in order to reduce the computation costs. After all, the failure probability conditional on a high discharge is higher and thus less realisations are needed to determine this conditional probability (see Equation 2.10 on page 11). Subsequently, the total failure probability can be computed by:

$$P_{f;trajectory} = \sum_{i=1}^{n} P(Q_i) \cdot P_{f;i} \tag{5.1}$$

where $P_{f;trajectory}$ is the total failure probability of the trajectory per year, $P(Q_i)$ is the probability of occurrence of river discharge Q_i $[1/year]$ and $P_{f;i}$ is the failure probability given discharge Q_i. The probabilities of occurrence can be derived from the empirical CDF. For this, the Hydra-NL data for 2075 has been interpolated logarithmically, which means that the logarithms of the probabilities are linearly interpolated for values of the discharge. The resulting CDF can be used to derive the probabilities of occurrence of certain discharges, as follows:

$$P(Q_i) \approx P(a < Q_i \leq b) = F_Q(b) - F_Q(a) = \int_a^b f_Q(u)du \tag{5.2}$$

in which a and b form a very small interval around Q_i. The results are shown in Table 5.5.

Since there has not been any flood event along this trajectory in the past 50 years, it is assumed the discharges with a smaller return period than 50 years do not lead to failure. From Figure D.1, it can be derived that a return period of 50 years corresponds to a peak discharge at Lobith of $10,800$ m^3/s. Therefore, discharges smaller than $10,000$ m^3/s are not considered within this study. For the wind, the probabilities of exceedance of the 12-hourly maximum wind speeds at Deelen, given the wind direction, are derived from Hydra-NL. These can be combined with the probabilities of occurrence of the corresponding wind directions. Subsequently, a Weibull distribution has been fit on the CDF of the Hydra-NL wind speed data for each wind direction, as can be seen in Figure D.3 on page 117. Again, the probabilities have been logarithmically interpolated for the wind speed.

Within the probabilistic model, the value of the river discharge will be translated to a water level for each dike section and each dike post. For this, the same DPa database is used as applied by the water authority. For the wave conditions, random samples of the wind direction are drawn first and then a random sample of the corresponding wind speed distribution is drawn - for each realisation of the Monte Carlo simulation. These are translated to the local wave conditions at each dike post, by means of the DPa database and the Bretschneider equations (see Section 4.1 on page 41). The model is capable of random sampling the river discharge from its distribution as well, if desired.

It is important to mention that the combination of the applied statistics and the translation database does not result in exactly the same hydraulic boundary conditions as applied in the assessment by the water authority. The difference mainly lies in the model uncertainty, which is not included in the hydraulic boundary conditions of this study. In the hydraulic boundary conditions that are used by the water authority, there is an extra stochast included for the model uncertainty. This model uncertainty is normally distributed with $\mu = 1$ and $\sigma = 15$ cm. It is added by Hydra-NL after the translation from discharge to water level statistics. In fact, a confidence interval is added to the (return period vs. water level)-graph. Thereafter, this confidence interval is 'integrated out', as explained in Section 4.4.2. It results in a shift of the water level statistics towards higher values, i.e. the same water level has a smaller return period if model uncertainties are included. This shift is more extreme for larger return periods (Pleijter et al., 2017). In other words, inclusion of this model uncertainty results in higher failure probabilities. Moreover, capping ('aftoppen') of the discharge statistics at $18,000$ m^3/s is not applied within this research, leading to somewhat different probabilities of the river discharge.

It would be possible to include the model uncertainty in the probabilistic assessments of this study, by the procedure as explained in Section 4.4.2. However, considering the aim of this research, which is not to exactly reproduce the results of the existing assessment, but to investigate the impact of aspects like correlations, it is decided that including model uncertainty is out of the scope of this research. Besides, the current WBI procedure of including these model uncertainty shows room for improvement and is the subject of recent research within the Big5-project (Strijker et al., 2020).

Table 5.5: Probabilities of occurrence of extreme peak discharges at Lobith..

Q_i $[m^3/s]$	$P(Q_i)$ $[1/year]$
$10,000$	$1.23 \cdot 10^{-2}$
$11,000$	$8.39 \cdot 10^{-3}$
$12,000$	$6.27 \cdot 10^{-3}$
$13,000$	$3.52 \cdot 10^{-3}$
$14,000$	$3.07 \cdot 10^{-3}$
$15,000$	$1.43 \cdot 10^{-3}$
$16,000$	$5.00 \cdot 10^{-4}$
$17,000$	$1.79 \cdot 10^{-4}$
$18,000$	$5.66 \cdot 10^{-5}$
$19,000$	$2.32 \cdot 10^{-5}$
$20,000$	$7.77 \cdot 10^{-6}$
$21,000$	$2.49 \cdot 10^{-6}$
$22,000$	$7.49 \cdot 10^{-7}$
$23,000$	$1.98 \cdot 10^{-7}$
$24,000$	$4.65 \cdot 10^{-8}$
$25,000$	$6.95 \cdot 10^{-9}$

5.3. Assessment of Overflow and Overtopping

Within the assessment by the water authority, overflow and overtopping are assessed by means of the HBN, which is in fact an assessment of the height. The assessment is based on the maximum allowable failure probability per dike section for overflow and overtopping (see Table 5.1). The assessment was at first semi-probabilistic with a critical overtopping discharge of $10\ L/m/s$, but also values of $q_c = 0.1$, 1.0, $5.0\ L/s/m$ had been assessed. The semi-probabilistic assessment had been supplemented with a probabilistic assessment in Riskeer, in which the resistance of the grass revetment - i.e. the critical overtopping discharge - is included as a stochastic variable. It was assumed that the grass quality is in the category *closed sod* (see Table 3.1 on page 19). It followed that a critical overtopping discharge with $\mu = 0.225\ m^3/s/m'$ and $\sigma = 0.250\ m^3/s/m'$ should be applied, based on the indicative wave height, conform WBI 2017, that leads to a wave height class of $0 - 1\ m$.

At each illustration point, the geometry of the dike cross-section had been defined. So, these are not necessarily the normative cross-sections of the zone for which the illustration point holds. For obstacles and transitions, a lower critical overtopping discharge was determined, based on BOI ('Beoordelings- en Ontwerpinstrumentarium'). It resulted in a mean critical overtopping discharge of $0.0076\ m^3/s/m'$ with $\sigma = 0.0037\ m^3/s/m'$. However, within this thesis, obstacles and transitions are disregarded. The resulting values of the HBN for the probabilistic assessment are summarised in Table 6 and 7 of the report 'Voorverkenning Sprok-Sterreschans: Rapportage GEKB & GEBU' by Broere and Leeuwdrent (2020) and the resulting failure probabilities for normative illustration points are shown in Figure 5.5.

5.3.1. Model verification

Within this research, the assessment for overtopping and overflow is full-probabilistic, meaning that the critical discharge is included as stochastic variable, conform Table 3.1. The assessment is executed by calling the 'overtopping' kernel that is used for WBI assessments - by means of a `dll`-file, as explained in Section 3.1.4. As mentioned above, the water authority made use of Hydra-NL for the definition of the hydraulic boundary conditions, which differ from the applied conditions of this study. Due to the absence of the model uncertainty the resulting failure probabilities for overtopping are smaller than the ones from the assessment by the water authority. This can be seen in Figure 5.5. Also the absence of 'capping' leads to different results. Alternatively, the correctness of the overtopping computations by the probabilistic model has been verified by means of results that were generated by the revetment prototype of Rongen et al. (2019), since both models make use of the same 'overtopping' kernel.

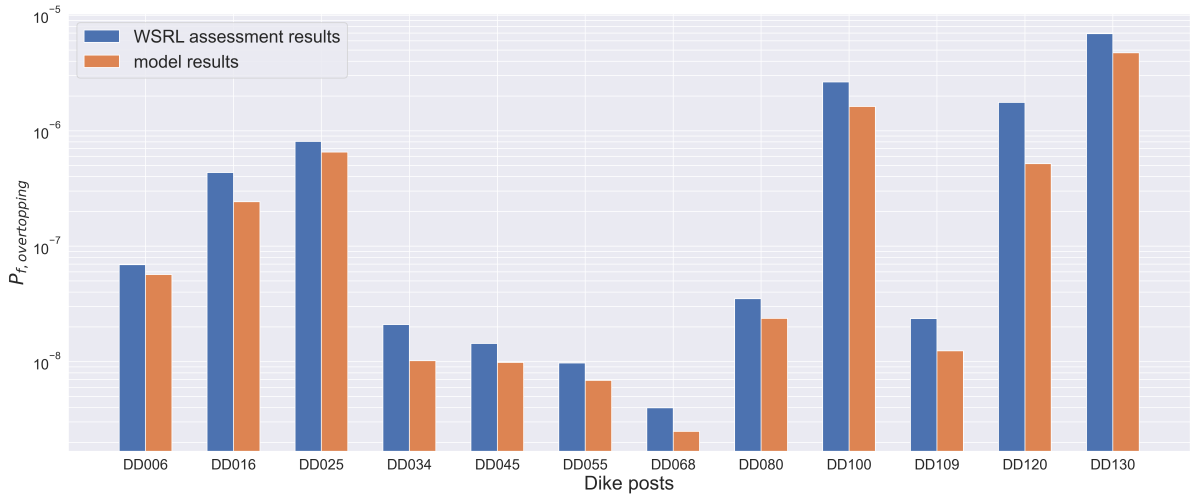

Figure 5.5: Verification of the assessment for overtopping.

5.4. Assessment of Erosion of the Outer Slope Grass Revetment

The water authority assessed erosion of the revetment in a semi-probabilistic way. The assessment was based on the computation model as described in Section 3.4 or in the 'Schematiseringshandleiding grasbekleding' by van Hoven (2019). The model assumes that the revetment has failed if a certain resistance time is exceeded. Only the wave impact zone is considered, since it is normative for a grass revetment slope, according to the 'Schematiseringshandleigding grasbekleding' van Hoven (2019). The grass quality is assumed to be *closed*, resulting in the following values for the computation of the resistance time of the top layer: $a = 1$, $b = -0.035$, $c = 0.25$. If the resistance time is exceeded, the underlying (clay) layer starts to erode, for the remaining storm duration.

Since there is a clay core present in this dike trajectory, a supplementary computation model had been applied to account for the residual strength. The applied erosion model for the clay core originates from the Deltares report 'Prediction of the erosion velocity of a slope of clay due to wave attack' by Mourik (2015) and is based on the erosion velocity (See Equation 3.50 on page 36). The formulas have been applied by means of an Excel sheet by Fugro. Based on these formulas, the erosion profile could be defined for every time step and it had been determined whether the residual profile was still sufficient. The allowable residual profile has a crest width of six metre with a slope of 1:2. The formulas are applicable for clay with a sand fraction of less than 40% (clay catergory 1 or 2). At most of the locations, these categories are present.

The water level had been varied in between the 1/10 year water level and the norm water level (probability of 1/10,000 per year), in steps of $0.5\ m$. It is assumed that the wave conditions sustain for 12 hours. Based on the hydraulic database, it was derived that the maximum wave height $H_s = 1.2\ m$. This wave height was applied for the computation of the resistance time of the grass revetment and for the residual strength of the clay.

Normative profile

The water authority assumed a fictitious profile for the geometry, that represents the most unfavourable (= steep slope) profile of the dike trajectory. If this profile suffices, the complete trajectory does. The profile of dike post DD010 had been chosen. So, the normative profile is characterised by:

- Outer slope of 1:2.5
- Inner slope of 1:3
- Foreshore level is NAP + 7.5 m, so it does not have any influence on the computed erosion volume
- Ground level inner side is NAP + 7.5 m as well.

5.4.1. Assessment

According to the assessment by the water authority, the resulting failure probability is very small and the normative profile easily suffices the norm. Therefore, it has been decided to not consider failure due to erosion of the outer slope grass revetment in the current study. Still, the failure mechanism is included in the probabilistic framework, to enable flexible usage and easy application of the model to different case studies in the future. The failure mechanism is implemented by the method as explained in Section 3.4.

5.5. Assessment of Piping

The semi-probabilistic assessment by the water authority was executed by means of a Python script in ArcGIS. For the hydraulic load, the norm water level (with probability 1/10,000 per year) was applied for each dike section. As explained in Section 3.3.1, the failure probability due to Piping is determined by the smallest probability out of the three sub-mechanisms uplift, heave and backward erosion. In this case, the sub-mechanism backward erosion is the normative mechanism - i.e. with the highest reliability index or lowest failure mechanism - for every normative exit point in the trajectory.

5.5.1. Model verification

As explained in Section 3.3, a Python script in which the piping formulas are already programmed is implemented in the probabilistic model. For verification purposes, the model is run for the design values and norm water levels, as applied in the semi-probabilistic computation by the water authority. In Figure 5.6, the assessment results per dike section by the water authority are shown in blue. The results by the model, applied in a semi-probabilistic manner, are shown in orange. It can be concluded that both assessments give more or less the same results and therefore the probabilistic model is verified for the failure mechanism piping.

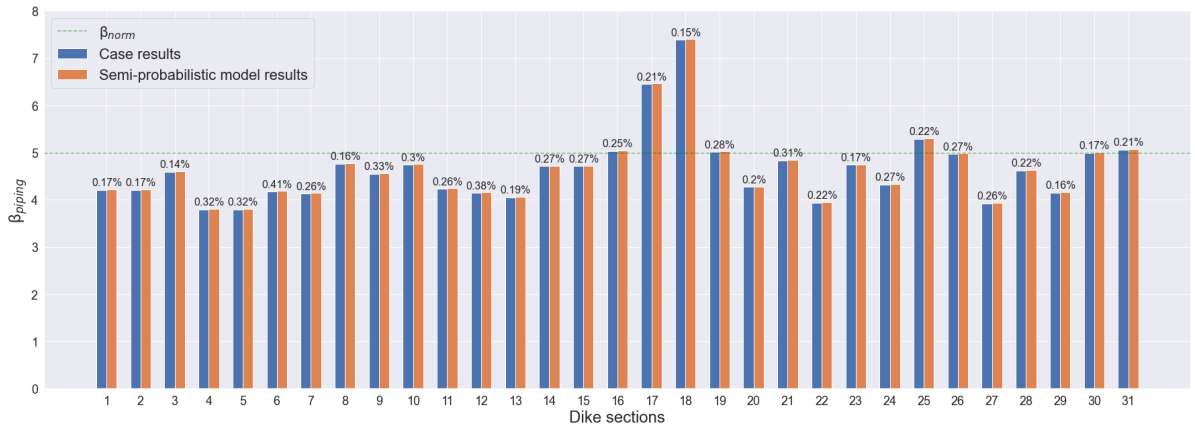

Figure 5.6: Verification of the model for piping.

5.6. Assessment of Macrostability

The water authority has performed a semi-probabilistic assessment for macrostability. For the hydraulic load, the corresponding norm water level (with probability 1/10,000 per year) was applied for each dike section. The assessment was executed in D-Stability, by means of the method LiftVan with strength parameters based on CSSM. If the cover layer has a thickness of less than four metre, a bursting zone was schematised. Otherwise, a head line schematisation without bursting was assumed. Between two soil measurement locations, it was assumed that soil layers run horizontally. Furthermore, it was assumed that every cohesive (blanket) layer shows undrained soil behaviour. Only if the OCR value is larger than three, the (undrained) cover layer was replaced by drained characteristics. The actual factor of safety had been computed for the normative cross-section of each dike section and had been compared to the required factor of safety. The required factor of safety is composed of a schematisation factor of 1.05 (as explained in the document 'Voorverkenning Sprok-Sterreschans - Rapportage STBI & STBU' by Broere and Knops (2020)), a damage factor of 1.17 (belonging to the dike trajectory)

and a model factor of 1.06 (belonging to LiftVan), leading to a required factor of safety equal to 1.30. The water authority also assessed macrostability during overtopping, assuming that the dike body is saturated. However, within this study, Macrostability during overtopping is not considered, since it is not a normative mechanism for failure due to macro-instability in general.

For the model of this study, it is decided to make use of the concept of metamodeling based on Gaussian process regression (GPR), in order to assess macrostability in a more efficient way. One calculation in D-Stability takes 10 to 60 seconds, depending on how fast the search algorithm finds the critical slip plane within the search limits. For a Monte Carlo simulation, more than 100,000 calculations are generally needed for one assessment. So, using D-Stability would lead to unacceptably long computation costs. Instead, assessing the factor of safety by means of a metamodel in Python takes less than a second - $0.078\ s$ for the used computer - within the probabilistic framework. From this, it can be concluded that applying a metamodel is roughly 300 times more efficient than calling D-Stability for each realisation of the model. The basics of metamodeling are explained inSection 3.2.7 and Appendix C. The application will be explained below.

5.6.1. Metamodeling

The 31 dike sections of the case study differ such that it is necessary to create customised metamodels for each section. The predictions of each metamodel are based on ten input variables. The metamodels are trained based on the geometry and soil characteristics of the normative cross-sections - that have been captured in D-Stability files by the water authority - for each dike section. It is assumed that this cross-section is indeed the most critical one and that it determines the safety of the complete corresponding dike section. For each dike section, a FORM analysis has been performed to find the parameters that have the largest influence on the failure probability. Based on this FORM analysis, the six most important soil parameters have been selected per dike section to be included in the ten input variables of the corresponding metamodel, as shown in Table C.1 on page 107. Besides, the water level is included as input variable. The other three input variables are reserved for parameters related to the phreatic line and head line - as explained below.

Phreatic lines and head lines

The water level is generally the most important input variable. However, if the water level increases, the phreatic line in the dike and the head line in the subsoil will also increase, as a consequence of infiltration via the outer dike slope and via the subsoil. These processes lead to the increase of the pore pressures and all together it results in a decrease of the shear strength of the subsoil and dike. It is therefore important to include this dependence on the water level of the phreatic line and head line in the metamodels. In order to achieve this, the following schematisations - as applied by the water authority - have been applied within the metamodel training data.

For the phreatic lines, this is a rather simple schematisation, as explained in Appendix C.3.1. A distinction is made based on the dike type: different schematisations for clay dikes, sand dikes and clay dikes with enclosed sand (‘zandscheg’). A clay dike with enclosed sand originates from previous reinforcements at the inner slope by sand, with a new clay cover layer on top. At these locations, the flood defence is described as a clay dike with enclosed sand (‘zandscheg’) and a different, rather conservative schematisation is applied by the water authority: The real dimensions of the sand containment are larger than those in the schematisation.

The head lines in the aquifers have been schematised in accordance with schematisation 4A of the ‘Technical Report for Pore Pressures in Dikes’ (TRWD) (TAW, 2004), that is applicable for flow in a sandy subsoil beneath an impermeable dike with poorly permeable blanket layers in the fore- and hinterland. If the blanket layer has a thickness of less than four metres, hydraulic heave, or bursting, is taken into account. Hydraulic heave can typically occur in situations where a Pleistocene sand layer is only covered by weak layers, as is the case at some of the dike sections of this study. In these cases, schematisation 4C of the TRWD has been applied, that is applicable in situations of aquifer flow beneath an impermeable dike in which the limit potential occurs in the hinterland.

The relation between outer water level, phreatic line and head line strongly depends on the subsoil geometry and soil characteristics. However, it is complicated to adjust the dike and subsoil geometry in the D-Stability files of each training data point. Therefore, it has been decided to consider the geometry

as deterministic and to include only the hydraulic conductivities of the aquifer, fore- and hinterland as stochastic input variables that define the head lines and preatic lines for the metamodels. In reality, there is of course an uncertainty in the soil geometry which should be taken into account, so it should be kept in mind that the current approach is certainly an approximation of reality.

A Python script has been developed that is able to construct and implement the phreatic lines and head lines into the D-Stability files of the training data for each metamode - depending on the parameters k, k_{v1} and k_{v3}. The script is based on the formulas above. In Table C.3 on page 111, it can be seen which schematisations are applied for each dike section.

Summarising, the metamodels for each dike section are based on ten input variables: six parameters related to the strength of the soil layers, the three hydraulic conductivities and the river water level. 1000 different D-Stability files are created per dike section, in which the ten input variables are deviating from the original D-Stabiliy schematisation of the corresponding dike section. These files - called the training data - are run in D-Stability to compute the corresponding factor of safety, which is the system's response to be predicted by the metamodel. The training data are created by drawing random samples of the ten input variables from normal distributions with a rather large standard deviation, by means of Latin hypercube sampling. This is done to cover the complete space of possible values of these parameters. The means of these normal distributions are equal to the corresponding design values. Examples of these input variable distributions for the creation of training data are shown in the Figures C.1 and C.6 on page 108 and 111. As a consequence, a relatively large part of the training data points result in a FoS that is close to the critical one, implying that the metamodels will perform best around failure. Note that these training data distributions are not the real distributions of these parameters. The real distributions are listed in Table 5.3.

Validation of the metamodel
After performing the 1000 computations in D-Stability for each dike section, 20% of these training data have been extracted for validation purposes. The GPR model is thereafter trained by the remaining 80% of the training data. Subsequently, the trained model is used to predict the factor of safety of the validation data. These predicted FoS are compared to the FoS that were computed by D-Stability for the validation data, in order to quantify the accuracy of the metamodels. For each metamodel, the percentage predictive error, the root mean square error (RMSE) and the coefficient of variation (CV) have been computed. As an example, this comparison and the error determination is shown in Figure 5.7 for dike section 23.

The mean errors and CV's for each dike section are presented in Table C.4. The mean percentage predictive error is -0.64%, implying that the metamodels have a very slight conservative bias. The mean RMSE is 0.092 and the mean coefficient of variation is 0.076. This is somewhat larger than the coefficient of variation of the Uplift-Van model in D-Stability, which is 0.033. At the same time, the uncertainty of the different soil parameters is generally larger, as can be concluded from Table 5.2. Therefore, it is considered an acceptable error and it is decided to continue working with these metamodels.

Figure 5.8 shows the predicted FoS for the case study dike sections in orange, including their uncertainty, and the assessed FoS by the water authority in blue. These predictions are based on a semi-probabilistic application of the metamodels, i.e. based on the design values of the corresponding input variables.

The fact that the metamodels do not have a notable bias means that they are not consistently under- or overestimating the FoS, implying that the errors might cancel out during a Monte Carlo simulation. Moreover, the metamodels give the best predictions close to the limit state, as it is the case for most dike sections of the case study. Therefore it is expected that the metamodels will perform even better during the probabilistics assessments of this study, even though these cannot be validated.

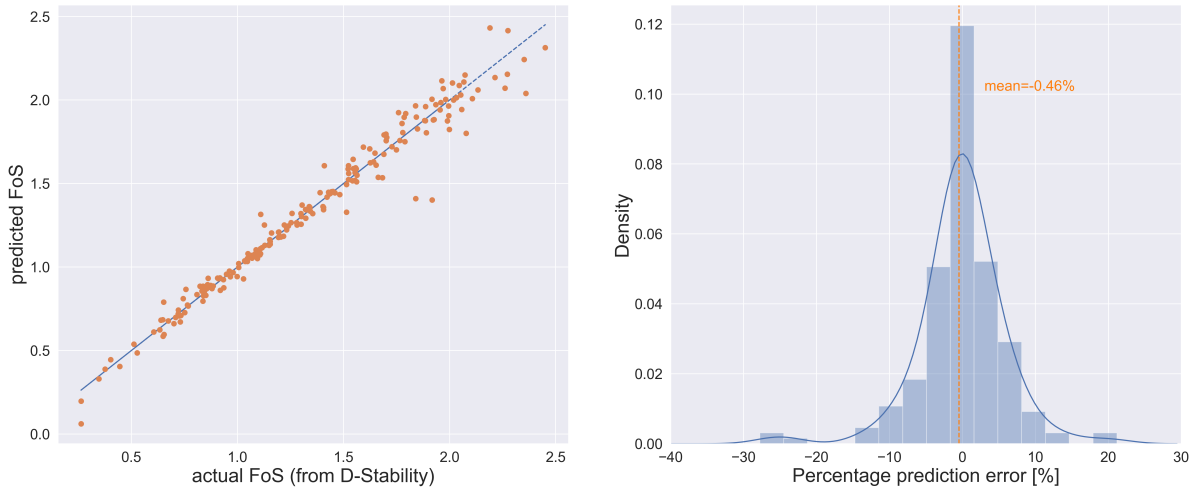

Figure 5.7: Validation of the metamodel of dike section 26.

Implementation of the metamodel
Now, the metamodel can be implemented into the integral probabilistic framework. The corresponding limit state function Z_{macro} is defined as:

$$Z_{macro} = \frac{FoS}{m_d} - 1 \tag{5.3}$$

where m_d is the model uncertainty. D-Stability makes use of the Uplift-Van model to determine the slip circle, which has an uncertainty parameter m_d with $\mu_{m_d} = 1.005$ and $\sigma_{m_d} = 0.033$ (Schweckendiek et al., 2017). Since the application of metamodeling leads to an increase of the uncertainty, the standard deviation of the model uncertainty has been set to $\sigma_{m_d} = 0.07$.

Importance of the metamodel input parameters
The contribution of each input parameter to the factor of safety is investigated by changing one-factor-at-a-time (OAT). This is a simple and common approach for sensitivity analyses. In this case, each input parameter is increased by 30% with respect to the case study design value. Subsequently, the relative difference between the resulting FoS and the reference FoS (based on the case study input values) is computed. The results of this analysis for each metamodel are shown in the Tables C.5 of Appendix C.3.3 on page 113. More or less the same order of importance resulted from FORM analyses in D-Stability for each dike section. However, D-Stability takes the volumetric weights and the water level as deterministic values and the hydraulic conductivities are not explicitly included, causing that no α-values can be obtained for these input parameters. Moreover, the metamodels are only based on ten input variables, while the corresponding D-Stability schematisations are dependent on many more parameters. Therefore, the importance factors obtained from D-Stability differ from the ones obtained by the OAT approach. For these reasons, it had been decided to base conclusions about the parameter contributions to the metamodels on the OAT approach, as shown in the Tables C.5.

It follows that the water level is the most important parameter for all dike sections. Regarding the contribution of the soil parameters, there are large differences between the dike sections. This is explained by (1) the large differences in dike and subsoil geometry of the dike sections of the case study and (2) the fact that it strongly depends on the location of the critical slip plane whether a parameter contributes to the resistance or to the load, and to what extent. For instance, the volumetric weights can have both a positive and a negative impact on the stability analysis, as they have an influence on the driving moment, the resisting moment and the shear strength, as explained in Section 3.2 (Schweckendiek et al., 2017). Moreover, in most cases it seems that there is not really one (or two) driving soil parameter(s). Most parameters do not contribute much to either the resistance or the load. These observations should be kept in mind when the impact of correlations is analysed in the following chapter.

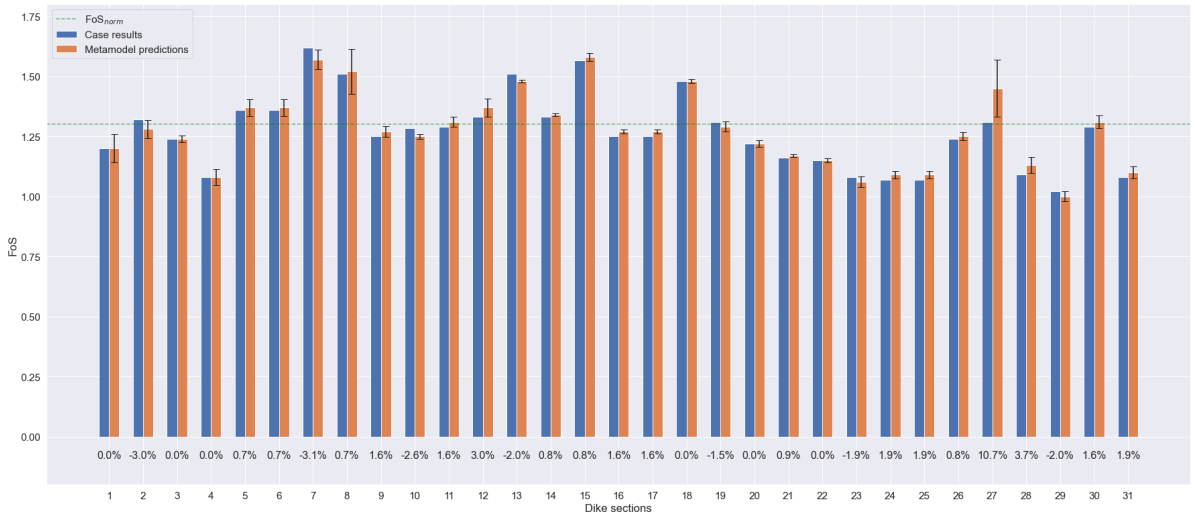

Figure 5.8: Validation of the model for macrostability, including error bars of $2 \cdot \sigma$. The mean error is 0.63%.

5.7. Assessment of the Outer Slope Stability

For the outer slope stability, one assessment was performed by the water authority, that describes the safety of the complete trajectory. This choice was based on the expectation that the trajectory would easily suffice the norm. For the normative cross-section, a profile with a steep slope and a large crest height was chosen, namely DD010. It is assumed that the water level decrease after a flood event ('mate van val') is equal to 4.5 metre. The analysis was executed in D-Stability, by means of LiftVan with strength parameters based on CSSM. It resulted in $P_f = 5.96 \cdot 10^{-9}$ due to outer slope instability, while the norm is equal to $2.2 \cdot 10^{-7}$. So, it could be concluded that the complete trajectory indeed suffices for outer slope stability. Traffic load is not included.

Since the failure probability due to outer slope instability is so small, according to the assessment by the water authority, it has been decided to not consider the failure mechanism in the current study.

5.8. Computational Set Up

The input parameters, implementation of the failure mechanisms and relevant mathematical concepts for the integral probabilistic model have been explained previously. In the current section, the set up of the model will be summarised. Figure 5.9 gives an illustration of the different computational steps.

5.8.1. Correlations

In Sections 3.2 and 3.3, it is explained that correlations exist between several parameters that play a role in the piping and macrostability mechanisms. Moreover, Section 5.2.2 proves that spatial correlations between geotechnical properties of the dike sections are very likely. The aim of this research is to investigate the effects of correlations. Therefore, the model is built in such a way that correlations can be implemented, by means of a Gaussian copula. The Gaussian copula is defined by a covariance matrix (upper left in Figure 5.9) and the marginal distributions of the parameters (upper right of Figure 5.9). In the covariance matrix, mutual correlations between all parameters can be defined by means of a Pearson's correlation coefficient ρ. In the uncorrelated case, the matrix is an $n \times n$ identity matrix, with n the total number of input variables. The real values of the (spatial) correlations are not known and cannot be derived from data. Therefore, the impact of correlations will be assessed by means of sensitivity analyses. The marginal distributions of the input parameters have been defined in this chapter and summarised in Table 5.2 and Table 5.4. For each iteration of the Monte Carlo simulation, random samples are drawn from the Gaussian copula, so that the defined correlations are taken into account.

As explained previously, the hydraulic loads are determined per dike section of dike post. The conditional river discharge is translated to water levels, by means of the DPa database. The wind conditions

are randomly sampled for each iteration within the Monte Carlo simulation and translated to the wave conditions of each dike section, based on the same database.

5.8.2. Total failure probability

For each iteration i, the different limit state function $Z_{j,k}$ are evaluated, for failure mechanism j and dike section k. If any of these evaluations is smaller than zero, failure is counted, see Figure 5.9. After N iterations of the Monte Carlo simulation, the total failure probabilities can be computed by dividing the total number of failure N_f by N (see Equation). Failure is also counted per dike section and per failure mechanism, in order to derive the total failure probability of a certain dike section and due to a certain mechanism, respectively.

WBI assemblage

The total failure probabilities are also computed according to the WBI assemblage procedure. As briefly explained in Chapter 1, the procedure consists of the following steps:

1. Estimate the failure probability of the dike trajectory, assuming mutual independence of the sections (upper bound):

$$P_{trajectory} = 1 - \prod_{i=1}^{N} (1 - P_i) \tag{5.4}$$

2. Estimate the failure probability of the dike trajectory, based on the largest failure probability of the sections (i.e. mutual dependence) and the estimated length-effect (lower bound):

$$P_{trajectory} = \max\{P_i\} \cdot N \tag{5.5}$$

3. Choose the minimum of the two estimated failure probabilities. By taking the minimum, a large overestimation of the trajectory failure probability is avoided.

The two different methods of assessing the total failure probability will be compared, for correlated and uncorrelated situations. The results are presented in the next chapter.

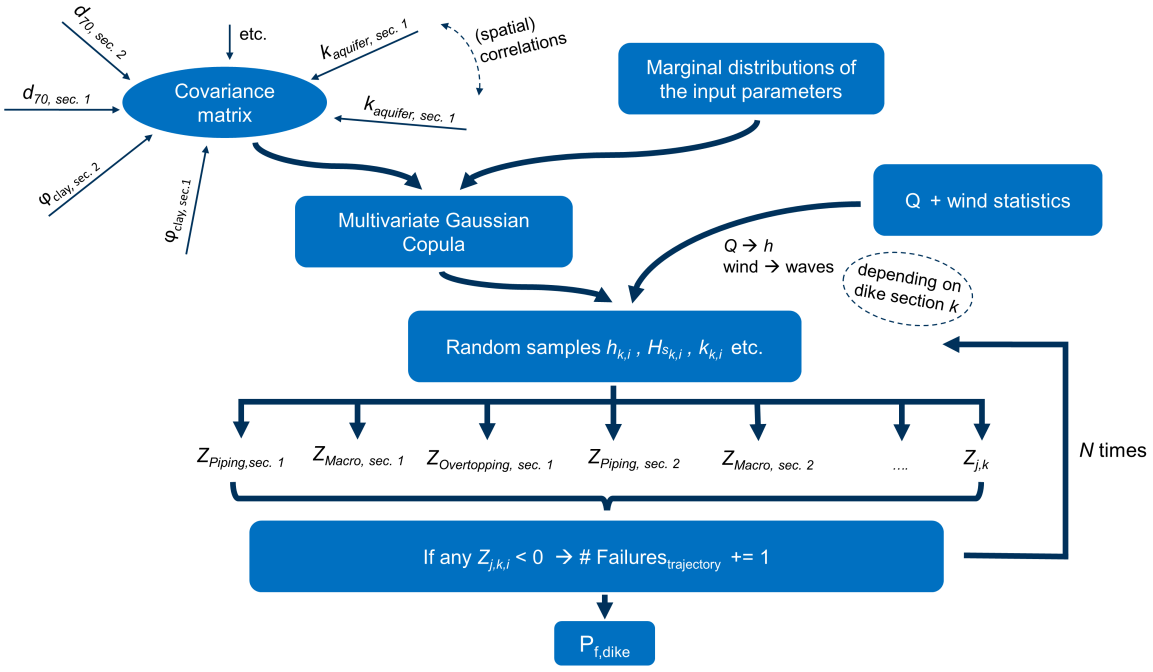

Figure 5.9: Illustration of the probabilistic model.

5.9. Conclusions

Before proceeding to the results of this study, a few important remarks and conclusions related to the model performance should be summarised.

Overtopping
As explained in Section 5.2.3, the hydraulic boundary conditions that are applied in the model differ from those applied by the water authority, due to neglecting the model uncertainty. Therefore, the resulting failure probabilities for overtopping are smaller than the ones from the assessment by WSRL. This difference did not pose a problem for the validation of piping or macrostability, since these were based on the norm water level. Since there are no correlations between parameters of overtopping and macrostability or piping, the analyses of this study are not focussed on overtopping. Thus, the fact that the results could not be fully verified does not pose a problem.

Macrostability
For macrostability, metamodels are created, in order to reduce the computation costs. It has been proved that the metamodels are indeed able to reduce the computation costs significantly, roughly by a factor of 300. Moreover, it was demonstrated that the metamodel predictions of the factor of safety are of acceptable accuracy for the current study, especially in the domain around failure. Since metamodeling is most effective for about a dozen input variables, including every parameter of every relevant soil layer into every metamodel is not feasible. A disadvantage of this is that the metamodels are based on only ten input variables, which differ per dike section. Therefore, it is not possible to incorporate and investigate every plausible (spatial) correlation within the model.

Piping
The assessment of piping is based on the Sellmeijer equations. Since these are also applied in the semi-probabilistic assessment by the water authority, the results could be easily verified.

Other failure mechanisms
The instability of the outer slope and the erosion of the outer grass revetment are not considered, since the corresponding failure probabilities are negligibly small.

III

Analysis

6

Results

Sensitivity analyses into the effects of different correlations on the failure probabilities have been executed. This has been performed for model input that is based on the case study - as described in the previous chapter. Firstly, correlations between different parameters and secondly correlations in space are considered. This chapter elaborates upon the findings of this study.

6.1. Correlations between Input Parameters

Firstly, correlations between variables are considered. In general, three situations have been implemented: no correlation ($\rho = 0$), a strong correlation of $\rho = \pm 0.8$ and a weak correlation of $\rho = \pm 0.2$. These values are chosen to investigate different extreme situations of correlation. They are not based on realistic values, since there is not sufficient data available to obtain the actual correlation coefficients at the locations under consideration. Also in literature not much was found. Only for the correlation between the hydraulic conductivity k and the grain size d_{70} a value of 0.70 of the Kendall coefficient was obtained for another dike trajectory, the Lekdijk. Also at other locations there is strong evidence for a significant correlation between k and d_{70} (Aguilar-López et al., 2016). The other correlations for piping are the result of the explicit definition of the exit potential Φ_{exit} and are therefore expected to be significant and positive. If not much was much found in literature about possible correlations between two parameters, both positive and negative correlations have been investigated. This applies to the soil strength parameters for macrostability. In some cases, correlations also result in dependency between failure due to piping and failure due to macrostability of a dike section, since the corresponding parameters are included in both mechanisms. In that case, the resulting correlation between the evaluations of the two Z-functions is investigated.

6.1.1. Piping

In Section 3.3, possible mutual correlations between the following piping parameters have been mentioned and explained: $(k - d_{70})$, $(k - \Phi_{exit})$, $(k_{v3} - \Phi_{exit})$, $(h_p - \Phi_{exit})$, $(D_{cover} - \Phi_{exit})$ and $(D - \Phi_{exit})$. In the following sections, the results of implementing weak and strong correlations between these parameters are presented. It is often referred to the importance or contribution of the piping parameters to failure, as listed in Table 3.3. The analyses have been executed conditional on a river discharge of $Q = 16,000\ m^3/s$ and for $N = 400,000$ iterations of the Monte Carlo simulation. The failure probabilities due to piping for dike section 17 and 18 are so small that convergence of the results is not achieved within this study. Therefore, the results of these two dike sections are not considered for the analyses and conclusions.

1. Hydraulic conductivity k and grain size d_{70} of the aquifer material

Implementation of strong, weak and no correlation between these two parameters resulted in the sectional failure probabilities due to piping as presented in Figure 6.1. The results for the three submechanisms of piping separately are shown in Figure E.1 and E.2 on page 123 and 124. Those two figures illustrate that a correlation between k and d_{70} only affects backward erosion, which is obvious since both parameters are only included in the assessment of this sub-mechanism. Therefore, the relative difference between the correlated and uncorrelated case are presented for the sub-mechanism backward erosion in Figure 6.2.

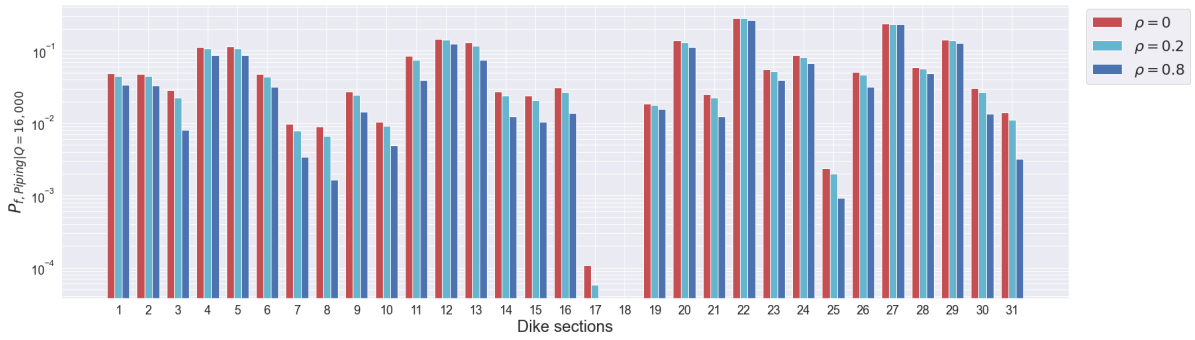

Figure 6.1: Sensitivity analysis into the impact of different scenarios of the correlation between k and d_{70} on the sectional failure probabilities due to piping, conditional on a river discharge of $Q = 16,000\ m^3/s$ and for $N = 400,000$.

From Figure 6.1 and 6.2 and from the figures in the appendix, it is apparent that the sub-mechanism backward erosion dominates the total failure mechanism piping, since the effect of the correlation is clearly affecting the total failure probability due to piping. As shown in Equation 3.37, piping is treated as a parallel system, implying that the sub-mechanism with the smallest probability of failure dominates the system (see Table A.1).

A strong positive correlation of $\rho = 0.8$ leads to an average reduction of approximately 40% of the sectional failure probabilities due to piping, with respect to the uncorrelated situation. A weak positive correlation of $\rho = 0.2$ leads to an average reduction of about 10%. This effect is expected, based on the Sellmeijer model as explained in Section 3.3. A large hydraulic conductivity k promotes the groundwater flow, while a large grain size d_{70} increases the resistance of the sand grains against erosion in the (partially developed) piping channels. Correlation implies that a high value of k is likely to occur at the same time as high value of d_{70}. So, in a correlated situation the effects of the two parameters compensate each other out, resulting in more 'safe' situations. However, the magnitude of the effect varies significantly per dike section. Dike sections with the smallest failure probabilities for the sub-mechanism backward erosion appear to experience the strongest reduction. The dike sections 22 and 27, where the effect of the correlation is almost negligible, have the largest failure probabilities.

The hydraulic conductivity of the aquifer k is also included in the assessment for macrostability. Consequently, a correlation between k and d_{70} also relates the two failure mechanisms to each other. However, the impact of k on the failure probabilities due to macrostability is very small, as shown in Table C.5. It is thus not surprising that the correlation between k and d_{70} does not lead to a higher degree of correlation between failure due to macrostability and due to piping, as becomes apparent in the scatter plot of the limit state function evaluations Z_{piping} versus Z_{macro} in Figure 6.9.

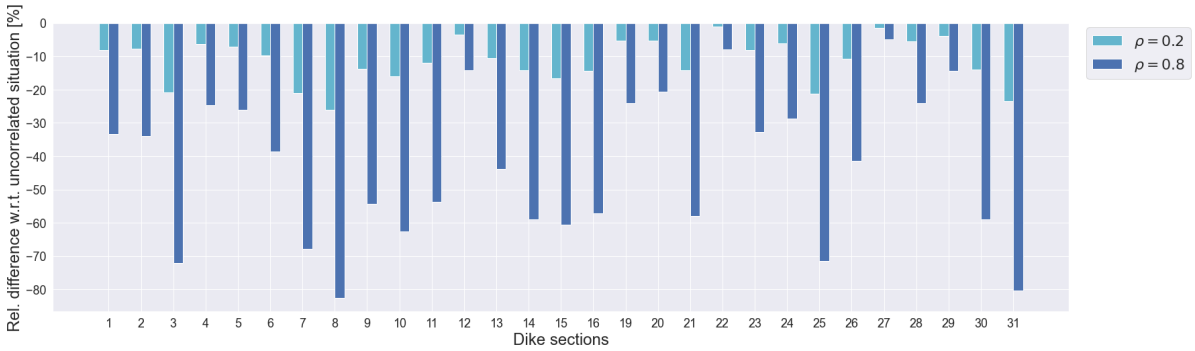

Figure 6.2: Relative difference in % between the failure probability due to the sub-mechanism backward erosion for situations with strong resp. weak correlation between k and d_{70}, with respect to a situation with no correlation, conditional on a river discharge of $Q = 16,000\ m^3/s$ and for $N = 400,000$.

2. Hinterland phreatic level h_p and exit point potential Φ_{exit}

The potential Φ_{exit} contributes to the load for the sub-mechanisms heave and uplift, while the phreatic level h_p contributes to the resistance of all three sub-mechanisms. So, a correlation between these two parameters directly affects the failure probabilities due to heave and uplift, but it also leads to mutual correlations between the three sub-mechanisms. For most dike sections, failure is dominated by the sub-mechanism backward erosion and not by heave or uplift. Therefore, a correlation between the phreatic level h_p and the potential Φ_{exit} generally appears to have a smaller impact on the failure probabilities than a correlation between k and d_{70}, as can be seen in Figure 6.3 and 6.4.

A strong positive correlation of $\rho = 0.8$ leads to an average reduction of about 7.5% of the sectional failure probabilities due to piping, with respect to the uncorrelated situation. A weak positive correlation of $\rho = 0.2$ leads to an average reduction of about 2%. Again, the magnitude of the effect is very dependent on the dike section. For some dike sections, the correlation strongly reduces the failure probability due to piping, while for others the effect is negligible or even an increase of the failure probability.

The impact on the failure probabilities due to heave and uplift is shown in Figure 6.4 and in Figure E.3 of the appendix. From these figures it becomes clear that the correlation leads to an increase of the sectional failure probabilities if these are higher than about 0.5. For dike sections for which the failure probabilities due to these two sub-mechanisms are significantly smaller, like 19 or 25, the correlation leads to a reduction of the failure probability.

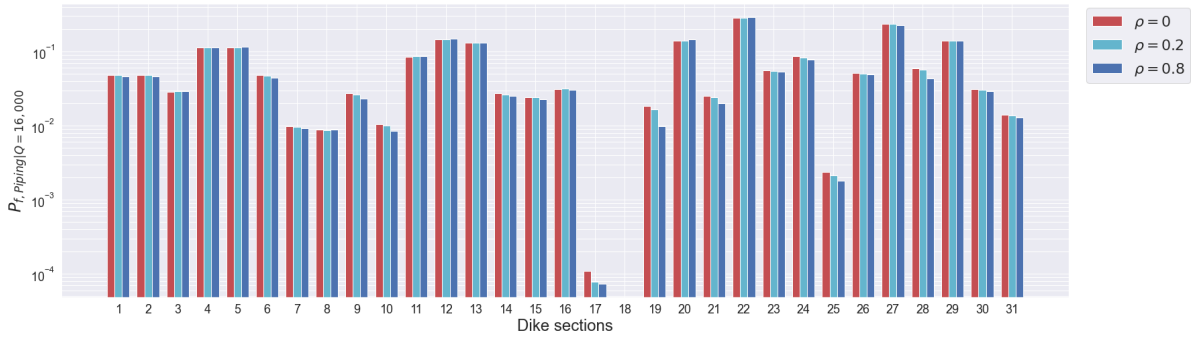

Figure 6.3: Sensitivity Analysis for correlations between h_p and Φ_{exit} for the failure mechanism piping, conditional on a discharge $Q = 16,000\ m^3/s$, for $N = 400,000$.

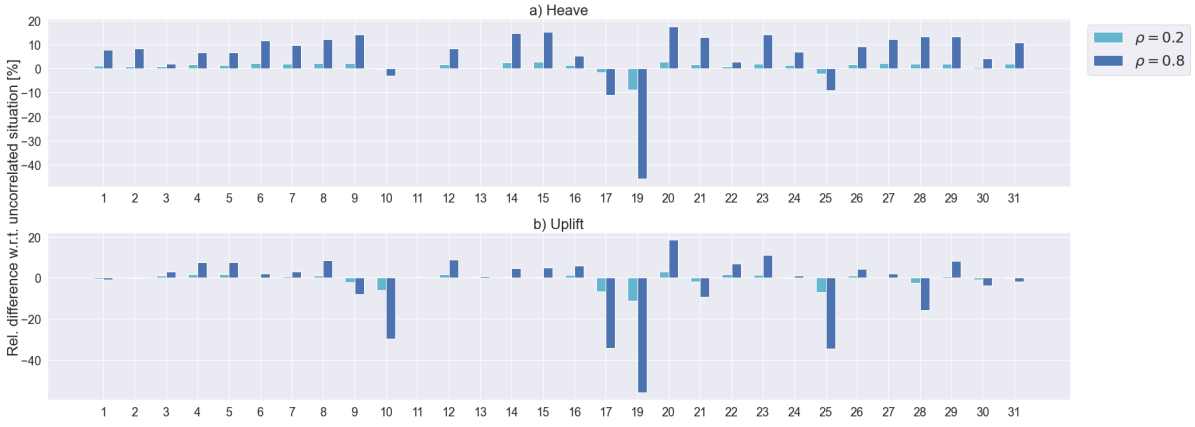

Figure 6.4: Relative difference in % between the failure probability due to uplift and heave for a situation with no correlation and situations with strong resp. weak correlation between h_p and Φ_{exit}, conditional on a discharge $Q = 16,000\ m^3/s$, for $N = 400,000$.

For dike section 19 the impact of the correlation is not only very apparent in the sub-mechanisms, it also results in a reduction of the total failure probability due to piping, as illustrated in the figure above. This is explained by the fact that the failure probability due to uplift becomes almost the same as the failure probability due to the sub-mechanism piping, when a correlation of 0.8 is included. In that case, uplift starts to become more dominant for the total failure probability and that explains why the impact of the correlation is so strong for dike section 19. Moreover, it can be seen in Figure 6.3 and 6.4 that for some dike sections, the correlation has a reducing effect on the total failure probability due to piping, while it has an increasing effect on the sub mechanisms uplift and heave.

3. Blanket layer thickness d and exit point potential Φ_{exit}
The blanket layer thickness contributes to the resistance of the sub-mechanisms backward erosion and uplift, while it contributes to the load for heave. However, it can be deduced from Table 3.3, that the parameter is of minor importance. Together with the fact that heave and uplift are generally not normative for failure due to piping, the impact of a correlation between d and Φ_{exit} is expected to be small. This is confirmed by the results in Figure 6.5.

A strong positive correlation of $\rho = 0.8$ leads to an average reduction of about 3.5% of the sectional failure probabilities due to piping, with respect to the uncorrelated situation. A weak positive correlation of $\rho = 0.2$ leads to an average reduction of about 1%. Again, the magnitude of the impact is very dependent on the dike section and can be explained in the same way as for the correlation between h_p and Φ_{exit} above.

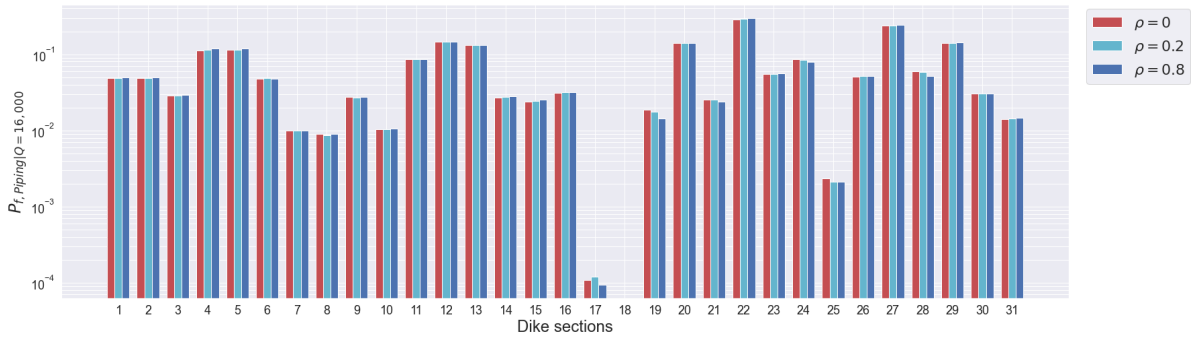

Figure 6.5: Sensitivity Analysis for correlations between d and Φ_{exit} for the failure mechanism piping, conditional on a discharge $Q = 16,000\ m^3/s$, for $N = 400,000$.

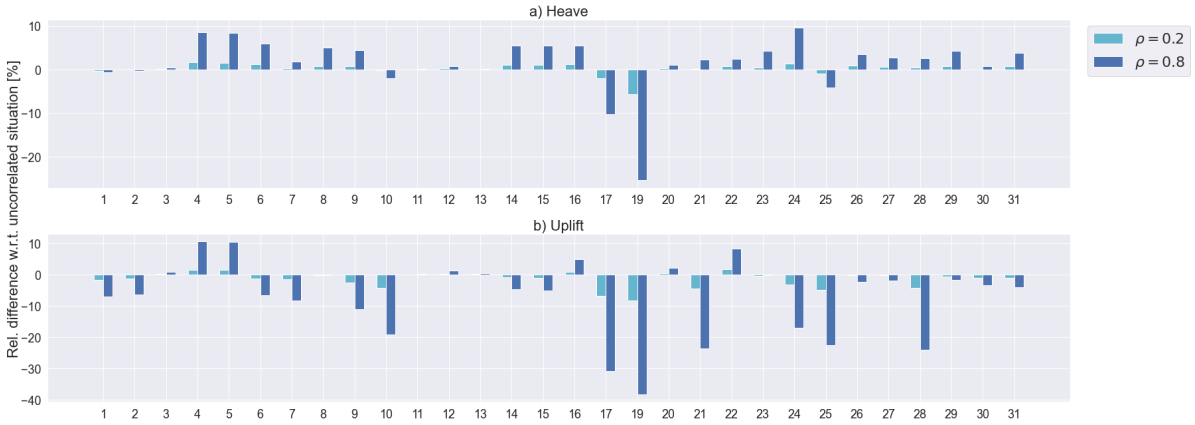

Figure 6.6: Relative difference in % between the failure probability due to heave and uplift for a situation with no correlation and situations with strong resp. weak correlation between d and Φ_{exit}, conditional on a discharge $Q = 16,000\ m^3/s$, for $N = 400,000$.

4. Aquifer thickness D and the exit point potential Φ_{exit}
Correlation between the aquifer thickness D and the exit point potential Φ_{exit} has a negligible impact on the sectional failure probabilities. This can be explained by the fact that Φ_{exit} only contributes to heave and uplift, while D only contributes to backward erosion. Moreover, the aquifer thickness is of minor importance. The results are shown in Appendix E.

5. Hydraulic conductivity of the aquifer k and exit point potential Φ_{exit}
The hydraulic conductivity k contributes to the load for backward erosion and the exit point potential Φ_{exit} to the load for uplift and heave. In that case, the correlation has no effect on the failure probabilities of the sub-mechanisms. But the correlation implies that failure due to the three sub-mechanisms is more likely to occur at the same time, resulting in a higher failure probability for the parallel system piping. This effect is apparent in Figure 6.7 and 6.8.

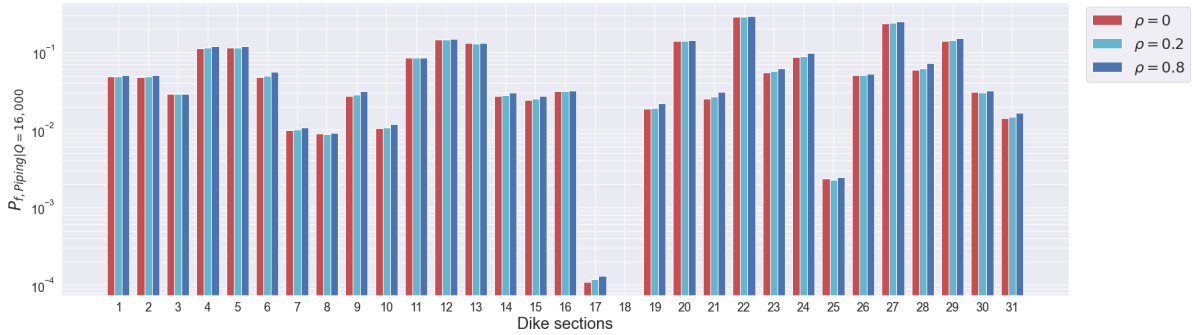

Figure 6.7: Sensitivity Analysis for correlations between k and Φ_{exit} for the failure mechanism piping, conditional on a discharge $Q = 16,000\ m^3/s$, for $N = 400,000$.

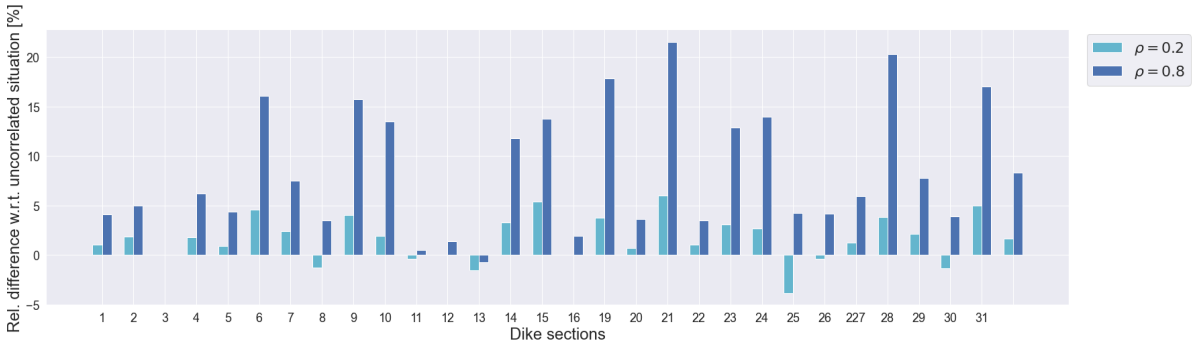

Figure 6.8: Relative difference in % between the failure probability due to piping for situations with strong resp. weak correlation between k and Φ_{exit}, with respect to a situation with no correlation, conditional on a river discharge of $Q = 16,000\ m^3/s$ and for $N = 400,000$.

6. Hydraulic conductivity of the blanket layer k_{v3} and exit point potential Φ_{exit}
Since the hydraulic conductivity of the blanket layer k_{v3} is not explicitly included in the assessment of failure due to piping, a correlation between k_{v3} and Φ_{exit} has no impact on sectional failure probabilities due to piping, as shown in Figure E.13 on page 129. At the same time, k_{v3} is included in the failure assessment due to macrostability, but Φ_{exit} is not, and thus also for the sectional failure probabilities due to macrostability no effect is seen (see Figure E.14). But again, this correlation links the two failure mechanisms to each other. Since k_{v3} is more important than k for most metamodels, as shown in Table C.5, the correlation becomes apparent in the scatter plot of the Z-evaluations for the two failure mechanisms, as shown in Figure 6.9. However, it is not strong ($\rho = 0.1$), since the importance of k_{v3} is still quite small.

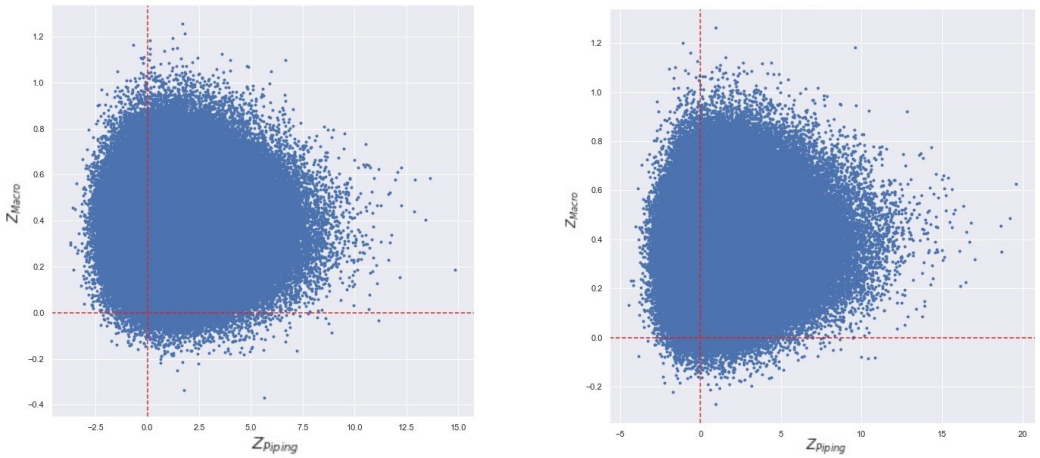

(a) Correlation of $\rho = 0.8$ between k and d_{70}.

(b) Correlation $\rho = 0.8$ between k_{v3} and Φ_{exit}.

Figure 6.9: Resulting correlations of $\rho = 0.1$ between the failure mechanisms piping and macrostability for dike section 9, conditional on a discharge $Q = 20,000\ m^3/s$, for $N = 400,000$.

6.1.2. Macrostability

It can be assumed that the undrained shear strength parameters S and m are positively correlated (Schweckendiek et al., 2017). Furthermore, evidence exists that the value of S increases with decreasing volumetric weight γ, which suggests a negative correlation (Leferink, 2020). In general, however, there is not much found in literature about correlations between the different soil strength parameters. Therefore, four different possibilities have been investigated: weak vs. strong negative vs. positive correlation. The analyses are executed conditional on a river discharge of $Q = 20,000\ m^3/s$ and for $N = 400,000$ iterations of the Monte Carlo simulation. At first, it is important to note that a different river discharge is used than for the sensitivity analyses of piping. The reason is that a Monte Carlo simulation of 400,000 iterations is not able to accurately capture failure probabilities smaller than the order of 10^{-3} (see Equation 2.10). This limit is indicated in the figures below by a horizontal line. In order to have as many as possible dike sections with failure probabilities in the accurate regime, an (unrealistically) high discharge has been chosen for these analyses. For the same reason, only the results for dike sections 4, 5, 6, 8, 9, 21, 23, 24, 25, 26, 27, 28, 29, 30 and 31 are considered to draw conclusions from: to ensure that conclusions are based on reliable results. The results will be presented below. It is often referred to the importance of the meta model input parameters, as presented in Table C.5 on page 113.

1. Shear strength ratio S and shear strength exponent m

Figure 6.10 and 6.11 illustrate that the impact of a correlation between the shear strength ratio S and the shear strength exponent m strongly differs per dike section. Both the magnitude - large versus small effect - and the direction - increasing versus decreasing effect - are dependent on the dike section.

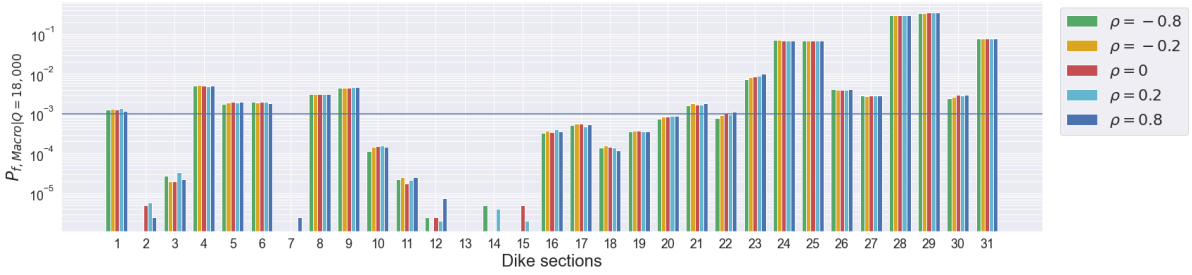

Figure 6.10: Sensitivity analysis for correlations between S and m for the failure mechanism macrostability, conditional on a discharge $Q = 20,000\ m^3/s$, for $N = 400,000$.

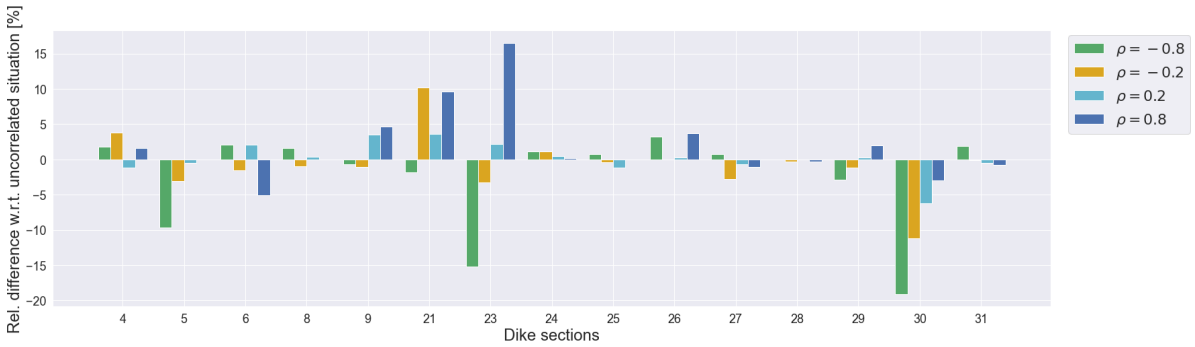

Figure 6.11: Relative difference in % between the failure probability due to macrostability for situations with strong resp. weak correlation between S and m, with respect to a situation with no correlation, conditional on a river discharge of $Q = 20,000$ m^3/s and for $N = 400,000$.

From Table C.5, it can be derived for which dike sections the largest impact is expected after inclusion of a correlation between S and m, based on the importance of these two parameters. These are the sections 23, 19, 14, 2, 30 and 3, ordered from highest importance to lowest. It can be seen that the dike sections 23 and 30 indeed show a significant impact of the correlations. Also for the dike sections 5, 6, 21 and 29 a medium impact was expected, based on the importance of S and m, and indeed a medium impact can be observed in the figures. For the dike sections 4 and 9, the impact is somewhat high, for no impact was expected since there is no m included in the metamodel. For the other dike sections, the impact was expected to be small and this is indeed confirmed by the results.

On average, a correlation of $\rho = 0.8$ and $\rho = 0.2$ result in an increase of approximately 2% and 0% of the failure probability due to macrostability, while a negative correlation of $\rho = -0.8$ and $\rho = -0.2$ lead to a reduction of 4% and 2%, respectively.

2. Shear strength ratio S and volumetric weight γ

Also the impact of several correlations between the shear strength ratio S and the volumetric weight γ of the same soil layer has been investigated. Again, it turned out that the impact differs per dike section, as shown in Figure 6.12 and 6.13. Dike sections for which a large impact was expected according to the Table C.5 are 1, 14, 21, 23, 26 and 27. From the figures it can be concluded that this is indeed visible in the results. The impact for dike section 21 and 23 might be somewhat unrealistically high. For dike sections 4, 5, 6, 7, 11, 16, 17, 19, 22 and 31 the parameters are not both included in the metamodels, so no impact is expected. For 4, 5, 6 and 31 it can be confirmed that a correlation between S and γ does indeed not have a noteworthy impact on the failure probabilities. For the other dike sections, one or both parameters are of minor importance, so a minor impact of the correlation was expected.

On average, a positive correlation leads to an increase of the failure probability due to macrostability of about 19% and 3%, for a correlation of $\rho = 0.8$ and $\rho = 0.2$, respectively and a negative correlation leads to a decrease of about 12% and 4% for $\rho = -0.8$ and $\rho = -0.2$, respectively.

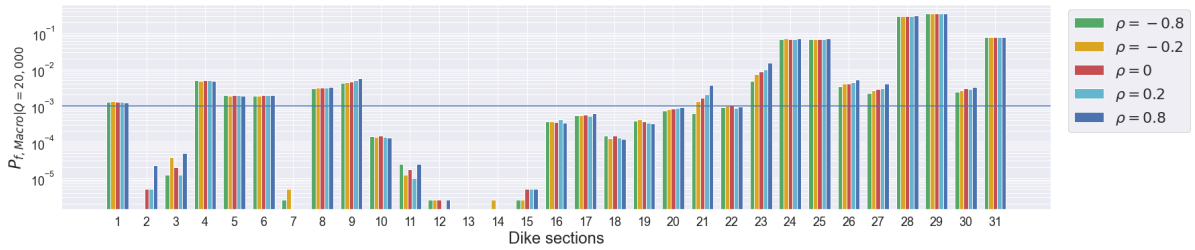

Figure 6.12: Sensitivity analysis for correlations between S and γ for the failure mechanism macrostability, conditional on a discharge $Q = 20,000$ m^3/s, for $N = 400,000$.

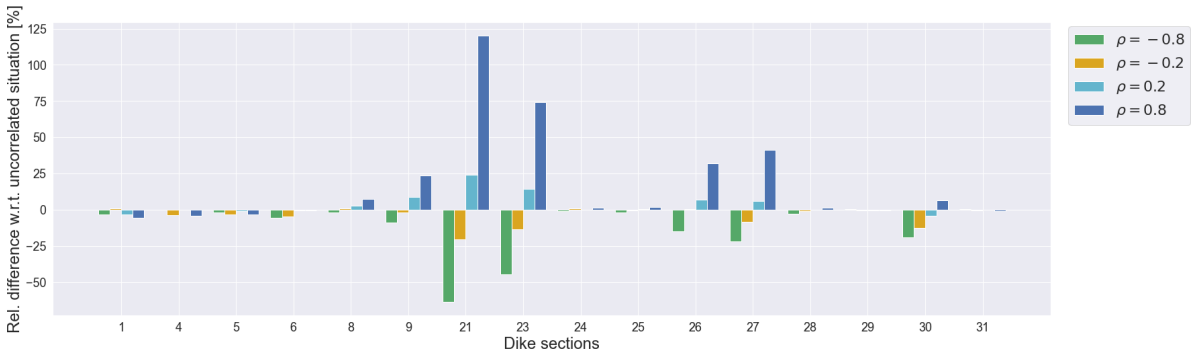

Figure 6.13: Relative difference in % between the failure probability due to macrostability for situations with strong resp. weak correlation between S and γ, with respect to a situation with no correlation, conditional on a river discharge of $Q = 20,000$ m^3/s and for $N = 400,000$.

Since the volumetric weight is also included in the assessments for piping, it is possible that a correlation between S and γ also results in a correlation between failure due to piping and due to macrostability. This has been analysed but it turned out to have a negligible effect, as can be seen in Figure E.15. This is explained by the fact that the volumetric weight only has a minor contribution to the sub-mechanism uplift, which in turn plays a minor role for the failure probability due to piping, for most dike sections of this case study.

3. Frictional angle φ and volumetric weight γ

As depicted in Figure 6.14, a correlation between the frictional angle φ and the volumetric weight γ does have an impact, however it differs per dike section whether it leads to a reduction or an increase of the failure probability. Positive correlations of $\rho = 0.8$ and $\rho = 0.2$ lead to an average reduction of 6% and 0.5%, respectively, with respect to the failure probability of the uncorrelated case. Meanwhile, a negative correlation of $\rho = -0.8$ and $\rho = -0.2$ results in a reduction of about 4% and 1.5%, respectively.

It seems remarkable that the correlation has such a large impact for dike section 9, but this can be explained as follows. As shown in Table C.5, the volumetric weight γ and the frictional angle φ of the clay layer are by far the most important resistance parameters of the metamodel for macrostability for dike section 9, and also φ and γ of the dike material are quite important. Therefore, correlation between these two parameters has a very strong impact. Dike sections for which the impact is negligible, like 8 and 23 are dike sections for which the parameters γ and φ of the same soil type are not both included in the corresponding metamodel or dike sections for which the contribution of these two parameters is very small.

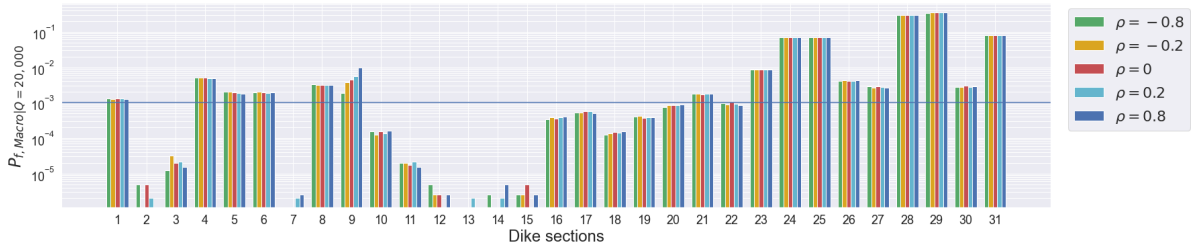

Figure 6.14: Sensitivity analysis for correlations between φ and γ for the failure mechanism macrostability, conditional on a discharge $Q = 20,000$ m^3/s, for $N = 400,000$.

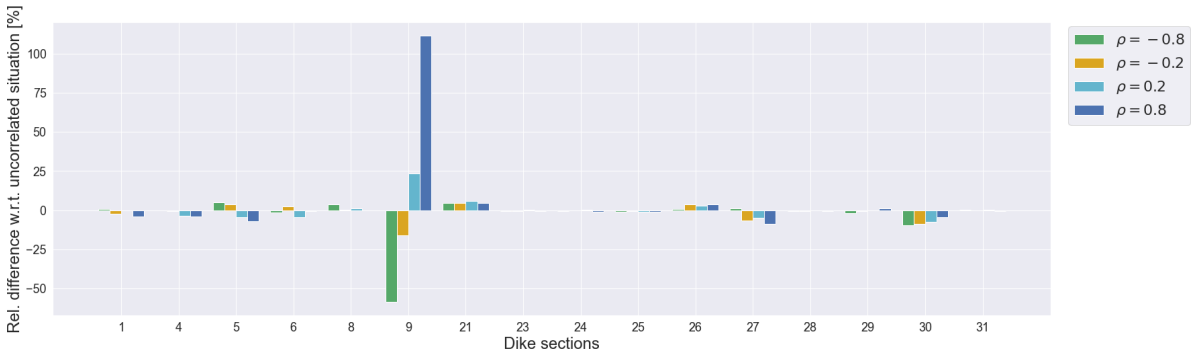

Figure 6.15: Relative difference in % between the failure probability due to macrostability for situations with strong resp. weak correlation between φ and γ, with respect to a situation with no correlation, conditional on a river discharge of $Q = 20,000$ m^3/s and for $N = 400,000$.

6.1.3. Impact of correlation vs. failure probability

A remarkable observation from the figures above is that it seems to depend on the order of magnitude of the failure probability whether the correlation has a small or large effect on the corresponding failure probability. Consider for example Figure 6.2: Dike sections 22 and 27 show a minimal reduction of the failure probability of less than 10%, while for other dike sections the correlation leads to a reduction of more than 50%. The dike sections 22 and 27 have the highest failure probabilities due to the sub-mechanism backward erosion, as can be seen in Figure E.1. At the same time, it can be interpreted from the same figures that the reduction of the failure probability is strongest for the dike sections with the smallest failure probabilities due to the sub-mechanism backward erosion. This trend seems to become even more extreme for very high failure probabilities in the order of 0.5, like for heave and uplift (see for example Figure 6.4 and Figure E.3). In those cases, a correlation that is expected to result in a reduction of the failure probability, leads to the opposite: an increase of the corresponding failure probability.

Based on these observations, it has been decided to analyse the impact of correlation for a varying order of magnitude of the failure probability - i.e. for a varying water level h. For this, one simplified dike section has been considered. All parameters have been included as deterministic values, except for the two correlated parameters. Then, failure probabilities for a situation with correlation ($\rho = 0.8$) and for a situation with no correlation have been assessed for different values of the water level h. In Figure 6.16, the results for correlation $k - d_{70}$ and $S - m$ are shown and they confirm that the effect of the correlation increases for decreasing failure probability (i.e. decreasing water level h).

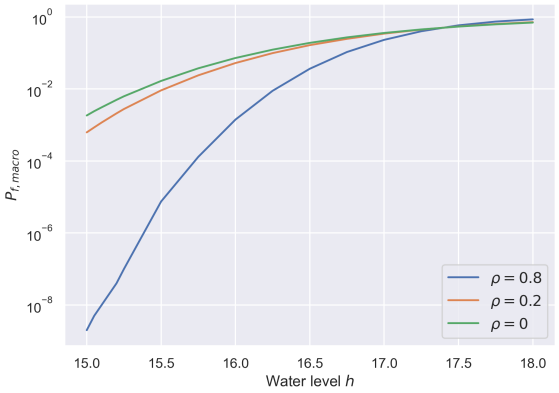

(a) Piping, correlation $k - d_{70}$.

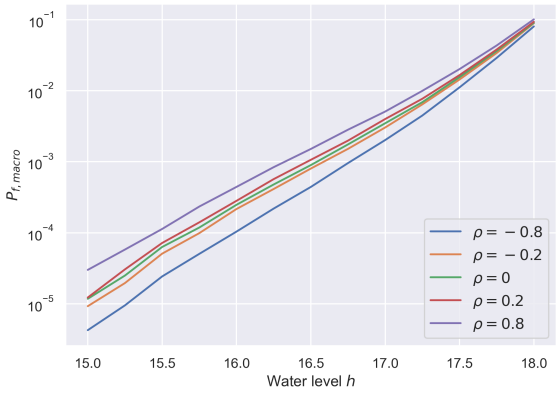

(b) Macrostability, correlation $S - m$.

Figure 6.16: The impact of correlation on the failure probability for varying water level h.

Table 6.1 shows the factor of the reduction or increase for different values of the water level. Note that a positive correlation between S and m for macrostability leads to an increase of the failure probability, as could be observed in the previous section as well. For small water levels, the effect of including a correlation between k and d_{70} is very significant. Including a correlation of $\rho = 0.8$ leads to a reduction of the failure probability from order 10^{-3} to order 10^{-7}, when all other parameters are taken as deterministic values. Besides, it can be observed that the effect is intensifying much more for $k - d_{70}$ than for $S - m$ when moving to smaller failure probabilities. Explanations for the observed effects will be given in the Discussion in Chapter 7.

Table 6.1: The factor of the reduction or increase of the failure probability: $P_{f,nocorr}/P_{f,corr}$ for a correlation of 0.8.

Water level [m]	$k - d_{70}$	$S - m$
15.0	92,138	0.89
15.5	2,238	0.77
16.0	51	0.68
16.5	5	0.59
17.0	1.6	0.56
17.5	0.9	0.56
18.0	0.8	0.54

6.1.4. Overtopping

Since the study area is located in the upper river reach, it is common practice to assume that the water level is entirely determined by the river discharge and that there is no correlation between the river discharge / water level and the wind. However, there is a correlation between the wind speed and the wind direction. In the Hydra-NL wind statistics, that are applied within this case study, this correlation is already included. No other correlations between input variables are assumed to be present for the failure mechanism overtopping.

6.1.5. Summary of the results

In Table 6.2 and 6.3, a summary is given of the results from the analyses that are elaborated in the previous sections. The relative differences for the three sub-mechanisms of piping are shown in Table E.1. The failure probabilities due to piping for dike section 17 and 18 are so small that a Monte Carlo simulation with 400,000 samples is not able to capture it accurately. Therefore the results for these two sections are not trusted and not included in the determination of the mean relative difference with respect to the uncorrelated situation. The reason for these very small failure probabilities for dike sections 17 and 18 is the particularly large blanket layer thickness of almost nine metre. The same holds for the dike sections that have small failure probabilities ($P_f < 10^{-3}$) due to macrostability.

Table 6.2: Summary of the results of the sensitivity analyses into correlations between piping parameters.

Correlated parameters	Relative difference w.r.t. uncorrelated situation [%]					
	$\rho = 0.8$			$\rho = 0.2$		
	min	median	max	min	median	max
k - d_{70}	-81.6	-37.5	-0.85	-25.0	-8.68	-0.42
Φ_{exit} - k	-0.76	$+5.93$	$+21.5$	-3.83	$+1.77$	$+5.98$
Φ_{exit} - h_p	-47.3	-3.74	$+5.76$	-9.73	-1.38	$+0.96$
Φ_{exit} - d	-22.7	$+1.09$	$+6.25$	-10.7	$+0.12$	$+2.08$
Φ_{exit} - D	-1.05	$+1.12$	$+6.38$	-4.26	0.0	$+2.88$
Φ_{exit} - k_{v3}	-1.64	0.0	$+1.55$	-2.27	0.0	1.05

Table 6.3: Summary of the results of the sensitivity analyses into correlations between macrostability parameters.

Correlated parameters	Relative difference w.r.t. uncorrelated situation [%]											
	$\rho = 0.8$			$\rho = 0.2$			$\rho = -0.2$			$\rho = -0.8$		
	min	median	max	min	median	max	min	median	max	min	median	max
S - m	-5.08	0.0	$+16.5$	-6.25	$+0.29$	$+3.59$	-11.2	-1.15	$+10.2$	-19.1	$+0.70$	$+2.03$
S - γ	-5.38	$+1.58$	$+120$	-4.28	0.0	$+24.0$	-20.4	-1.38	$+0.97$	-63.8	-2.89	0.51
φ - γ	-8.74	-0.48	$+112$	-7.57	0.0	$+23.3$	-16.0	-0.37	$+4.79$	-58.7	-0.17	$+5.10$

6.2. Spatial Correlations

Now spatial correlations in the soil parameters are considered. The choice of which spatial correlations should be investigated is based on an analysis of the spatial distribution of geological deposits in the area of the case study. This analysis has been elaborated in Section 5.2.2 of the previous chapter. Moreover, the hydraulic load is assumed to be fully correlated in space. After all, the river discharge is the same everywhere along the trajectory, so a high river discharge results in high water levels for each dike section at the same time. However, most analyses of this study are executed conditional on the discharge, so for a fixed value of the river discharge. Therefore, the spatial correlation of the water level is not visible in the results.

Spatial correlations are expected to have no impact on the sectional failure probabilities, but lead to dependency between failure of neighbouring dike sections or to dependency in failure of two different failure mechanisms within one dike section. It is assumed that spatial correlations are always expressed in positive correlations. In other words, spatial correlations imply that drawing a high realisation of a soil parameter in dike section 1 increases the chances of drawing a high realisation of the same soil parameter in dike section 2. Different scenarios of spatial correlation in the soil parameters have been investigated:

- No spatial correlations;
- Spatially correlated aquifer parameters;
- Spatially correlated dike material;
- Spatial correlations for the layers that are listed in Table D.2;
- Spatial correlations for all layers.

The first two scenarios will be elaborated in more detail, while the other results will be summarised in a few graphs and plots.

1. No spatial correlations

First, the model is run for a situation of no correlations between the parameters of two neighbouring dike sections. Figure 6.17 shows scatter plots of the simultaneous realisations of the limit state functions Z of two neighbouring dike sections for (a) piping; for (b) macrostability; and for (c) piping and macrostability of the same dike section. These graphs illustrate the resulting dependencies between failure of the sections and failure mechanisms when no spatial correlations are included in the model. It can be seen that a situation with no spatial correlations obviously results in uncorrelated failure between dike sections and failure mechanisms. This scenario is used as the reference scenario, in order to investigate the effect of including spatial correlations.

Table 6.4: Overview of the total failure probabilities in the uncorrelated situation, conditional on a river discharge of $Q = 20,000$ m^3/s. First column: according to the method of the model. Second column: according to the WBI assemblage procedure.

	Counting failure integrally	WBI procedure	Relative difference
$P_{f,total}$	$9.992 \cdot 10^{-1}$	$9.992 \cdot 10^{-1}$	-0.005%
$P_{f,piping}$	$9.979 \cdot 10^{-1}$	$9.978 \cdot 10^{-1}$	$+0.007\%$
$P_{f,macro}$	$6.482 \cdot 10^{-1}$	$6.484 \cdot 10^{-1}$	-0.040%

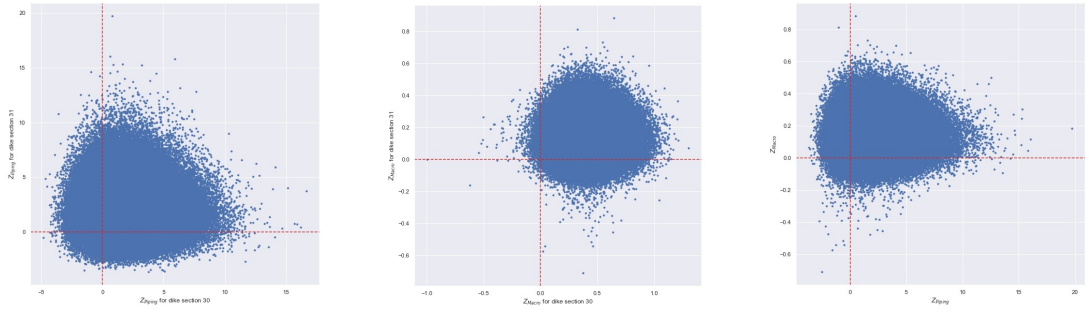

(a) Scatter plot of Z for Piping of dike section 30 vs. dike section 31 .

(b) Scatter plot of Z for Macrostability of dike section 30 vs. dike section 31.

(c) Scatter plot of Z for Piping vs. Macrostability for dike section 31.

Figure 6.17: Resulting dependencies in failure for a situation with no spatial correlations, conditional on a river discharge of $Q = 20,000\ m^3/s$ and $N = 400,000$.

As explained in the previous chapter and in Chapter 1, the model makes use of an alternative method to compute the total failure probabilities when compared to the standard WBI procedure. In the model, failure is counted at the end of each Monte Carlo realisation if one or more Z-values of the different failure mechanisms and different dike sections are smaller than zero. In this way, simultaneous failure of dike sections or failure mechanisms, as it is likely to occur in correlated scenarios, is only counted once for the assessment of the total failure probability. The WBI procedure of assembling the failure probabilities is explained in Section 5.8.2. In Table 6.4, the resulting total failure probabilities of the uncorrelated scenario are summed. The last row gives the relative difference between the failure probability computed by the method of the integral probabilistic model, with respect to the failure probability computed by the WBI procedure. It can be seen that the failure probabilities by counting failure are practically the same as the failure probabilities according to the WBI assembling procedure, for the uncorrelated scenario.

2. Spatial correlations for the Pleistocene sand layer (aquifer)
Now, spatial correlations are included. From Section 5.2.2, it was concluded that it is very likely that the aquifer properties are correlated along the dike trajectory Sprok-Sterreschans, since there is one large Pleistocene sand layer present. Therefore, the first situation that has been analysed is the situation in which the aquifer parameters are spatially correlated over the complete trajectory. A positive spatial correlation between neighbouring dike sections has been applied for the hydraulic conductivity k, the grain size d_{70} and the frictional angle of the Pleistocene sand φ_{pl} of the aquifer. k and d_{70} are included in the assessment for piping. k and φ_{pl} are included in the assessment for macrostability, where k is included in all metamodels, while φ_{pl} is only included in some of the metamodels (see Table C.1).

Figure 6.18 and 6.19 illustrate that spatial correlations have a negligible effect on the sectional failure probabilities, which is logical since the two correlated parameters play a role in different dike sections. However, this observation is again based on the dike sections with failure probabilities that are higher than the order of 10^{-3}, since it is clearly visible that the results for dike sections with lower failure probabilities are unreliable.

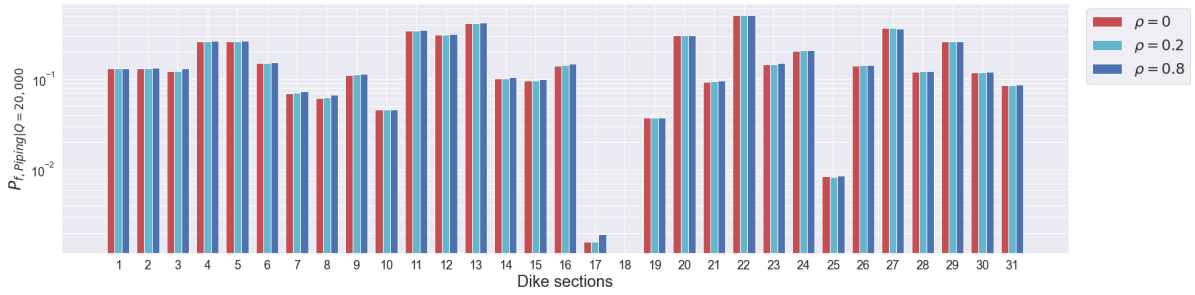

Figure 6.18: Resulting sectional failure probabilities for piping, conditional on a river discharge $Q = 20,000\ m^3/s$, for two different situations of spatially correlated aquifer properties.

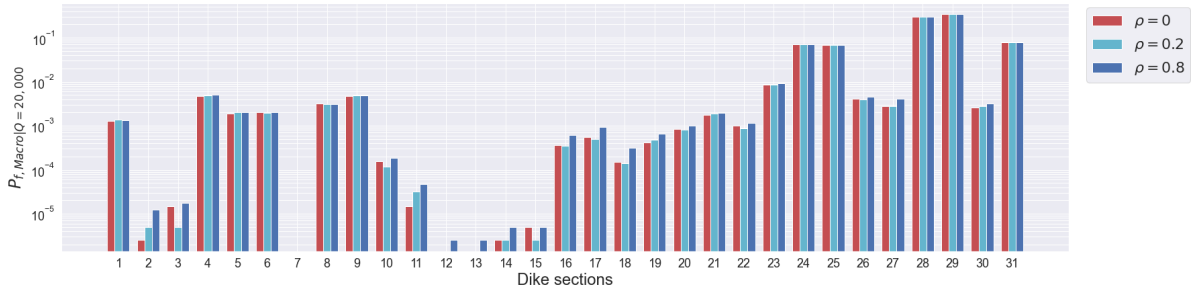

Figure 6.19: Resulting sectional failure probabilities for macrostability, conditional on a river discharge $Q = 20,000\ m^3/s$, for two different situations of spatially correlated aquifer properties.

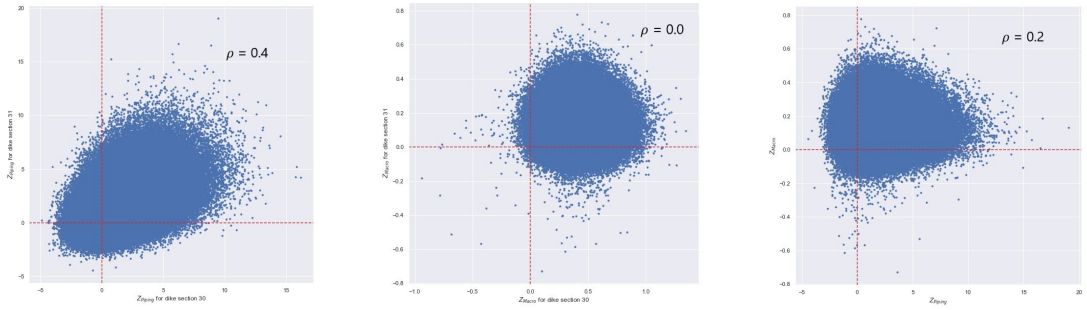

(a) Scatter plot of Z for piping of dike section 30 vs. dike section 31 .

(b) Scatter plot of Z for macrostability of dike section 30 vs. dike section 31.

(c) Scatter plot of Z for piping vs. macrostability for dike section 31.

Figure 6.20: Resulting dependencies in failure for a situation with a correlation of $\rho = 0.8$ between the aquifer properties, conditional on a river discharge of $Q = 20,000\ m^3/s$ and $N = 400,000$.

It is expected that the spatial correlations will result in correlated failure between neighbouring dike sections and/or failure mechanism. In Figure 6.20, the resulting dependencies are shown. It can be seen that it indeed leads to a correlation between failure due to Piping of neighbouring dike sections. However, no effect is present in failure due to macrostability of neighbouring dike sections or in failure due to the two mechanisms within one dike section. This can be explained by the fact that the parameters k and φ_{pl} have a negligible effect on failure for macrostability (see Table C.5), while k and d_{70} are quite important for piping. The example is given for dike section 31, but the same holds for the other dike sections.

3. Other scenarios of spatial correlations

For all other scenarios, including spatial correlations of the geotechnical parameters of a soil layer result in dependencies in failure for piping, with a Pearson's coefficient $\rho = 0.4$ maximum. Still, the effect is not really visible in a reduction of the total failure probability, when counting failure within the integral model. For macrostability, the spatial correlations generally lead to a somewhat weaker dependency in failure between two dike sections than for piping. A correlation between failure due to piping and due to macrostability within one dike section is not visible. For the scenario of spatial correlations for all soil layers, dependencies in failure became the most apparent for dike section 24 and 25, although they are still quite weak (see Figure 6.21). This can be explained by the fact that the dike sections 24 and 25 make use of the same metamodel. In that scenario, all parameters of the same soil layer type were correlated to the corresponding parameter of the same soil layer type of a neighbouring dike section.

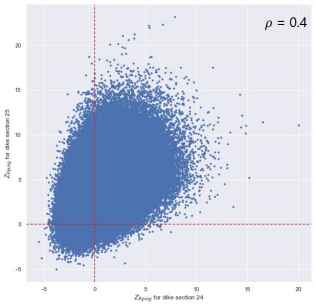

(a) Scatter plot of Z for piping of dike section 24 vs. dike section 25 .

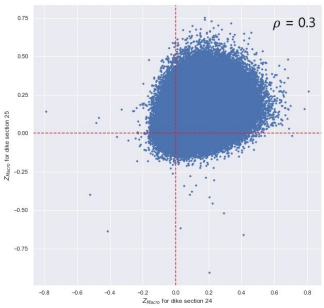

(b) Scatter plot of Z for macrostability of dike section 24 vs. dike section 25.

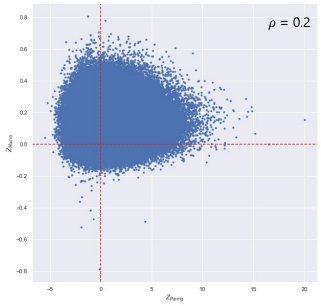

(c) Scatter plot of Z for piping vs. macrostability for dike section 24.

Figure 6.21: Resulting dependencies for a situation with a correlation of $\rho = 0.8$ between all properties of the same soil layer, conditional on a river discharge of $Q = 20,000\ m^3/s$ and $N = 400,000$.

6.2.1. Summary of the results

The relative difference of the computed failure probabilities with respect to the uncorrelated situation or the WBI procedure are listed in Table 6.5. In the table, the effect of including spatial correlations on the total failure probabilities is shown, in terms of the relative difference between the correlated scenario and the uncorrelated scenario (left columns) and between the correlated scenario and the failure probabilities according to the WBI procedure (right columns). It can be seen that the effect is negligible for most cases, while it was expected that it would be more significant. The results will be interpreted and discussed in the next chapter.

To summarise, the total failure probabilities related to the most likely scenario of spatial correlations, conditional on a river discharge of $Q = 20,000\ m^3/s$ and for $N = 400,000$ are:

- $P_{f,tot,uncorr} = 9.992 \cdot 10^{-1}$
- $P_{f,tot,corr} = 9.985 \cdot 10^{-1}$
- $P_{f,tot,WBI} = 9.992 \cdot 10^{-1}$

These failure probabilities correspond to the third row of Table 6.5, with spatial correlations according to Table D.2 for a correlation of $\rho = 0.8$.

Table 6.5: Relative differences in % between the failure probabilities including correlations, with respect to (1) the uncorrelated situation and (2) the failure probabilities computed by the WBI assemblage procedure.

Situation	ρ	$P_{f,tot}$		$P_{f,pip}$		$P_{f,macro}$	
		no corr	WBI	no corr	WBI	no corr	WBI
Aquifer properties spatially correlated	0.8	−0.04	−0.05	−0.15	−0.13	+0.20	−0.10
	0.2	−0.02	−0.02	−0.06	−0.03	−0.16	−0.07
Spatial correlations according to Table D.2	0.8	−0.07	−0.07	−0.17	−0.15	−3.8	−4.1
	0.2	−0.02	−0.01	−0.06	−0.03	−0.98	−0.97
Dike properties spatially correlated	0.8	−0.01	−0.00	−0.04	−0.00	−2.5	−3.3
	0.2	−0.04	−0.02	−0.02	−0.00	−0.35	−0.41
All properties of a layer spatially correlated	0.8	−0.13	−0.15	−0.39	−0.40	−1.4	−3.3
	0.2	−0.02	−0.03	−0.06	−0.08	−0.98	−0.97

7

Discussion

The main objective of this study is to investigate the effects of including correlations in the assessment of the failure probability of a dike trajectory within one integral, full-probabilistic model framework. In this chapter, the results of this study, that were presented in the previous chapter, will be interpreted, discussed and compared to the results of other studies. Also, the limitations of this research and the relevance of the results will be explored.

7.1. Interpretation of the Results

In the following two subsections, the results - as presented in Chapter 6 - will be explained. First, the correlations between variables will be discussed and second the spatial correlations.

7.1.1. Correlations between variables

In Section 6.1, the impact of different plausible correlations between variables of the piping and macrostability assessments were investigated. From the results, it can be interpreted that the magnitude and direction of the effect of correlations depend on the following aspects:

1. The importance and contribution of the correlated parameters;
2. For piping: the sub-mechanism in which the correlated parameters play a role;
3. The order of magnitude of the corresponding failure probability.

1. The importance and contribution of the correlated parameters

A correlation has a more significant effect if both parameters are of large importance for failure. This explains why a correlation between the shear strength ratio S and the volumetric weight γ shows the largest impact for macrostability and between the hydraulic conductivity k and the grain size d_{70} for piping. Correlations related to macrostability generally have a smaller impact than to piping. Macrostability is a complex, non-linear process and there are many different parameters that play a minor role in failure. Moreover, it depends on the location of the slip circle whether a parameter contributes to the resistance or to the load, so the contribution, as well as the importance of a parameter, can vary. On the contrary, failure due to piping is more linear and there are less parameters that determine failure, leading to a generally stronger impact of correlations.

Whether a correlation leads to a reduction or to an increase of the failure probability strongly depends on the importance and contribution of the parameters. This can be explained by taking k and d_{70} as an example: k contributes to the load and d_{70} contributes to the resistance. If these two parameters are positively correlated it means that a high realisation of k is more likely to be drawn at the same time as a high realisation of d_{70}. A high realisation of k would probably lead to an unsafe Z-value, while a high realisation of d_{70} would most probably lead to a safe value of Z and vice versa. So, these two effects cancel each other out, leading to more 'safe' realisations of Z. Therefore, the correlation between k and d_{70} leads to a reduction of the failure probability due to piping. This conclusion is confirmed by Aguilar López et al. (2014), where different copula types were applied to model the correlation between k and d_{70}. No matter which copula type was chosen, the Sellmeijer limit state function showed a reduction in the failure probability due to piping for a higher degree of correlation.

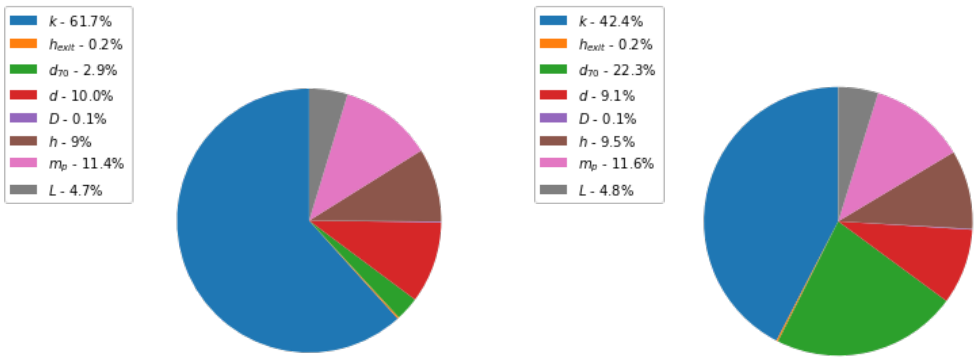

(a) No correlation between k and d_{70}.

(b) Correlation of $\rho = 0.8$ between k and d_{70}.

Figure 7.1: The importance of the stochastic parameters for the assessment of the sub mechanism backward erosion, expressed by the FORM Importance factors (α-values).

On the contrary, correlating two resistance parameters to each other leads to an increase of the failure probabilities. After all, a positive correlation between two resistance (or two load) parameters implies that low or high realisations of both parameters are likely to occur at the same time and thus will result in more unsafe evaluations of Z. This is often the case within macrostability.

At the same time, including correlation changes the importance of the corresponding parameters. This can be illustrated by performing a FORM analysis for the sub-mechanism backward erosion, for the uncorrelated and for the correlated situation of $k - d_{70}$ ($\rho = 0.8$). Figure 7.1 illustrates that the importance of the grain size d_{70} increases significantly when the correlation between k and d_{70} is included in the FORM analysis.

2. For piping: the sub-mechanism in which the correlated parameters play a role
Piping is assessed as a parallel system of the three sub-mechanisms uplift, heave and backward erosion. This implies that the sub-mechanism with the lowest probability determines the total failure probability of piping. Therefore, a correlation between parameters that are included in the assessment of the sub-mechanism with the lowest probability, will have the most significant effect on the total failure probability. The sub-mechanism backward erosion dominates failure for this case study, explaining the strong impact of a correlation between $k - d_{70}$.

Correlation between two load parameters of different mechanisms of a parallel system leads to an increase of the failure probability, since the sub-mechanisms are more likely to fail at the same time. This is the case for a correlation between the hydraulic conductivity k and the exit potential Φ_{exit}, for example.

3. The order of magnitude of the failure probability
In Section 6.1.3, it could be observed that (1) the smaller the failure probability, the stronger the impact of correlations and (2) this effect is stronger for a correlation between the hydraulic conductivity k and the grain size d_{70} than for the shear strength ratio S and the shear strength exponent m. In order to explain these observations, the realisations of the correlated parameters and the histogram of the resulting evaluations of the limit state function Z are analysed. This is presented in Figure 7.2 for correlated and uncorrelated scenarios of k and d_{70}. First for a lower water level h (i.e. lower failure probability) and then for a very high water level. All other parameters than k and d_{70} have been included deterministically. Realisations of k and d_{70} that lead to failure ($Z < 0$) are plotted in red in Figure 7.2. Again, it can be observed that the reduction of the failure probability, due to inclusion of the correlation, is much stronger for the case with smaller failure probabilities ($h = 16$). But now the figure also provides an explanation: It can be observed in the most right panels that the width of the histogram - i.e. the variance of the model - decreases when the correlation is included. This happens for both scenarios of the water level. For $h = 16$, the failure domain of the histogram ($Z < 0$) is very small and thus the difference between the area for $\rho = 0.8$ and $\rho = 0$ is relatively large. Therefore, the failure probability including correlation is significantly smaller than the uncorrelated failure probability: due to the decrease of the variance.

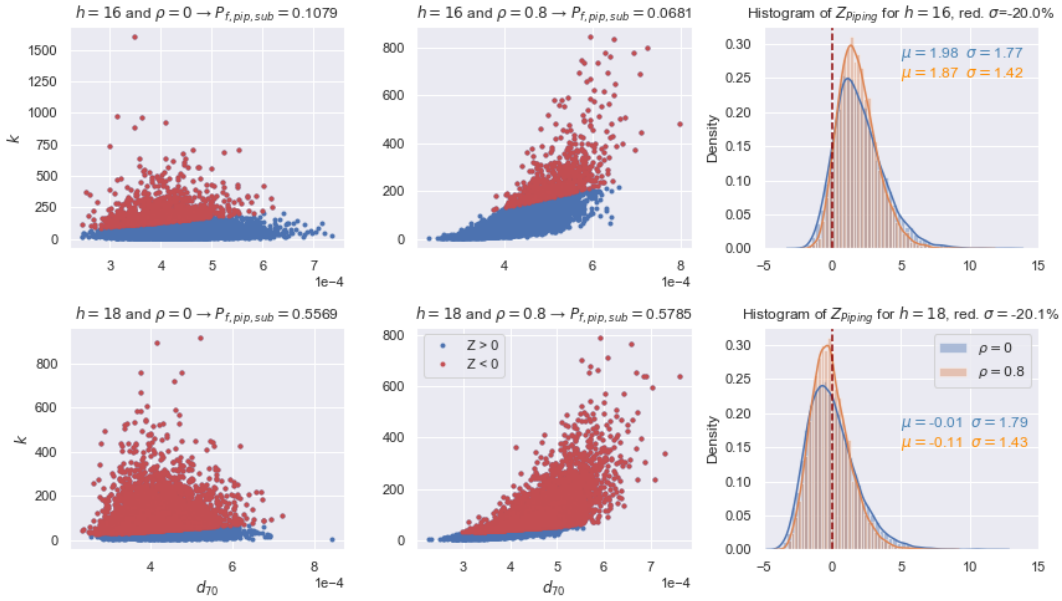

Figure 7.2: Scatter plots of the realisations of d_{70} vs. k. For the uncorrelated (left) and the correlated case (middle). Right: the histogram of the evaluations of Z_{piping}. Conditional on a water level of h = 16 m+NAP (upper) and h = 18 m (lower).

For $h = 18$, the failure domain is much larger, almost half of the histogram. In the lower histogram plot it can be seen that the area in the failure domain of the histogram for $\rho = 0.8$ is larger than the area of $\rho = 0$. This is because the decrease of the variance is more evident in the right-hand tail, while most Z-realizations for $\rho = 0.8$ are located around $Z < 0$. This explains why the correlated failure probability is larger than the uncorrelated failure probability for $h = 18$. In short, the impact of correlation can be explained by the decrease of the model variance.

Why this effect is more extreme for the correlation between k and d_{70} than for the correlation between S and m, can be partly explained by the marginal distributions of the parameters. Although all four parameters are described by a lognormal distribution, the standard deviations differ. If the analysis as shown in Figure 7.2 is repeated for a smaller standard deviation of k, the decrease of the variance of the Z-histogram is even stronger. This is shown in Figure E.16 of the appendix (p.130).

For a full explanation of this effect, it would be interesting to perform a variance-based sensitivity analysis in order to investigate the contribution of the input variables and combinations of variables to the output variance. However, this is out of the scope of this research.

7.1.2. Spatial correlations and the total failure probability

From Table 6.5 on page 78, it can be concluded that spatial correlations have a negligible effect on the total failure probability of this case study. This is a rather surprising conclusion, since it was expected that the impact would be stronger, especially with the alternative way of counting failure within the Monte Carlo simulation. However, the minor impact can be explained by two aspects:

1. The heterogeneity of the dike sections and failure mechanisms
2. The number of stochastic parameters

These aspects will be discussed below and illustrated by means of a simple, theoretical example of two to three dike sections.

1. Heterogeneity of the dike sections and failure mechanisms

The major reason why the effect of spatial correlation cannot be fully expressed within this study is the heterogeneity of the dike sections of the case study. The dike sections differ significantly from each other in terms of order of magnitude of the failure probabilities and subsoil geometry. The latter leads to the fact that the different metamodels of the dike sections are based on different ten input variables,

because the importance of the soil parameters varies. So, even though there might be one clay layer that extends over multiple dike sections, it does not mean that the strength properties of this layer are included in all metamodels. Therefore, this spatial correlation cannot be fully included in the model and its full impact is not reflected in the resulting dependencies and failure probabilities. If the dike sections would have a similar geometry and subsoil, the corresponding parameters would be equally important for all sections and it would be possible to use one metamodel - or at least similar metamodels - that are based on the same input variables. So, it is expected that spatial correlations have a more significant impact if the (subsoil) geometry is more or less constant in space.

Moreover, the method of counting failure if one or more negative evaluations of $Z_{j,k}$ occur, gives the largest reduction of the total failure probability - compared to the uncorrelated situation or the WBI assemblage - if all sectional failure probabilities are in the same order of magnitude. This can be explained as follows: the method gives a reduction of the total failure probability if failure due to one mechanism or dike section happens most often at the same time as failure due to another mechanism or dike section (i.e. in correlated situations). However, if the failure probability of the first element is in the order of e.g. 10^{-2}, while the failure probability of the other is in the order of e.g. 10^{-5}, the combined failure probability for a correlated situation would be in the order of 10^{-2} and in the order of $10^{-2} + 10^{-5} = 10^{-2}$, for the uncorrelated situation. In other words, the reduction of the total failure probability due to inclusion of spatial correlation is minimal in that case. This is what happened for the case study of this research. The same line of reasoning explains why the method has a larger impact if both sectional failure probabilities are in the same order of magnitude. Theoretically, it could lead to a halving of the failure probability if failure of the two elements always occurs at the same time and if their failure probabilities are the same.

2. Number of stochastic parameters
The assessments for macrostability of dike sections 5 and 6 are based on metamodels that have the same input parameters. Still, the effects of correlations differ. This can be explained by the randomness of the realisations and by the complexity of macrostability. Apparently, the *combination* of the drawn realisations of *all* parameters within an iteration really determines the Z-value for macrostability, and not the realisations of the two correlated parameters in particular. This is explained by the fact that there is often not really one parameter that dominates the mechanism macrostability within a section. Therefore, correlation between two parameters is in most situations not influential enough to show a consistent trend in the failure probabilities for macrostability. It is expected that the impact of correlation would be more evident if the other parameters than the correlated ones would be considered as deterministic. The same holds for piping.

7.1.3. Effectiveness of the model

The predominantly insignificant effect of spatial correlations, in combination with the integral approach, can be explained by the large differences between the dike sections. The dike sections have very different failure probabilities, as could be observed in for example Figure 6.19 on page 77. Also the subsoil geometry varies. It is expected that spatial correlations probably have a more significant impact on the total failure probability in more homogeneous situations. This is proved by assessing a theoretical dike trajectory of three dike sections with the same geometry and metamodels by means of the integral model.

Table 7.1: Upper: Failure probabilities for a situation with different failure probabilities for piping and macrostability, for a spatially correlated and uncorrelated k. Lower: Total failure probabilities for a situation with similar failure probabilities for piping and macrostability. For $N = 400,000$ realisations of the Monte Carlo simulation and all other parameters deterministic.

k	$P_{f,pip}$	$N_{f,pip}$	$P_{f,macro}$	$N_{f,macro}$	$P_{f,tot}$	$N_{f,tot}$	$P_{f,tot,WBI}$	Diff w.r.t. WBI	Diff w.r.t. ref
$\rho = 0$	$2.22 \cdot 10^{-2}$	8862	$5.00 \cdot 10^{-5}$	20	$2.22 \cdot 10^{-2}$	8881	$2.22 \cdot 10^{-2}$	-0.0063%	ref
$\rho = 0.8$	$2.17 \cdot 10^{-2}$	8674	$7.25 \cdot 10^{-5}$	29	$2.17 \cdot 10^{-2}$	8674	$2.18 \cdot 10^{-2}$	-0.33%	-2.33%
$\rho = 0$	$3.15 \cdot 10^{-4}$	126	$3.43 \cdot 10^{-4}$	137	$6.75 \cdot 10^{-4}$	263	$6.57 \cdot 10^{-4}$	2.68%	ref
$\rho = 0.8$	$3.25 \cdot 10^{-4}$	130	$4.55 \cdot 10^{-4}$	182	$4.55 \cdot 10^{-4}$	182	$7.80 \cdot 10^{-4}$	-41.66%	-32.59%

Table 7.2: Reduction of the total failure probability due to macrostability after inclusion of spatial correlation for different parameters. All other parameters are included deterministic. The order of magnitude of the sectional failure probabilities is 10^{-3}.

Parameter	Diff w.r.t. WBI	Diff w.r.t. no corr
S_{clay}	-30.6%	-30.6%
m_{clay}	-22.3%	-23.0%
φ_{dike}	-90.4%	-91.7%

The effectiveness for different orders of magnitude of the sectional failure probabilities is investigated. Therefore, two different scenarios of failure probabilities have been considered, both with and without spatial correlation for the hydraulic conductivity k. The results are listed in Table 7.1. The first two rows show the results for dike sections with a relatively high P_f for piping and a small P_f for macrostability. The number of failures shows that including the correlation indeed causes the failures for macrostability and piping to occur at the same time. However, it can be concluded that this only reduces the failure probability by 2.3% with respect to the uncorrelated situation. This is due to the small number of failures for macrostability. In the lower two rows of the table, however, the effect is much larger. Now the failure probabilities due to piping and macrostability are both in the order of 10^{-4} and it can be seen that inclusion of the spatial correlation for k reduces the failure probability by more than 40%. This reduction is much more significant than the ones achieved for the case study in the previous chapter.

Furthermore, the effect of using the same metamodel for multiple dike sections can be illustrated by means of this theoretical case. In Table 7.2, the impact of including spatial correlations is shown for three soil parameters. These parameters are likely to be spatially correlated in reality. All dike sections have the same metamodel, and all other parameters are deterministic. The frictional angle of the dike material φ_{dike} has the largest importance factor in this theoretical case. It can be concluded that the effect of spatial correlation is now much more notable. This also becomes clear from the scatter plots for Z, as shown in Figure 7.3. Including the correlation leads to a much more visible dependence in failure of two neighbouring dike sections than previously for the case study.

So, including spatial correlation of an important parameter can give a reduction of the failure probability of approximately 90% - a factor 10 - as listed below for spatial correlation of φ_{dike} for a trajectory of three dike sections and all other parameters deterministic:

- $P_{f,macro,tot,corr,WBI} = 1.47 \cdot 10^{-2}$
- $P_{f,macro,tot,nocorr} = 1.47 \cdot 10^{-2}$
- $P_{f,macro,tot,corr} = 9.95 \cdot 10^{-4}$

At the same time, the more parameters are included as stochastic, the more randomness is added to the model. The effects of the different parameter realisations partly cancel each other out and smoothen the effect of spatial correlation. Still, the reduction of the failure probability as a consequence of spatial correlation for φ_{dike} is about 20% if all other parameters are stochastic and identical metamodels for all three dike sections. This is still much more than for the case study Sprok-Sterreschans where the dike sections are more heterogeneous and the metamodels differ along the trajectory.

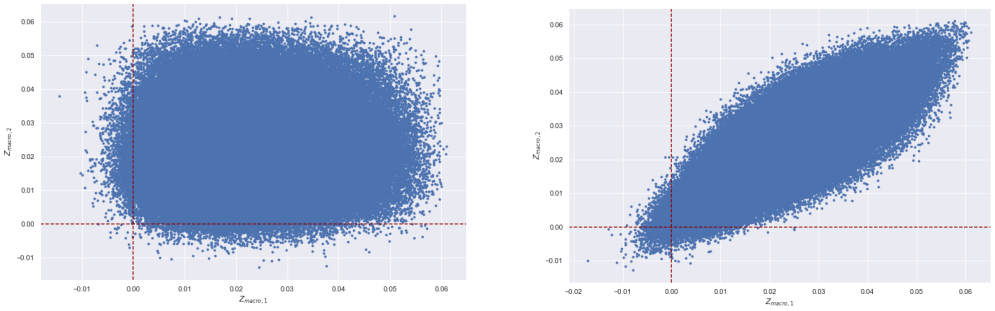

(a) No correlation for φ_{dike}.

(b) $\rho = 0.8$ for φ_{dike}.

Figure 7.3: Scatter plots of Z_{macro} for dike section 1 vs. dike section 2, for uncorrelated and correlated dike material φ_{dike}.

7.2. Limitations of the Study

From the discussions above, a few limitations of the model already became clear. The most important are listed and discussed below.

Metamodeling
Metamodels are most accurate for about a dozen input parameters (Pedregosa et al., 2011), while macrostability is a complex failure mechanism with many more parameters involved. Since the dike sections of the trajectory have different geometries and subsoil layers, the ten input variables differed per dike section. As a consequence, it was not possible to include every plausible spatial correlation that was observed in the subsoil schematisations as described in Section 5.2.2. This became evident in the relatively small impact of spatial correlation for the case study. Moreover, the uncertainty in the subsoil geometry is not included. The layer structure, as schematised by the water authority in D-Stability, has been considered as deterministic. To include this uncertainty, the layer thickness should be treated as stochastic and different scenarios of the subsoil structure should be considered. This would make the creation of the metamodels much more complicated and time-consuming and could be a research topic itself.

Reliability vs. computation time
Most of the analyses have been performed with 400,000 iterations of the Monte Carlo simulation. With 400,000 iterations, a coefficient of variation of 0.05 can be achieved for failure probabilities in the order of 10^{-3} (see Equation 2.10 on p.11). For smaller failure probabilities, the simulation does not provide a reliable estimate of the failure probability, which explains the rather strange results for dike sections with smaller failure probabilities. Obviously, this could be solved by taking more iterations for the Monte Carlo simulation. But then the computation time comes into play: with the used computer 400,000 iterations already take about 18 hours for an assessment of the complete dike trajectory and with all input parameters as stochastic. Increasing the number of iterations by a factor ten or more, which would be required to have reliable estimates for failure probabilities in the order of 10^{-4} or lower, results in unfeasible computation time, for the available compute power. This is one of the major disadvantages of the model and of Monte Carlo simulations in general. Monte Carlo simulations can be made more efficient by means of importance sampling for example. However, for high-dimensional reliability problems including correlations, the application of importance sampling is rather complex and still in development (Liu and Elishakoff, 2020).

It also explains why an unrealistically high conditional discharge of $Q = 20,000\ m^3/s$ was applied for the assessments of macrostability. Such an extreme value of the river discharge at Lobith is in reality very unlikely to occur and is often not considered in the assessment of flood defences. Nevertheless, such a high value had been chosen in order to obtain as many high, and thus reliable, failure probabilities as possible. For piping, a value of $Q = 16,000\ m^3/s$ was applied, since the sectional failure probabilities are higher. For overtopping and erosion of the grass revetment on the outer slope, the sectional failure probabilities of the case study trajectory are so small ($< 10^{-6}$) that the results of the integral model are not reliable.

Copula choice
A Gaussian copula had been chosen to model the correlations. The Gaussian copula does not induce any specific tail dependence. Tail dependence can be important in reliability assessments, where extreme values are considered. Still, the choice for a Gaussian copula is justified if there is no evidence from data for a particular type of correlation, which is the case for this research. However, it should be kept in mind that a different copula model may lead to a different effect of including correlations. This became evident in the research of Aguilar-López et al. (2016), where the correlation between the hydraulic conductivity k and the grain size d_{70} of the aquifer was studied for different copula models.

Lack of data
An elaborate analysis of which copula to choose only makes sense if the amount of available data is large enough to accurately derive the correlation structure between parameters from. For most cases, just like the case study of this research, not many measurements are available for the different geotechnical parameters. Thus, it is not even possible to define a value of the correlation coefficient ρ between parameters from data. The same holds for the marginal distributions of the parameters.

Hydraulic loads
In Section 5.3.1 it was concluded that the failure probabilities for overtopping could not be exactly reproduced by the model. This could be mainly explained by neglecting the model uncertainty. The model uncertainty is an important aspect in the definition of the hydraulic boundary conditions and neglecting it leads to an underestimation of the failure probabilities. However, the aim of this research is more of qualitative nature than quantitative, which is why it has been decided to focus on other aspects than on improving the accuracy of the hydraulic loads. Therefore, the resulting failure probabilities of this research are not very accurate, but they enable the investigation of the impact of correlations.

Definition of the exit point potential Φ_{exit} for piping
In the case study, the exit point potential Φ_{exit} was included as an explicit stochastic variable in the assessment for piping. This was done to stay close to the assessment by the water authority. However, it would be closer to reality to define Φ_{exit} as a function of the water level h, phreatic level h_p and the damping factor λ, as described in Equation 3.21 and 3.22 on page 29. In that case, Φ_{exit} would be dependent on the hydraulic conductivities (k and k_{v3}) and the thickness of the aquifer D and blanket layer d. Since these parameters partly play a role in both piping and macrostability, it would result in more dependency between these mechanisms.

From a quick theoretical analysis with the model, it could be concluded that an implicit definition of Φ_{exit} (by Equations 3.21 and 3.22) leads to somewhat smaller failure probabilities for piping in the uncorrelated case - a reduction of 5% in particular - when compared to the model with explicit definition of Φ_{exit} as a stochastic input variable. The total failure probabilities are almost the same. Subsequently, including a correlation for k and d_{70} gives similar reductions of the failure probabilities for both variants of the model, in the order of -30%.

So, it seems that for this case study the explicit definition of Φ_{exit} leads to similar results as an implicit definition would do. Still, it is recommended for future studies to use the implicit definition, as it is closer to reality and enables the investigation of more correlations between the mechanisms.

7.3. The Relevance of an Integral Model

It can be concluded that the effect of the integral model was not very significant for the case study, in which large differences between sections and mechanisms exist. But, it has also been demonstrated that a significant reduction of the failure probabilities can be achieved if the different elements have similar failure probabilities. This is a very interesting conclusion for design situations: In dike design, the aim is to have similar failure probabilities for the different elements. So, in those situations, there is a lot to be gained with this integral model - failure probability reductions in the order of 40% are achievable. Especially in view of the rather conservative assessments within the current, conventional approach, this is very relevant. A less conservative approach can lead to a smaller dike reinforcement task, and thus less costs.

This thesis nicely aligns with the demand for less conservatism. An integral approach regards an assessment from a different perspective: A flood defence is considered as a whole, in which the different dike sections and failure mechanisms interact and in which the assessment is more event-based. Event-based refers to the fact that the integral model does not unnecessarily double-count failure for multiple mechanisms due to the same water level. Hence, the integral approach is closer to reality, in which a dike is one continuous soil structure that experiences load from the same water system.

In the conventional approach, the different elements are assessed independently. The norm failure probability of a trajectory is broken down to sectional failure probabilities per mechanism, by means of the failure probability distribution and the length effect. After assessment of these loose elements, they are accumulated again by means of the assembly procedure, in which semi-probabilistic results are translated into estimates of sectional failure probabilities. The procedure is cumbersome and it is often difficult to determine where unrealistic results arise (ENW, 2020). With the integral model, this procedure is not needed, since the different elements are assessed simultaneously. The result is a total failure probability that can be directly compared to the norm. Furthermore, it is easier to trace back the origin of (unrealistically) high failure probabilities, e.g. by investigating the impact of a certain parameter or a specific dike section.

If dike sections and failure mechanisms are assessed integrally, the inclusion of many correlations - that are likely to be present in reality - is possible. For instance, it is often the case that there is one geological sand deposit that spans large parts of the dike trajectory and that functions as the aquifer for different dike sections. It is logical to assume that its properties are strongly correlated between the different dike sections. This kind of dependency is not incorporated in the conventional approach, while it can partly resolve the conservatism. As an example: solely by implementing one and the same probabilistic parameter for the hydraulic conductivity k for both piping and macrostability, the total failure probability could be reduced by 40%. For reference, in the conventional procedure, these mechanisms are assessed independently and sometimes even with different design values for k within the same dike section, which is not realistic. But, it is also important to mention that many other correlations between parameters only have a limited effect within this study.

And finally, an integral approach offers possibilities for more investigations regarding the coherence between failure of different dike sections and mechanisms. For example, how does macrostability evolve when the revetment has eroded? How does a slope instability affect piping? The integral model provides a flexible basis that can be extended in order to answer these kind of questions.

8

Conclusion

The assessment of a Dutch flood defence within the current procedure is subdivided into different failure mechanisms and dike sections that are assessed independently. In reality, a dike is of course one earthen structure with interactions in the failure behaviour, between the failure mechanisms and in space. These interactions take place, because the different dike sections and failure mechanisms are dependent on the same hydraulic loads, the same dike geometry and the same subsoil structure and characteristics. Especially for the geotechnical failure mechanisms. Regarding the different failure mechanisms and dike sections as independent assessments is thus an approximation of reality. For a more accurate reliability assessment, these dependencies should be taken into account. Dependencies are commonly expressed in statistical correlations between parameters. The aim of this thesis is to investigate the impact of including correlations in the reliability assessment of a dike trajectory. To achieve this, an integral, full probabilistic model is created that enables the simultaneous assessment of dike sections and failure mechanisms, while accounting for uncertainties and (spatial) correlations within the model input. The research is conducted on the basis of a case study for the dike trajectory 43-4 between Sprok and Sterreschans. This chapter presents the conclusions that can be drawn from the investigations by providing an answer to the main research question:

What is the effect of assessing the failure probability of a dike trajectory in one integral full-probabilistic framework that includes correlations?

The short answer to the question is: The assessment of a flood defence in an integral, probabilistic manner and with inclusion of the most important correlations can reduce the failure probability significantly, by more than a factor ten in some situations. The reduction of the failure probability is caused by two aspects of this study: (1) the inclusion of correlations between parameters; and (2) the inclusion of spatial correlation of a parameter combined with an alternative method to compute the total failure probability.

In the common practice, the total failure probability is determined by combining the independently computed sectional failure probabilities per mechanism according to the so-called *assemblage* procedure. The current research method counts failure within the Monte Carlo simulation whenever at least one failure mechanism of one dike section results in a negative limit state evaluation Z. In other words, it does not matter for the total failure probability how many elements of the trajectory fail simultaneously for the same realisation of the input, since a dike breach at one location is just as much failure as dike breaches at several locations at the same time. Both situations lead to inundation, and thus imply failure of the trajectory. If failure mechanisms and dike sections are assessed independently, simultaneous failure due to the same realisation of input (i.e. due to the same flood event) cannot be recognised and is included multiple times when the sectional failure probabilities per mechanisms are assembled to a total failure probability. This method results in a lower trajectory failure probability with respect to the assembled trajectory failure probability as soon as failure between mechanisms and sections is correlated. However, it is important to emphasise that the impact of both aspects strongly depends on the situation.

Impact of correlations
Statistical correlations and their effects are a complex mathematical concept. The effect of including a certain correlation is in the first place dependent on the importance and contribution of the correlated parameters. But it should be kept in mind that the importance factors can change significantly in a correlated situation. Whether a correlation leads to an increase or decrease of the corresponding failure probability depends on whether the parameters contribute to the load or resistance of the corresponding mechanism. Moreover, the effect strengthens for small failure probabilities. In a situation where failure is dominated by a few parameters and the failure probability is in the order of 10^{-3} or smaller, inclusion of a realistic degree of correlation between those parameters can reduce the failure probability by a factor 1000. This situation generally applies to piping, where a correlation between the hydraulic conductivity k and the grain size d_{70} is present. On the other hand, for macrostability - which is a more complex, non-linear mechanism where many different parameters play a minor role - the effect of correlation is less significant: A reduction or increase of the failure probability of about 50% for failure probabilities in the order of 10^{-3} is achieved, for correlation between the strength parameters S and m.

Furthermore, it could be concluded that the more stochastic parameters are involved, the less apparent the effect of a correlation becomes. This is explained by the fact that the α-values, i.e. the importance of the correlated parameters, decrease for an increasing number of stochastic variables. The resulting reductions due to correlations as mentioned above are based on situations in which most parameters are included as deterministic. More stochastic parameters imply more randomness in the realisations and less influence of the correlated parameters on failure. This is evident from the results for the case study, where the effect of including correlations was much smaller than for a theoretical case.

Metamodeling
The minor influence of some correlations for the case study is also due to use of metamodels for the assessment of macrostability. Implementation of macrostability within a full-probabilistic Monte Carlo framework is complicated and generally leads to unacceptable computation costs. These issues were tackled by the implementation of metamodeling based on Gaussian process regression. The metamodels are able to predict the factor of safety of a dike section based on the ten most important soil strength parameters, with a mean error of 5%, which is in the same order of magnitude as other sources of uncertainty. An assessment by means of a metamodel reduced the computation costs by a factor of roughly 300 with respect to an assessment by means of D-Stability. The downside of metamodeling is that the mechanism is simplified to a model that depends on only ten geotechnical parameters. Therefore, only if both metamodels of neighbouring dike sections include the corresponding correlated parameters, the effect would be noticeable and thus the total impact of including a certain correlation was small. In general, it can be concluded, however, that the concept of metamodeling is a very promising method to enable the assessment of complex mechanisms like macrostability within a time-consuming full-probabilistic reliability method like Monte Carlo, if some improvements are made.

Integral assessment
The combined effect of spatial correlations and the method of counting failure works best for dike sections and mechanisms with failure probabilities in the same order of magnitude. If one element always dominates failure, correlations between other elements and counting (simultaneous) failure does not make the difference. However, for a situation of homogeneous dike sections for which a few parameters are the most important regarding failure, the integral model including correlations does lead to less conservative assessments of the failure probability. This makes the model especially interesting for design situation, in which it is aimed to achieve the same failure probabilities for the different elements.

The integral set up of the probabilistic model has definitely potential. The set up of an assessment of a complete dike trajectory within one probabilistic model might seem complicated at first. However, many steps of the current assessment procedure can be skipped, making the method not so complex at all. For example, the distribution of the target failure probability over the mechanisms or the assemblage for upscaling to a total failure probability are not needed any more. Moreover, the integral assessment of a dike trajectory is closer to reality and provides more feeling about interactions and the importance of a certain mechanism or parameter during a certain flood event. Even though the model is simplified in many aspects, it provides a solid, working basis that can easily be extended and improved.

9

Recommendations

Based on the findings of this thesis, several points of improvements of the research can be indicated, as well as recommendations for dike managers and topics that are interesting to be further studied in the future.

1. It is recommended to explore the possibilities to increase the efficiency of the model, to reduce the computation costs. Possible approaches to investigate would be importance sampling or FORM.
2. Different degrees of correlation have been investigated within this study, but it is not known how much correlation is actually realistic to assume between certain parameters. More data should be obtained and further research should be done into the degree of correlation between soil parameters in different areas of the Netherlands.
3. It is recommended to study the effect of correlations based on different copula models. Only the Gaussian copula has been applied, while other copula models give a better representation of tail dependencies, which could lead to different results.
4. Include model uncertainties for the hydraulic loads in order to be able to provide more accurate estimations of the failure probabilities.
5. Apply the model to a different case study. In particular, a sea dike would be interesting. Sea dikes are often more homogeneous in space and the failure mechanisms overtopping and erosion of the outer grass revetment are more important, due to extreme wave loads. It is expected that more significant reductions of the failure probabilities can be achieved with the model in a case with homogeneous dike sections.
6. Investigate possible improvements and alternatives of the metamodeling approach. The current research does not take the uncertainty in the soil geometry into account. Including a stochastic soil structure would facilitate the investigation of more interactions between mechanisms and would result in more accurate assessments of the failure probability. Also, other metamodeling methods than the Gaussian process regression, or other combinations of parameters, could be investigated.
7. Include the progression of failure. After sliding of a dike slope or erosion of the revetment has occurred, some properties of the dike change, e.g. the geometry or the saturation of the dike body. It would be interesting to investigate the impact of these interactions on other failure mechanisms or dike sections, which was not part of this study. Also including time dependence would improve the model.
8. For dike assessments, it is recommended to apply an integral model like this in situations with homogeneity along the trajectory. This is the case if there is strong evidence that geological deposits span large areas and if the dike geometry is homogeneous along the trajectory. In those situations, it is likely that the failure probabilities of different elements are similar and that spatial correlations exist. Considering these aspects can result in more realistic and less conservative assessments of the failure probability.

Bibliography

J.P. Aguilar López, J.J. Warmink, R.M.J. Schielen, and S.J.M. Hulscher. Flood defence design parameters correlation influence on failure probability – case study of backward erosion piping. In *3rd IAHR Europe Congress, Book of Proceedings*, number April, Porto, 2014. ISBN 9789899647923.

J.P. Aguilar-López, J.J. Warmink, R.M.J. Schielen, and S.J.M.H. Hulscher. Soil stochastic parameter correlation impact in the piping erosion failure estimation of riverine flood defences. *Structural Safety*, 60:117–129, 2016. ISSN 01674730. doi: 10.1016/j.strusafe.2016.01.004.

K. Bailey. Gaussian Processes for Dummies, 2019. URL https://katbailey.github.io/post/gaussian-processes-for-dummies/.

A. Broere and D. Knops. Voorverkenning Sprok-Sterreschans: Rapportage STBI & STBU. Technical report, Waterschap Rivierenland, Tiel, 2020.

A. Broere and W. Leeuwdrent. Voorverkenning Sprok-Sterreschans: Rapportage GEKB & GEBU. Technical report, Waterschap Rivierenland, Tiel, 2020.

B. Brookhuis and R. Beekx. Basisspecificatie Dijk, Versie 1.0. Technical report, Waterschap Rivierenland, Tiel, 2017.

R.P. Chapuis. Predicting the saturated hydraulic conductivity of soils: A review. *Bulletin of Engineering Geology and the Environment*, 71(3):401–434, aug 2012. ISSN 14359529. doi: 10.1007/s10064-012-0418-7.

H. Chbab and J. Groeneweg. Modelonzekerheid belastingen - Wettelijk Toetsinstrumentarium WTI-2017. Technical report, Deltares, 2015.

CUR and TAW. Probabilistic design of flood defences. Technical report, Gouda, 1990.

K. de Bruijn and M. van der Doef. Gevolgen van overstromingen-Informatie ten behoeve van het project Waterveiligheid in de 21e eeuw. Technical report, Deltares, 2011.

H. de Waal and A. van Hoven. Failure Mechanism Module Grass Wave Runup Zone Requirements and Functional Design. Technical report, Deltares, 2015.

J.P. de Waal. Basisrapport WBI 2017. Technical report, 2016.

J.P. de Waal and A. van Hoven. Failure Mechanism Module Grass Wave Impact Zone - Requirements and Functional Design. Technical report, Deltares, 2019.

Deltares. Complete WTI parameterlijst Aquo, 2016.

Deltares. R&D Highlights. Technical report, Deltares, Delft, 2020.

F.L.M. Diermanse and R. Jongejan. WBI - Onzekerheden. Technical report, Deltares, Delft, 2016.

F.L.M. Diermanse, K.L. Roscoe, J. Lopez de la Cruz, H. Steenbergen, and A.C.W.M. Vrouwenvelder. Hydra Ring - Scientific Documentation. Technical report, Deltares, Delft, 2013.

F.L.M. Diermanse, K.S. Lam, and H. Knoeff. Assemblageprotocol WBI2017. Technical report, Deltares, Delft, 2016.

M. Duits and B. Kuijper. Hydra-NL Systeemdocumentatie. Technical report, HKV, Rijkswaterstaat, 2019.

B. Echard, N. Gayton, and M. Lemaire. AK-MCS: An active learning reliability method combining Kriging and Monte Carlo Simulation. *Structural Safety*, 33(2):145–154, mar 2011. ISSN 01674730. doi: 10.1016/j.strusafe.2011.01.002.

ENW. Naar geloofwaardige overstromingskansen. Technical report, Expertise Netwerk Waterveiligheid, Utrecht, 2020.

C. Fonnesbeck. Fitting Gaussian Process Models in Python, 2017. URL https://blog.dominodatalab.com/fitting-gaussian-process-models-python/.

C. Geerse. Werkwijze uitintegreren onzekerheden basisstochasten voor Hydra-NL. Technical report, RWS-WVL, 2015.

C. Genest and A. C. Favre. Everything you always wanted to know about copula modeling but were afraid to ask. *Journal of Hydrologic Engineering*, 12(4):347–368, 2007. ISSN 10840699. doi: 10.1061/(ASCE)1084-0699(2007)12:4(347).

J. Görtler, R. Kehlbeck, and O. Deussen. A Visual Exploration of Gaussian Processes. *Distill*, 4(4): e17, apr 2019. ISSN 2476-0757. doi: 10.23915/distill.00017. URL https://distill.pub/2019/visual-exploration-gaussian-processes.

M. Hegnauer, J.J. Beersma, H.F.P. van den Boogaard, T.A. Buishand, and R.H. Passchier. Generator of Rainfall and Discharge Extremes (GRADE) for the Rhine and Meuse basins - Final report of GRADE 2.0. Technical report, Deltares, 2014.

M.P. Hijma and K.S. Lam. Globale stochastische ondergrondschematisatie (WTI-SOS) voor de primaire waterkeringen. Technical report, Deltares, 2015.

HWBP. Waterveiligheidsportaal Landelijk veiligheidsbeeld, 2021. URL https://waterveiligheidsportaal.nl.

R. Jongejan, B. Maaskant, W. Ter Horst, F. Havinga, N. Roode, and H. Stefess. The VNK2-project: A fully probabilistic risk analysis for all major levee systems in the Netherlands. *IAHS-AISH Publication*, 357:75–85, 2013. ISSN 01447815.

S.N. Jonkman, A.C.W.M Vrouwenvelder, R.D.J.M. Steenbergen, O. Morales-Nápoles, and J.K. Vrijling. *Probabilistic Design: Risk and Reliability Analysis in Civil Engineering, Lecture notes CIE4130*. Delft University of Technology, Delft, 3rd edition, 2017. ISBN 9780784412558.

S.N. Jonkman, R.E. Jorissen, T. Schweckendiek, and J.P. Van Den Bos. *Flood defences Lecture notes CIE5314*. Delft University of Technology, Delft, 3rd edition, 2018.

W. Kanning. *The Weakest Link - Spatial Variability in the Piping Failure Mechanism of Dikes*. Phd thesis, Delft University of Technology, 2012.

W. Kanning, M. Huber, M. van der Krogt, T. Schweckendiek, and A. Martins Teixeira. Derivation of the semi- probabilistic safety assessment rule for inner slope stability. Technical report, Deltares, 2015.

D. Kentrop. *A Metamodelling Approach to Reliability Updating with Dike Construction Survival*. Msc thesis, Delft University of Technology, 2021.

M. Klein Breteler, A. Capel, G. Kruse, G. Mourik, and D. Kaste. Erosie van een dijk na bezwijken van de steenzetting door golven. Technical report, 2012.

KNMI. Klimaat in de 21e eeuw - vier scenario's voor Nederland. Technical report, De Bilt, 2006.

M. Kok, R. Jongejan, M. Nieuwjaar, and I. Tánczos. *Grondslagen voor hoogwater-bescherming*. Ministerie van Infrastructuur en Milieu en het Expertise Netwerk Waterveiligheid, 2nd edition, 2017. ISBN 978-90-8902-151-9.

KPR. Factsheets Gebundeld. Technical report, Team Kennisplatform Risicobenadering (KPR), 2019.

D. Kristjanson Duvenaud. *Automatic Model Construction with Gaussian Processes Declaration*. Phd thesis, University of Cambrigde, 2014.

B. Kuijper, M.T. Duits, R.G. Kamp, and J.P. de Waal. Wave overtopping at dikes - kernel. Technical report, Deltares, 2017.

W. Leeuwendrent and G. van Zwol. Veiligheidsanalyse dijkversterking Sprok Heteren - Uitgangspunten. Technical report, Waterschap Rivierenland, Tiel, 2020.

F.H. Leferink. *Research into the application of undrained analysis with critical state soil mechanics approach for the design of a quay wall*. Msc thesis, Delft University of Technology, 2020.

S. Lerman. *Encyclopedia of Mathematics Education*. Springer, 2014. ISBN 978-94-007-4977-1. doi: 10.1007/978-94-007-4978-8.

X.X. Liu and I. Elishakoff. A combined Importance Sampling and active learning Kriging reliability method for small failure probability with random and correlated interval variables. *Structural Safety*, 82:101875, jan 2020. ISSN 01674730. doi: 10.1016/j.strusafe.2019.101875.

E. Marsden. Copula and multivariate dependencies, 2017.

MathWorks. *MATLAB Statistics and Machine Learning Toolbox™ User's Guide*. 11.7 edition, 2020. URL https://nl.mathworks.com/help/stats/copulas-generate-correlated-samples.html.

G.C. Mourik. Prediction of the erosion velocity of a slope of clay due to wave attack – WTI2017. Technical report, Deltares, 2015.

K.P. Murphy. *Machine Learning A Probabilistic Perspective*. MIT Press, Massachusetts, 2nd edition, 2021. ISBN 9780262018029.

F. Pedregosa, G. Varoquaux, Al. Gramfort, Vi. Michel, B. Thirion, O. Grisel, M. Blondel, P. Prettenhofer, R. Weiss, V. Dubourg, J. Vanderplas, A. Passos, D. Cournapeau, M. Brucher, M. Perrot, and É. Duchesnay. Scikit-learn: Machine Learning in Python. Technical Report 85, 2011. URL http://scikit-learn.sourceforge.net.

G. Pleijter, B. Maaskant, R. Daggenvoorde, and G. Rongen. Hydraulische Randvoorwaarden Waal t.b.v. HWBP Projecten. Technical report, Waterschap Rivierenland & HKV, 2017.

T. Pullen, N.W.H. Allsop, T. Bruce, A. Kortenhaus, H. Schüttrumpf, and J.W. van der Meer. EurOtop - Wave overtopping of sea defences and related structures: Assessment manual. Technical report, 2007.

C.E. Rasmussen and C.K.I. Williams. *Gaussian Processes for Machine Learning*. The MIT Press, Massachusetts, 2006. ISBN 026218253X.

Rijkswaterstaat. Schematiseringshandleiding microstabiliteit (WBI 2017). Technical Report december 2016, Ministerie van Infrastructuur en Milieu, 2016.

Rijkswaterstaat. Regeling veiligheid primaire waterkeringen 2017 - Bijlage III Sterkte en veiligheid. Technical Report april 2016, Ministerie van Infrastructuur en Milieu, 2017.

Rijkswaterstaat. Schematiseringshandleiding macrostabiliteit. Technical Report november, Ministerie van Infrastructuur en Waterstaat, 2019a.

Rijkswaterstaat. Schematiseringshandleiding Hoogte. Technical report, Ministerie van Infrastructuur en Waterstaat, 2019b.

Risk Engineering. Copula methods: Modelling correlation between risks, 2017. URL https://risk-engineering.org/copula-multivariate-dependencies/.

G. Rongen. MEMO Probabilistische bekledingberekeningen. Technical report, HKV, 2020.

G. Rongen, J. Stenfert, G. Depuits, and C.M. Barbosa. Time dependent loads on revetments. Technical report, HKV & Deltares, 2019.

G. Rongen, M. Huis In 't Veld, and G. Dupuits. Time dependent loads on grass revetments. Technical report, HKV, 2020.

T. Schweckendiek, M. van der Krogt, B. Rijneveld, and A. Martins Teixeira. Handreiking Faalkansanalyse Macrostabiliteit - Groene Versie. Technical report, Deltares, Delft, 2017.

T.D.Y.F. Simanjuntak, H.L. Bakker, M. De Koning, D.G. Goeman, J.K. Haasnoot, and C. Bisschop. Macro-stability assessment of dikes using two different probabilistic models Évaluation de la macro-stabilité des digues à l'aide de deux modèles probabilistes différents. *ECSMGE 2019*, 2019. doi: 10.32075/17ECSMGE-2019-0058.

B. Strijker, J. Stijnen, C. Geerse, and L. Lokin. BIG5 - Modelonzekerheid in waterstanden. Technical report, HKV, 2020.

R. 't Hart, H. de Bruijn, and G. de Vries. Fenomenologische beschrijving. page 208, 2016.

TAW. Technisch rapport golfoploop en golfoverslag bij dijken. Technical report, Technische Adviescommissie voor de Waterkeringen (TAW), Delft, 2002.

TAW. *Technisch Rapport Waterspanningen bij dijken*. Number september. 2004. ISBN 9036955653.

B. Thonus. Memo Lengte-effect. Technical report, HKV, 2003.

TNO. Detaillering van de bovenste lagen met GeoTOP, 2020. URL https://www.dinoloket.nl/detaillering-van-de-bovenste-lagen-met-geotop.

W. van Balen, K. Wojciechowska, F. Diermanse, T. Vrouwenvelder, H. Steenbergen, J. Lopez de la Cruz, and K. Roscoe. Hydra-Ring: Technical Reference Manual. Technical report, Deltares, Delft, 2016.

J. Van Der Meer and T. Bruce. New Physical Insights and Design Formulas on Wave Overtopping at Sloping and Vertical Structures. *Journal of Waterways, Port, Coastal and Ocean Engineering*, 140 (6), nov 2014. doi: 10.1061/(ASCE)WW.1943-5460.0000221.

R. van der Meij. D-Stability: User Manual. Technical report, Deltares, 2019.

A. van Hoven. Schematiseringshandleiding grasbekleding. Technical Report november, Ministerie van Infrastructuur en Waterstaat, 2019.

E. van Meijgaard, L.H. van Ulft, W.J. van de Berg, F.C. Bosveld, B.J.J.M. van den Hurk, G. Lenderink, and A.P. Siebesma. The KNMI regional atmospheric climate model RACMO version 2.1. Technical report, KNMI, De Bilt, 2008.

S. Vorogushyn, B. Merz, and H. Apel. Development of dike fragility curves for piping and micro-instability breach mechanisms. *Natural Hazards and Earth System Sciences*, 9(4):1383–1401, aug 2009. ISSN 1684-9981. doi: 10.5194/nhess-9-1383-2009.

T. Vrouwenvelder. Spatial effects in reliability analysis of flood protection systems. *Proceedings of 2nd International Forum on Engineering Decision Making*, pages 1–12, 2006.

Y. Wang and O.V. Akeju. Quantifying the cross-correlation between effective cohesion and friction angle of soil from limited site-specific data. *Soils and Foundations*, 56(6):1055–1070, dec 2016. ISSN 00380806. doi: 10.1016/j.sandf.2016.11.009.

Waterschap Rivierenland. Bijlage 2 - proevenverzameling Waal - Samenvatting. Technical report, 2018.

A

Reliability Theory

A.1. Reliability Index

If the limit state function Z only depends on two independent variables, r and s, it holds that:

$$f_{RS}(r,s) = f_R(r) \cdot f_S(s) \tag{A.1}$$

where f_{RS} is the joint probability density function. This can be illustrated as shown in Figure 2.1 on page 8. If R and S are independent normally distributed random variables, then also Z is normally distributed with:

$$\mu_Z = \mu_R - \mu_S, \qquad \sigma_Z = \sqrt{\sigma_R^2 + \sigma_S^2} \tag{A.2}$$

where μ denotes the mean value and σ the standard deviation. X_i are the variables of R and S. In general, μ_Z is positive, because otherwise failure would even occur under 'normal' conditions (van Balen et al., 2016). Subsequently:

$$P_f = P[Z < 0] = \Phi\left[\frac{0 - \mu_Z}{\sigma_Z}\right] = \Phi(-\beta) = 1 - \Phi(\beta) \tag{A.3}$$

or

$$\beta = \Phi^{-1}(1 - P(Z < 0)) \tag{A.4}$$

where Φ denotes the standard normal distribution function. β is the reliability index, which is defined as the distance between μ_Z and $Z = 0$ in σ_Z units. For example, if $\beta = 4$, failure occurs if a random sample of Z is more than $4 \cdot \sigma_Z$ lower than the mean. The reliability index is a measure for the probability of failure of a system and is often defined for a given time period. Note that if β is defined as μ_Z/σ_Z, Equation A.3 does not necessarily hold if Z is not normally distributed. However, often β is computed directly from Equation A.4 in which case it is an exact representative of the failure probability by definition (van Balen et al., 2016). If β is small, it indicates a large probability of failure. In other words, it can be said that larger values of β indicate that more extreme events are required for failure to occur, meaning a lower probability of failure and a larger reliability of the system.

Note that most of the equations above only hold for linear Z-functions and for independent input variables that are normally distributed.

A.2. Covariance

An important property in the definition of dependence is the *covariance*:

$$\mathrm{cov}(XY) = E\{(X - \mu_X)(Y - \mu_Y)\} = E(XY - \mu_X Y - X\mu_Y + \mu_X\mu_Y) = E(XY) = \mu_X\mu_Y \tag{A.5}$$

where μ_i are the mean values of X and Y and $E(XY)$ is the expectation or mean of XY.

The covariance matrix, often denoted as Σ, models the variance along each dimension and determines how the different random variables are correlated. The covariance matrix is always square, symmetric and positive semi-definite (Lerman, 2014). The diagonal of Σ consists of the variance σ_i^2 of the i-th

random variable. And the off-diagonal elements σ_{ij} describe the covariance or correlation between the i-th and j-th random variable.

$$\Sigma = \mathrm{Cov}\left(X_i, X_j\right) = E\left[\left(X_i - \mu_i\right)\left(X_j - \mu_j\right)^T\right] \tag{A.6}$$

There are a number of additional rules that further restrict the patterns of permissible values among their elements. The numbers on the diagonal (the variance) must all be positive. The values on the diagonal restrict the range of possible off-diagonal values: Covariance coefficients σ_{ij} must not be greater in absolute value than $(\sigma_i^2\sigma_j^2)^{1/2}$. Or equivalently, correlations must fall into the range between -1 and 1.

The admissible range of a correlation between variables i and j is codetermined by the correlations of all other variables with i and j. The triangular inequality condition restricts the range of permissible values for the correlation of variables i and j to fall between the two limiting values:

$$\cos[\arccos(\rho_{ik}) - \arccos(\rho_{jk})] \tag{A.7}$$

and

$$\cos[\arccos(\rho_{ik}) + \arccos(\rho_{jk})] \tag{A.8}$$

where the index k stands for any arbitrary third variable in the same correlation matrix. In larger matrices there are additional, higher-order rules. For instance, the two ranges implied for the correlation between i and j by a third variable k and a fourth variable l must have a common non-empty intersection.

A.3. Joint Distribution Functions and Copulas

Joint probability distributions are defined as:

$$f(x,y) = P(X = x, Y = y) \tag{A.9}$$

representing the probability that events x and y occur at the same time. The Cumulative Distribution Function (CDF) for a joint probability distribution is given by:

$$F_{XY}(x,y) = Pr(X \leq x, Y \leq y) \tag{A.10}$$

Each of the random variables in X can be transformed to independent standard normal variables $U = (U_1, \ldots U_n)$. If all the X-variables are mutually independent, this transformation can be described as follows:

$$\Phi\left(u_i\right) = F_i\left(x_i\right) \Rightarrow u_i = \Phi^{-1}\left[F_i\left(x_i\right)\right] \Rightarrow x_i = F_i^{-1}\left(\Phi\left(u_i\right)\right) \tag{A.11}$$

where:

- Φ = Standard normal distribution function
- F_i = Distribution function (CDF) of x_i, the i-th variable in X
- u_i = Realisation of the i-th variable in U, corresponding to the i-th variable in X

In any multivariate normal distribution it holds that each underlying random variable is distributed normally and that their (conditional) joint distributions are also normal.

A.3.1. Copulas

To get a feeling for the dependence between variables X and Y, it is traditional to look at the scatter plot of the pairs (X_1, Y_1),...,(X_n, Y_n). However, the pair of ranks (R_1, S_1),...,(R_n, S_n) associated with the sample (X, Y) contain a greater amount of information and are therefore an important ingredient in the application of copulas. R_i stands for the rank of X_i among X_1,...,X_n and S_i stands for the rank of Y_i among Y_1,...,Y_n.

The probability that $X < x$ and $Y < y$ can be expressed by the CDF:

$$Pr(X < x \,\mathrm{AND}\, Y < y) = F_{XY}(x,y) = t \quad with \quad t \in (0,1) \tag{A.12}$$

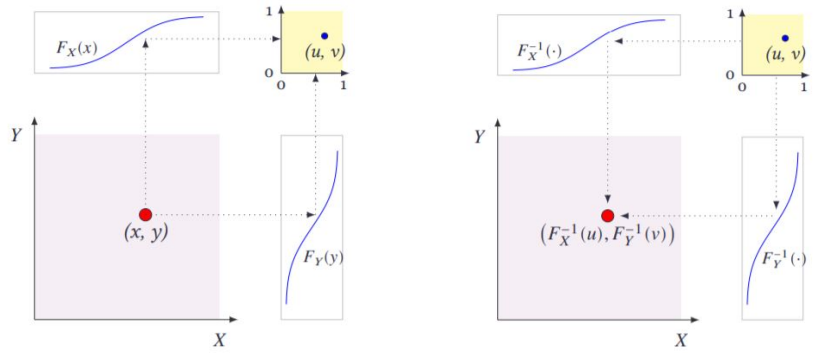

(a) From (x, y) to (u, v).

(b) from (u, v) back to (x, y).

Figure A.1: Illustration of the transformations within the concept of copulas (Marsden, 2017).

We can use the marginal CDF's to map from (x, y) to a point (u, v) on the unit square. Conversely we can use the marginal inverse CDF's to map from (u, v) to $(F_X^{-1}(u), F_Y^{-1}(v))$. So, it also holds that:

$$F_{XY}(x, y) = F_{XY}(F_X^{-1}(u), F_Y^{-1}(v)) = C(u, v) = t \tag{A.13}$$

with $u = F_X(x)$ and $v = F_Y(y)$, meaning that the copula function lets us map directly from the unit square to the joint distribution. It lets us express the joint probability as a function of the marginal distributions.

We can generate random points on $[0, 1]^2$ using the copula function random generator. Then, we can use the inverse CDF's to generate points in the space of the real variables. The joint distribution of these points has marginals F_X and F_Y, with the required dependency structure.

By definition, applying the normal cumulative distribution function (CDF), denoted by Φ, to a standard normal random variable results in a random variable that is uniform on the interval $[0, 1]$. To see this, if Z has a standard normal distribution, then the CDF of $U = \Phi(Z)$ is:

$$Pr\{U \leq u\} = Pr\{\Phi(Z) \leq u\} = Pr\{Z \leq \Phi^{-1}(u)\} = u \tag{A.14}$$

which is the CDF of a $U(0, 1)$-random variable. Applying the inverse CDF of any distribution F to a $U(0, 1)$-random variable results in a random variable whose distribution is exactly F. This two-step transformation can be applied to each variable of a standard bivariate normal, resulting in dependent random variables with arbitrary marginal distributions. Since the transformation works on each component separately, the two resulting random variables are not required to have the same marginal distributions.

The correlation parameter ρ of the underlying bivariate normal determines the dependence between X_1 and X_2 in this construction. However, in more general cases such as the combination of a Gamma and a t marginal distribution, the linear correlation between X_1 and X_2 is difficult or impossible to express in terms of ρ. That is because the linear correlation coefficient expresses the linear dependence between random variables. However, if nonlinear transformations are applied to those random variables, linear correlation is not preserved. In that case, a rank correlation coefficient, such as Kendall's τ or Spearman's ρ, is more suitable (MathWorks, 2020). Simply said, these rank correlations measure the degree to which large or small values of one random variable associate with large or small values of another. Unlike the linear correlation coefficient, they measure the dependence only in terms of ranks. As a result, the rank correlation is preserved under any monotonic transformation. So, knowing the rank correlation of the bivariate normal Z exactly determines the rank correlation of the final transformed random variables X. Still, the linear correlation coefficient ρ is required to parametrise the underlying bivariate normal. At the same time, Kendall's τ and Spearman's ρ are more useful for describing the dependence between random variables, since they are invariant to the choice of marginal distribution. For the bivariate normal, there is a simple one-to-one mapping between Kendall's τ or Spearman's ρ, and the linear correlation coefficient ρ:

$$\tau = \frac{2}{\pi}\arcsin(\rho) \quad \text{or} \quad \rho = \sin\left(\tau\frac{\pi}{2}\right)$$
$$\rho_s = \frac{6}{\pi}\arcsin\left(\frac{\rho}{2}\right) \text{ or } \rho = 2\sin\left(\rho_s\frac{\pi}{6}\right) \tag{A.15}$$

Therefore, by choosing the correct ρ parameter value for the linear correlation between Z_1 and Z_2, it is not difficult to create the desired rank correlation between X_1 and X_2, regardless of their marginal distributions.

The concept described above is known as the bivariate Gaussian copula. A copula is a multivariate probability distribution, where each random variable has a uniform marginal distribution on the unit interval $[0, 1]$. These random variables may be completely independent, deterministically related, or anything in between (MathWorks, 2020). A copula can be used to construct a new multivariate distribution for dependent variables, in the case of dependence among variables. Each variable is transformed separately, possibly using different CDF's. This enables that arbitrary marginal distributions are possible. Such multivariate distributions are often useful in simulations, where the different random inputs are not independent of each other.

A.4. System Reliability

A dike trajectory is a series system for which the failure probability is determined by combining the different failure mechanisms and dike sections. This has already been visualised by a fault tree in Figure 1.2. The general formulation of the failure probability for a series system, consisting of m components is:

$$P_f = P\left[Z_1(u_{11},...,u_{1n}) < 0 \cup ... \cup Z_m(u_{m1},...,u_{mn}) < 0\right] = P\left[\bigcup_{i=1}^{m} Z_i(u_{i1},...,u_{in}) < 0\right] \tag{A.16}$$

in which u_{ij} is the j^{th} variable of the Z-function of the i^{th} component. For different components i and k, the j^{th} random variables (i.e. u_{ij} and u_{kj}) in principle refer to the same load or strength variable, but the sampled values can be different because they refer to different components. For instance, the j^{th} variable may refer to the thickness of a clay layer. This thickness will be different for different dike segments.

The system failure probability can easily be computed as long as the components are either mutually exclusive, independent or fully dependent (i.e. $\rho = 0$ or $\rho = \pm 1$), as shown in Table A.1. For other cases and values of the correlation coefficient ρ, the failure probability will be between the upper and lower bound and the calculation is very challenging. Different approaches are possible though, for example the Hohenbichler method.

Table A.1: System reliability for generic cases (Jonkman et al., 2017).

System	Gate	Operator	Components		
			Mutually exclusive	Independent	Fully dependent
series		$\bigcup$	$\sum_{i=1}^{n} P_i$ (upper bound)	$1 - \prod_{i=1}^{n}(1 - P_i)$	$\max\{P_i\}$ (lower bound)
parallel		$\bigcap$	0 (lower bound)	$\prod_{i=1}^{n} P_i$	$\min\{P_i\}$ (upper bound)

B

Failure Mechanisms

B.1. Macrostability: Sliding of the Outer Slope

Macro-instability can, under certain circumstances, also occur on the river/sea side of a dike. This failure mechanism generally does not occur during normative circumstances, as it most likely occurs *after* a flood event or heavy rainfall, that is assumed to be independent of a flood event. Thus, the water retaining function of the dike is not directly endangered, which makes outer slope macrostability an indirect failure mechanism (’t Hart et al., 2016).

This failure mechanism is very much alike macrostability of the inner slope. Just like inner slope instability, also outer slope instability is caused by a loss of equilibrium of a soil body. This loss of equilibrium can be caused by an increase of the pore pressures in the soil, resulting in a decrease of the shear strength. High water pressures in the dike are again the result of a high (river) water level, of heavy rainfall or of deformations. During a flood event, the high water level on the outer side of the dike provides a counteracting moment, which ensures that the equilibrium can often be preserved, even though the pore pressures may be high. The stability of the outer slope is only at risk if the outer water level decreases so rapidly, that the phreatic line in the dike does not have enough time to follow. The shear strength of the saturated soil is very small and the weight is large, while the stabilising effect of the outer water level has disappeared. Consequently, the outer slope can slide, following a straight or circular slip plane. Since this mechanism mostly occurs after a flood event, it is assumed that there should almost always be enough time to repair the damage before the next event. Macro-instability of the outer slope is largely dependent on the same parameters as for inner slope stability: The most important factors are dike geometry, the pore pressures and the structure of the subsoil (’t Hart et al., 2016).

In a correct assessment of the probability of flooding due to sliding of the outer slope, the correlation between (extreme) rain events and (high) water levels should be included. Moreover, the probability distribution of the time interval between two flood events - or the conditional probability of occurrence of a second flood event given that a first flood event has occurred shortly before - should be accounted for. Furthermore, the probability of flooding due to sliding of the outer slope is very dependent of the location of the entry point of the slip plane and of the residual strength of the dike. For example, if this entry point is located in the crest, then there will still be a part of the dike body that remains. If and when flooding will occur then, depends on any subsequent slidings and on the erosion speed of the remaining dike body. Since a revetment is not present any more after sliding, this can go very fast for dikes with a sandy core. This mechanism again depends on the water level and wave load after sliding has occurred. The probability of subsequent sliding is smaller for the outer slope than for the inner slope, since the residual dike profile is on the land side and thus less saturated as for the situation where sliding occurs at the inner slope and the rest profile is on the water side (’t Hart et al., 2016). If the crest height is reduced as a result of sliding and the water level is sufficiently high, overflow will occur, leading to more erosion and possibly inundation of the hinterland.

B.2. Microstability

Micro-instability concerns the loss of stability of soil layers with a very limited thickness at the surface of the inner slope, caused by ground water seepage through the soil body. Micro-instability manifests itself for example as wash out of core material of sandy dikes or as instability of the clayey top layer at the inner slope. In the case of dikes, this phenomenon usually occurs in the lower section of the inner slope during or shortly after high water levels. The area over which the groundwater emerges from the dike is called the seepage area CUR and TAW (1990). For micro-instability to occur, the phreatic surface, an imaginary line or surface that bounds a saturated zone from above, has to reach the inner slope and seepage flow has to develop. Under normal circumstances, the phreatic level lies below the toe level. As a result of high outer water levels and infiltration in the run-up zone, the phreatic surface will rise. The course of the rise and the final height of the phreatic surface below the inner slope is dependent on several factors (Rijkswaterstaat, 2016):

- The elevation of the phreatic surface before the flood event
- The course of the high water levels and waves in time during the event and the total duration.
- The permeability of the outer slope revetment. If this layer is poorly permeable (e.g. an asphalt revetment or a very thick clay layer), water cannot easily enter the dike core, leading to a very limited rise of the phreatic level.
- The core material, concerning the storage capacity and the permeability of the soil. For clayey dikes (i.e. cohesive soil) problems related to micro-instability rarely occur. For dikes with a permeable revetment and a sandy core (i.e. low cohesion), the phreatic line can easily rise, such that the exit point may reaches the inner slope.

Whether micro-instability will lead to problems, also depends on the steepness and material of the inner slope. The exit point of the phreatic line determines the height at which the slope failure starts, if the effective weight and force exerted by the flow exceed the resisting shear stress. A hole will develop at the inner slope of the dike. If the phreatic line remains high, more grains will be washed out and more slidings will occur, leading to growth of the hole. It is assumed that the gap can grow so far that the inner slope (and crest) will be undermined, such that that a large part of the slope will slide. If the failure profile is high enough to damage the dike crest, it is assumed that it can lead to dike failure (Vorogushyn et al., 2009). This process is illustrated in Figure B.1.

In view of the small-scale character of the phenomenon (washing-out of small soil elements) it is common to consider not the equilibrium of moments like for macrostability, but the equilibrium of forces parallel to the slope. In the report by CUR and TAW (1990), several limit state functions are described: one for groundwater flowing out of a slope above the water level and one for groundwater flowing out of a slope below the water level. If the limit state of micro-instability is exceeded, this will not necessarily lead at once to loss of the water-retaining function of the dike. For slopes above the water level it is possible to make an approximate estimate of the damage profile based on assumptions (CUR and TAW, 1990). The dike is assumed to collapse if so much material is moved from the inner slope to the toe that the crest of the dike is affected. As shown in Figure B.2, this means that the level of point A attains the crest level h_o. The reliability function for failure is:

$$Z_{micro} = h_o - h_a \tag{B.1}$$

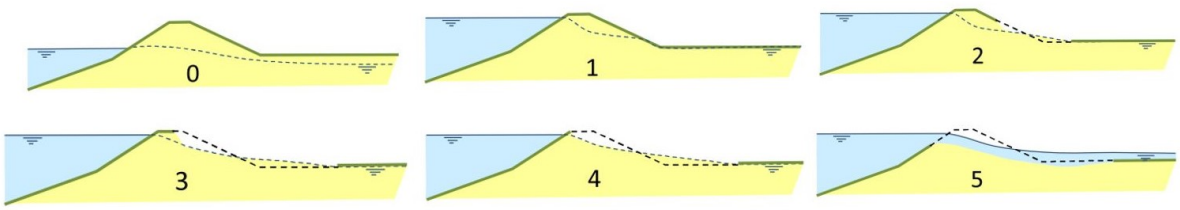

Figure B.1: Schematic overview of the process leading to dike failure due to micro-instability ('t Hart et al., 2016).

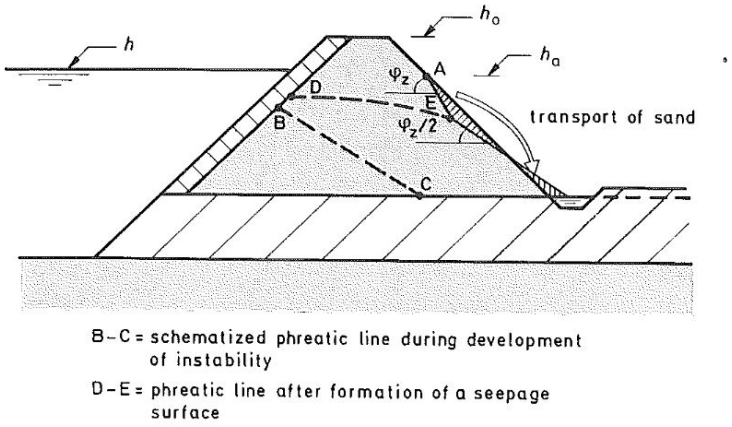

Figure B.2: Mechanism of micro-instabillity of the inner slope (CUR and TAW, 1990).

Flooding due to only micro-instability has never been observed ('t Hart et al., 2016). However, micro-instability does have an influence on the occurrence of other failure mechanisms or can lead to failure in combination with other mechanisms. The stability of the inner slope is affected by micro-instability and the combination of overtopping, overflow and micro-stability will most likely result in dike failure. On the other hand, erosion or sliding of the outer slope can enhance the process of micro-instability. There is no relation between micro-instability and piping. To assess microstability in a realistic way, these interactions between failure mechanisms should be taken into account.

Micro-instability is often confused with instability as a result of infiltration and erosion due to overtopping. The difference, however, is that micro-instability concerns seepage through the dike and water that flows from inside outwards, while for infiltration due to overtopping the water flows is from outside inwards. Besides infiltration, some water will flow down the inner slope, resulting in erosion. Moreover, water will seep through the dike during overtopping, as it also occurs during micro-instability.

If there is a significant amount of wave overtoping, the failure mechanism *Sliding of the grass revetment at the inner slope* (GABI) will be normative, above the failure mechanism *Micro-instability* (STMI). If there is however no significant overtopping, the mechanism micro-instability is normative above GABI. The limit value for significant overtopping is $0.1\ L/s/m$. If the overtopping rate is larger than this limit value, micro-instability is not considered ('t Hart et al., 2016).

B.3. Sliding of the Grass Revetment at the Outer Slope

The grass revetment concerns the grass, including the clay layer underneath, that lies on a sand layer or sand core. If the grass revetment lies directly on a clay core, sliding of the grass revetment cannot occur ('t Hart et al., 2016). The mechanism regards the loss of stability of the revetment. If the pressure difference over the clay layer is too large, the revetment can undergo uplifting, sliding or a combination of the two.

The critical situation for the stability of the revetment on the outer slope most likely occurs during extreme conditions of a high water level and high waves. A high phreatic line in the sand underneath the clay layer leads to high outward directed pressures on the clay layer. During the moment of wave run-down, the inward directed pressure on the outer slope is small. Consequently, there is an outward directed resulting force on that part of the clay layer. Where the run-down is maximum, the effective stress on the interface between clay and sand layer will be reduced such that loss of stability of the clay layer can occur. Sliding of the outer revetment can only occur if the phreatic surface in the sand core lies sufficiently high. This can happen for several reasons: if relatively permeable locations are present in the revetment or if the sand body is relatively small. It can also happen if drainage of the sand core is insufficient under normal conditions, in combination with a prolonged rainy period. Another important factor for sliding of the outer revetment to occur is the wave height. The larger the wave height, the more unfavourable the situation.

Whether sliding or uplift occurs depends on the strength, thickness and weight of the clay layer, the pressure distribution over the clay layer and the slope. Moreover, it is possible that the clay layer bursts open if the pressure is too high. This will lead to progressive erosion. The same will happen after a part of the revetments has slided. Note that the flood safety is only endangered in the case that sliding occurs during a flood event.

B.4. Sliding of the Grass Revetment at the Inner Slope

Just like sliding of the grass revetment on the outer slope, this failure mechanism concerns the loss of stability. Infiltration due to wave overtopping and due to a high outer water level leads to an increase of the pore pressures underneath the inner slope. As a result of the large pressure difference over the revetment, it can lift up, slide or a combination of the two can happen. Furthermore, sand might washes out, caused by an outward directed gradient of water flowing out of the dike. Further erosion can result in progressive erosion of the dike core and eventually a dike breach. The increase of the pore pressure depends on the course of the water level in time during an extreme event, the duration, the amount and intensity of wave overtopping and the permeability of the revetment. Furthermore, it depends a lot on the type of dike, clay vs. sandy core.

As mentioned already in Appendix B.2, the mechanism is closely related to micro-instability. The difference is that sliding of the grass revetment at the inner slope is caused by wave overtopping (as well as seepage through the core). The stability problems are the same for the two mechanisms, but the cause is different.

B.5. Time Dependent Loads on Revetments

The purpose of the prototype is to give insight into the sensitivity of the most important parameters for the evaluation of grass revetments under time varying hydraulic loads. The erosion model for a sand and clay dike core from Kaste and Klein Breteler (2015) is adopted in the prototype to incorporate the residual strength. Combined with a probabilistic and time-varying approach of loads it is possible to obtain a flooding probability for dike erosion (Rongen et al., 2019). The prototype has been tested with a large number of time dependent and realistic load patterns from GRADE and RACMO.

In an follow-up study of the prototype ((Rongen et al., 2020)), it has been researched what time aspects of the hydraulic loads are relevant for revetment strength, by simulating a high number of storms on several dikes. The assessments led to smaller failure probabilities than by the WBI method. The method by Rongen et al. (2020) to define the loads was as follows: The first step is selecting a representative set of storms from ECMWF data. All storms with a peak above a certain surge or a certain wind speed are selected. To calculate a failure probability, every storm condition must also be assigned a probability. Storms are then grouped to reduce the number of storms to around 1000. After this, the storms are combined with river discharges. Nine levels discharge are chosen for the discharge at Lobith. The course of the discharge wave is not included. The momentary probability of a discharge is used to determine the probability of a discharge being within a certain range, at any moment. These can be calculated with Hydra-NL. With these boundary conditions, the SOBEK-RE simulations are done. Each of the roughly 1000 storms was simulated with each of the 9 discharge levels. These result in water levels, which are combined with wind data to form the boundary conditions for the dikes.

This prototype consists of 4 separate kernels, each describing a different physical processes:

- Wave impact: a Python model based on de Waal and van Hoven, 2019.
- Wave run-up: a Python model (Python) based on de Waal and van Hoven, 2015. The `dllLeveesOvertopping64.dll` is used for calculating the run-up height.
- Residual strength: a Python erosion model based on Kaste and Klein Breteler, 2015. It simulates the dike profile after the revetment has failed due to impact or run-up.
- Overtopping and overflow, calculated with `dllLeveesOvertopping64.dll` and `CombOverloopOverslag64.dll` respectively. Overtopping is calculated for the current profile, meaning that the profile is updated during erosion of the dike body.

In the model, the revetment is divided into segments, for example with a height of 0.5 m. Per segment, the cumulative load is calculated over time. When the critical cumulative load is reached at one of the segments, the outer revetment has failed and erosion will occur. The cumulative load depends on the load from wave run-up and wave impact. The threshold value for the deterioration depends on the state of the revetment: closed or open turf (RWS, 2018). Three types of load input can be used in the prototype:

1. A time series with at each time step the water level, wind speed and wind direction. The Bretschneider equations are used to convert the input values to the wave height and period.
2. A time series of wave conditions. This should contain at least water level, significant wave height, wave direction and one or both of the peak period and spectral period. When only one period is given, the other is calculated form the present one: $T_p = 1.1 \cdot T_{m-1,0}$ and vice versa.
3. Constant values of: wave height, wave period, wave direction, duration of storm and the time step. This last option is useful for test purposes.

B.6. WBI 2017 Procedure

In the WBI, the failure mechanisms are assessed by different assessment tracks. An assessment track is the way in which a mechanism is assessed. The assessment tracks can be subdivided into five groups, based on the available computation methods and whether they are related to direct or indirect mechanisms (Rijkswaterstaat, 2017). The following four groups are relevant for dikes:

1. Group 1: The detailed assessment per section is executed by a probabilistic analysis.
2. Group 2: Assessment tracks for which the detailed assessment per section is executed by a semi-probabilistic analysis, which is translated to a distance to the norm by extrapolation.
3. Group 3: The detailed assessment per section is semi-probabilistic. The safety coefficients have been derived anew for the WBI 2017. Separate computations are needed to find the distance to the norm.
4. Group 4: No probabilistic or semi-probabilistic computation with new safety coefficients is available. These assessment tracks have not been modified with respect to the former assessment method or a detailed assessment is not available.

For group 1, the failure probability per section is the result of a computation. For the other groups however, the result is an approximation of the failure probability (Rijkswaterstaat, 2017). A summary of the assessment method per failure mechanisms, and their codes in the WBI, are given in Table B.1.

Table B.1: Assessment tracks or failure mechanisms within WBI 2017.

Assessment tracks for dikes	Code	Group	Reliability method
Macro stability (sliding inner slope)	STBI	2	semi-prob.
Macro stability (sliding outer slope)	STBU	4	det. / semi-prob. old
Internal erosion / piping	STPH	2	semi-prob.
Micro stability	STMI	4	det. / semi-prob. old
Wave impact on asphalt revetment	AGK	3	semi-prob.
Water overpressure for asphalt revetment	AWO	4	det. / semi-prob. old
Erosion grass revetment outer slope	GEBU	3	semi-prob.
Sliding grass revetment outer slope	GABU	4	det. / semi-prob. old
Erosion grass revetment crest and inner slope	GEKB	1	probabilistic
Sliding grass revetment inner slope	GABI	4	det. / semi-prob. old
Stability of stone revetment	ZST	3	semi-prob.

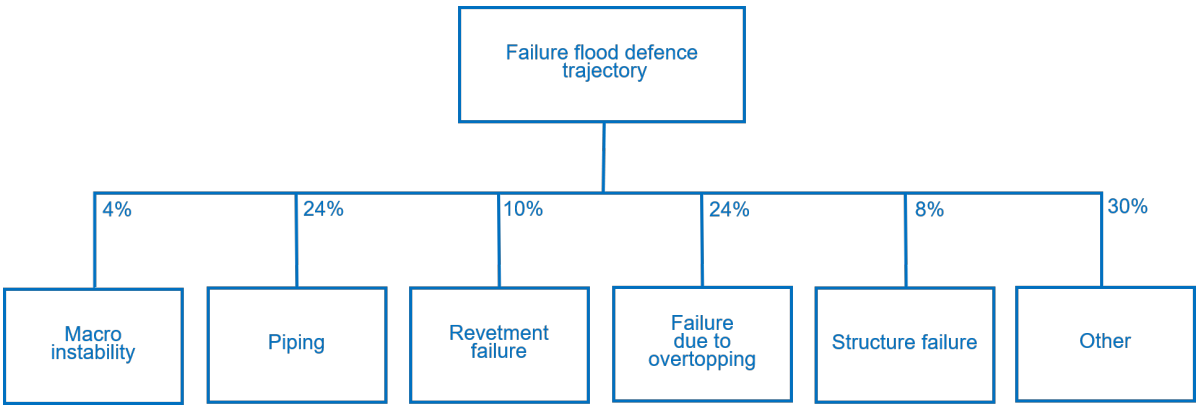

Figure B.3: Distribution of the probability of failure over the different mechanisms ('Faalkansbegroting').

B.6.1. Failure probability distribution

The target failure probability is distributed over the failure mechanisms by default values for their maximum contribution ω_j ('faalkansruimtefactor'). The target probability per failure mode ($\omega_j \cdot P_{req}$) accounts for the fact that each failure mode can lead to system failure. The default values of the maximum contributions per failure mechanism (ω_j) are based on the conservative assumption that the failure mechanisms are statistically independent - or strictly speaking mutually exclusive - implying that the sum of these contributions should be smaller or equal to one ($\sum \omega_j \leq 1$). In this way it is ensured that if the failure mechanisms satisfy their individual target probabilities, also the system target probability is met with certainty (Jonkman et al., 2018). The default values of ω_j are illustrated in Figure B.3 (Rijkswaterstaat, 2017).

B.6.2. The length-effect

The next step is to divide the target failure probability per mechanism over the corresponding dike sections. For this, the length-effect should be taken into account, by introducting the length-effect factor N_j. The length-effect basically means that a failure probability increases with the length of the flood defence system. In other words, the probability that failure occurs at any location is larger than the probability that failure occurs at one specific location. In practice, this uncertainty mainly arises from the fact that measurements are not available for every location continuously. Because of this, it is never exactly known in practice where the weakest spot is located and how weak this spot is exactly. The longer the dike, the larger the probability of occurrence of a weak spot. The length-effect also arises from the spatial variability of the load and resistance parameters (KPR, 2019). The length-effect is relatively small for failure mechanisms with a high level of dependence (correlation), such as overtopping. N_j will be in the order of 1 or 2. The effect is larger for failure mechanisms that behave more independently, like stability or piping. For these failure mechanisms, the additive effect of individual sectional failure probabilities on trajectory reliability is stronger. N will be more in the order of 10 to 100. The exact values can be determined consulting the WBI 2017 documents.

The subdivision method for the norm can be summarised by the following formula:

$$P_{req,i,j} = \frac{\omega_j}{N_j} \cdot P_{req} \tag{B.2}$$

where P_{req} denotes the annual norm of a trajectory and $P_{req,i,j}$ the target reliability for section i and failure mechanism j $[1/year]$.

C

Metamodeling

C.1. Kriging and ERRAGA

Kriging has been developed for geostatistics by Krige and then by Matheron in the fifties and sixties. Kriging is an exact interpolation method, meaning that the prediction in a point belonging to the experimental data is the exact value of the performance function in this point. Also, Kriging provides not only predicted values in any point, but also estimations of the local variance of the predictions. This variance defines the local uncertainty on the prediction and is called the Kriging variance. It is understood in the way that the higher the variance, the less certain the prediction. Echard et al. (2011) have proposed a promising surrogate modelling method called Active learning Kriging based Monte Carlo simulation (AK-MCS), that has shown to be an efficient way of approximating failure probabilities. It consists of an Active learning reliability method combining Kriging and Monte Carlo simulation. Active learning means that an iterative process is used in which the training set is updated by adding a new point to the training data set, where this point is being selected based on its expected improvement on the Kriging model. This decreases the uncertainty of the model, especially in the region of interest (i.e. region near the limit state). The process is repeated until a chosen convergence criterion is met. The metamodel is used in a Monte Carlo simulation to determine the system response of interest.

Recently, a two stage AK-MCS metamodel has been developed by Deltares for modelling noisy and incomplete models, called ERRAGA. A model is incomplete if it does not return an answer for some combinations of input parameters. The first stage of the two-stage model is therefore used for classification. It estimates whether a combination of parameters is feasible or not. The feasible ones proceed to the second stage, where the model response is determined by the surrogate model. The two-stage approach allows the model to be used in a reliability updating context, in which one of the stages would be used for identifying consistency with the observation. This way the failure probability given consistency can be determined (Kentrop, 2021).

C.2. Gaussian Process Regression

A common applied statistics task involves building regression models to characterise non-linear relationships between variables. It is possible to fit such models by assuming a particular non-linear functional form, such as a sinusoidal, exponential, or polynomial function, to describe a variable's response to the variation in other variables. Unless this relationship is obvious from the outset, however, it involves possibly extensive model selection procedures to ensure the most appropriate model is retained. Alternatively, a Bayesian non-parametric approach can be adopted (Fonnesbeck, 2017).

C.2.1. Non-parametric Bayesian approach

In a Bayesian model, a full probability model is specified for the problem at hand, assigning probability densities to each model variable. For example, parametric Bayesian linear regression finds the distributions over the parameters of the function $f(x) = \theta_0 + \theta_1 \cdot x$. $f(x)$ is the function to model and predict the dependent variable y, as a function of an independent variable x: $y = f(x) + \epsilon$, where ϵ is the error term, representing the error of the measurements.

In a parametric approach, the number of parameters θ_i has to be specified upfront, while in a non-parametric approach every possible function that matches the data is considered, independent of the number of parameters involved. Non-parametric in fact means that there are infinitely many parameters (Fonnesbeck, 2017).

C.2.2. Approach

Gaussian processes (GP) define a probability distribution over all possible functions. GP assume that $p(f(x_1), ..., f(x_N))$ is jointly Gaussian (Murphy, 2021). Adopting a set of Gaussians - a multivariate normal vector - confers a number of advantages. First, the marginal distribution of any subset of elements from a multivariate normal distribution is also normal. Conditional distributions of a subset of the elements of a multivariate normal distribution (conditional on the remaining elements) are normal too. A Gaussian process generalises the multivariate normal to infinite dimensions: An infinite collection of random variables, with any marginal subset having a Gaussian distribution (Fonnesbeck, 2017).

Visually, the multivariate Gaussian distribution is centred around the mean and the shape is determined by the covariance matrix, in which the correlations between the variables are defined. Each sample of the multivariate normal distribution represents one realisation of the function values. Because this distribution is a multivariate Gaussian distribution, the distribution of functions $p(f(x_1), ..., f(x_N))$ is normal too. Similarly, this distribution of functions is fully specified by a mean function and a covariance function:

$$p(x) \sim \mathcal{GP}\left(m(x), k\left(x, x'\right)\right) \tag{C.1}$$

The essential ingredients for GP are the training data set Y with data points x for which the outcome / function values $f(Y)$ have been observed, and the test data set X with data points denoted as t or x_* for which we would like to estimate/predict the function value $f_* = f(X)$. For now, let's consider the case where we have not yet observed any training data. In the context of Bayesian inference, this is called the prior distribution P_X. In order to set up the prior distribution, μ and Σ have to be defined. In Gaussian processes it is often assumed that $\mu = 0$, which simplifies the necessary equations for conditioning. It is always possible to assume this, even if $\mu \neq 0$. We can always add μ back to the resulting function values after the prediction step. But also, it turned out that most of the learning in the GP involves the covariance function and its hyperparameters, so very little is gained in specifying a complicated mean function (Fonnesbeck, 2017). The prior distribution will have the same dimensionality as the number of training data variables $N = |X|$. Setting up the covariance matrix Σ is a bit more complex. The covariance matrix will not only describe the shape of the distribution, but ultimately determines the characteristics of the function to be predicted. The kernel is used to define the entries of the covariance matrix. The kernel k receives two test points x_* , $x'_* \in \mathbb{R}^n$ (or sometimes called t, t') as an input and returns a similarity measure between those points in the form of a scalar:

$$k : \mathbb{R}^n \times \mathbb{R}^n \to \mathbb{R}, \quad \Sigma = \mathrm{Cov}\left(X, X'\right) = k\left(t, t'\right) \tag{C.2}$$

This function is evaluated for each pairwise combination of the test points to retrieve the covariance matrix. As mentioned earlier, the entry Σ_{ij} describes how much influence the i-th and j-th point have on each other. The covariance matrix will have dimensions of $N \times N$. Consequently, the covariance matrix determines which type of functions from the space of all possible functions are more probable. As the prior distribution does not yet contain any additional information, it is very suited to visualise the influence of the kernel on the distribution of functions.

In order to perform regression on the training data, the problem is treated as Bayesian inference. The essential idea of Bayesian inference is to update the current hypothesis as new information, i.e. the training data, becomes available (Görtler et al., 2019). The key idea is to model the underlying distribution of test data X together with training data Y as a multivariate normal distribution, where the training and the test points are linked to each other, to compute the corresponding covariance matrix. That means that the joint probability distribution $P_{X,Y}$ spans the space of possible function values for the function that we want to predict and it can be described as:

$$\begin{pmatrix} f \\ f_* \end{pmatrix} \sim \mathcal{N}\left(\begin{pmatrix} \mu \\ \mu_* \end{pmatrix}, \begin{pmatrix} K & K_* \\ K_*^T & K_{**} \end{pmatrix}\right) \tag{C.3}$$

where K is the matrix that is obtained by applying the kernel function k to the training data, i.e. the similarity of each observed x to each other observed x. K_* gives the similarity of the training data to the

test data whose output values we are trying to estimate. K_{**} gives the similarity of the test data points to each other. This joint distribution of test and training data has $|X| + |Y|$ dimensions.

By means of *conditioning*, it is possible to derive the conditional probability $P_{X|Y}$ from $P_{X,Y}$. By definition, $P_{X|Y}$ is normally distributed as well and the dimension is the number of test points X. The conditional distribution $P_{X|Y}$ forces the set of functions to precisely pass through each training point. Deriving this conditional probability is how the posterior is derived from the prior and the observations in a GP: With the joint distribution $p(f, f_*)$ known, it is possible to obtain the conditional $p(f_*|f)$ (or $p(f_*|x_*, x, f)$), resulting in the mean μ_* and covariance matrix Σ_* that define the distribution $f_* \sim \mathcal{N}(\mu_*, \Sigma_*)$. The last step is to sample from this distribution. By *marginalising* each random variable, we can extract the respective mean function value μ_{*i} and standard deviation $\sigma_{*i}(= \Sigma_{*ii})$ for the i-th test point, that can provide us with the desired predicted values.

C.2.3. Kernels for Gaussian Processes

Kernels, or *covariance functions* as they are often called in the context of GP, are a crucial ingredient. The kernel describes the similarity between the values of the function and subsequently it encodes the assumptions on the function - i.e. similar data points should lead to similar function values. Therefore, it also controls the possible shape that a fitted function can adopt. When choosing a kernel it should be ensured that the resulting matrix adheres to the properties of a covariance matrix, as described in Appendix A.2. Many kernels conceptually embed the input points into a higher dimensional space in which they then measure the similarity (Görtler et al., 2019). There are two categories of kernels that can be distinguished: *stationary* kernels and *non-stationary* kernels. Stationary kernels are functions that depend only on the distance of two data points and not on their absolute values and are thus invariant to translations in the input space, and the covariance of two points is only dependent on their relative position. Stationary kernels can be further subdivided into *isotropic* and *anisotropic* kernels, where isotropic kernels are also invariant to rotations in the input space (Pedregosa et al., 2011). Non-stationary kernels also depend on the specific values of the data points. Common kernels for Gaussian processes are the following:

- RBF kernel: It uses the Squared Exponential and is known as the Gaussian or Radial Basis Function (RBF) kernel. It calculates the squared distance between points and converts it into a measure of similarity, controlled by a tuning parameter (Bailey, 2019). It is a stationary kernel and defined as:

$$k(t, t') = \sigma^2 \exp\left(-\frac{\|t - t'\|^2}{2l^2}\right) \tag{C.4}$$

  where σ is the variance that determines the average distance away from the function's mean. Decreasing the variance Σ therefore results sampled functions that are more concentrated around the mean μ and thus in a narrow confidence bound of the resulting function. The length l determines the reach of influence on neighbours. A large value for l gives a smooth function, while a small value results in a wiggly function.

- Periodic kernel: It is a stationary kernel and suitable for periodic functions, defined as:

$$k(t, t') = \sigma^2 \exp\left(-\frac{2\sin^2(\pi |t - t'| / p)}{l^2}\right) \tag{C.5}$$

  where p is the periodicity that determines the distance between repetitions. Here, a large value of l results in a quite constant periodic function, while a small value gives a wiggly/irregular periodic function. The larger p, the larger the period of the periodic function.

- Linear kernel: It is a non-stationary kernel and it is suitable for linear functions:

$$k(t, t') = \sigma_b^2 + \sigma^2 (t - c)(t' - c) \tag{C.6}$$

  where σ_b determines the certainty around c which is the offset that determines the intersection point of all functions. Setting the variance $\sigma_b = 0$ results in a set of functions constrained to perfectly intersect the offset point c. If we set $\sigma_b > 0$, we can model uncertainty, resulting in functions that pass close to c.

There are many more kernels that can describe different classes of functions, which can be used to model the desired shape of the function. It is also possible to combine several kernels . A good overview of different kernels is given by Kristjanson Duvenaud (2014).

C.3. Application

Table C.1: Input variables for the metamodels per dike section. Beside these parameters, the metamodels are based on the hydraulic conductivities k, k_{v1}, k_{v3} and the water level h.

Dike section	Parameters					
DV1	φ dike	γ dike	φ sand pl	φ clay sand	S clay sand	γ clay sand
DV2	φ dike	γ dike	φ clay sand	S clay sand	m clay sand	γ clay sand
DV3	φ dike	φ sand pl	φ clay sand	S clay sand	m clay sand	γ clay sand
DV4	φ dike	S dike	φ clay sand	S clay sand	φ clay silt	S clay silt
DV5 & 6	γ dike	φ sand pl	S clay sand	φ clay silt	S clay silt	m clay silt
DV7	φ dike	γ dike	φ clay sand	S clay sand	φ clay silt	S clay silt
DV8	φ dike	γ sand hol	φ clay silt	S clay silt	m clay silt	γ clay silt
DV9	φ dike	S dike	γ dike	φ drained clay	γ drained clay	S drained clay
DV10	φ dike	S dike	γ dike	φ sand pl	φ clay sand	S clay sand
DV11	φ dike	φ clay sand	S clay sand	φ clay silt	S clay silt	m clay silt
DV12	φ dike	γ dike	φ hol sand	φ clay sand	S clay sand	γ clay sand
DV13	φ dike	γ dike	φ clay sand	S clay sand	m clay sand	γ clay sand
DV14	φ dike	φ sand hol	φ clay sand	S clay sand	m clay sand	γ clay sand
DV15	φ dike	γ dike	φ clay sand	S clay sand	m clay sand	γ clay sand
DV16 & 17	φ dike	φ clay sand	S clay sand	φ clay hum	S clay hum	m clay hum
DV18	φ dike	S dike	φ sand hol	φ clay sand	S clay sand	γ clay sand
DV19	φ dike	φ sand hol	γ sand hol	φ clay silt	S clay silt	m clay silt
DV20	φ dike	γ dike	φ sand hol	φ clay sand	S clay sand	γ clay sand
DV21	φ dike	φ sand pl	φ clay sand	S clay sand	m clay sand	γ clay sand
DV22	φ dike	φ sand hol	φ sand pl	φ clay silt	S clay silt	m clay silt
DV23	φ dike	γ sand hol	φ clay hum	S clay hum	m clay hum	γ clay hum
DV24	φ dike	γ dike	φ clay sand	S clay sand	m clay sand	γ clay sand
DV25	φ dike	γ dike	φ clay sand	S clay sand	m clay sand	γ clay sand
DV26	φ dike	φ sand hol	φ clay sand	S clay sand	φ drained clay sand	γ drained clay sand
DV27	φ dike	φ sand pl	φ clay sand	S clay sand	m clay sand	γ clay sand
DV28	φ dike	γ dike	φ sand pl	φ clay sand	S clay sand	γ clay sand
DV29	φ dike	γ dike	φ clay silt	S clay silt	m clay silt	γ clay silt
DV30	φ dike	γ dike	φ clay silt	S clay silt	m clay silt	γ clay silt
DV31	φ dike	γ dike	φ sand pl	φ clay silt	S clay silt	m clay silt

Table C.2: Description of the input variables and their values that are used in the original D-Stability schematisations.

Abbreviation	Description	γ [kN/m^3]	φ [deg]	S [-]	m [-]
dike	the total dike material (clay)	18.54	30	0.34	0.87
clay sand	silty, sandy clay layer with γ > 17.5 kN/m^3	18.73	29.7	0.28	0.85
clay silt	silty clay layer with γ = 16 - 17 kN/m^3	16.82	28.7	0.25	0.86
clay hum	silty, humous clay layer with γ = 14 - 16 kN/m^3	15.15	27.7	0.21	0.87
drained clay sand	drained silty, sandy clay layer with γ > 17.5 kN/m^3	18.73	29.7	-	-
sand hol	holocene sand layer	18 (unsat) ; 20 (sat)	31.3	-	-
sand pl	pleistocene sand layer	17 ; 20	31.3	-	-

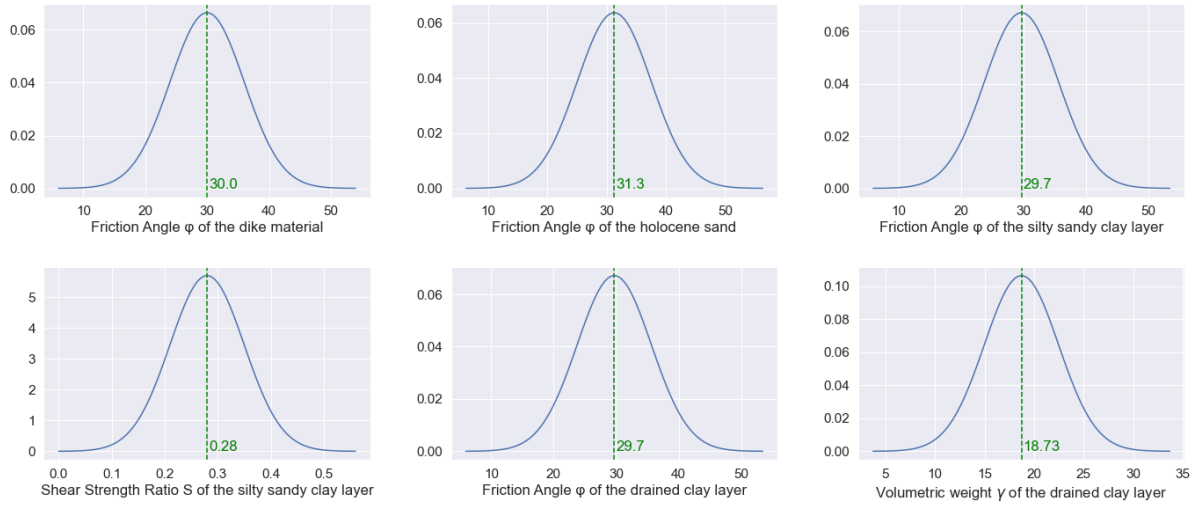

Figure C.1: Distributions from which the samples of the soil strength parameters have been drawn for training the metamodel of dike section 23, as an example..

C.3.1. Phreatic lines and head lines

1. Phreatic Lines for clay dikes

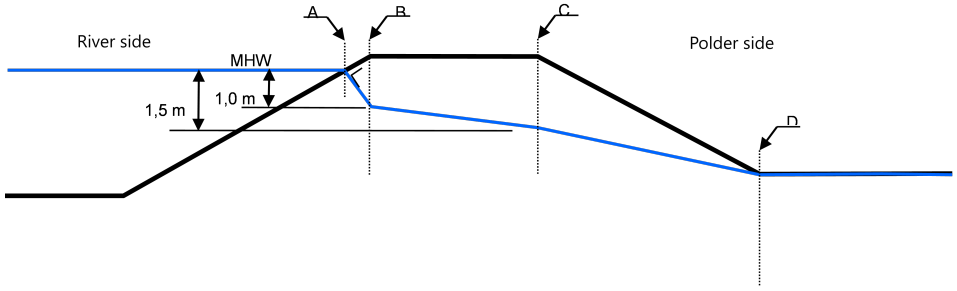

Figure C.2: Schematisation of the phreatic line in clay dikes (Brookhuis and Beekx, 2017). A is the intersection point of the normative river water level (MHW) and the outer dike slope, B is always 1.0 m below MHW and below the outer edge of the dike crest, C is below the inner edge of the crest and 1.5 m below MHW and D is located at the inner toe.

2. Phreatic line at sand containments ('zandscheg')

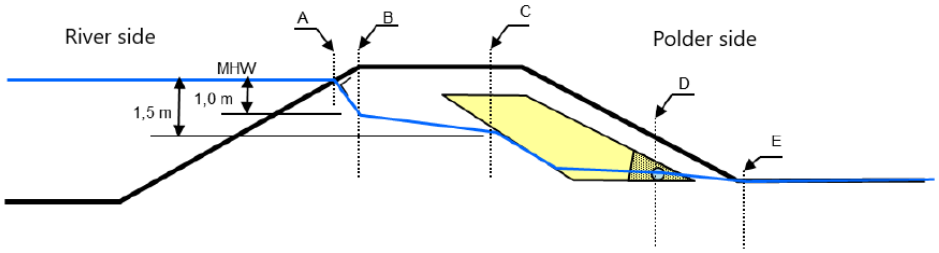

Figure C.3: Schematisation of the phreatic line at sand containments (Brookhuis and Beekx, 2017). Point C is located below the inner crest edge and 1.5 m below the normative water level, just like in the schematisation for clay dikes. From point C, a slope of 1:2 towards the ground level of the land side. From this point, a horizontal connection to the inner toe of the dike where the phreatic line is located at the ground level.

3. Aquifer Head Line

According to schematisation 4A of the TRWD ('Technical Report for Pore Pressures in Dikes') (TAW, 2004), the head line in the aquifer can be approximated as explained below.

The head at the inner toe of the dike is then [m+NAP]:

$$\varphi_2 = \varphi_3 + (\varphi_0 - \varphi_3)\frac{W_3}{\Sigma W} = \varphi_3 + (\varphi_0 - \varphi_3)\frac{\lambda_3 \tanh\frac{L_3}{\lambda_3}}{\lambda_1 \tanh\frac{L_1}{\lambda_1} + L_2 + \lambda_3 \tanh\frac{L_3}{\lambda_3}} \tag{C.7}$$

The head at the outer toe [m+NAP]:

$$\varphi_1 = \varphi_3 + (\varphi_0 - \varphi_3)\frac{W_2 + W_3}{\Sigma W} = \varphi_3 + (\varphi_0 - \varphi_3)\frac{L_2 + \lambda_3 \tanh\frac{L_3}{\lambda_3}}{\lambda_1 \tanh\frac{L_1}{\lambda_1} + L_2 + \lambda_3 \tanh\frac{L_3}{\lambda_3}} \tag{C.8}$$

Next, the head line beneath the foreland can be schematised by:

$$\varphi(x) = \varphi_0 - (\varphi_0 - \varphi_1)\frac{\sinh\frac{a+L_1+x}{\lambda_1}}{\sinh\frac{L_1}{\lambda_1}} \tag{C.9}$$

the head line beneath the dike:

$$\varphi(x) = \frac{(\varphi_1 + \varphi_2)}{2} - \frac{(\varphi_1 - \varphi_2)}{2}\frac{x}{a} \tag{C.10}$$

And the head line underneath the hinterland:

$$\varphi(x) = \varphi_3 + (\varphi_2 - \varphi_3)\frac{\sinh\frac{a+L_3-x}{\lambda_3}}{\sinh\frac{L_3}{\lambda_3}} \tag{C.11}$$

In these equations, $\lambda_{1,3} = \sqrt{k \cdot D \cdot c_{1,3}}$ is the leakage factor of the fore- and hinterland respectively [m], in which $c_{1,3} = d_{1,3}/k_{v1,3}$ is the resistance of the blanket layers [d], with $k_{v1,3}$ the hydraulic conductivities of the blanket layers. φ_0 is equal to the river water level and φ_3 to the polder level [m+NAP]. The head lines and their parameters are illustrated in Figure C.4.

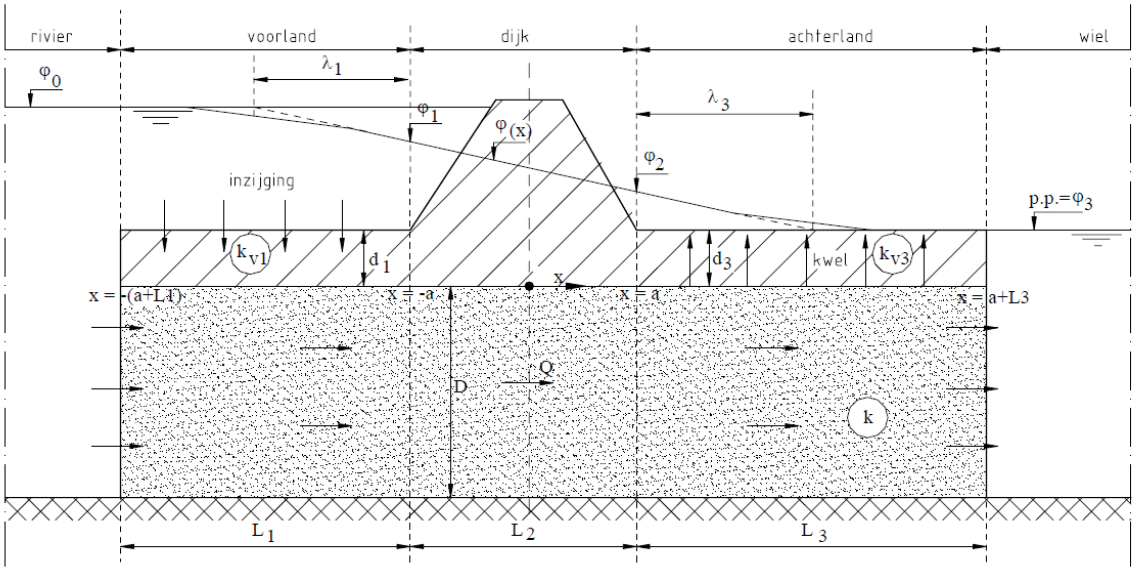

Figure C.4: Schematisation of the groundwater flow in a clay dike (TAW, 2004).

4. Head line in case of bursting

Hydraulic heave occurs if the pore pressures in the aquifer in the hinterland of the dike are equal to the weight of the overlying soil. The effective stress on the interface is then equal to 0. The occurring potential is called the limit potential φ_g ('grenspotentiaal') (TAW, 2004):

$$\varphi_g = \frac{\sigma'_{vs}}{\gamma_w} + \varphi_p = \frac{\sum(\gamma_{si} d_i)}{\gamma_w} + \varphi_p - d_z \tag{C.12}$$

In which σ_{vs} is the vertical soil stress at the interface [kN/m^2], φ is the polder level [m], γ_{si} is the saturated volumetric weight of soil layer i [kN/m^3], d_i is the thickness of layer i [m] and d_z is the depth of the aquifer with respect to the polder level [m].

For the approximation of the aquifer head line in a situation in which hydraulic heave can occur, schematisation 4C of the TRWD is applicable. Beneath the foreland and dike, the same approximation as in 4A can be applied. However, the head at the end of the inner berm [m+NAP] is now:

$$\varphi_3 = \varphi_g + \Delta\varphi_u = \varphi_g + (\varphi_0 - \varphi_g)\frac{0,44D}{\lambda_1 \tanh\left(\frac{L_1}{\lambda_1}\right) + L_2 + L_3 + 0,44D} \tag{C.13}$$

and the head at the inner toe [m+NAP]:

$$\varphi_2 = \varphi_g + (\varphi_0 - \varphi_g)\frac{L_3 + 0,44D}{\lambda_1 \tanh\left(\frac{L_1}{\lambda_1}\right) + L_2 + L_3 + 0,44D} \tag{C.14}$$

The head line and its parameters are illustrated in Figure C.5. The water authority schematised the bursting zone as 3 times the thickness of the cover layer and no strength is assigned to the cover layer within this zone.

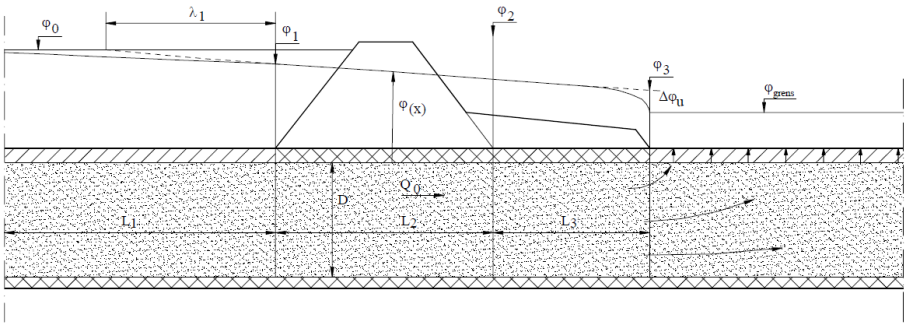

Figure C.5: Schematisation of the groundwater flow with the occurrence of the limit potential (TAW, 2004).

Table C.3: Phreatic and head line schematisations per dike section. 4A refers to schematisation 4A of the TRWD (TAW, 2004), that is applicable for flow in a sandy subsoil beneath an impermeable dike with poorly permeable blanket layers in the fore- and hinterland. 4C refers to schematisation 4C of the TRWD, that is applicable in situations of aquifer flow beneath an impermeable dike in which the limit potential occurs in the hinterland.

Dike section	Phreatic Line	Head Line
DV1	sand containment	4A
DV2	sand containment	4C
DV3	sand containment	4C
DV4	sand containment	4A
DV5	sand containment	4A
DV6	sand containment	4A
DV7	sand containment	4A
DV8	sand containment	4A
DV9	sand containment	4A
DV10	clay dike	4A
DV11	sand containment	4C
DV12	sand containment	4C
DV13	sand containment	4C
DV14	sand containment	4C
DV15	sand containment	4C
DV16	sand containment	4A
DV17	sand containment	4A
DV18	sand containment	4C
DV19	sand containment	4A
DV20	sand containment	4A
DV21	sand containment	4C
DV22	sand containment	4C
DV23	clay dike	4C
DV24	clay dike	4A
DV25	clay dike	4A
DV26	sand containment	4A
DV27	sand containment	4C
DV28	clay dike	4C
DV29	clay dike	4C
DV30	clay dike	4C
DV31	clay dike	4A

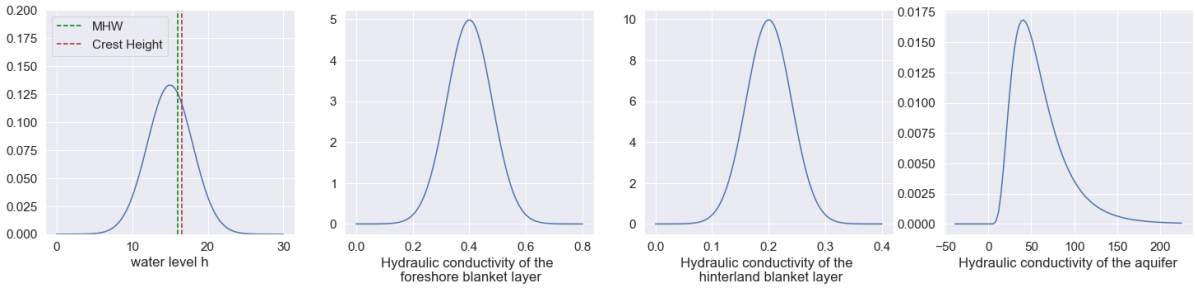

Figure C.6: Distributions from which the realisations of h, k_{v1}, k_{v3} and k have been drawn for training the metamodel.

C.3.2. Validation of the metamodel

Table C.4: Errors of the metamodels.

Dike section	Percentage Prediction Error	RMSE	CV
DV1	-0.67%	0.168	0.134
DV2	-1.27%	0.129	0.106
DV3	-0.09%	0.055	0.047
DV4	-0.46%	0.086	0.070
DV5	-0.69%	0.119	0.088
DV6	-0.69%	0.119	0.088
DV7	-1.97%	0.125	0.085
DV8	-0.41%	0.222	0.166
DV9	0.31%	0.074	0.061
DV10	-0.19%	0.043	0.035
DV11	-0.47%	0.092	0.075
DV12	0.69%	0.126	0.103
DV13	-0.14%	0.040	0.027
DV14	0.04%	0.050	0.038
DV15	-0.93%	0.072	0.049
DV16	-0.76%	0.057	0.046
DV17	-0.76%	0.057	0.046
DV18	-0.34%	0.039	0.027
DV19	-2.39%	0.085	0.072
DV20	-0.11%	0.060	0.046
DV21	-0.11%	0.040	0.035
DV22	-0.31%	0.056	0.050
DV23	0.39%	0.094	0.092
DV24	-0.74%	0.086	0.082
DV25	-0.74%	0.086	0.082
DV26	-0.46%	0.086	0.064
DV27	-3.50%	0.231	0.208
DV28	-2.82%	0.111	0.106
DV29	-0.19%	0.056	0.060
DV30	-0.76%	0.083	0.071
DV31	0.32%	0.087	0.084
mean:	**-0.64**	**0.092**	**0.076**

C.3.3. Contribution of the input parameters

Table C.5: Importance of the input parameters of the metamodels per dike section. Each parameter has been multiplied by 1.3 (increased by 30%) and the relative difference of the resulting FoS with respect to the FoS based on the case study input values of the parameters has been computed. These are listed below. If the relative difference is negative, it means that the corresponding parameter contributes to the load, while a positive value means that it contributes to the resistance.

Dike section 1		Dike section 2		Dike section 3		Dike section 4		Dike section 5 & 6	
h	-71.97%	h	-93.23%	h	-40.82%	h	-46.93%	h	-57.65%
$\Phi_{sand,pl}$	14.68%	$S_{c,s}$	11.42%	$S_{c,s}$	10.30%	S_{dike}	10.44%	γ_{dike}	-6.66%
$\gamma_{c,s}$	14.17%	$m_{c,s}$	6.36%	Φ_{dike}	6.93%	$S_{c,silt}$	10.31%	$m_{c,silt}$	6.26%
γ_{dike}	10.94%	Φ_{dike}	5.60%	$\Phi_{sand,pl}$	5.97%	$S_{c,s}$	5.09%	$S_{c,s}$	3.67%
Φ_{dike}	9.77%	k_{v1}	-3.49%	$m_{c,s}$	4.31%	k_{v3}	4.36%	$S_{c,silt}$	3.30%
$S_{c,s}$	6.16%	γ_{dike}	-2.57%	$\gamma_{c,s}$	2.95%	k_{v1}	-3.59%	k_{v3}	2.41%
k_{v3}	4.80%	k	2.23%	k	0.83%	$\Phi_{c,silt}$	-1.59%	$\Phi_{c,silt}$	1.29%
$\Phi_{c,s}$	2.89%	k_{v3}	-1.48%	k_{v1}	-0.65%	Φ_{dike}	0.77%	$\Phi_{sand,pl}$	0.89%
k	1.46%	$\Phi_{c,s}$	0.65%	k_{v3}	-0.48%	k	-0.33%	k_{v1}	0.43%
k_{v1}	-1.00%	$\gamma_{c,s}$	-0.03%	$\Phi_{c,s}$	0.45%	$\Phi_{c,s}$	0.29%	k	-0.11%

Dike section 7		Dike section 8		Dike section 9		Dike section 10		Dike section 11	
h	-51.99%	h	-57.57%	h	-71.01%	h	-51.94%	h	-37.08%
Φ_{dike}	7.63%	k_{v3}	7.13%	$\gamma_{c,dr}$	31.03%	Φ_{dike}	19.82%	Φ_{dike}	7.05%
γ_{dike}	-6.54%	$m_{c,silt}$	4.44%	$\Phi_{c,dr}$	12.50%	γ_{dike}	7.77%	$S_{c,silt}$	4.20%
$S_{c,s}$	5.91%	k_{v1}	-4.02%	γ_{dike}	-5.51%	$S_{c,s}$	1.49%	$m_{c,silt}$	4.02%
$\Phi_{c,s}$	-3.67%	Φ_{dike}	3.49%	Φ_{dike}	4.66%	k_{v1}	-0.33%	S_{cs}	2.20%
$\Phi_{c,silt}$	1.35%	$\gamma_{sand,hol}$	3.08%	k_{v3}	3.99%	S_{dike}	-0.17%	k_{v1}	-1.34%
k_{v3}	1.20%	S_{csilt}	1.72%	k_{v1}	-2.90%	k	-0.17%	k_{v3}	-1.04%
k	1.09%	$\gamma_{c,silt}$	1.34%	k	0.96%	$\Phi_{sand,pl}$	0.16%	k	1.02%
k_{v1}	0.91%	$\Phi_{c,silt}$	0.36%	S_{dike}	0.79%	k_{v3}	0.12%	$\Phi_{c,s}$	-0.28%
$S_{c,silt}$	-0.34%	k	-0.05%	$S_{c,s}$	0.32%	$\Phi_{c,s}$	-0.11%	$\Phi_{c,silt}$	-0.13%

Dike section 12		Dike section 13		Dike section 14		Dike section 15		Dike section 16 & 17	
h	-43.23%	h	-41.47%	h	-28.39%	h	-53.22%	h	-34.04%
Φ_{dike}	11.72%	Φ_{dike}	8.01%	$S_{c,s}$	14.53%	Φ_{dike}	12.00%	$S_{c,hum}$	6.37%
γ_{dike}	2.98%	$S_{c,s}$	7.78%	$\gamma_{c,s}$	9.86%	$S_{c,s}$	9.92%	$S_{c,s}$	5.91%
k_{v1}	-2.88%	γ_{dike}	5.49%	$\Phi_{sand,hol}$	6.90%	$m_{c,s}$	4.24%	Φ_{dike}	3.41%
$\Phi_{sand,hol}$	2.35%	$m_{c,s}$	4.08%	$m_{c,s}$	5.23%	γ_{dike}	2.22%	$m_{c,hum}$	2.91%
$S_{c,s}$	2.25%	$\gamma_{c,s}$	0.34%	Φ_{dike}	5.09%	$\Phi_{c,s}$	1.47%	k_{v3}	0.73%
k	1.87%	k	0.18%	$\Phi_{c,s}$	0.58%	$\gamma_{c,s}$	0.94%	$\Phi_{c,hum}$	-0.69%
$\gamma_{c,s}$	-1.00%	k_{v3}	-0.15%	k	0.46%	k_{v1}	-0.65%	$\Phi_{c,s}$	-0.66%
k_{v3}	-0.64%	k_{v1}	-0.05%	k_{v3}	-0.25%	k	0.13%	k_{v1}	-0.61%
$\Phi_{c,s}$	-0.15%	$\Phi_{c,s}$	0.03%	k_{v1}	-0.12%	k_{v3}	0.09%	k	0.54%

Dike section 18		Dike section 19		Dike section 20		Dike section 21		Dike section 22	
h	-16.98%	h	-72.68%	h	-69.01%	h	-41.76%	h	-37.16%
$S_{c,s}$	9.12%	$S_{c,silt}$	14.99%	Φ_{dike}	12.45%	$\gamma_{c,s}$	16.56%	$\Phi_{sand,pl}$	7.97%
S_{dike}	7.51%	$\gamma_{sand,hol}$	13.96%	$\gamma_{c,s}$	10.36%	$S_{c,s}$	8.30%	$S_{c,silt}$	7.19%
$\Phi_{sand,hol}$	6.84%	$m_{c,silt}$	8.65%	$\Phi_{sand,hol}$	8.87%	$\Phi_{sand,pl}$	6.45%	Φ_{dike}	6.39%
$\gamma_{c,s}$	2.22%	Φ_{dike}	5.72%	γ_{dike}	6.50%	$m_{c,s}$	5.54%	$\Phi_{sand,hol}$	4.93%
Φ_{dike}	1.31%	k_{v3}	4.05%	$S_{c,s}$	2.60%	Φ_{dike}	5.03%	$m_{c,silt}$	4.33%
k	0.64%	$\Phi_{sand,hol}$	-1.79%	k_{v1}	-1.91%	k	0.89%	k	1.22%
$\Phi_{c,s}$	-0.30%	$\Phi_{c,silt}$	1.33%	k_{v3}	1.87%	k_{v1}	-0.63%	$\Phi_{c,silt}$	0.40%
k_{v1}	-0.27%	k_{v1}	-1.17%	k	0.42%	k_{v3}	0.50%	k_{v1}	-0.40%
k_{v3}	0.05%	k	-1.09%	$\Phi_{c,s}$	0.28%	$\Phi_{c,s}$	0.20%	k_{v3}	-0.35%

Dike section 23		Dike section 24 & 25		Dike section 26		Dike section 27	
h	-33.41%	h	-64.65%	h	-56.58%	h	-43.91%
$S_{c,hum}$	22.63%	Φ_{dike}	23.75%	$\gamma_{c,dr}$	30.25%	$S_{c,s}$	-10.98%
$\gamma_{c,hum}$	15.54%	γ_{dike}	9.28%	$\Phi_{c,dr}$	8.93%	$\gamma_{c,s}$	-10.19%
$m_{c,hum}$	11.61%	$m_{c,s}$	4.27%	k_{v3}	3.92%	$\Phi_{c,s}$	5.59%
$\gamma_{sand,hol}$	9.76%	k	2.40%	$S_{c,s}$	2.79%	$m_{c,s}$	-2.66%
Φ_{dike}	4.11%	$S_{c,s}$	-1.20%	k_{v1}	-2.31%	k_{v1}	-2.54%
k	-0.23%	$\gamma_{c,s}$	0.63%	Φ_{dike}	1.45%	k	1.14%
$\Phi_{c,hum}$	0.20%	k_{v1}	0.16%	$\Phi_{sand,hol}$	1.23%	$\Phi_{sand,pl}$	-1.14%
k_{v1}	-0.18%	k_{v3}	0.07%	$\Phi_{c,s}$	1.10%	k_{v3}	-1.00%
k_{v3}	0.00%	$\Phi_{c,s}$	-0.01%	k	-0.92%	Φ_{dike}	0.48%

Dike section 28		Dike section 29		Dike section 30		Dike section 31	
h	-76.09%	h	-64.08%	h	-48.60%	h	-66.34%
γ_{dike}	15.85%	Φ_{dike}	19.05%	$S_{c,silt}$	10.61%	Φ_{dike}	15.45%
Φ_{dike}	14.90%	$m_{c,silt}$	6.23%	$m_{c,silt}$	6.19%	γ_{dike}	4.53%
$S_{c,s}$	-3.28%	γ_{dike}	4.75%	k_{v3}	5.56%	$S_{c,silt}$	-1.52%
$\gamma_{sand,hol}$	-3.03%	$S_{c,silt}$	1.10%	$\gamma_{c,silt}$	4.99%	$\Phi_{sand,pl}$	1.41%
$\Phi_{c,s}$	-1.73%	$\gamma_{c,silt}$	-1.05%	Φ_{dike}	4.43%	k_{v3}	0.70%
$\gamma_{c,s}$	1.60%	k_{v3}	-0.68%	γ_{dike}	-2.90%	k_{v1}	0.17%
k	0.83%	$\Phi_{c,silt}$	-0.50%	k	2.65%	$m_{c,silt}$	0.15%
k_{v1}	0.80%	k_{v1}	-0.47%	k_{v1}	-1.48%	$\Phi_{c,silt}$	0.08%
k_{v3}	-0.18%	k	0.44%	$\Phi_{c,silt}$	-0.35%	k	0.00%

For comparison, the resulting parameter contributions for dike section 1, based on a FORM analysis in D-Stability, are listed below:

- $\Phi_{sand,pl} = 0.756$
- $\Phi_{dike} = 0.541$
- $\Phi_{cs} = 0.368$
- $S_{cs} = 0.368$
- $m_{cs} = 0.024$ (not included in the metamodel)

D

Detailed Model Input

D.1. Dike Section Division

Table D.1: Dike section division.

New dike sections			Old dike sections macrostability				Old dike sections piping		
Dike section	From	To	Dike section	From	To	Normative profile	Dike section	From	To
DV1	DD001	DD002	DV1b	DD001	DD002	DD001+046M	DV1	DD000	DD004
DV2	DD002	DD004+50	DV1c	DD002	DD004+50	DD004+010M			
DV3	DD004+50	DD015+50	DV2	DD004+50	DD015+50	DD012+97M	DV2	DD004	DD015+50
DV4	DD015+50	DD019	DV3	DD015+50	DD019	DD015+104M	DV3	DD015+50	DD022
DV5	DD019	DD022	DV4	DD019	DD025	DD019+19M			
DV6	DD022	DD025					DV4	DD022	DD025
DV7	DD025	DD031+50	DV5	DD025	DD031+50	DD031+46M	DV5	DD025	DD032
DV8	DD031+50	DD036+50	DV6	DD031+50	DD036+50	DD033+75M	DV6	DD032	DD036+50
DV9	DD036+50	DD040	DV7	DD036+50	DD040	DD039+23M	DV7	DD036+50	DD040
DV10	DD040	DD045+50	DV8	DD040	DD045+50	DD040+66M	DV8	DD040	DD045
DV11	DD045+50	DD047	DV9	DD045+50	DD047	DD045+91M	DV9	DD045	DD046+50
DV12	DD047	DD050	DV10	DD047	DD050	DD049+39M	DV10	DD046+50	DD050
DV13	DD050	DD053	DV11	DD050	DD053	DD052+99M	DV11	DD050	DD053+50
DV14	DD053	DD061	DV12	DD053	DD061	DD059+4M	DV12	DD053+50	DD064
DV15	DD061	DD064	DV13	DD061	DD064	DD061+55M			
DV16	DD064	DD070+50	DV14	DD064	DD075+50	DD071+91M	DV13	DD064	DD070+50
DV17	DD070+50	DD075+50					DV14	DD070+50	DD075
DV18	DD075+50	DD077+50	DV15	DD075+50	DD077+50	DD075+78M	DV15	DD075	DD077+50
DV19	DD077+50	DD080+50	DV16	DD077+50	DD080+50	DD079+78M	DV16	DD077+50	DD080+50
DV20	DD080+50	DD085	DV17	DD080+50	DD085	DD083+75M	DV17	DD080+50	DD085
DV21	DD085	DD093	DV18	DD085	DD093	DD087+8M	DV18	DD085	DD091
DV22	DD093	DD097	DV19	DD093	DD097	DD094+56M	DV19	DD091	DD097
DV23	DD097	DD100+50	DV20	DD097	DD100+50	DD099+54M	DV20	DD097	DD100+50
DV24	DD100+50	DD107+50	DV21	DD100+50	DD107+50	DD107+31M	DV21	DD100+50	DD107+50
DV25	DD107+50	DD109+50	DV22	DD107+50	DD109+50	-	DV22	DD107+50	DD110
DV26	DD109+50	DD112+50	DV23	DD109+50	DD112+50	DD111+43M	DV23	DD110	DD112+50
DV27	DD112+50	DD121	DV24	DD112+50	DD121	DD113+22M	DV24	DD112+50	DD121
DV28	DD121	DD126	DV25	DD121	DD126	DD126+0M	DV25	DD121	DD126
DV29	DD126	DD128+50	DV26	DD126	DD128+50	DD127+78M	DV26	DD126	DD128+50
DV30	DD128+50	DD130	DV27	DD128+50	DD130	DD129+57M	DV27	DD128+50	DD130
DV31	DD130	DD133+50	DV28	DD130	DD133+50	DD131+88M	DV28	DD130	DD133+50

D.2. Load Input

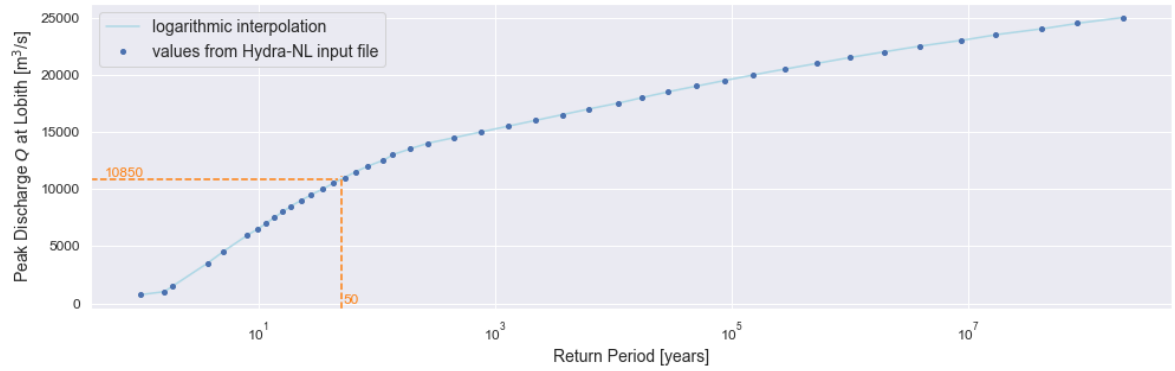

Figure D.1: Return periods for the peak river discharge at Lobith, derived from the OI2014 input file for Hydra-NL, including statistical uncertainty, based on climate scenario W+ and interpolated for the year 2075. In dashed orange lines, the river discharge that corresponds to a return period of 50 years is shown, to mark the lower limit of discharges that are considered in this research.

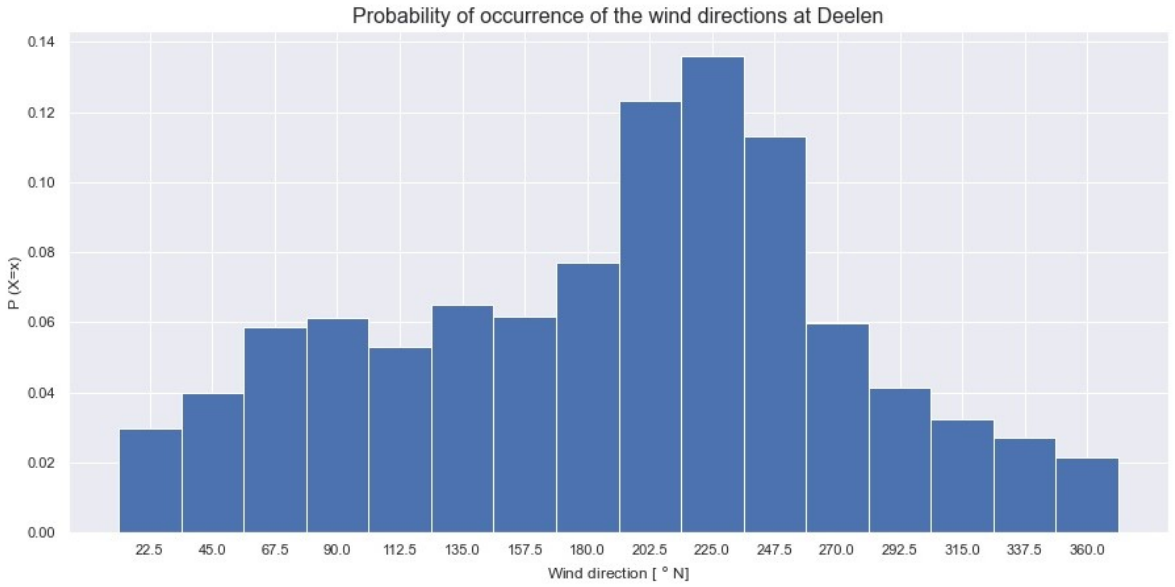

Figure D.2: Probabilities of occurrence of the wind directions at Deelen, to sample from within the MC simulation.

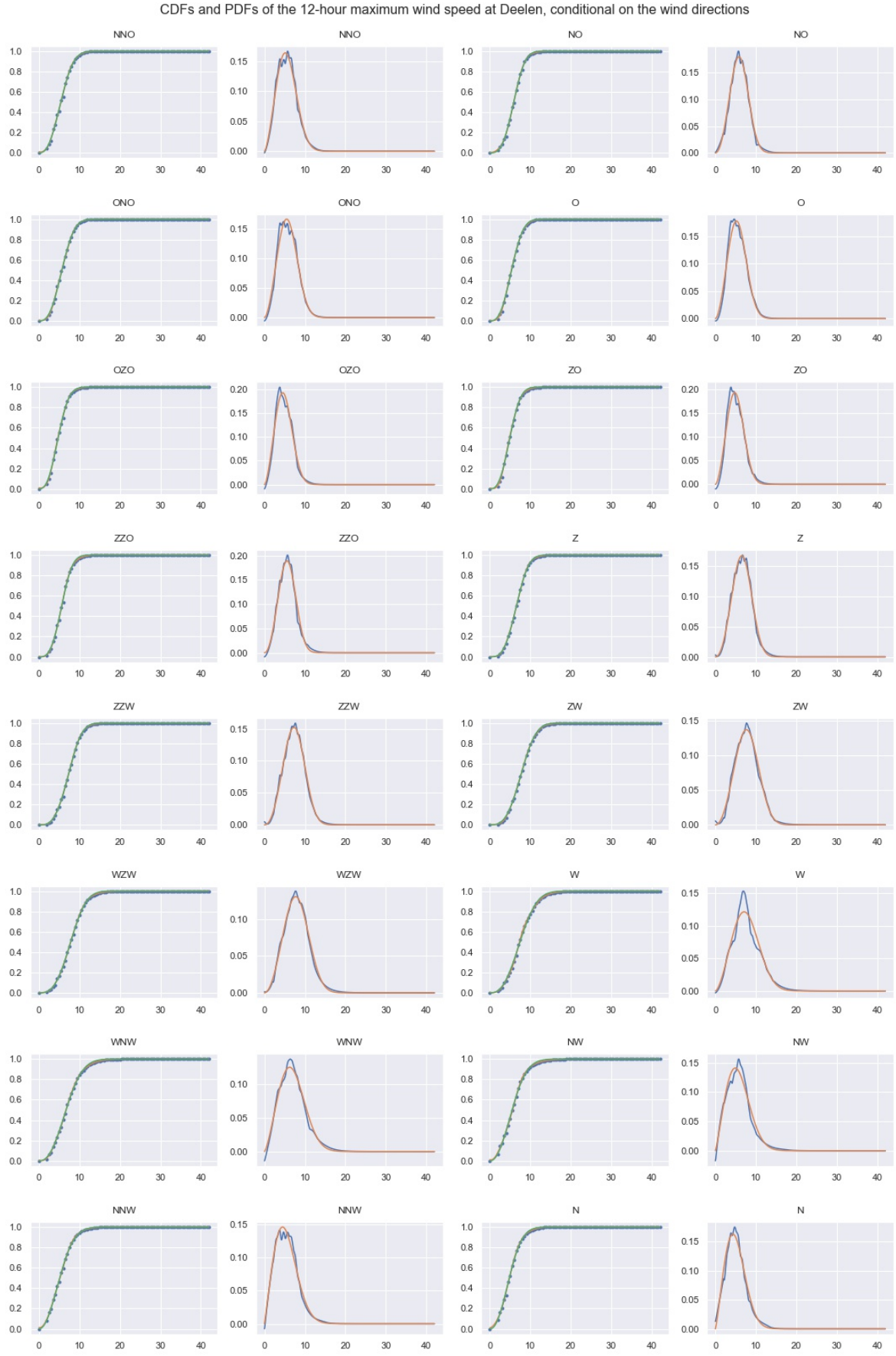

Figure D.3: Statistics of the 12-hourly maximum wind speed at Deelen, given the wind direction.

D.3. Geotechnical Input

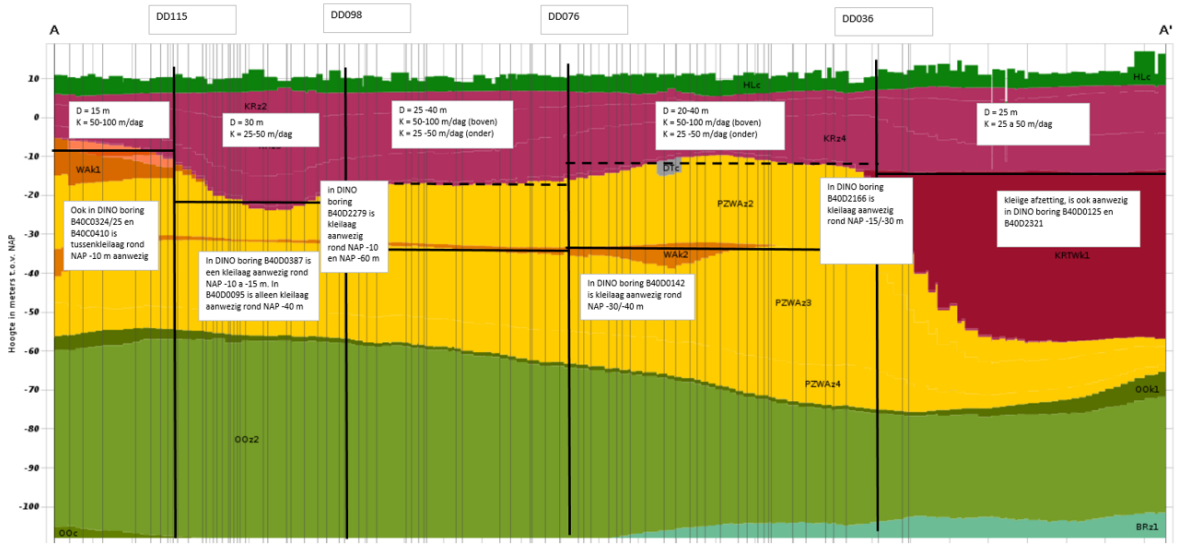

Figure D.4: A REGIS section for Sprok-Sterreschans.

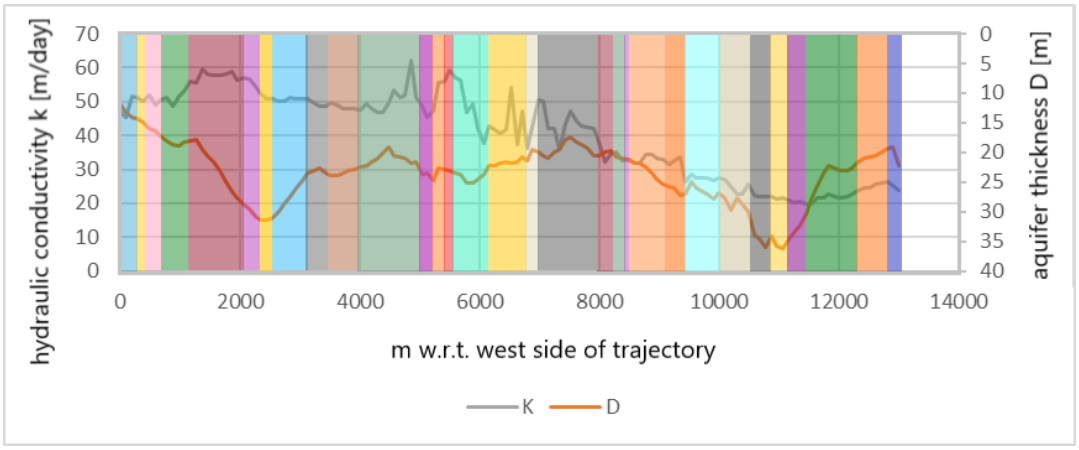

Figure D.5: Hydraulic conductivity and thickness of the aquifer according to MORIA. The dike sections (from DV31 to DV1) are shown in the same colors as in Figure 5.1.

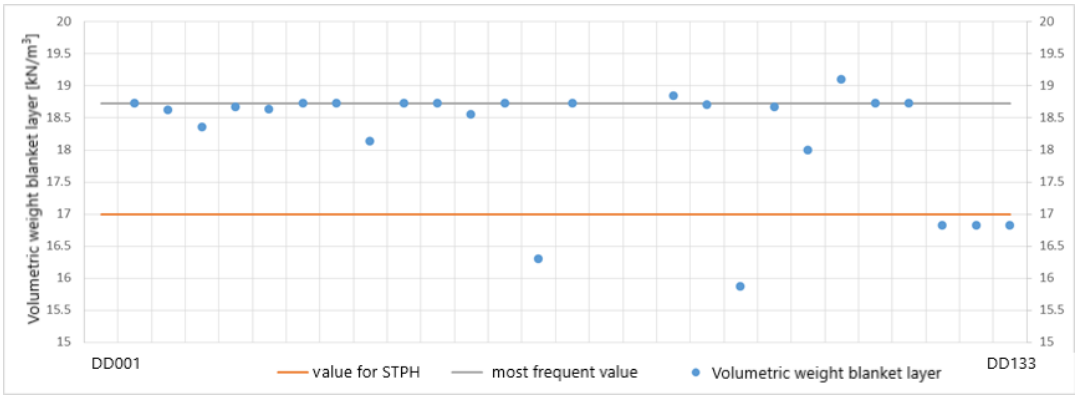

Figure D.6: Saturated volumetric weight γ_{sat} of the blanket layer along the trajectory .

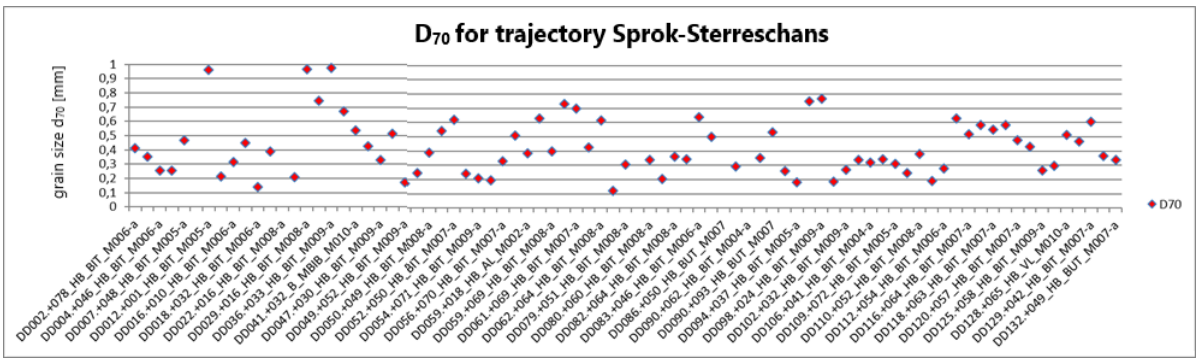

Figure D.7: d_{70} values from measurements along the trajectory.

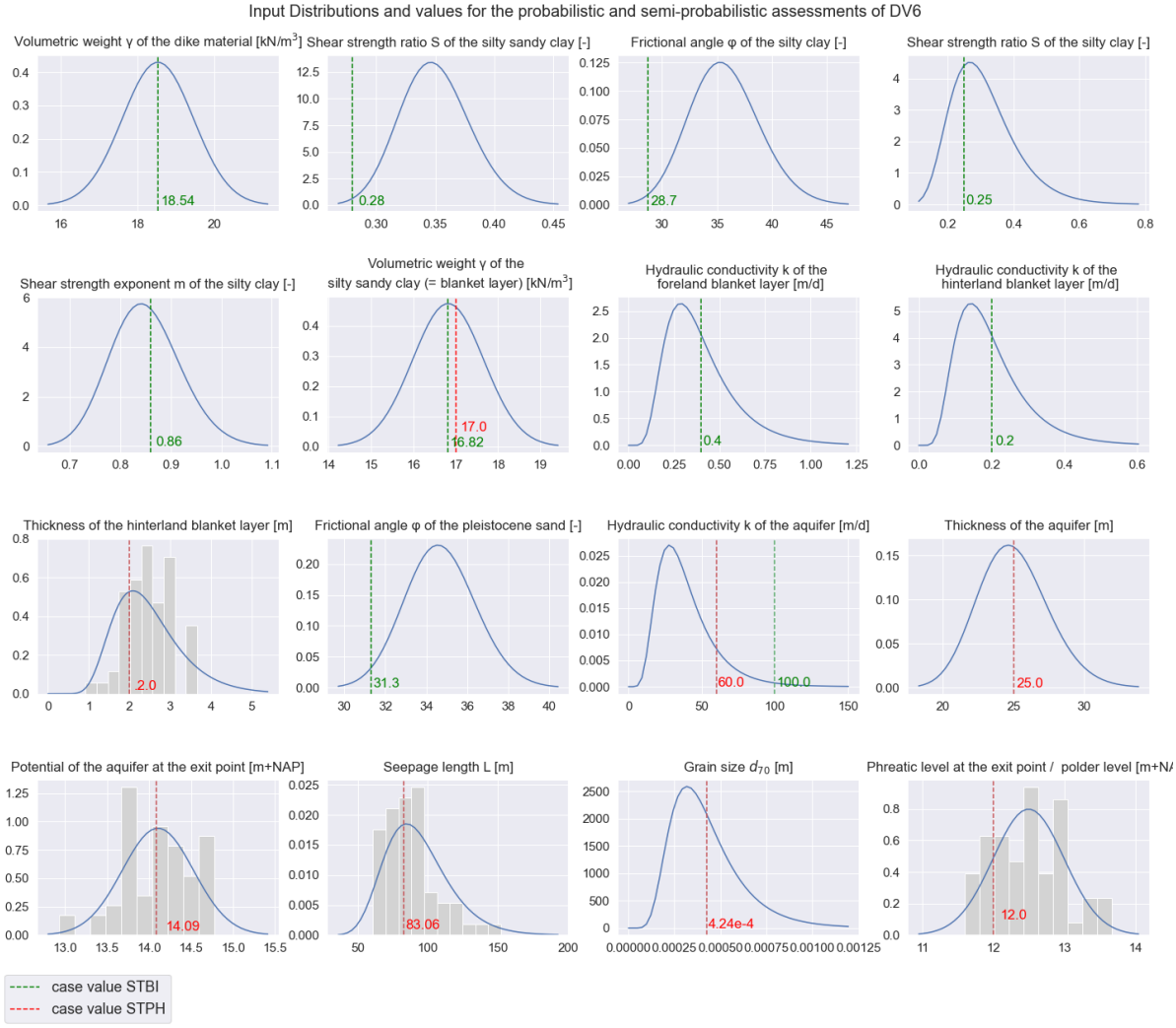

Figure D.8: Input distributions for dike section 6.

D.4. Geological Deposits and Spatial Correlations

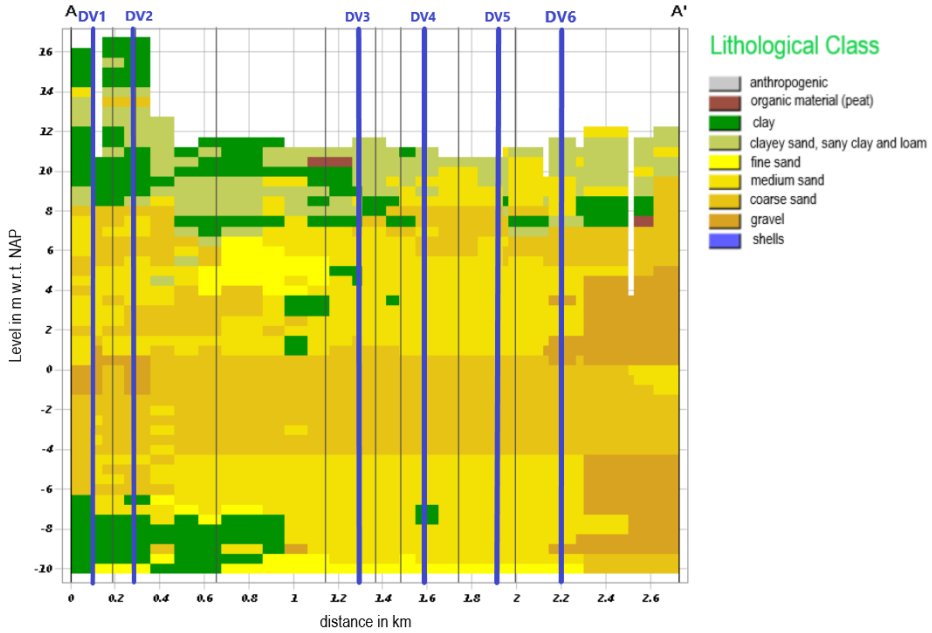

Figure D.9: GeoTOP schematisation for dike section 1-6.

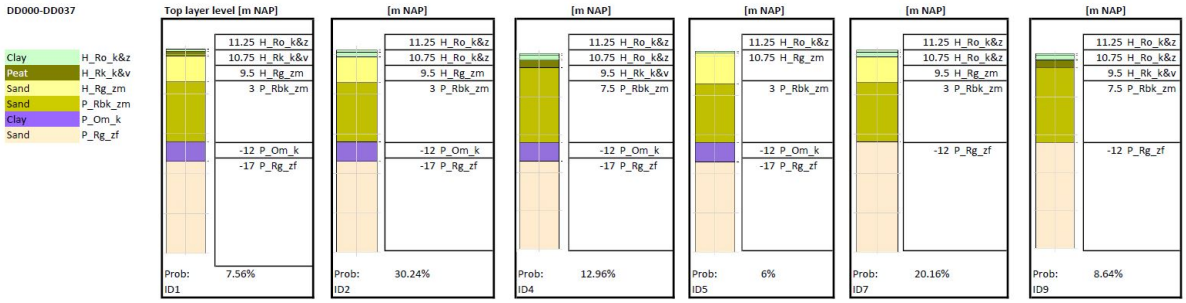

Figure D.10: SOS Schematisation for dike section 1-6.

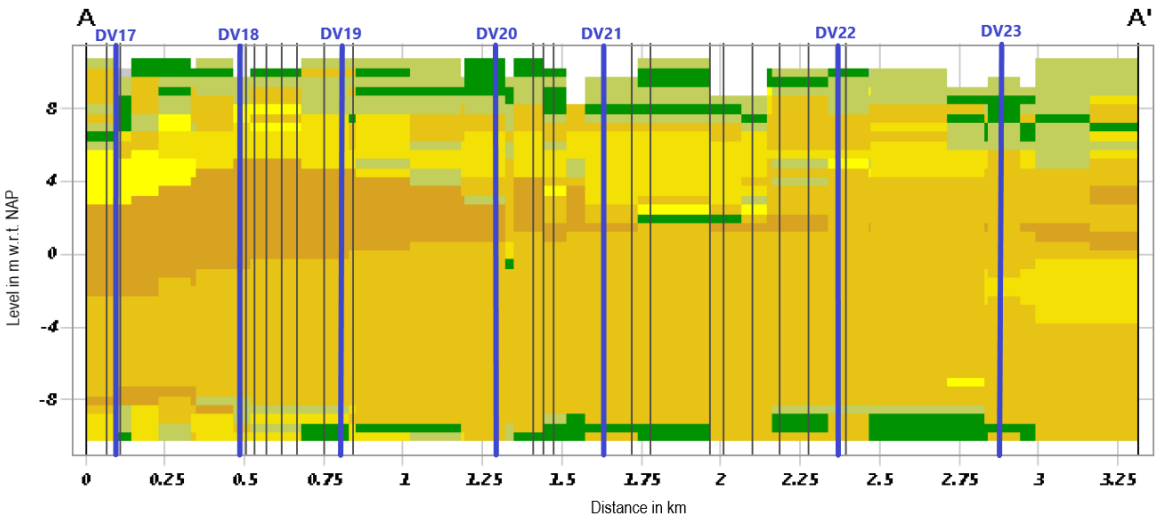

Figure D.11: GeoTOP schematisation for dike section 17-23 .

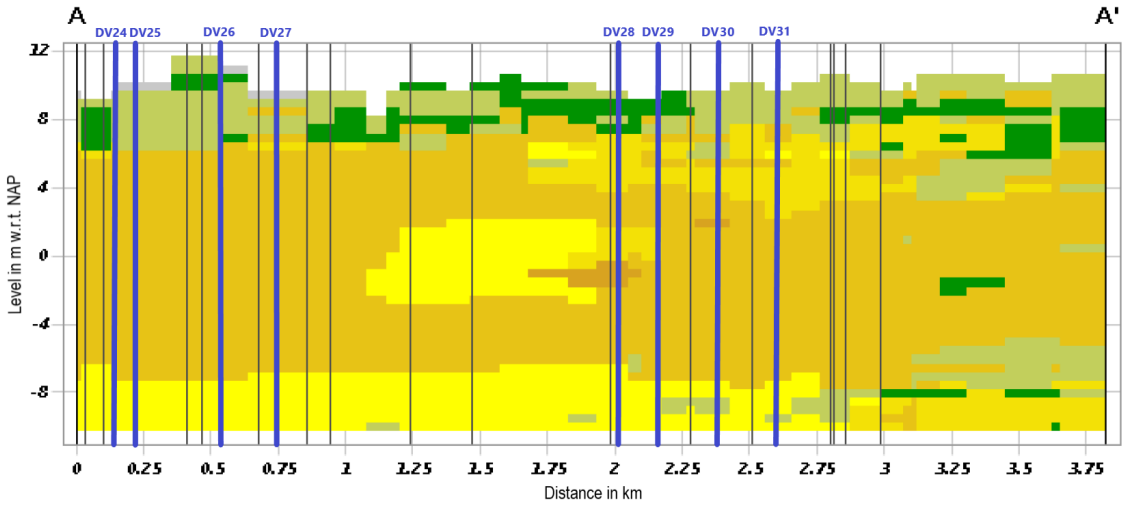

Figure D.12: GeoTOP schematisation for dike section 24-31.

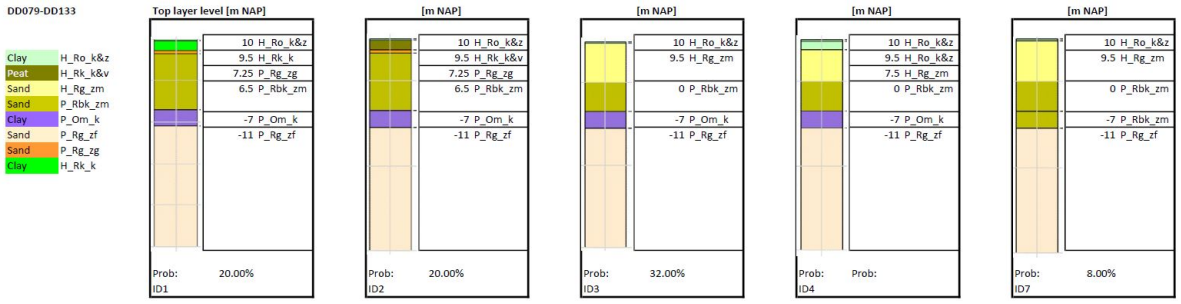

Figure D.13: SOS Schematisation for dike section 16-31.

Table D.2: Spatial correlations between soil layers in dike sections.

Dike sections	Layers
DV1 & DV2	**Dike material**, **silty sandy clay**, silty clay, holocene sand
DV3 & DV4	**Dike material**, **silty sandy clay**, holocene sand
DV4 & DV5	Dike material, **silty clay**, **silty sandy clay**, holocene sand
DV5 & DV6	holocene sand
DV7 & DV8	**Dike material**, silty sandy clay, holocene sand
DV9 & DV10	**Dike material**, **silty sandy clay**, silty clay, holocene sand
DV11 & DV12	Holocene sand
DV12 & DV13	Holocene sand
DV14 & DV15	Holocene sand
DV18 & DV19	**Holocene sand**, silty sandy clay
DV19 & DV20	Silty sandy clay, **holocene sand**
DV20 & DV21	Holocene sand
DV21 & DV22	Holocene sand
DV22 & DV23	**Dike material**, silty sandy clay
DV24 & DV25	**Dike material**, **silty sandy clay**, holocene sand
DV25 & DV26	**Silty sandy clay**, holocene sand
DV26 & DV27	**Silty sandy clay**, holocene sand
DV28 & DV29	**Dike material**, silty clay, holocene sand
DV29 & DV30	Holocene sand
DV30 & DV31	Silty sandy clay, **silty clay**, holocene sand

E

Detailed Results

E.1. Correlations between Variables

E.1.1. Piping

Table E.1: Summary of the impact of several correlations on the failure probabilities of the piping sub-mechanisms.

Correlated parameters	Mean relative difference w.r.t. uncorrelated situation					
	Heave		Uplift		Backward erosion	
	$\rho = 0.2$	$\rho = 0.8$	$\rho = 0.2$	$\rho = 0.8$	$\rho = 0.2$	$\rho = 0.8$
k - d_{70}	-0.0015%	+0.0058%	+0.050%	+0.12%	-43.2%	-11.3%
Φ_{exit} - h_p	+6.3%	+1.1%	-1.7%	-0.44%	+0.28	+0.12%
Φ_{exit} - k	-0.028%	+0.017%	+0.019%	-0.017%	+0.13%	-0.30%
Φ_{exit} - D	-0.023%	-0.012%	+0.015%	+0.056%	-0.022%	-0.29%
Φ_{exit} - D_{cover}	+2.0%	+0.33%	-5.7%	-1.2%	+0.13%	-0.10%

1. Hydraulic conductivity k - grain size d_{70}

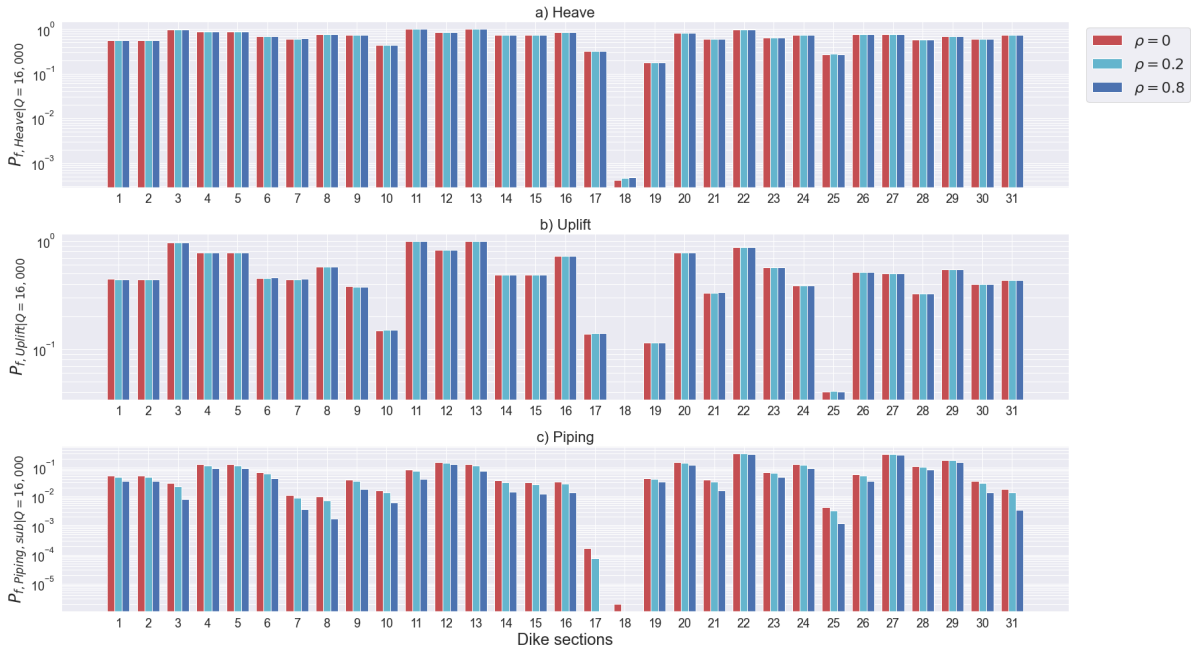

Figure E.1: Sensitivity analysis into the impact of different scenarios of the correlation between k and d_{70} on the sectional failure probabilities due to the sub-mechanisms of piping, conditional on a river discharge of $Q = 16,000$ m^3/s and for $N = 400,000$.

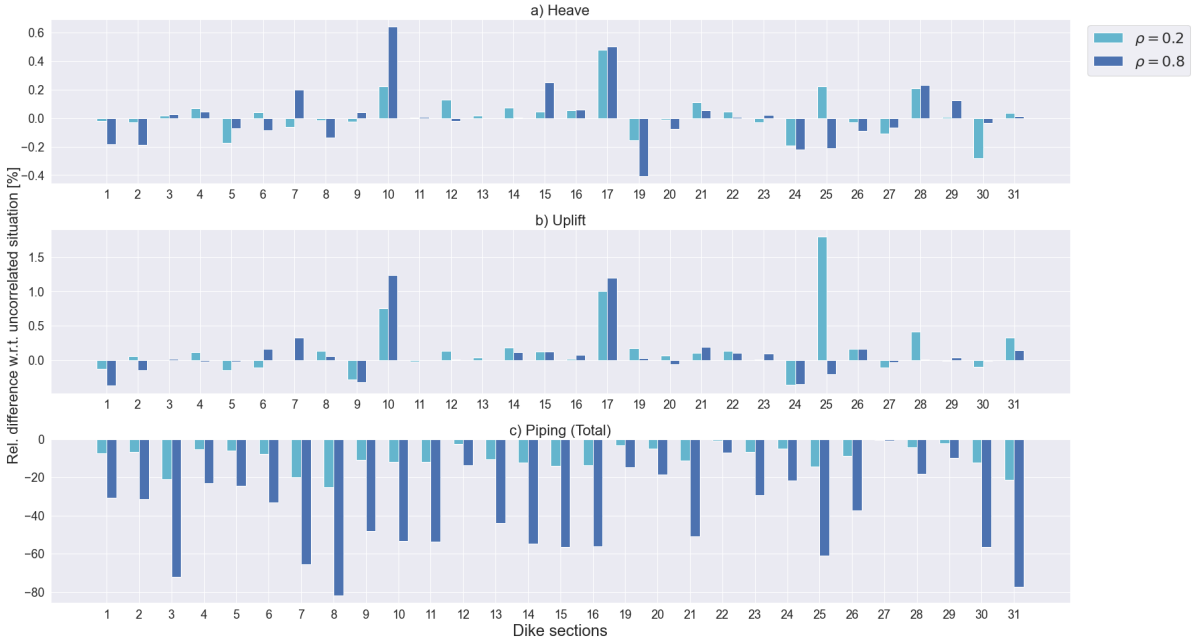

Figure E.2: Relative differences in % between the situations with correlation between k and d_{70}, compared to the situation with no correlation. The figures correspond to the sectional failure probabilities due to the sub-mechanisms uplift and heave and the failure probabilities due to piping in total, conditional on $Q = 16,000$ m^3/s and $N = 400,000$.

2. h_p - Φ_{exit}

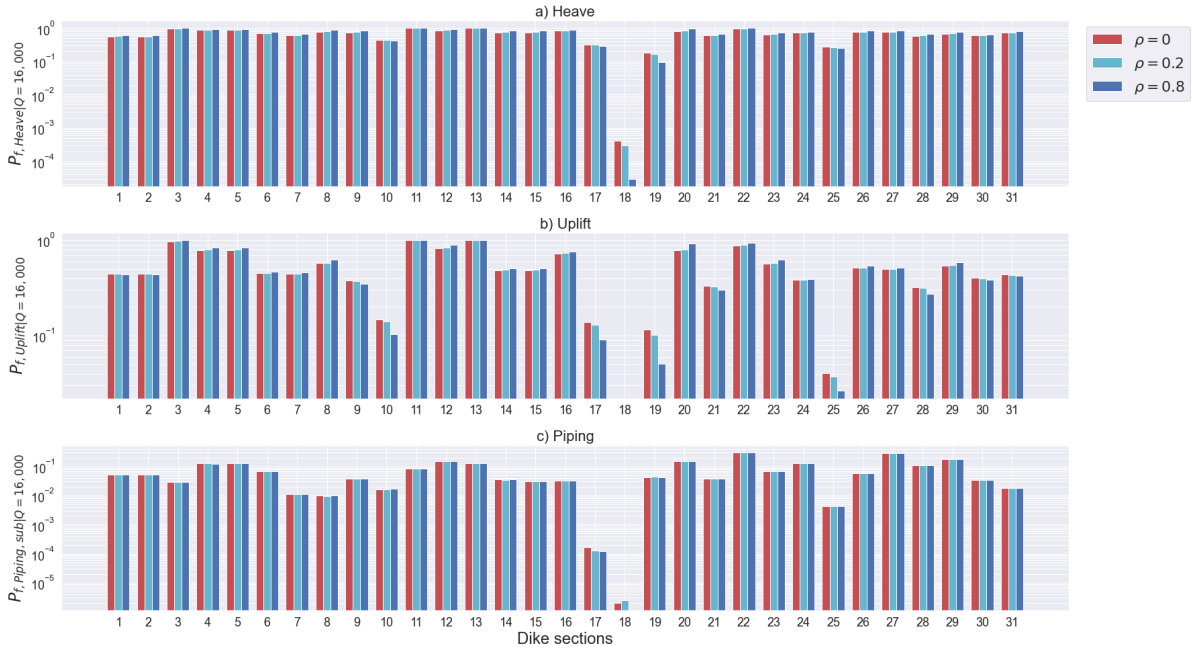

Figure E.3: Sensitivity analysis for correlations between h_p and Φ_{exit} for the sub-mechanisms of piping, conditional on a discharge $Q = 16,000$ m^3/s and $N = 400,000$.

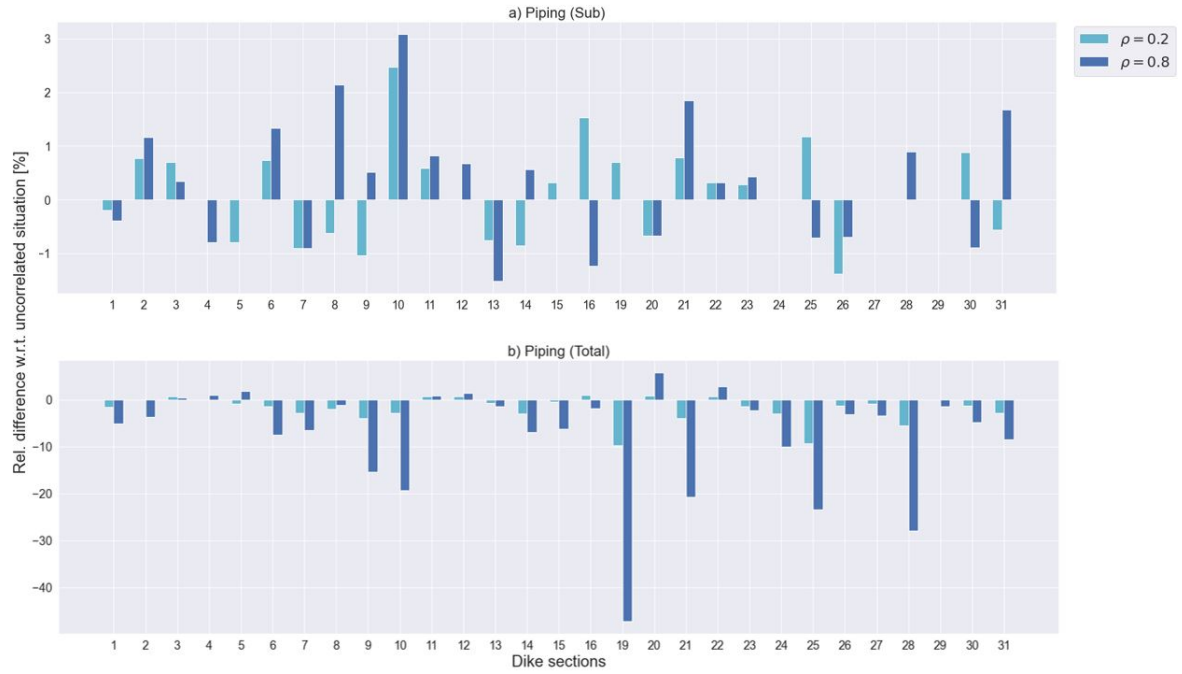

Figure E.4: Relative difference between the failure probabilities including correlation between h_p and Φ_{exit} for the sub-mechanism backward erosion and the total failure mechanism piping, with respect to the situation with no correlation, in percentages..

2. d - Φ_{exit}

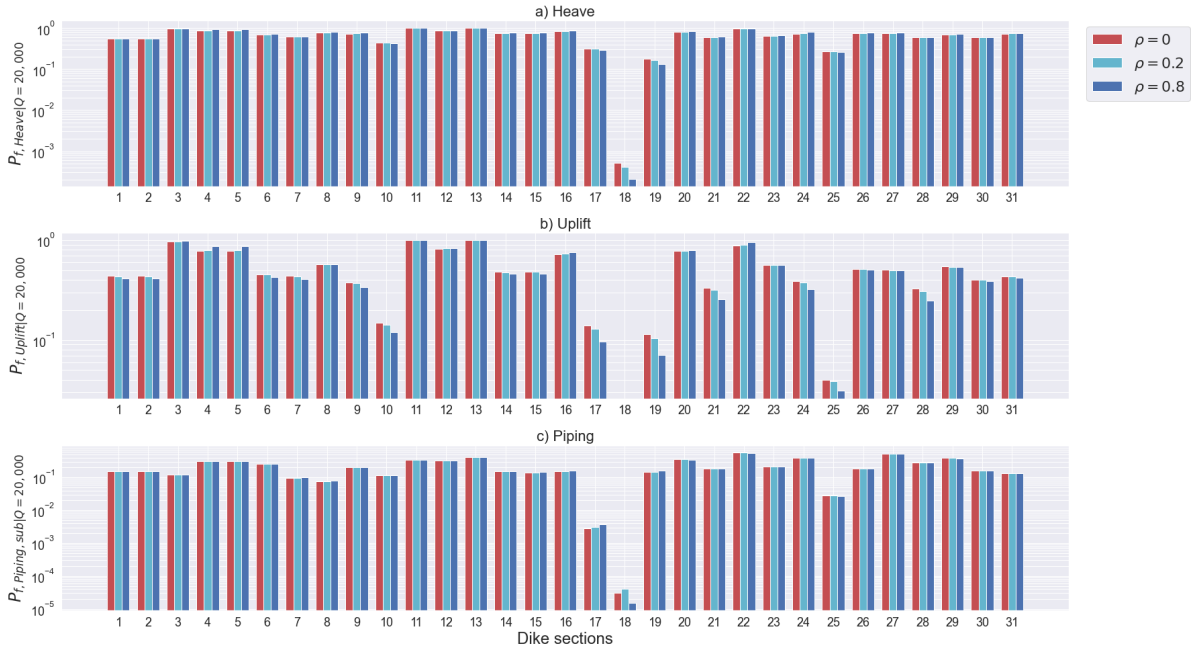

Figure E.5: Sensitivity analysis for correlations between d and Φ_{exit} for the sub-mechanisms of piping, conditional on a discharge $Q = 20,000$ m^3/s and $N = 400,000$..

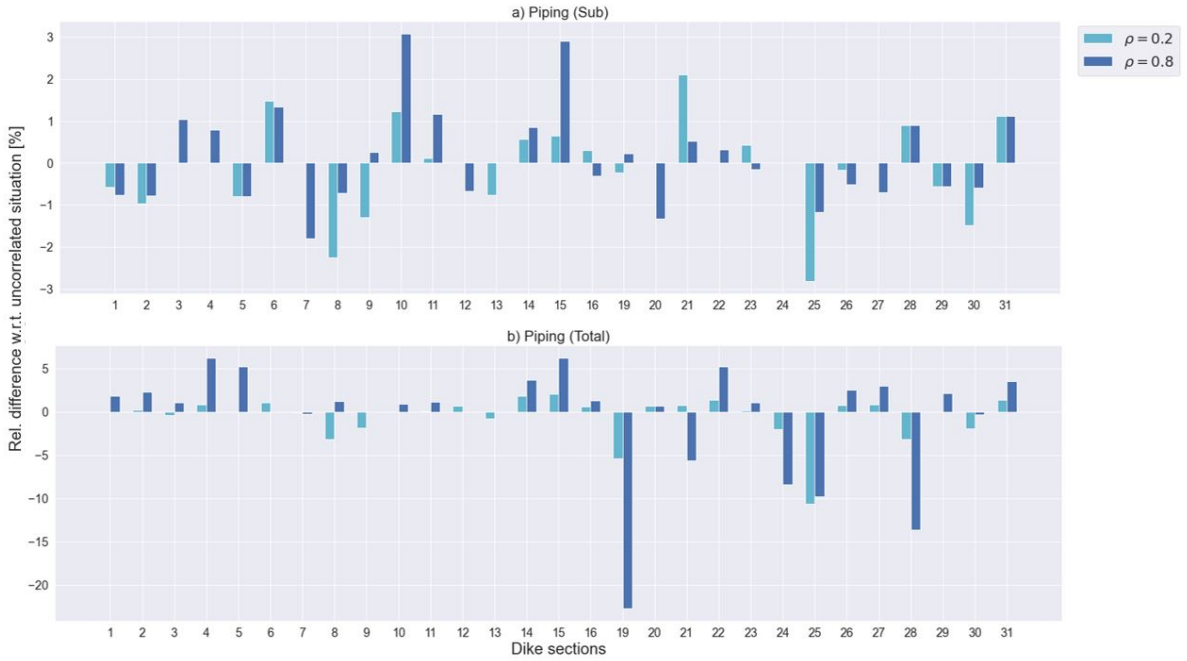

Figure E.6: Relative difference between the failure probabilities for the sub-mechanism backward erosion and the total failure mechanism piping including correlation between d and Φ_{exit}, with respect to the situation with no correlation, in percentages..

3. D - Φ_{exit}

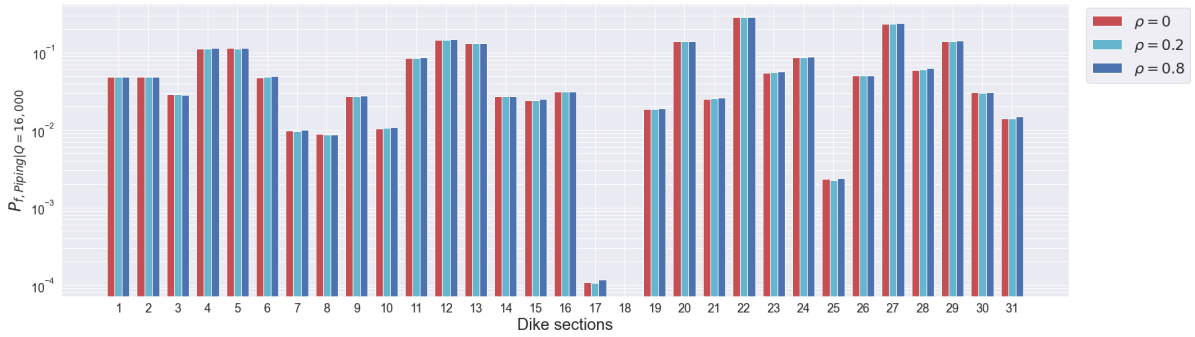

Figure E.7: Sensitivity analysis for correlations between D and Φ_{exit} for the failure mechanism piping, conditional on a discharge $Q = 16,000$ m^3/s, for $N = 400,000$.

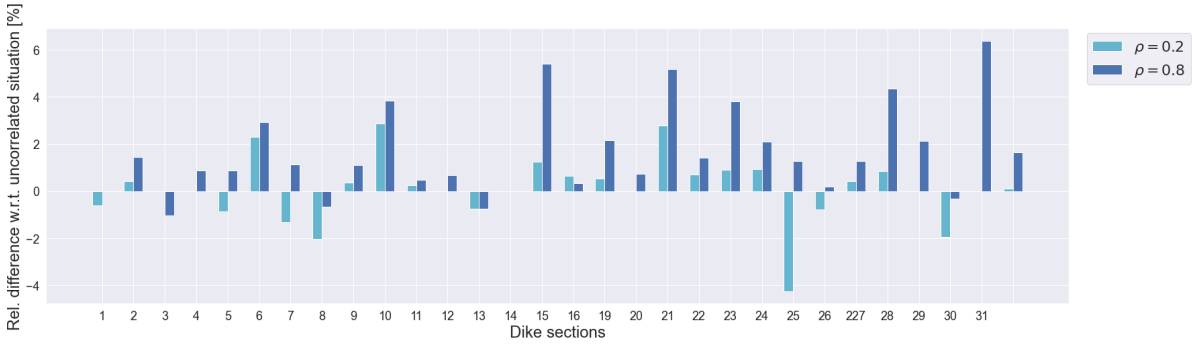

Figure E.8: Relative difference in % between the piping failure probabilities including correlation between D and Φ_{exit}, with respect to the situation with no correlation.

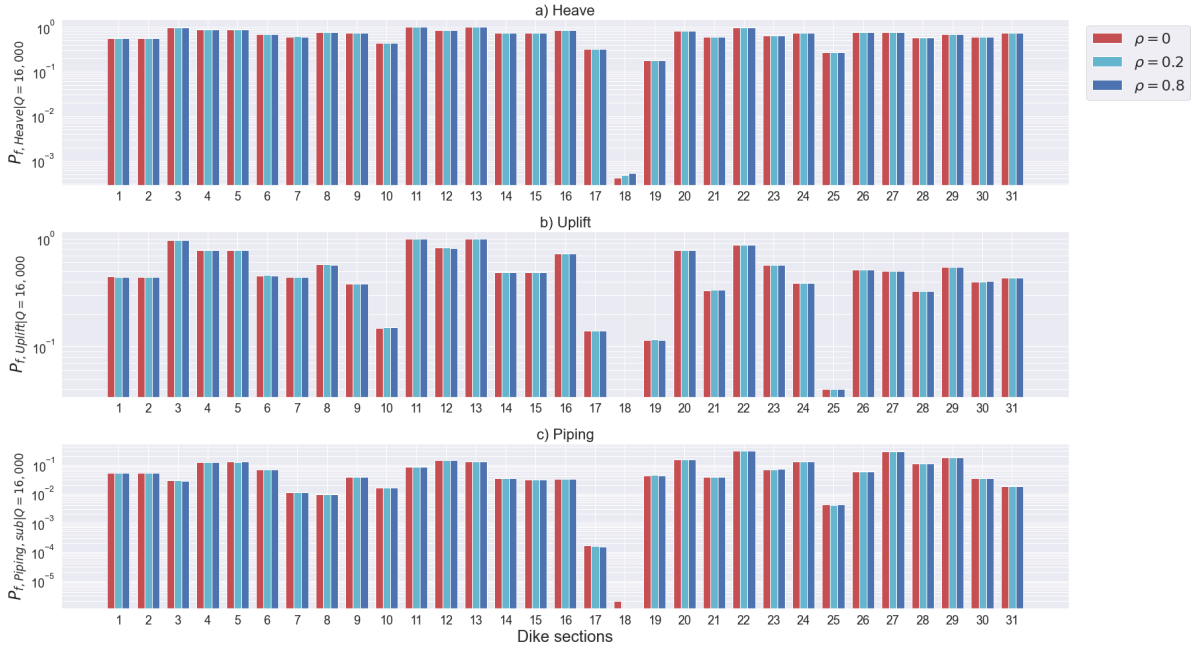

Figure E.9: Sensitivity analysis for correlations between D and Φ_{exit} for the sub-mechanisms of piping, conditional on a discharge $Q = 16,000$ m^3/s and $N = 400,000$.

Figure E.10: Relative difference between the failure probabilities including correlation between D and Φ_{exit} for the sub-mechanisms of piping, with respect to the situation with no correlation, in percentages..

3. k - Φ_{exit}

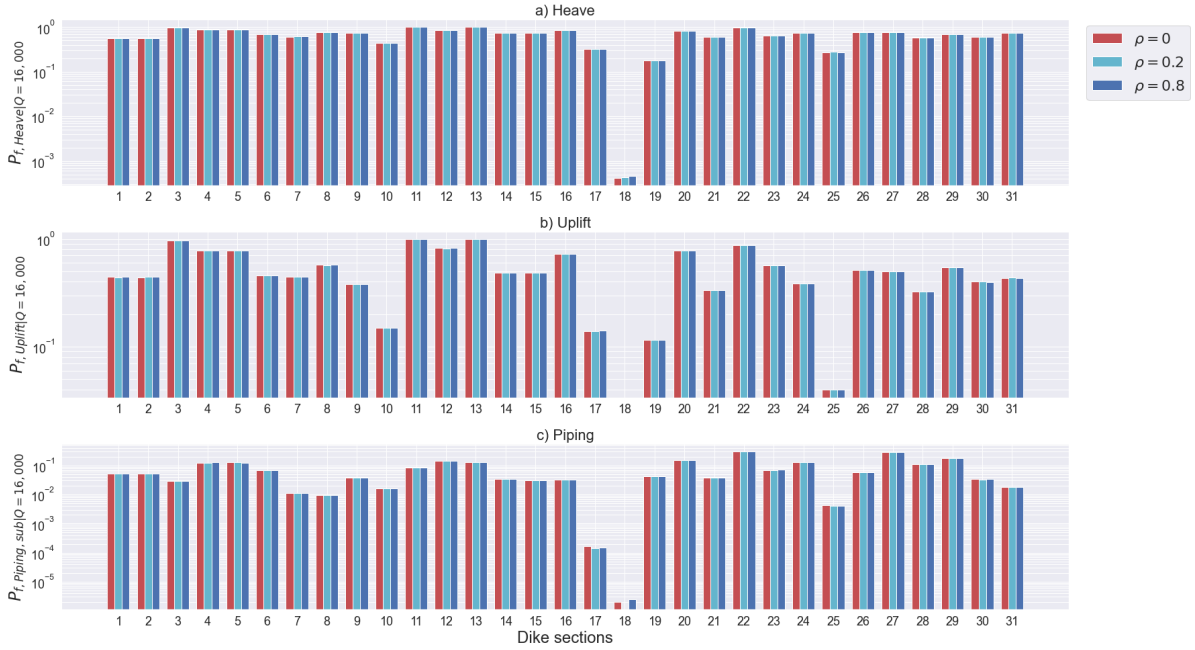

Figure E.11: Sensitivity analysis for correlations between k and Φ_{exit} for the sub-mechanisms of piping, conditional on a discharge $Q = 16,000$ m^3/s and $N = 400,000$.

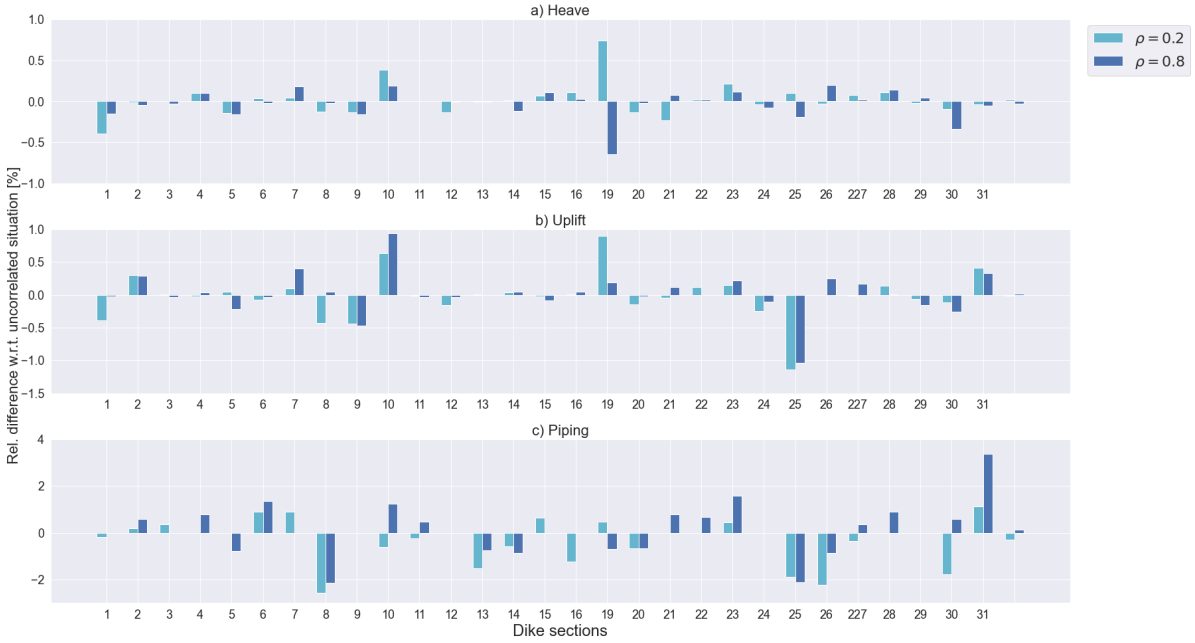

Figure E.12: Relative difference between the failure probabilities of the sub-mechanisms of piping including correlation between k and Φ_{exit}, with respect to the situation with no correlation, in percentages..

4. k_{v3} - Φ_{exit}

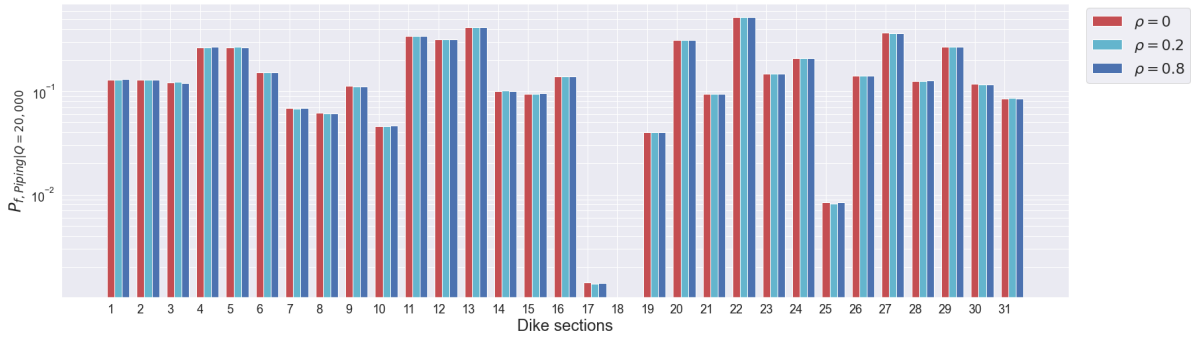

Figure E.13: Sensitivity analysis for correlations between k_{v3} and Φ_{exit} for the failure mechanism piping, conditional on a discharge $Q = 20,000$ m^3/s, for $N = 400,000$.

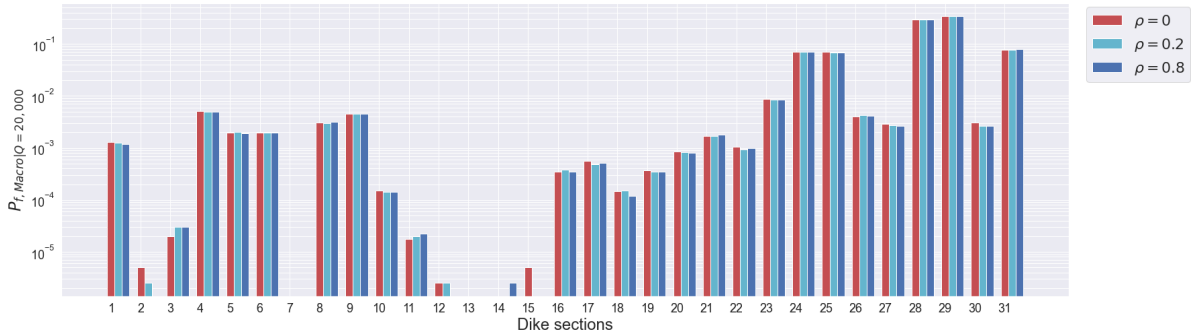

Figure E.14: Sensitivity analysis for correlations between k_{v3} and Φ_{exit} for the failure mechanism macrostability, conditional on a discharge $Q = 20,000$ m^3/s, for $N = 400,000$.

E.1.2. Macrostability

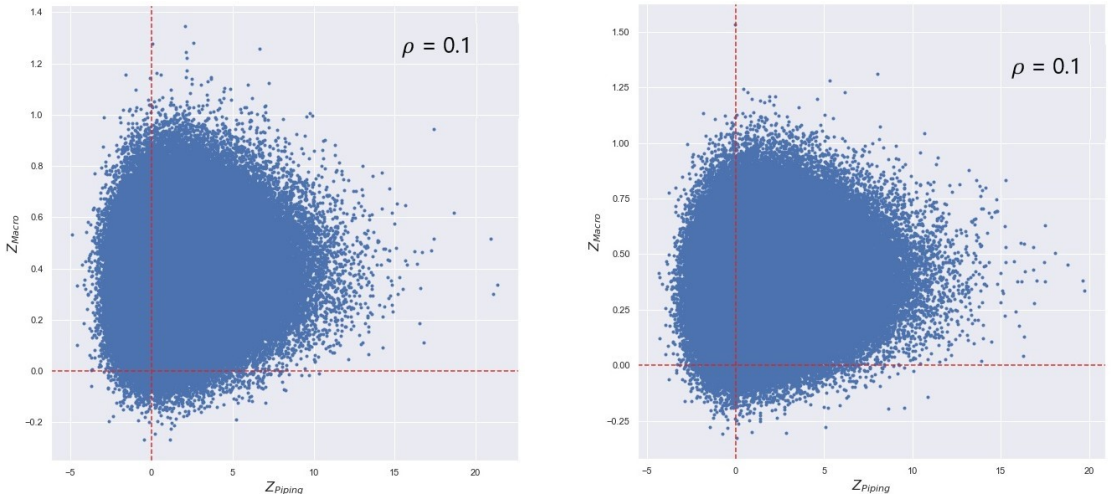

(a) Correlation of $\rho = 0.8$ between S and γ.

(b) Correlation $\rho = 0.8$ between φ and γ.

Figure E.15: Resulting dependencies between the failure mechanisms piping and macrostability for dike section 9, conditional on a discharge $Q = 20,000$ m^3/s, for $N = 400,000$.

E.1.3. Impact for varying water level

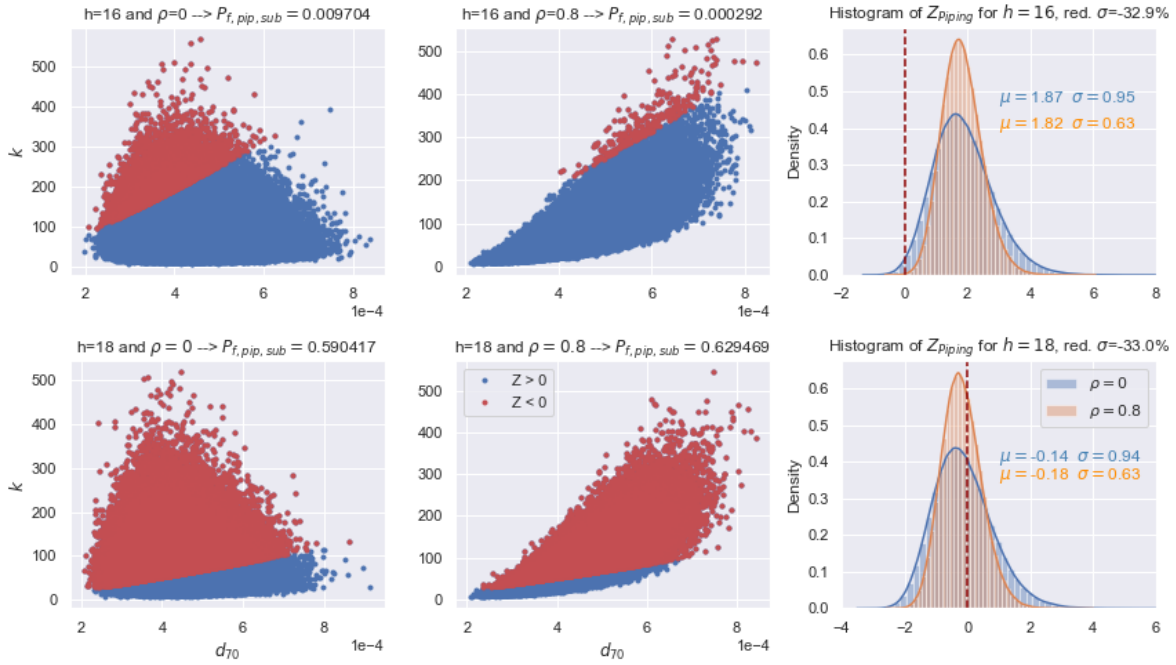

Figure E.16: Scatter plots of the realisations of k and d_{70} for the uncorrelated case (left column) and for the correlated case ($\rho = 0.8$, center column), for a water level of $h = 16$ and $h = 18$. The realisations that lead to a $Z < 0$ are shown in red. The right column shows the histograms of the resulting Z-values for piping, in orange for the correlated case and in blue for the uncorrelated case. The red dotted line indicates the limit state $Z = 0$. A coefficient of variance of $CV = 0.5$ is used for k .

List of Symbols and Abbreviations

Abbreviations

BOI	Beoordelings- en Ontwerpinstrumentarium
CDF	Cumulative distribution function
CSSM	Critical State Soil Mechanics
FORM	First Order Reliability Method
GABI	Gras erosie binnentalud = erosion of the inner slope grass revetment
GEBU	Gras erosie buitentalud = erosion of the grass revetment at the outer slope
GEKB	Gras erosie kruin en binnentalud = Erosion of the crest and inner slope grass revetment
GEV	Generalized Extreme Value distributions
GP	Gaussian processes
GPR	Gaussian Process Regression
GRADE	Generator of Rainfall and Discharge Extremes
HBN	Hydraulisch Belasting Niveau
HLCD	Hydraulic Loads Configuration Database
KNMI	Koninklijk Nederlands Meteorologisch Instituut = Dutch Institute for Meteorology
LEM	Limit Equilibrium Models
LHS	Latin hypercube sampling
MCS	Monte Carlo simulations
NAP	Normaal Amsterdams Peil = mean sea level
OAT	One-At-a-Time method for sensitivity analysis
PDF	Probability density function
RMSE	Root Mean Square Error
SHANSEP	Stress History and Normalised Soil Engineering Properties
SOS	Stochastische Ondergrond Schematisatie = Stochastic suboil schematisation
STBI	Stabiliteit binnenwaarts = inner slope stability
STMI	Micro-instability
STPH	Stabiliteit na piping en opbarsten (heave) = stability after piping and heave
SWL	Still water level
TAW	Technische adviescommissie voor de waterkeringen
TRWD	Technisch Rapport Waterspanningen bij Dijken
WBI	Wettelijk Beoordelingsinstrumentarium
WSRL	Waterschap Rivierenland
WTI	Wettelijk Toets Instrumentarium

Symbols

α	Slope angle of the dike	[°]
α_i	FORM influence coefficient of parameter i	-
$\alpha_{M,z}$	Factor for increased load at transitions and objects, $\alpha_{M,z} \geq 1$ (1.0 by default)	-
$\alpha_{S,z}$	Factor for decreased strength at transitions and objects, $\alpha_{S,z} \geq 1$ (1.0 by default)	-
β	Angle of wave attack. $\beta = 0$ for perpendicular wave attack	[°]
β_T	Target reliability index	-
β_{norm}	Required reliability index of the dike trajectory	-
Δh^*	Error in the local water level	$[m]$
Δh_c	Additional height for overflow to occur	$[m]$
ΔT	Time interval	$[hr]$
$\Delta\Phi$	Critical head difference for uplift	$[m]$
ϵ	Error term in regression	-
η	Drag factor coefficient	-
γ	Volumetric weight of the soil	$[kN/m^3]$
γ_b	Reduction factor for the presence of a berm	-
γ_d	Model factor	-
γ_f	Reduction factor for the roughness of the slope	-
γ_i	Safety factor of parameter i	-
γ_s	Volumetric weight of sand grains (= 26.5)	$[kN/m^3]$
γ_v	Reduction factor for the presence of a wall	-
γ_w	Saturated volumetric weight of water (= 10)	$[kN/m^3]$
γ_β	Reduction factor for oblique waves	-
γ_{sat}	Saturated volumetric weight of the aquitard	$[kN/m^3]$
$\hat{B}$	Intersection point for breaking and non-breaking waves	$[m + NAP]$
λ	Damping factor	-
λ_h	Leakage-factor for the hinterland section	$[m]$
μ	Mean value	-
ω_j	Contribution of failure mechanism j to the failure probability	-
$\mathrm{cov}(XY)$	Covariance batween the stochastic variables X and Y	-
Φ	Standard (cumulative) normal distribution	-
Φ_{exit}	Potential at the exit point	$[m]$
ψ	Angle of dilatancy	[°]
ψ	Orientation of the dike normal	$[°N]$
ρ	Pearson's correlation-coefficient	-
$\rho_k(\Delta x)$	Correlation of stochastic variable X_k between cross-sections with distance Δx	-
$\rho_{x,k}$	Residual correlation of variable X_k	-
Σ	Covariance matrix	-

σ	Standard deviation	-
σ'	Vertical effective stress along a slip plan	$[kPa]$
$\sigma'_{v,i}$	In-situ effective vertical stress	$[kPa]$
$\sigma'_{v,y}$	Vertical yield stress	$[kPa]$
τ	Kendall's correlation coefficient	-
τ	Shear stress of the soil	$[kPa]$
θ	Bedding angle	$[°]$
υ	kinematic viscosity of water ($= 1.33 \cdot 10^{-6}$)	$[m^2/s]$
φ	Friction angle of the soil	$[°]$
φ	Wave direction	$[°N]$
$\xi_{m-1,0}$	Breaker parameter based on the spectral period	-
B	Width of the dike	$[m]$
B_t	Width of the erosion terrace of a sandy dike	$[m]$
c	Cohesive strength of the soil	$[kPa]$
$C(u, v; \theta)$	Copula with parameter θ representing the dependence structure	-
c_d	Correction factor for the sand content of the clay	-
CV	Coefficient of variation	-
D	Thickness of the aquifer	$[m]$
d	Thickness of the hinterland aquitard at the exit point	$[m]$
d	Water depth	$[m]$
d_c	Thickness of the top and underlying clay layer	$[m]$
d_e	Erosion depth	$[m]$
D_f	The unsafe domain	-
d_{70m}	Reference value for d_{70}	$[m]$
d_{70}	70%-fraction of the grain size distribution	$[m]$
D_{crit}	Critical value for the cumulative overload for wave run-up	$[m^2/s^2]$
$D_{load,z}$	Cumulative overload at level z	$[m^2/s^2]$
$d_{x,k}$	Correlation length	$[m]$
$E(XY)$	Expectation or mean of X	-
F	Effective fetch length	$[m]$
f_b	Model factor for breaking waves	-
f_n	Model factor for non-breaking waves	-
$f_S(x)$	Sampling probability density function for importance sampling in MCS	-
F_X	Cumulative distribution function of X	-
f_β	Reduction factor for the angle of wave attack	-
F_{f,cmb,z_j,t_i}	Failure fraction of the combination of top + sub layer at level z_j for time interval t_i	-
F_{f,cum,top,z_j,t_i}	Cumulative failure fraction of top layer for level z_j for all time intervals before t_i	-

$F_{f,storm,z_j}$	Cumulative failure fraction over the time intervals of a storm, for evaluation level z_j	-
F_{f,top,z_j,t_i}	Contribution of time interval t_i to failure fraction of top layer at evaluation level z_j	-
$f_{RS}(r,s)$	Joint probability density function of the resistance and load	-
f_{runupi}	Model factors for wave run-up	-
F_{sand}	Sand fraction in the clay	-
$f_{shallow}$	Model factor for shallow water waves	-
FoS	Factor of safety	-
FoS_h	Factor of safety for heave	-
FoS_p	Factor of safety for backward erosion	-
FoS_u	Factor of safety for uplift	-
$FoS_{d;i}$	Stability factor for scenario i, based on the design value for the shear strength	-
g	Gravitational acceleration	$[m/s^2]$
H	Head difference between the water and land side	$[m]$
h	Still river water level with respect to mean sea level	$[m+NAP]$
$H(x,y)$	Joint cumulative distribution function of random vector (X,Y) of continuous variables	-
h_a	Actual water level	$[m]$
H_c	Critical head difference	$[m]$
h_c	Crest height of the dike	$[m]$
h_p	Phreatic level of the hinterland with respect to mean sea level	$[m+NAP]$
H_{m0}	Spectral significant wave height	$[m]$
$i_{c,h}$	Critical heave gradient	-
k	Hydraulic conductivity of the aquifer	$[m/s]$
$k(x_i,x_j)$	Covariance / kernel function	-
k_h	Hydraulic conductivity of the hinterland section	$[m/s]$
L	Seepage length	$[m]$
L_f	Length of the effective foreshore	$[m]$
m	Strength increase exponent	-
m^3/s	Erosion coefficient of the clay type	$[m^3/s]$
m_a	Model factor for the actual overtopping discharge	-
m_c	Model factor for the critical overtopping discharge	-
m_d	Model uncertainty factor for macrostability	-
m_p	Model factor for backward erosion	-
M_R	Resisting moment for slope stability	$[kNm]$
M_S	Driving moment for slope stability	$[kNm]$
m_u	Model factor for uplift	-
m_{z2}	Model factor describing the uncertainty of the wave run up $z_{2\%}$	-
N	Number of incident waves	-

N	Number of iterations of the Monte Carlo simulation	-
n	Porosity	-
N_f	Number of realisations of the Monte Carlo simulation that lead to failure	-
N_j	Length-effect factor of element j	-
OCR	Over-consolidation ratio	-
$P(Q_i)$	Probability of occurrence of river discharge Q_i	$[1/year]$
$P(S_i)$	Probability of occurrence of scenario i	$[1/year]$
$P_{f,i}$	Failure probability of element i	$[1/year]$
$P_{f;cs}$	Failure probability per cross-section	$[1/year]$
$P_{f;i}$	Probability of failure of scenario / element / mechanism i	$[1/year]$
$P_{f;trajectory}$	Failure probability of a dike trajectory	$[1/year]$
P_{req}	Required failure probability for an entire flood defence system	$[1/year]$
POP	Pre-overburden pressure	$[kPa]$
q_a	Actual overtopping discharge	$[m^3/s/m]$
Q_b	Dimensionless overtopping discharge for breaking waves	-
q_c	Critical overtopping discharge	$[m^3/s/m]$
Q_n	Dimensionless overtopping discharge for non-breaking waves	-
R	Resistance	-
R_c	Crest freeboard	$[m]$
$r_{X,Y}$	Spearman's tank correlation coefficient between two stochastic variables X and Y	-
Ru_i	Run-up level with respect to the still water level	$[m]$
$Ru_{2\%}$	2% run-up height, relative to the still water level	$[m]$
S	Load	-
S	Undrained shear strength ratio (normally consolidated)	-
s_u	Undrained shear strength of soils according to CSSM	$[kPa]$
s_{op}	Wave steepness	-
t_i	Time interval i of stationary hydraulic loads at the toe of the dike	$[s]$
T_m	Mean wave period	$[s]$
T_p	Wave spectral peak period	$[s]$
t_{load,z_j,t_i}	Load duration of time interval t_i at evaluation level z_j	$[hr]$
$T_{m-1,0}$	Spectral wave period	$[s]$
t_{s,sub,z_j,t_i}	Strength duration of the sub layer during time interval t_i at evaluation level z_j	$[hr]$
t_{s,top,z_j,t_i}	Strength duration of top layer in time interval t_i at evaluation level z_j	$[hr]$
U	Standard normal space	-
u	Wind speed	m/s
U_c	Critical front velocity along the dike slope	$[m/s]$
$U_{i,z}$	Front velocity along the slope of running-up wave i at level z	$[m/s]$

U_{max}	Maximum front velocity of a running-up wave	$[m/s]$
V_e	Erosion volume of the clay	$[m^3/m]$
V_{P_f}	Coefficient of variation of the resulting failure probability from MCS	-
X	Random variable or stochastic parameter	-
x_{exit}	Distance of the exit point from the center of the dike footprint	$[m]$
y_N	Crest level with respect to mean sea level	$[m + NAP]$
Z	Limit state function	-
Z_h	Limit state function for heave	-
z_j	Evaluation level j at the outer dike slope	$[m + NAP]$
Z_p	Limit state function for backward erosion	$[m]$
Z_u	Limit state function for uplift	$[m]$
$z_{2\%}$	2% wave run-up	$[m + NAP]$
z_{eval}	Level of interest on the outer dike slope for wave run-up	$[m + NAP]$
Z_{impact}	Limit state function for wave impact	-
$Z_{j,k}$	Limit state function for failure mechanism j of dike section k	-
Z_{macro}	Limit state function for macrostability	-
$Z_{overflow}$	Limit state function for overflow	$[m]$
$Z_{overtopping}$	Limit state function for overtopping	$[m^3/s/m]$
Z_{run-up}	Limit state function for wave run-up	$[m^2/s^2]$

List of Figures

List of Tables